



Universiteit
Leiden
The Netherlands

Using functional genetic screens to understand and overcome PARP inhibitor resistance

Paes Lobo Lopes Dias, M.

Citation

Paes Lobo Lopes Dias, M. (2023, January 18). *Using functional genetic screens to understand and overcome PARP inhibitor resistance*. Retrieved from <https://hdl.handle.net/1887/3512289>

Version: Publisher's Version

License: [Licence agreement concerning inclusion of doctoral thesis in the Institutional Repository of the University of Leiden](#)

Downloaded from: <https://hdl.handle.net/1887/3512289>

Note: To cite this publication please use the final published version (if applicable).

USING FUNCTIONAL GENETIC SCREENS TO UNDERSTAND AND OVERCOME PARP INHIBITOR RESISTANCE

Mariana Paes Lobo Lopes Dias



Mind the ssDNA GAP

Mariana Paes Lobo Lopes Dias

**Using functional genetic screens
to understand and overcome PARP
inhibitor resistance**

2022

About the cover:

One of the main findings of this thesis is that induction of post-replicative single-stranded DNA (ssDNA) gaps can revert resistance to PARP inhibitors in cancer cells. This cover depicts a subway-like network where each line represents a replicating DNA strand. Divergent lines represent replication forks and spaces between thinner lines indicate the ssDNA gaps. The “Mind the ssDNA gap” symbol alludes to the widely known London Tube “Mind the gap” warning.

Cover design: Ilse Modder | www.ilsemodder.nl

Cover concept: Mariana Paes Lobo Lopes Dias

Thesis lay-out: Ilse Modder | www.ilsemodder.nl

Printing: Gildeprint Enschede | www.gildeprint.nl

© Copyright, Mariana Paes Lobo Lopes Dias, 2022

ISBN: 978-94-6419-668-9

All rights reserved. No part of this book may be reproduced in any form or by any means without permission of the author.

Using functional genetic screens to understand and overcome PARP inhibitor resistance

Proefschrift

ter verkrijging van
de graad van doctor aan Universiteit Leiden,
op gezag van rector magnificus prof.dr.ir. H. Bijl,
volgens besluit van het college voor promoties
te verdedigen op woensdag 18 januari 2023
klokke 15:00 uur

door

Mariana Paes Lobo Lopes Dias
geboren te Faro, Portugal
in 1994

Promotor:

Prof.dr. J.M.M. Jonkers

Prof.dr. S. Rottenberg (University of Bern)

Co-promotor:

Dr. R.J.P. Bouwman

Promotiecommissie:

Prof. dr. H. Irth

Prof. dr. J.A. Bouwstra

Prof. dr. H. van Attikum

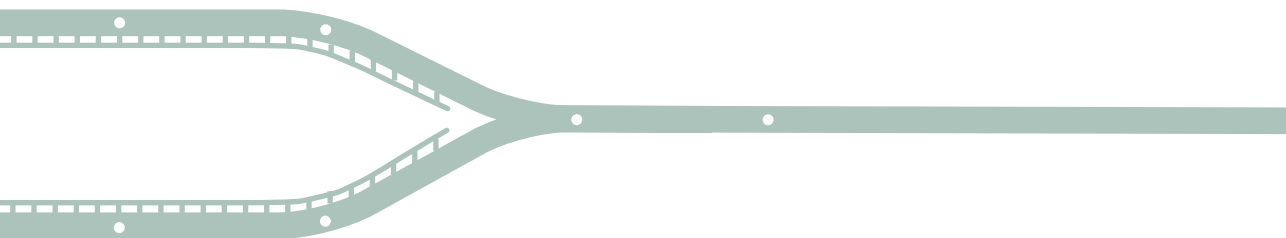
Prof. dr. M. Tijsterman

Dr. J. J. L. Jacobs (Netherlands Cancer Institute)

The research described in this thesis was performed at the Division of Molecular Pathology of the Netherlands Cancer Institute – Antoni van Leeuwenhoek Hospital (NKI-AVL) (Amsterdam, The Netherlands) and was financially supported by the European Union Horizon 2020 research and innovation program under the Marie Skłodowska-Curie grant (agreement 722729) and by the OncoCode Institute and Cancer Genomics Netherlands.

TABLE OF CONTENTS

Chapter 1	Scope of thesis	9
Chapter 2	General introduction: Understanding and overcoming resistance to PARP inhibitors in cancer therapy <i>Nature Reviews Clinical Oncology, 2021, 18,773-791</i>	15
Chapter 3	Multi-omics analysis reveals distinct non-reversion mechanisms of PARPi resistance in BRCA1- versus BRCA2-deficient mammary tumors <i>Submitted, BioRxiv, 2022; 2022.09.07.506927</i>	59
Chapter 4	Loss of nuclear DNA ligase III reverts PARP inhibitor resistance in BRCA1/53BP1 double-deficient cells by exposing ssDNA gaps <i>Molecular Cell, 2021, 81, 4692–4708</i>	93
Chapter 4 addendum	Filling in the gaps in PARP inhibitor-induced synthetic lethality <i>Molecular Cell Oncology, 2021; 8(6):2010512</i>	141
Chapter 5	Genome-wide dropout screens in BRCA1/53BP1 double-deficient cells as an approach to identify vulnerabilities of PARPi-resistant cells <i>Manuscript in preparation</i>	149
Chapter 6	Functional genetic dropout screens and <i>in vivo</i> validation of candidate therapeutic targets using mouse mammary tumoroids. <i>STAR Protocols, 2022, 3(1):101132</i>	185
Chapter 7	General conclusions and discussion	207
Appendices	English summary	222
	Nederlandse samenvatting	224
	Curriculum vitae	226
	List of publications	227



Chapter 1

Scope of the thesis

1

Developing targeted therapies that kill cancer cells while sparing non-malignant tissues is one of the main goals of current cancer research. Many of the currently available targeted therapeutics are inhibitors of oncogenes such as kinases, which have been one of the most successful classes of cancer drugs developed to date. However, strategies to specifically target cancer cells carrying loss-of-function mutations in tumor suppressor genes are less straightforward. After all, how can a mutated protein that is no longer working, or even produced at all, be targeted? The answer to this question relies on the identification of synthetic lethal interactions. Synthetic lethality in a cell or organism describes the situation where a defect in either one of two genes has little or no effect, whereas the combination of defects in both genes results in cell death. This phenomenon was discovered exactly a century ago, in 1922, by the *Drosophila melanogaster* geneticist Calvin Bridges, and the term synthetic lethality was coined a couple of decades later by Theodor Dobzhansky, in 1946^{1,2}. Synthetic lethal relationships create drug discovery opportunities to selectively kill cancer cells carrying loss-of-function mutations while leaving nonmalignant cells largely unaffected. To date, the use of poly(ADP-ribose) polymerase (PARP) inhibitors in patients with homologous recombination (HR)-deficient tumors, such as *BRCA1/2*-mutated cancers, provides one of the best examples of synthetic lethality that has been successfully translated into the clinic^{3,4}.

BRCA1 and *BRCA2* are tumor suppressor genes that, when heterozygously mutated in the germ line, confer a considerably higher risk of breast and ovarian cancer. It is estimated that the cumulative breast cancer risk to age 80 years is 72% for *BRCA1* mutation carriers and 69% for *BRCA2* carriers, whereas the cumulative ovarian cancer risk to age 80 years is 44% for *BRCA1* carriers and 17% for *BRCA2* carriers⁵. While initially associated with hereditary breast and ovarian cancer (HBOC) syndrome, inherited mutations in *BRCA1/2* also predispose to other types of cancer, including prostate and pancreatic cancer⁶. Functional *BRCA1* and *BRCA2* proteins are crucial for the error-free repair of DNA double-strand breaks (DSBs) by HR and, consequently, for the maintenance of genomic stability⁷. Tumors arising in *BRCA1/2* mutation carriers frequently show loss of the wild-type allele and therefore cannot employ HR to repair DSBs, a defect that renders cells vulnerable to PARPi. Inhibition of PARP leads to collapsed replication forks and consequently to an increase in DSBs during the S phase of the cell cycle. *BRCA1/2*-deficient tumor cells can only resolve PARPi-induced DSBs via error-prone mechanisms, resulting in an accumulation of chromosomal rearrangements that ultimately leads to mitotic catastrophe.

The success of PARPi-induced synthetic lethality in *BRCA1/2*-deficient tumors has so far led to the approval of four different PARPi for the treatment of patients with advanced breast, ovarian, pancreatic and prostate cancers. Unfortunately, despite initial and often dramatic responses, patients receiving PARPi often develop resistance to the treatment. The major focus of my thesis is to understand the molecular mechanisms behind PARPi resistance in order to improve patient stratification and to find combination treatments to overcome resistance to PARPi by preventing, delaying or targeting resistant clones.

Chapter 2 provides a general introduction to this topic and a comprehensive summary of the currently known processes underlying PARPi resistance. Chapter 2 also discusses the potential strategies that might overcome PARPi resistance, such as combinations with chemotherapies, targeting the acquired vulnerabilities of PARPi-resistant tumors and suppressing the mutator phenotype of *BRCA1/2*-mutated tumors.

Preclinical studies have identified several PARPi resistance mechanisms, such as upregulation of drug efflux transporters, drug target-related mechanisms, restoration of HR via *BRCA1/2* reactivation or via loss of DNA end-protection, and restoration of replication fork stability⁷. Yet, for most of these mechanisms, their relevance in the clinic remains elusive. In **Chapter 3**, we combined molecular profiling and functional analysis of the HR status of a unique collection of matched PARPi-naïve and PARPi-resistant tumors derived from genetically engineered mouse models (GEMMs) of *BRCA1/2*-associated breast cancer to investigate which *BRCA1/2*-independent mechanisms drive spontaneous resistance *in vivo*. While HR restoration was observed in the majority of PARPi-resistant *BRCA1*-mutated tumors, our data strongly suggests that HR cannot be reactivated in the absence of *BRCA2*. Moreover, our data suggests that 53BP1 loss is the prevalent resistance mechanism in HR-restored *BRCA1*-deficient tumors, whereas resistance in *BRCA2*-deficient tumors is mainly induced by PARG loss. These results may help the investigation of *BRCA1/2*-independent PARPi resistance in the clinic.

Preclinical studies have shown that HR can be restored in *BRCA1*-deficient cells through the loss of components of the 53BP1-RIF1-Shieldin DNA end-protection complex, resulting in PARPi resistance^{8–16}. In **Chapter 4** and **Chapter 5**, we used functional genetic dropout screens to identify vulnerabilities of *BRCA1/53BP1* double-deficient cells that could potentially be exploited therapeutically to overcome PARPi resistance. In **Chapter 4**, we used a DNA damage response (DDR) library and identified nuclear DNA ligase III (LIG3) as a critical mediator of PARPi resistance in *BRCA1/53BP1* double-deficient cells *in vitro* and *in vivo*, rendering LIG3 a potential therapeutic target. Importantly, loss of nuclear LIG3 does not revert HR restoration but exposes cells to MRE11-mediated post-replicative single-stranded DNA (ssDNA) gaps upon treatment with PARPi, leading to accumulation of chromosomal abnormalities and cell death. Moreover, this work suggests that ssDNA gaps are a novel determinant of PARPi response which creates new opportunities for designing combination therapies (**Chapter 4 addendum**). In **Chapter 5**, we looked beyond the DDR domain by using a genome-wide library to screen for acquired vulnerabilities of *BRCA1/53BP1* double-deficient cells. We found that loss-of-function of multiple candidate genes improved response to PARPi, with the majority of the hits associated with DDR, including recombination and meiosis genes such as *GGNBP2* and *SWAP1*. These results suggest that rewiring of DDR is the most promising approach of reverting PARPi resistance in *BRCA1/53BP1* double-deficient cells. Nevertheless, we also identified candidate genes not involved in DDR, including many subunits from mitochondrial Complex I. Unfortunately, individual validation of these subunit genes was technically hard to achieve and further

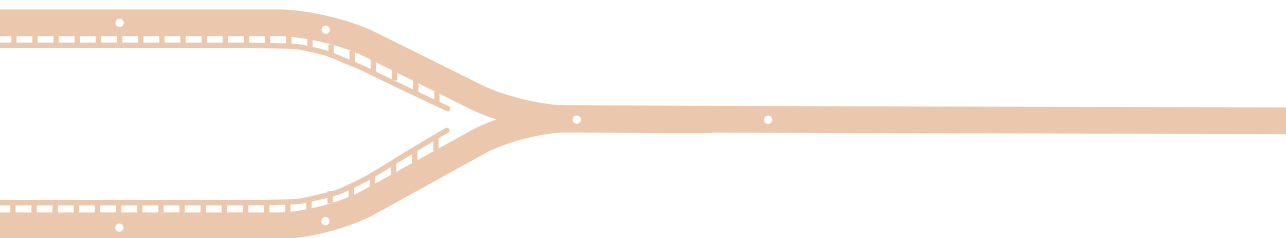
studies are required to understand how inactivation of complex I of the mitochondrial respiratory chain can modulate PARPi response.

Finally, in **Chapter 6** we describe a detailed protocol for the use of three-dimensional (3D) mouse mammary tumoroids (tumor-derived organoids) to carry out functional genetic dropout screens and orthotopic transplantations in mice. These 3D tumoroids may be used to screen for new therapeutic targets to improve response to PARPi. In addition, they allow rapid and straightforward *in vivo* validation of candidate genes.

Altogether, the work described in this thesis extends our knowledge of the mechanisms behind PARPi response and resistance, and identifies potential therapeutic candidates to improve response to this tailored therapy. **Chapter 7** provides a general discussion in which we highlight some of the remaining questions.

REFERENCES

1. Bridges, C. B. The Origin of Variations in Sexual and Sex-Limited Characters. *Am. Nat.* **56**, 51–63 (1922).
2. Dobzhansky, T. Genetics of natural populations; recombination and variability in populations of *Drosophila pseudoobscura*. *Genetics* **31**, 269–290 (1946).
3. Farmer, H. *et al.* Targeting the DNA repair defect in BRCA mutant cells as a therapeutic strategy. *Nature* **434**, 917–921 (2005).
4. Bryant, H. E. *et al.* Specific killing of BRCA2-deficient tumours with inhibitors of poly(ADP-ribose) polymerase. *Nature* **434**, 913–917 (2005).
5. Kuchenbaecker, K. B. *et al.* Risks of Breast, Ovarian, and Contralateral Breast Cancer for BRCA1 and BRCA2 Mutation Carriers. *JAMA* **317**, 2402–2416 (2017).
6. Pilarski, R. The Role of BRCA Testing in Hereditary Pancreatic and Prostate Cancer Families. *Am. Soc. Clin. Oncol. Educ. book. Am. Soc. Clin. Oncol. Annu. Meet.* **39**, 79–86 (2019).
7. Paes Dias, M., Moser, S. C., Ganesan, S. & Jonkers, J. Understanding and overcoming resistance to PARP inhibitors in cancer therapy. *Nature Reviews Clinical Oncology* 1–19 (2021). doi:10.1038/s41571-021-00532-x
8. Xu, G. *et al.* REV7 counteracts DNA double-strand break resection and affects PARP inhibition. *Nature* **521**, 541–544 (2015).
9. Boersma, V. *et al.* MAD2L2 controls DNA repair at telomeres and DNA breaks by inhibiting 5' end resection. *Nature* **521**, 537–40 (2015).
10. Bouwman, P. *et al.* 53BP1 loss rescues BRCA1 deficiency and is associated with triple-negative and BRCA-mutated breast cancers. *Nat. Struct. Mol. Biol.* **17**, 688–695 (2010).
11. Bunting, S. F. *et al.* 53BP1 Inhibits Homologous Recombination in Brca1-Deficient Cells by Blocking Resection of DNA Breaks. *Cell* **141**, 243–254 (2010).
12. Chapman, J. R. *et al.* RIF1 Is Essential for 53BP1-Dependent Nonhomologous End Joining and Suppression of DNA Double-Strand Break Resection. *Mol. Cell* **49**, 858–871 (2013).
13. Escibano-Díaz, C. *et al.* A Cell Cycle-Dependent Regulatory Circuit Composed of 53BP1-RIF1 and BRCA1-CtIP Controls DNA Repair Pathway Choice. *Mol. Cell* **49**, 872–883 (2013).
14. Noordermeer, S. M. *et al.* The shieldin complex mediates 53BP1-dependent DNA repair. *Nature* **560**, 117–121 (2018).
15. Ghezraoui, H. *et al.* 53BP1 cooperation with the REV7–shieldin complex underpins DNA structure-specific NHEJ. *Nature* **560**, 122–127 (2018).
16. Dev, H. *et al.* Shieldin complex promotes DNA end-joining and counters homologous recombination in BRCA1-null cells. *Nat. Cell Biol.* **20**, 954–965 (2018).



Chapter 2

General introduction: Understanding and overcoming resistance to PARP inhibitors in cancer therapy

Mariana Paes Dias^{*}, Sarah C. Moser^{*},
Shridar Ganesan and Jos Jonkers

^{}equal contribution*

ABSTRACT

Developing novel targeted anticancer therapies is a major goal of current research. The use of poly (ADP-ribose) polymerase (PARP) inhibitors in patients with homologous recombination-deficient tumours provides one of the best examples of a targeted therapy that has been successfully translated into the clinic. The success of this approach has so far led to the approval of four different PARP inhibitors for the treatment of several types of cancers, and a total of seven different compounds are currently under clinical investigation for various indications. Clinical trials have demonstrated promising response rates among patients receiving PARP inhibitors, although the majority will inevitably develop resistance. Preclinical and clinical data have revealed multiple mechanisms of resistance and current efforts are focused on developing strategies to address this challenge. In this Review, we summarize the diverse processes underlying resistance to PARP inhibitors and discuss potential strategies that might overcome these mechanisms, such as combinations with chemotherapies, targeting the acquired vulnerabilities associated with resistance to PARP inhibitors or suppressing genomic instability.

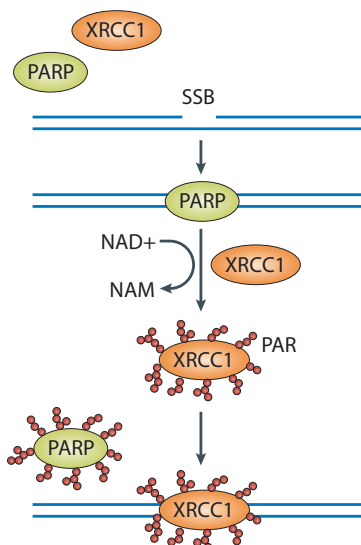
INTRODUCTION

Targeted killing of cancer cells while sparing surrounding nonmalignant tissues is a major goal of current treatment strategies. In 2005, two landmark studies demonstrated that inhibition of poly (ADP-ribose) polymerase 1 (PARP1) activity is specifically cytotoxic to cells lacking functional forms of the tumour suppressors BRCA1 or BRCA2^{1,2}. This finding demonstrates that both PARP1 and BRCA1/2 are crucial for the efficient repair of DNA damage.

PARP1 is a nuclear enzyme that regulates multiple cellular processes through PARylation, including DNA damage signalling, chromatin remodelling, transcription, stabilization of replication forks, sensing of unligated Okazaki fragments during replication, inflammation and metabolism³⁻⁵. PARP1 has a crucial role in the timely and accurate repair of DNA damage. Upon DNA damage, PARP1 is rapidly recruited to single-strand breaks (SSBs) and double-strand breaks (DSBs), where, upon binding single-stranded DNA, it PARylates itself and other proteins resulting in the recruitment of downstream DNA repair factors⁵ (**Box 1**). BRCA1 and BRCA2 are then recruited further downstream to regulate one of the two major pathways for DSB repair during the S and G2 phases of the cell cycle, homologous recombination (HR). Unlike the other DSB repair pathways, HR repair is largely error free. BRCA1 is required for initiation of HR by promoting end-resection of the DSB and then acts further downstream together with BRCA2 and PALB2 to stimulate the recruitment of RAD51 to the resected single DNA strand⁶. HR then enables accurate repair of the DNA lesion using the newly replicated sister chromatid as a template⁷.

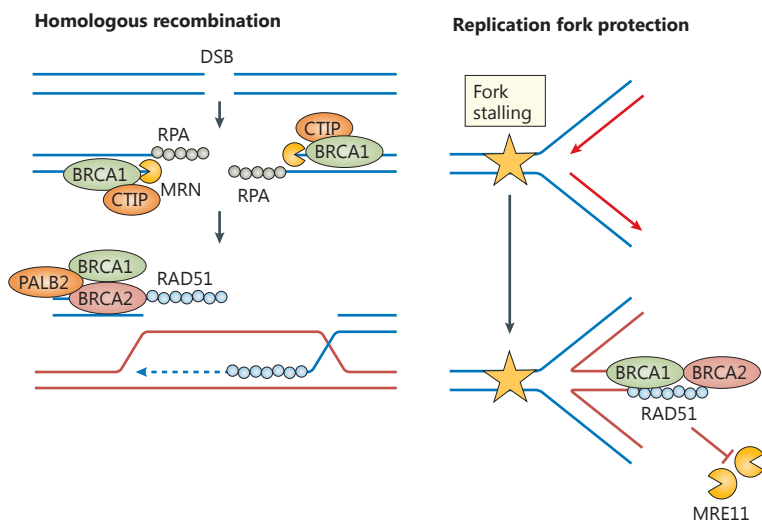
In addition to their role in HR, BRCA1 and BRCA2 are also crucial during S phase of the cell cycle, in which they protect stalled replication forks from degradation by nucleases, such as MRE11^{8,9} (**Box 2**). As a consequence of the above-mentioned roles of BRCA1 and BRCA2, heterozygous germline mutations in either of these genes confer a strong predisposition to breast¹⁰, ovarian¹¹, prostate¹²⁻¹⁴ and pancreatic cancers¹⁵, which arise through loss of the remaining wild-type allele and are associated with high levels of genomic instability owing to loss of HR. These HR-deficient *BRCA1/2*-mutant tumours are also dependent on compensatory DNA repair pathways. Pharmacological inhibition of key components of these pathways, such as PARP1, leads to DNA damage that, in the absence of BRCA1/2, triggers critical levels of genomic instability, mitotic catastrophe and cell death, ultimately resulting in a strong synthetic lethal relationship between BRCA1/2 and PARP¹⁶. BRCA1/2-deficient tumours often also have a pronounced level of sensitivity to other DNA-damaging agents, including platinum-based chemotherapies, topoisomerase (TOP) inhibitors and bifunctional alkylators, which likely generate classes of DNA lesions that are lethal to cells with deficient BRCA1/2 function¹⁷⁻¹⁹.

The interaction between BRCA1/2 and PARP1 is the best studied synthetic lethal relationship to date and has been rapidly translated to the clinic through the development of small-molecule inhibitors of PARP enzymes. To date, several PARP inhibitors targeting the catalytic centre of the enzyme have been developed and approved for various clinical



Box 1 | PARP enzymes and PARylation. Poly (ADP-ribose) polymerase (PARP) 1 is the most abundant of a 17-member family of enzymes that share a common ADP-ribosyltransferase motif. By hydrolysing nicotinamide adenine dinucleotide (NAD⁺), PARP1 post-translationally modifies itself and/or other proteins with negatively charged poly (ADP-ribose) (PAR) moieties, a process known as PARylation²⁰. Following DNA damage, PARP1 is rapidly recruited to DNA single-strand breaks, where it initiates a series of PARylation events, serving as a cellular sensor of DNA breaks and as a platform for the recruitment of downstream repair factors. In this process, PARP1 also autoPARylates, promoting its release from DNA²¹. In addition to PARP1, PARP2 and PARP3 are also activated by binding to DNA breaks^{22–26}. PARP1 is responsible for more than 80% of PAR synthesis, while PARP2 accounts for the remainder^{22,23}. Unlike PARP1 and PARP2, PARP3 modifies proteins primarily with mono (ADP-ribose)^{24,25}. PARylation is a highly dynamic and reversible modification as its rapid turnover is mediated by PAR glycohydrolase (PARG), which degrades PAR^{20,21}. ADP-ribosylhydrolase 3 (ARH3) is another PAR-degrading enzyme^{27,28}. PARG has both endoglycosidase and exoglycosidase activities, while ARH3 seems to exert only exoglycosidase activity^{27,29}. The eviction of PARP1 from sites of DNA damage is additionally regulated by the E3 ubiquitin ligase CHFR, which has been proposed to ubiquitinate the PARylated form of PARP1, resulting in PARP1 targeting for proteasomal degradation³⁰. The removal of PARP1 from DNA is crucial for successful DNA repair and to prevent the collapse of replication forks owing to PARP1 trapping. Further studies attempting to understand which factors mediate the removal of PARylated PARP1 from DNA will be vital for optimizing the efficacy of PARP inhibitors and to uncover additional genetic vulnerabilities that could be exploited therapeutically. NAM, nicotinamide; SSB, single-strand break; XRCC1, X-Ray repair cross complementing 1.

indications³¹, while numerous clinical trials that could further expand their use are currently ongoing. However, as also experienced with many other anticancer therapeutics, despite initial and often dramatic responses, patients receiving PARP inhibitors often ultimately develop treatment resistance. Therefore, the field is currently striving towards a better understanding of resistance to these agents and possible methods of overcoming this effect. In this Review, we summarize the various mechanisms of resistance to PARP inhibitors that have been reported and discuss several approaches that could be used to overcome or delay acquired resistance to these agents.



Box 2 | BRCA1/2 – similar names, different functions. BRCA1 and BRCA2 do not share homology and, although acting via a common pathway, also have several differing additional functions. Both factors are involved in homologous recombination (HR) and prevent replication-associated DNA damage, although BRCA1 is also known to regulate cell-cycle checkpoint activation as well as transcription³². BRCA1 and BRCA2 act at different levels during HR, resulting in functionally distinct mechanisms of resistance to PARP inhibitors. Resistance to PARP inhibitors via restoration of replication fork protection is observed in both BRCA1-deficient and BRCA2-deficient tumours, whereas reactivation of HR owing to loss of 53BP1 and its downstream factors is only reported in BRCA1-deficient tumours. The mutational signatures of BRCA1-deficient tumours and BRCA2-deficient tumours feature notable differences¹⁰. Small tandem duplications (<10 kb) are exclusively found in BRCA1-mutated tumours, although large deletions (beyond 100kb) are shared between tumours harbouring mutations in BRCA1 or BRCA2, thus further emphasizing the different implications of loss of BRCA1 versus BRCA2 function for DNA repair. BRCA1-deficient tumours and BRCA2-deficient tumours also differ on a pathological level. BRCA1-deficient tumours are usually of a basal-like or triple-negative subtype, while BRCA2-mutated cancers are not biased towards a specific subtype³³. PALB2 has been reported to interact with BRCA2 and is required for its recruitment and DNA strand invasion during HR³⁴. In line with its biological function, PALB2 mutations have been shown to confer an increased risk of developing breast cancer³⁵. DSB, double-strand break; MRE11, meiotic recombination 11; MRN, MRE11-RAD50-NBS1 complex; PALB2, partner and localizer of BRCA2; RAD51, RAD51 recombinase; RPA1, replication protein A1.

TARGETING PARP IN CANCER

Mechanism of action

Four small-molecule PARP inhibitors are currently approved for clinical use (olaparib, rucaparib, niraparib and talazoparib) and a further three are being tested in phase III trials (veliparib, pamiparib and fluzoparib). In-depth discussions of these trials are provided elsewhere^{36–38}. PARP inhibitors were thought to act by preventing the repair of SSBs, which accumulate during S phase of the cell cycle and pose a threat to replication fork progression^{1,2}. However, genetic depletion or inhibition of PARP1 was soon discovered to not affect the number of SSBs occurring within a cell^{39,40}. Additionally, depletion of XRCC1, a factor interacting with PARP1 during base-excision repair, failed to reveal any synthetic

lethal relationship with BRCA2 deficiency⁴¹. This led to the hypothesis that the antitumour activity of PARP inhibitors can be explained by trapping of PARP1 at DNA lesions and the formation of so-called DNA–protein crosslinks. These crosslinks then trigger the collapse of replication forks that encounter trapped PARP1, resulting in the accumulation of DSBs during S phase of the cell cycle. HR-deficient tumour cells are dependent on BRCA1/2-mediated repair to resolve DSBs in an error-free way; therefore, PARP inhibitors can induce DNA lesions that are lethal to such cells^{1,2} (**Fig. 1**).

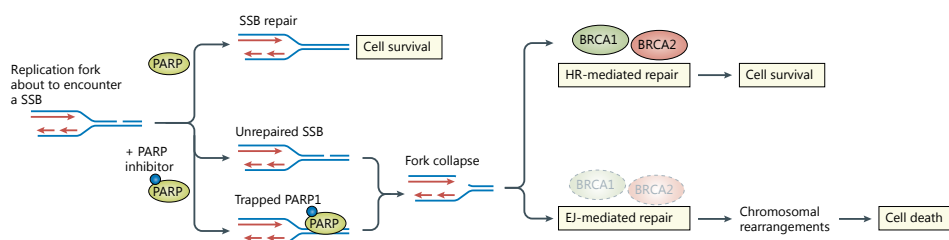


Figure 1 | PARP inhibitors and their mechanism of action. Poly (ADP-ribose) polymerase (PARP) inhibitors were initially thought to inhibit PARylation and thereby cause cytotoxicity; however, the main cause of tumour cell death was subsequently found to be trapping of PARP1 enzyme at DNA lesions. Single-strand breaks caused by DNA damage are faithfully repaired in the presence of PARP1; however, when trapped, PARP1 enzymes can cause a threat to replication forks during S-phase of the cell cycle, ultimately leading to collapse of the replication fork, resulting in double-strand breaks. In BRCA-proficient cells, homologous recombination (HR) enables the error-free repair of such breaks. By contrast, BRCA1/2-deficient cells are HR-deficient and are therefore reliant upon error-prone DNA end joining pathways such as classical nonhomologous end joining or alternative end joining to resolve the double strand breaks caused by replication fork collapse, triggering the accumulation of chromosomal aberrations and cell death by mitotic catastrophe.

The PARP1 trapping theory is currently supported by data from numerous studies. First, functional PARylation has been shown to be required for the release of PARP1 from DNA, indicating that trapped DNA–PARP complexes are indeed formed⁴². Second, the various PARP inhibitors have different levels of cytotoxicity, despite a generally similar capacity to inhibit the catalytic activity of PARP1⁴³ (**Table 1**). As reported by Murai et al.⁴⁴, an apparent correlation exists between the relative ability of these compounds to trap PARP1 onto DNA and their cytotoxicity. The PARP inhibitor with the greatest PARP-trapping ability, talazoparib, is approximately 100 times more potent in trapping PARP1 than niraparib, which in turn is able to trap PARP1 more potently than olaparib and rucaparib^{43,45}. Conversely, veliparib appears to have a limited ability to trap PARP1, despite its ability to inhibit PARylation, and fails to elicit the same level of synthetic lethality in preclinical models, compared with more effective PARP1 trappers^{43,45,46}. PARP inhibitors not only differ in their ability to trap PARP1; they have also been shown to have differing allosteric effects. Release of PARP1 from the DNA is prevented by talazoparib and olaparib, but promoted by rucaparib,

niraparib and veliparib, which might further explain their differing *in vitro* potency⁴⁷. As a result, the maximum-tolerated dose of PARP inhibitors decreases with increasing levels of PARP-trapping activity, and more potent PARP trappers often have to be administered at lower doses in the clinic^{48–50}. Conversely, the main adverse effects observed in patients receiving these various agents (nausea, vomiting, fatigue, as well as anaemia) seem to largely overlap⁵¹.

Data from the past few years suggest that PARP inhibitors might have a broader effect on cellular processes than previously anticipated. For example, PARP inhibitor-induced DNA–protein crosslinks have been found to occur not only in DNA lesions, but also at ssDNA during DNA replication and at genome-embedded ribonucleotides^{4,52}. Additionally, cells that enter mitosis after sustained PARP inhibitor-induced damage during S phase often contain mitotic defects such as chromatin bridges and lagging chromosomes, which ultimately lead to cell death⁵³. Data published in 2018 suggest that treatment with high doses of PARP inhibitors triggers an acceleration of replication fork elongation, which reduces the fidelity of DNA polymerases as well as promoting activation of the DNA damage response⁵⁴. However, more research is needed to better understand how these novel mechanisms add to the cytotoxicity of PARP inhibitors, and whether their contribution is dependent on BRCA1/2-deficiencies. The broad range of DNA substrates and the various processes that PARP inhibitors are thought to target imply that PARP inhibitors might also reduce the survival of BRCA1/2-wild-type cells as well as other DNA repair-deficient cell lines, which is the rationale of current clinical trials testing PARP inhibitors in patients with cancers other than HR-deficient breast and ovarian cancers.

Clinically approved PARP inhibitors

In 2014, the first PARP inhibitor, olaparib, was approved for the treatment of women with *BRCA1/2*-mutated metastatic ovarian cancer who have received three or more prior lines of chemotherapy (**Supplementary table 1**)^{68,69}; and for the maintenance treatment of women with *BRCA1/2*-mutated ovarian cancers who are in complete or partial remission after platinum-based chemotherapy⁷⁰. In 2016, a second PARP inhibitor, rucaparib, was authorized for the treatment of women with advanced-stage ovarian cancers harbouring deleterious *BRCA1/2* mutations who have received two or more prior lines of chemotherapy^{71–73}. In 2019, niraparib was approved for the treatment of patients with HR-deficient advanced-stage ovarian cancer who have received three or more prior chemotherapy regimens^{74,75}.

A retrospective analysis of the data from the clinical trials leading to the approval of olaparib in 2014 demonstrated a progression-free survival (PFS) benefit even for patients with *BRCA1/2*-wild-type ovarian cancer, suggesting that some patients with *BRCA1/2*-wild-type ovarian cancer might benefit from PARPi maintenance therapy⁷⁶. Within three years, phase III trials testing either olaparib^{76,77}, niraparib⁷⁸ or rucaparib^{79,80} demonstrated statistically significant improvements in the PFS of women with ovarian cancer harbouring either mutated or wild-type *BRCA1/2*. These observations led to the approval of these

Table 1 | Pharmacological characteristics of PARP inhibitor.

Drug	IC ₅₀ (nM)	Trapping ability ^{45,55}	P-glycoprotein substrate ⁵⁵⁻⁵⁹	Targets ⁶⁰	CNS penetration ⁶¹⁻⁶³ a small molecule inhibitor of poly (ADP-ribose)	T _{1/2} (hours) ^{55-59,65,66} recom- mended phase II dose (RP2D)	Bioavailability ^{59-59,67}	Known off-target interactions
Olaparib	1	+	Yes	PARP1/2/3/4	+	11.9	55-60% in mice; 79% in dogs; <20% in rats	CYP3A4
Rucaparib	1	+	Yes	PARP1/2/3/4, TNKS1	+	25.9	36%	CYP enzymes
Niraparib	4	+	Weak	PARP1/2	++	48-51	75%	Dopamine, norepinephrine or serotonin transporters
Talazoparib	0.6	++	Weak	PARP1/2	-	90 ± 58 h	41%	None
Veliparib	2	-	No	PARP1/2/3	+	4.1-8.2	NA	NA
Pamiparib	0.83	+	No	PARP1/2	++	NA	NA	NA
Fluzoparib	1.5	NA	NA	PARP1/2	NA	?	35.8% in mice	NA

CNS, central nervous system; CYP, cytochrome P450; IC50, half maximal inhibitory concentration; NA, not available; PARP, poly(ADP- ribose) polymerase; TNKS1, tankyrase 1; -, poor; +, modest; ++, good.

three PARP inhibitors as maintenance therapies for patients with recurrent ovarian cancer, regardless of *BRCA1/2*-mutation status. This experience suggests that a subset of *BRCA1/2*-proficient cancers might nonetheless also harbour clinically relevant HR defects, either owing to mutations in other HR-related genes (such as *RAD51* paralogues) or other mechanisms.

PARP inhibitors have also been approved as first-line systemic therapies for women with ovarian cancer. In 2018, results from phase III trials demonstrated that maintenance therapy with olaparib provided a substantial PFS benefit for women with newly diagnosed *BRCA1/2*-mutant advanced-stage ovarian cancer, reducing the risk of disease progression or death by 70% compared with placebo⁸¹. This extension of PFS led to the approval of olaparib as a first-line maintenance therapy for women with *BRCA1/2*-mutated advanced-stage ovarian cancer⁸¹. In 2020, niraparib was approved for first-line maintenance therapy in patients with advanced-stage, platinum-sensitive ovarian cancer, regardless of *BRCA1/2* status⁸².

Data from the OlympiAD trial led to the 2018 approval of olaparib as the first PARP inhibitor indicated for the treatment of patients with metastatic HER2-negative, *BRCA1/2*-mutant breast cancer who had previously received chemotherapy⁸³. This decision was soon followed by the approval of talazoparib for similar indications⁸⁴. In 2019, olaparib also became the first PARP inhibitor to be approved for the maintenance treatment of patients with *BRCA1/2*-mutated metastatic pancreatic adenocarcinoma⁸⁵. In 2020, the use of PARP inhibitors was further expanded to include men with prostate cancer, with the approval of olaparib for patients with metastatic, castration-resistant prostate cancers (CRPC) harbouring mutations in HR-related genes after disease progression on enzalutamide, or abiraterone⁸⁶. This approval is the first to permit the use of olaparib in patients with tumours harbouring mutations in genes other than *BRCA1/2*. Whether olaparib has any substantial efficacy in such tumours remains unclear due to the fact that PFS analysis in this study was performed in subgroups containing mutations in 15 DNA repair genes including *BRCA1* and *BRCA2*. This makes it difficult to determine the contribution of mutations in individual genes to the observed PFS benefit. Compared to patients with *BRCA1/2* mutations, patients with mutations in *ATM* and other DDR genes showed little PFS benefit from olaparib^{86,87}. Following the 2020 approval of olaparib, rucaparib received accelerated approval for the treatment of men with *BRCA1/2*-mutant metastatic CRPC who have previously received androgen receptor-directed therapy and taxane-based chemotherapy⁸⁸.

Veliparib does not yet have an approved label and its use is being investigated mostly in combination with chemotherapy or targeted therapies in a range of solid tumours (such as NCT02032277, NCT02152982, NCT02163694, NCT02264990 and NCT02470585), likely owing to its reduced ability to trap PARP1 and, consequently, limited synthetic lethality and limited single-agent activity. The PARP inhibitors pamiparib and fluzoparib have been developed over the past few years and it remains to be determined whether they have advantages over currently approved agents. Pamiparib has shown a favourable safety profile

and preliminary antitumour activity in phase I testing^{89,90}, resulting in the initiation of a phase III trial with pamiparib versus placebo as maintenance therapy for women with platinum-sensitive advanced-stage ovarian cancer (NCT03519230). A phase III trial exploring the use of pamiparib in patients with inoperable locally advanced or metastatic gastric cancer with a previous response to platinum-based first-line chemotherapy has also been initiated (NCT03427814).

Data on the efficacy of fluzoparib remain limited, although preclinical data indicate a favourable safety profile and robust *in vivo* antitumour activity, with similar potency to that of olaparib⁶⁷. Phase III studies investigating the use of fluzoparib as maintenance therapy in patients with platinum-sensitive recurrent ovarian cancer (NCT03863860) and as maintenance therapy in patients with *BRCA1/2* or *PALB2*-mutated pancreatic cancer that has not progressed on first-line platinum-based chemotherapy (NCT04300114) are currently ongoing.

PFS is currently the most widely used primary outcome in clinical trials testing PARP inhibitors. Since most studies have been initiated within the past few years, overall survival (OS) data remains limited. OS data have been published for olaparib in HER2-negative breast cancer and pancreatic cancer patients, but the results are mixed and the OS data from both studies might be underpowered since OS was not the primary end point^{84,86}. In an analysis of OS data from a phase II trial, patients with recurrent platinum-sensitive advanced-stage *BRCA*-mutated ovarian cancer receiving olaparib maintenance monotherapy after platinum-based chemotherapy have both improved PFS and OS outcomes, although the OS benefit (29.8 months versus 27.8 months with placebo) did not reach statistical significance⁹¹. In November 2020, new data from the SOLO1 trial showed that maintenance treatment with olaparib in women with newly diagnosed advanced platinum-sensitive *BRCA1/2*-mutant ovarian cancer extended the median PFS by 42 months in comparison to placebo⁹². Strikingly, in patients with complete response at baseline, the risk of disease recurrence or death was reduced by 63%. Although OS data are not yet available in this setting, the significant increase in PFS may translate in an OS benefit. In March 2021, a preplanned OS analysis on the phase III SOLO2 trial demonstrated that maintenance treatment with olaparib extends the median OS of patients with relapsed platinum-sensitive advanced-stage *BRCA1/2*-mutant ovarian cancer by 12.9 months in comparison to placebo⁹³. Importantly, this is the first report of improved OS with PARP inhibitors used as maintenance therapy. Nonetheless, OS benefit remains to be determined for other PARP inhibitors and for indications other than platinum-sensitive *BRCA1/2*-mutant ovarian cancer. Moreover, while emerging data show that PARP inhibitors delay disease recurrence and prolong patient survival, most patients receiving PARP inhibitors ultimately will eventually experience disease progression, thus indicating a need to better understand mechanisms of resistance and how to delay or overcome resistance.

Beyond *BRCA1/2* mutations

The benefits of PARP inhibitors seem to be greatest in patients with germline and/or somatic *BRCA1/2* mutations, although data from several clinical studies suggest that PARP inhibitors might also provide benefit for patients lacking these mutations, albeit to a lesser extent^{78,80}. For example, a phase III trial of maintenance rucaparib in women with recurrent ovarian cancer with a response to platinum-based chemotherapy found an increase in median PFS from 5.4 months to 16.6 months in patients with *BRCA1/2*-deficient disease, while less pronounced but statistically significant effects were observed for those with *BRCA1/2*-wild-type but HR-deficient tumours (13.6 months) and the entire cohort (10.8 months)⁸⁰. In line with these observations, several other trials have reported a statistically significant improvement in PFS in patients with *BRCA1/2*-wild-type ovarian cancers^{82,94,95}, and as a consequence, niraparib maintenance therapy was approved by the FDA for women with advanced-stage ovarian cancer regardless of HR status in April 2020.

These observations suggest that *BRCA1/2* mutations do not entirely account for the benefits derived from PARP inhibitors. Indeed, preclinical data have long suggested that deficiencies in other HR genes might also confer sensitivity to PARP inhibitors⁹⁶. Several studies involving patients with ovarian^{72,97} and prostate^{98,99} cancers have demonstrated that those with *BRCA1/2*-wild-type tumours harbouring deleterious variants in other DNA repair genes, such as *PALB2*, various *RAD51* homologues, *ATM*, *CHEK2*, *CDK12*, *FANCA*, *RAD54L* and *BRIP1* might benefit from PARP inhibitors. Notably, data from an increasing number of studies indicate that mutations in *PALB2*, a factor acting together with *BRCA1* and *BRCA2* during HR (**Box 2**), are a strong indicator of sensitivity to PARP inhibitors^{35,100,101} and several others are currently ongoing (NCT02401347 and NCT03330847). Mutations in other core HR-related genes, such as *RAD51* paralogues, also likely confer sensitivity to PARP inhibitors¹⁰². It remains unclear whether mutations in other DNA damage response (DDR) related genes, such as *ATM* and *CHEK2*, impart a clinically relevant sensitivity to PARP inhibitors, and this possibility is currently being investigated in several ongoing clinical trials^{100,103}.

Apart from key DNA repair factors, mutations in chromatin regulators, such as *ARID1A*¹⁰⁴ and *BAP1*^{105,106}, have also been suggested to result in increased sensitivity to PARP inhibitors *in vitro*. Furthermore, indirect downregulation of HR-related proteins owing to mutations in genes involved in the Krebs cycle, such as *IDH1/2*, *FH* and succinate dehydrogenases, are reported to result in downregulation of HR-related proteins and increased sensitivity to PARP inhibitors in preclinical models^{107,108}. Notably, certain cancers that lack mutations in HR-related genes (such as small-cell lung cancers) have demonstrated some sensitivity to PARP inhibitors^{109,110}, possibly owing to increased levels of replication stress arising from *RB1* mutations. Moving beyond a focus on mutations in *BRCA1/2* and on deficient HR repair and establishing a rationale for broadened use of PARP inhibitors for a wider range of cancers will therefore be important. Several diagnostic tools have been developed to

identify HR-deficient tumours irrespective of *BRCA1/2* mutation status, such as assays designed to determine *RAD51* status or assessments of mutational signatures and genomic instability associated with HR-deficiency, which might aid in identifying novel groups that derive benefit from PARP inhibitors¹¹¹. However, differentiating between the general effects of PARP trapping — which might not provide a greater therapeutic window than conventional chemotherapies — from cancer-specific vulnerabilities to PARP inhibitors will be crucial.

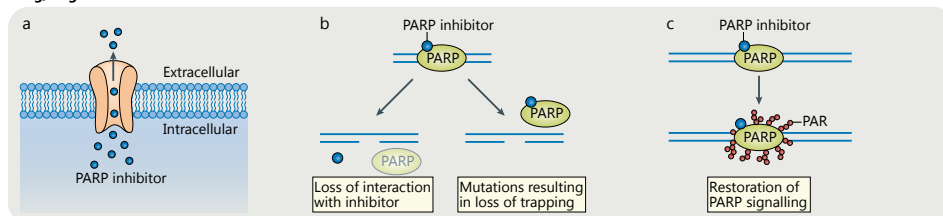
RESISTANCE TO PARP INHIBITION

PARP inhibitors frequently elicit a good initial response, although most patients develop resistance to these agents, resulting in disease relapse. Acquired resistance to PARP inhibitors can develop via three general mechanisms: drug target-related effects, such as upregulation of drug efflux pumps or mutations in PARP or functionally related proteins; restoration of HR, owing to restoration of *BRCA1/2* function; or loss of DNA end protection and/or restoration of replication fork stability (**Fig. 2**).

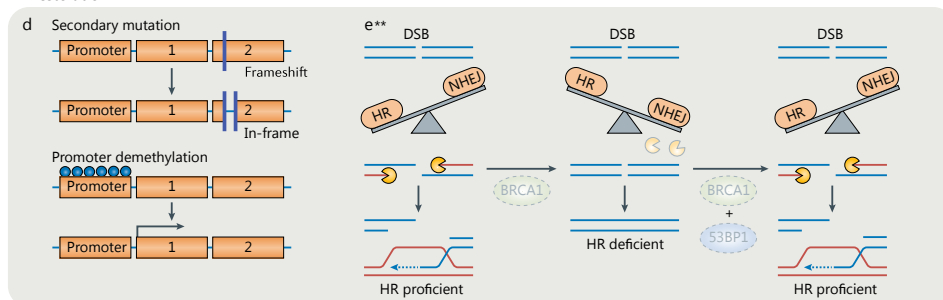
Upregulation of drug efflux pumps

Upregulation of the drug efflux transporter ABCB1, also known as P-glycoprotein, was one of the first mechanisms proposed to trigger resistance to PARP inhibitors. ABCB1 belongs to a family of ATP-binding cassette (ABC) transporters, which are an established source of resistance to multiple chemotherapies and other agents by preventing their intracellular accumulation. ABCB1-induced resistance to PARP inhibitors was initially observed in *BRCA1/2*-deficient mouse models developing spontaneous mammary tumours. Long-term exposure of these models to olaparib resulted in the outgrowth of resistant, ABCB1-overexpressing tumours^{112,113}. Importantly, resistance could be reversed by a combination of olaparib and the ABCB1 inhibitor tariquidar, proving that increased drug efflux is indeed the cause of resistance. Although, the clinical relevance of this mechanism is still unclear, upregulation of ABCB1 has been reported in chemotherapy-resistant ovarian cancers¹¹. Even though all PARP inhibitors were designed to inhibit the same target domain, some inhibitors, such as veliparib and niraparib, are poor substrates for ABCB1, suggesting that these agents should circumvent ABCB1-induced resistance. Furthermore, it should be noted that ABCB1 overexpression frequently induces cross-resistance to chemotherapies, such as taxanes and doxorubicin; therefore, PARP inhibitors that are not transported by ABCB1 might be more effective in patients that have previously received chemotherapy^{113,114}.

Drug/target-related alterations



HR restoration



Restoration of replication fork stability

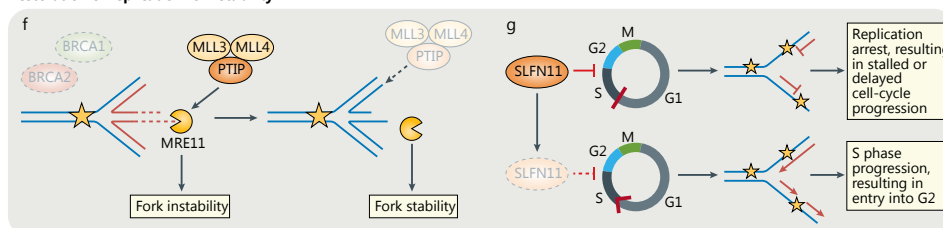


Figure 2 | Mechanisms of resistance to PARP inhibitors. Long-term follow-up data from clinical trials exploring the efficacy of various different poly(ADP-ribose) polymerase (PARP) inhibitors have demonstrated durable responses, although the majority of patients inevitably develop resistance. Clinical and preclinical studies indicate that such resistance occurs via one of three general mechanisms. Alterations related to the drug (or target) as observed with chemotherapies, such as upregulation of the efflux transporter P-glycoprotein (**a**), downregulation of or mutations in PARP1, which is restricted to cells expressing residual levels of BRCA1/2 (**b**) or loss of poly(ADP-ribose) glycohydrolase (PARG) (**c**). Restoration of homologous recombination (HR), which can occur either through reactivation of BRCA1/2 function (**d**) or loss of DNA end-protection (**e**), which is restricted to loss of BRCA1 and may occur via loss of the non-homologous end-joining (NHEJ) factor 53BP1. Restoration of replication fork stability via increased protection from fork degradation (**f**), for example, by loss of PTIP expression or loss of cell-cycle checkpoint arrest owing to loss of Schlafen 11 (SLFN11) (**g**). PAR, poly(ADP-ribose); DSB, double-strand break; MLL3, histone lysine N-methyltransferase 2C; MLL4, histone lysine N-methyltransferase 2B; MRE11, Meiotic recombination 11; PTIP, Pax2 transactivation domain-interacting protein.

Target-related mechanisms of resistance

All current PARP inhibitors target the catalytic domain of PARP enzymes by competing with the cofactor NAD⁺. Resistance might therefore arise from mutations in *PARP1* that either reduce its affinity to PARP inhibitors or preserve endogenous functions of the enzyme when

bound to PARP inhibitor¹¹⁵. Data from *in vitro* studies demonstrate that point mutations associated with resistance to PARP inhibitors are not exclusively found in the catalytic site of the enzyme, but also in domains necessary for trapping PARP1 onto DNA^{115,116}. Corroborating these results, a mutation in *PARP1* that did not affect the recruitment of PARP1 to sites of DNA damage but nonetheless prevented efficient PARP1 trapping was identified in a PARP-inhibitor-resistant ovarian tumour¹¹⁵. Importantly, mutations in *PARP1* can only confer resistance in HR-proficient cells or in cells with hypomorphic *BRCA1* mutations and residual levels of *BRCA1* activity, owing to the synthetic lethal effect of combined loss of PARP1 and *BRCA1* function.

The enzyme that removes PAR chains from target proteins, poly (ADP-ribose) glycohydrolase (PARG), is another crucial factor in the development of resistance to PARP inhibitors both *in vitro* as well as *in vivo*. For example, loss of PARG confers resistance to PARP inhibitors in genetically engineered mouse models that develop *BRCA1/2*-deficient mammary tumours¹¹⁷. Interestingly, PARG depletion was able to partially rescue PARylation levels in cells exposed to PARP inhibitors in these models, suggesting that inhibition of PARP1 only reduces but does not fully inhibit PARylation. PARG-deficient cells exposed to PARP inhibitors are thought to retain sufficient PARylation of target proteins to induce the DNA damage signalling cascade and reduce the trapping of PARP1 onto DNA, owing to residual PARP activity¹¹⁷. Although clinical evidence remains limited, PARG-negative areas have been detected in tumours from a fraction of patients with triple-negative breast cancers (TNBCs) (76.8%) or ovarian carcinomas (78.4%), both of which are eligible for treatment with PARP inhibitors.

Restoration of *BRCA1/2* function

The best clinically documented mechanism of resistance to PARP inhibitors occurs through reversion mutations or epigenetic alterations that induce the re-expression of a *BRCA1* or *BRCA2* wild-type protein or result in hypomorphic variants. Reversion of protein-truncating *BRCA1/2* mutations was originally described *in vitro* using *BRCA2*-mutated ovarian and pancreatic cancer cell lines following prolonged exposure to PARP inhibitors or cisplatin^{118,119}. *BRCA1/2*-deficient cells have high levels of genomic instability, which are exacerbated by cisplatin and PARP inhibitors; therefore, the authors suggested that these cells accumulate further genetic alterations, resulting in the subsequent re-expression of novel *BRCA2* isoforms. In line with the expected resistance to PARP inhibitors and cisplatin, cells of this revertant phenotype were again capable of recruiting RAD51 to sites of DNA damage and had reduced levels of genomic instability. Studies involving patient-derived xenograft (PDX) models of *BRCA1*-mutated and *BRCA1*-methylated TNBC revealed acquired resistance to PARP inhibitors driven by intragenic deletions that restored the reading frame of mutant *BRCA1*, as well as a loss of *BRCA1* promoter hypermethylation and de novo gene fusions causing re-expression of epigenetically silenced *BRCA1*¹²⁰. Similarly, methylation of all *BRCA1* copies in PDX models of *BRCA1*-methylated ovarian cancer was associated with a response to PARP

inhibitors, whereas heterozygous methylation was associated with resistance¹²¹. In line with these preclinical findings, complete *BRCA1* methylation might predict clinical response to PARP inhibitors, and methylation loss can occur as a result of prior chemotherapy¹²¹.

Over the past years, several other studies have reported genetic reversions of *BRCA1/2* as a mechanism of resistance to PARP inhibitors in patients with breast^{122–124}, ovarian^{102,118,123–127}, pancreatic¹²⁸ or prostate^{129,130} cancers. An analysis of all reversion events in HR-related genes that have been previously associated with resistance to PARP inhibitors or platinum-containing chemotherapy was published in July 2020. Most reversions were found to be unique, although several positional hotspots could be identified across the coding sequence of *BRCA2*, suggesting that mutations in these positions might be more likely to lead to reversion, and thereby the development of resistance to PARP inhibitors, than others¹³¹. Importantly, reversions associated with resistance to PARP inhibitors are not exclusively found in *BRCA1/2* but have also been identified in other HR-related genes, such as *RAD51C*, *RAD51D* and *PALB2*^{102,130}. The selection for reversion mutations during treatment with platinum-containing chemotherapies or PARP inhibitors also demonstrates that genomic instability induced by loss of *BRCA1/2* function or that of other HR-related proteins is only required for initiation of tumorigenesis and dispensable for tumour maintenance. As such, therapy resistance induced by reversion mutations is an example of what can be called 'tumour suppressor tolerance', in which restoration of tumour suppressor gene function in an initially mutant cancer might actually increase fitness.

Owing to PARP inhibitors only being used clinically over the past few years and the complexities associated with the detection of reversion mutations, large-scale studies to estimate the frequency of *BRCA1/2* reactivation in patients with PARP-inhibitor-resistant tumours are still unavailable. The fact that these agents were initially approved for second-line maintenance therapy, following first-line treatment with platinum-based chemotherapies, might bias the results of such investigations because reactivation of *BRCA1/2* has been shown to be the main mechanism of platinum resistance in *BRCA1/2*-mutated tumours^{123–126}. Future studies involving patients receiving PARP inhibitors as first-line therapies will enable a better understanding of shared mechanisms of resistance to platinum-based agents and PARP inhibitors, which might result in cross resistance to both classes of therapies, and to identify mechanisms of resistance specific to PARP inhibitors.

BRCA1-independent restoration of HR

BRCA1 and *BRCA2* reversion events are found in a substantial proportion of patients with PARP inhibitor-refractory tumours, although they do not account for all cases of resistance¹³², implying the existence of additional mechanisms. Indeed, data from preclinical studies indicate that restoration of HR can also be achieved by compensatory mutations that result in rewiring of the DDR (**Fig. 3**). The first example of such a mechanism came from three landmark studies demonstrating that loss of the nonhomologous end joining (NHEJ) factor 53BP1 partially counteracts the effects of *BRCA1* loss on HR and genomic instability^{133–135}. Knockout of *53bp1*

in mice rescues embryonic lethality and attenuates tumorigenesis and chromosomal instability caused by BRCA1 deficiency⁹⁵. In addition, data from *in vitro* studies demonstrate that loss of 53BP1 restores DNA end-resection in BRCA1-deficient cells and, as a result, rescues the HR defect and renders cells resistant to PARP inhibitors^{133,134}. Importantly, 53BP1 loss does not restore HR in BRCA2-deficient cells, consistent with the different roles of BRCA1 and BRCA2 in HR (**BOX 2**). Follow-up studies identified several proteins downstream of 53BP1, such as RIF1^{136–140}, REV7^{141,142} and the shieldin complex^{143–149}, which are also thought to act as antagonists of end-resection and that confer resistance to PARP inhibitors in BRCA1-deficient cells and mouse mammary tumours upon inactivation. Additional evidence that loss of the 53BP1–RIF1–REV7–shieldin anti-resection signalling pathway mediates resistance to PARP inhibitors comes from *in vivo* studies in mouse models of BRCA1-deficient breast cancer. Prolonged exposure of these mice to PARP inhibitors resulted in acquired resistance, which was frequently associated with de novo mutations, DNA copy number aberrations and loss of *Trp53bp1*, *Rev7*, *Rif1* and *Shld2* expression¹⁵⁰ (and our own unpublished data). Loss of 53BP1 and shieldin components has also been observed in PDX models with acquired resistance to PARP inhibitors^{144,151}. Furthermore, several cases of resistance associated with BRCA-independent restoration of HR (owing to *MRE11* amplification or mutations in *TP53BP1*) have been reported in patients with BRCA1-associated breast cancer receiving platinum chemotherapy or a PARP inhibitor^{152,153}.

Apart from 53BP1–RIF1–REV7–shieldin signalling, several other factors have been reported to modulate end-resection, although clinical data on these factors are limited. The CTC1–STN1–TEN1 (CST) complex, located downstream of 53BP1–RIF1–REV7–shieldin, has been reported to prevent end-resection at DSBs, and loss of components of this complex leads to restoration of end-resection in the absence of BRCA1, resulting in resistance to PARP inhibitors^{154,155}. Interestingly, loss of the CST complex seems to have a milder effect on resistance to PARP inhibitors than disruption of 53BP1–RIF1–REV7–shieldin signalling, indicating that additional mechanisms might protect DSBs from end-resection. HELB and DYNLL1 act downstream of 53BP1 to antagonize multiple components of the DNA end-resection machinery, and loss of these factors results in hyper-resected DNA ends and renders BRCA1-deficient tumour cells resistant to PARP inhibitors^{156–158}. In addition to inhibition of end-resection factors, DYNLL1 might also promote NHEJ by stimulating 53BP1 oligomerization, thereby promoting recruitment and binding to DSBs¹⁵⁸. Further upstream, loss of ERCC6L2, an accessory NHEJ factor, has also been shown to restore DNA end-resection, resulting in partial restoration of HR and resistance to PARP inhibitors in BRCA1-deficient cells^{159,160}. Similarly, overexpression of factors promoting HR and suppression of NHEJ, such as TIRR¹⁶¹, TRIP13¹⁶² and miRNA-622¹⁶³ have also been shown to rescue HR and reduce the sensitivity of BRCA1-deficient cells to PARP inhibitors. Taken together, these data reinforce the notion that resistance to PARP inhibitors emerges via loss of DNA end-protection in cells lacking functional BRCA1. Moreover, the studies mentioned above demonstrate that, although BRCA1 is partially dispensable for the distal steps of RAD51-

mediated HR, BRCA2 is crucial for this pathway.

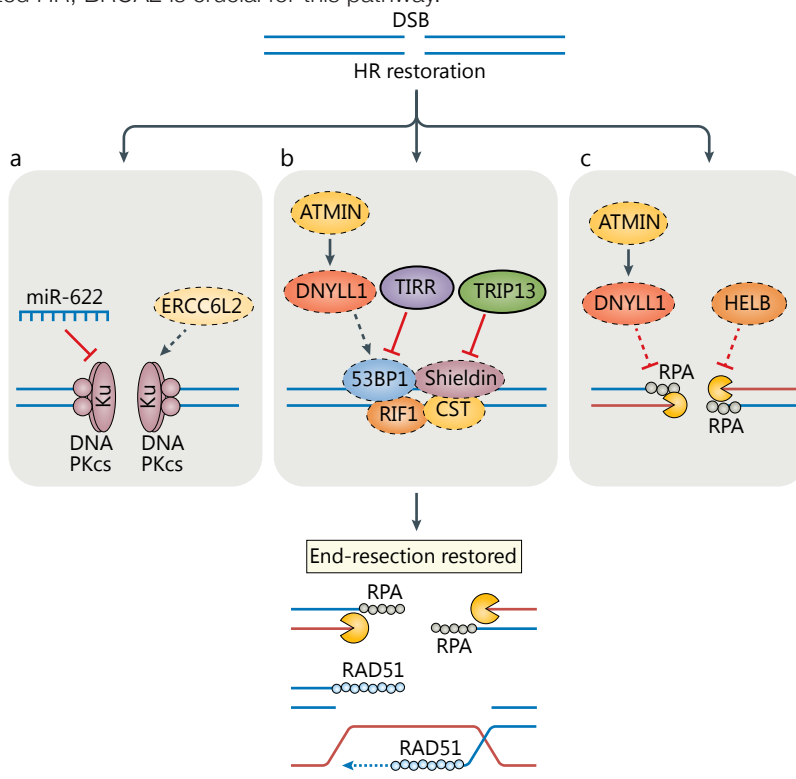


Figure 3| Mechanisms of BRCA1-independent restoration of HR. Various different mechanisms have been reported to enable the partial restoration of homologous recombination (HR) in BRCA1-deficient cells. **a** | Upstream of 53BP1, the DNA excision repair protein ERCC6L2 promotes nonhomologous end-joining (NHEJ), possibly by interacting with the Ku complex, and its loss leads to the restoration of DNA end-resection. Also upstream of 53BP1, overexpression of the microRNA miR-622 downregulates expression of the Ku complex, which in turn promotes HR. **b** | DYNLL1 stimulates 53BP1 oligomerization and promotes its recruitment and binding to DSBs. Consequently, loss of DYNLL1 or its transcriptional activator ATM/ATR results in restoration of HR. In addition, loss of any of the components of the 53BP1–RIF1–REV7–Shieldin pathway or of the CTC1–STN1–TEN1 (CST) complex results in loss of end-protection and, consequently, in restoration of end-resection. Accordingly, HR in BRCA1-deficient cells might be restored by overexpression of factors that suppress NHEJ, such as TIR/TPR, which antagonizes 53BP1 localization to DSBs, or the E3 ubiquitin ligase TRIP13, which catalyses the dissociation of the REV7–Shieldin complex. **c** | HELB acts downstream of 53BP1 through interaction with the major single-stranded DNA binding protein RPA to prevent long-range end-resection during the G1 phase of the cell cycle. Consequently, loss of HELB results in hyper-resected DNA and restoration of HR. DYNLL1 also prevents multiple components of the DNA end-resection machinery, such as MRE11, from localizing to sites of DNA damage. Therefore, loss of DYNLL1 or of its transcriptional activator ATM/ATR promotes end-resection and enables HR to proceed in the absence of BRCA1.

Restoration of fork stability

Restoration of HR by perturbation of 53BP1 and downstream factors involved in end-resection and/or protection is restricted to BRCA1-deficient cells, whereas acquired resistance to PARP inhibitors arising from restoration of fork stability is a mechanism

common to cells deficient in either BRCA1 or BRCA2. As mentioned previously, BRCA1 and BRCA2 are not only required for HR; these proteins also govern the stability and protection of replication forks under replicative stress (**Box 2**).

MRE11 and MUS81 are nucleases whose activity is required for the processing of stalled replication forks. In the absence of BRCA1/2, uncontrolled resection of unprotected, stalled forks by MRE11 leads to fork collapse and contributes to increased genomic instability^{164–167}. In line with this observation, depletion of the MLL3/4 complex protein PTIP or the nucleosome remodeling factor CHD4 prevents MRE11 recruitment to stalled forks, resulting in fork protection and resistance to PARP inhibitors in BRCA1/2-deficient cells^{164,168}. The chromatin-remodelling complex SMARCA1 has also been shown to promote the MRE11-dependent degradation of nascent DNA in BRCA1/2-deficient cells^{169,170}. In a manner similar to loss of PTIP, SMARCA1 depletion decreases the sensitivity of BRCA1-deficient tumour cells to PARP inhibitors, although this effect seems to be cell type-specific¹⁶⁹.

RAD51 is another factor involved in replication fork protection; depletion of this factor in BRCA2-deficient cells also restores fork protection and alleviates the cytotoxic effects of PARP inhibitors¹⁷¹. Limiting the recruitment of MUS81 through inhibition of the methyltransferase EZH2 has also been shown to result in fork protection and partial resistance to PARP inhibitors, specifically in BRCA2-deficient cells¹⁷²; however, conflicting data exist on the role of MUS81, including reports suggesting that this nuclease either protects^{173,174} or disrupts^{171,172} unprotected forks; thus how MUS81 affects the cytotoxicity of PARP inhibitors in BRCA1/2-deficient cells remains controversial¹⁷⁴.

Notably, depletion of either PTIP, EZH2 or RAD51 does not ameliorate HR function in BRCA1/2-deficient cells, suggesting that restoration of replication fork protection is a crucial component of resistance to PARP inhibitors^{164,171,172}. Data from previous studies suggest that restoration of fork protection depends on the source of replication stress, the genetic context and the specific fork structures formed, which should all be considered in an attempt to better understand replication fork instability and how it can be exploited in cancer treatment.

Finally, and importantly, PARP1 is known to mediate the recruitment of MRE11 to stalled replication forks. PARP1 depletion results in synthetic lethality in BRCA1/2-deficient cells, whereas downregulation of PARP1 before BRCA1/2 loss restores the stability of stalled forks and promotes cell survival, likely by limiting the accumulation of MRE11 at replication forks^{164,175}. Given the multifunctional role of PARP1 at replication forks, further studies are required to understand how it can potentially affect the results of combination therapies involving PARP inhibitors.

Schlag 11 (SLFN11) is another factor implicated in replication stress. SLFN11 was originally identified by pharmacogenomic analyses of cancer cell databases as a strong determinant of response to multiple replication stress-inducing agents, including TOP I inhibitors, TOP II inhibitors, alkylating agents, DNA synthesis inhibitors and PARP inhibitors^{176–180}. Studies conducted over the past few years suggest that, upon replicative

damage, cells undergo irreversible cell-cycle arrest at G1/S phase, mediated by the engagement of SLFN11 with the replication helicase complexes¹⁸⁰. Binding of SLFN11 to stressed forks promotes chromatin relaxation and blocks cellular replication, which ultimately results in cell death¹⁸¹. Consequently, loss of SLFN11 impairs prolonged G1/S-phase arrest, thereby enabling cells to progress through S phase in the presence of replicative stress¹⁸¹. In line with this, loss of SLFN11 decreases the cytotoxicity of PARP inhibitors in both BRCA1/2-proficient and BRCA2-deficient cells¹⁸⁰. Importantly, HR is functional in both SLFN11-proficient and SLFN11-deficient cells, indicating that this protein acts in parallel with HR¹⁸⁰.

STRATEGIES TO OVERCOME RESISTANCE

Further studies are required to develop therapeutic strategies that combat or delay the emergence of acquired resistance and to determine the extent of cross resistance between the various therapeutic options. Surgical debulking, a strategy pursued mostly in women with ovarian cancer, might reduce or even eliminate resistant clones and thus, theoretically, delay the onset of resistance. Other potential strategies to tackle resistance to PARP inhibitors include: combination therapies aimed at further amplifying the antitumour effects of PARP inhibitors; targeting the acquired vulnerabilities of PARP inhibitor-resistant cancers; and/or delaying the emergence of resistance through suppression of the mutator phenotype, which arises in *BRCA1/2*-mutated tumours. In this section, we will describe current developments and findings exploiting these three approaches (Fig. 4 and 5).

Combination strategies

Suppression of alternative HR pathways

BRCA1-deficient cells are HR-deficient, nonetheless, DNA end-resection still takes place in these cells, albeit with delayed kinetics^{182–185}. This observation suggests that BRCA1 has other roles in HR beyond promoting end-resection. Indeed, BRCA1 has been shown to recruit the PALB2–BRCA2 complex to ssDNA, thus promoting the BRCA2-mediated assembly of RAD51 nucleoprotein filaments (BOX 2). Data from the past few years indicate that PALB2 is recruited to ssDNA in an RNF168-dependent manner in BRCA1-deficient cells^{186–189}. This finding implies that HR reactivation in BRCA1/53BP1-double-deficient cells is enabled by both RNF168-dependent recruitment of PALB2 and increased end-resection owing to loss of the 53BP1–RIF1–REV7–Shieldin axis^{187,189–191}. The extent of HR restoration enabled by 53BP1 loss depends on the type of *BRCA1* mutation because the overall efficiency of RAD51 loading (and, consequently, the extent of resistance to PARP inhibitors) is enhanced by the presence of hypomorphic *BRCA1* alleles that retain the ability to associate with PALB2^{186,189}. In line with its role in mediating PALB2 recruitment, loss of RNF168 compromises HR in *BRCA1* heterozygous cells and in BRCA1/53BP1-

double-deficient cells, thus rendering these cells sensitive to PARP inhibitors¹⁸⁹. Therapeutic targeting of RNF168 might therefore be a useful method of inhibiting BRCA1-independent PALB2/BRCA2 recruitment and thus improving the efficacy of PARP inhibitors against *BRCA1*-mutant cancers with acquired resistance to PARP inhibitors via loss of the 53BP1–RIF1–Shieldin end-protection pathway.

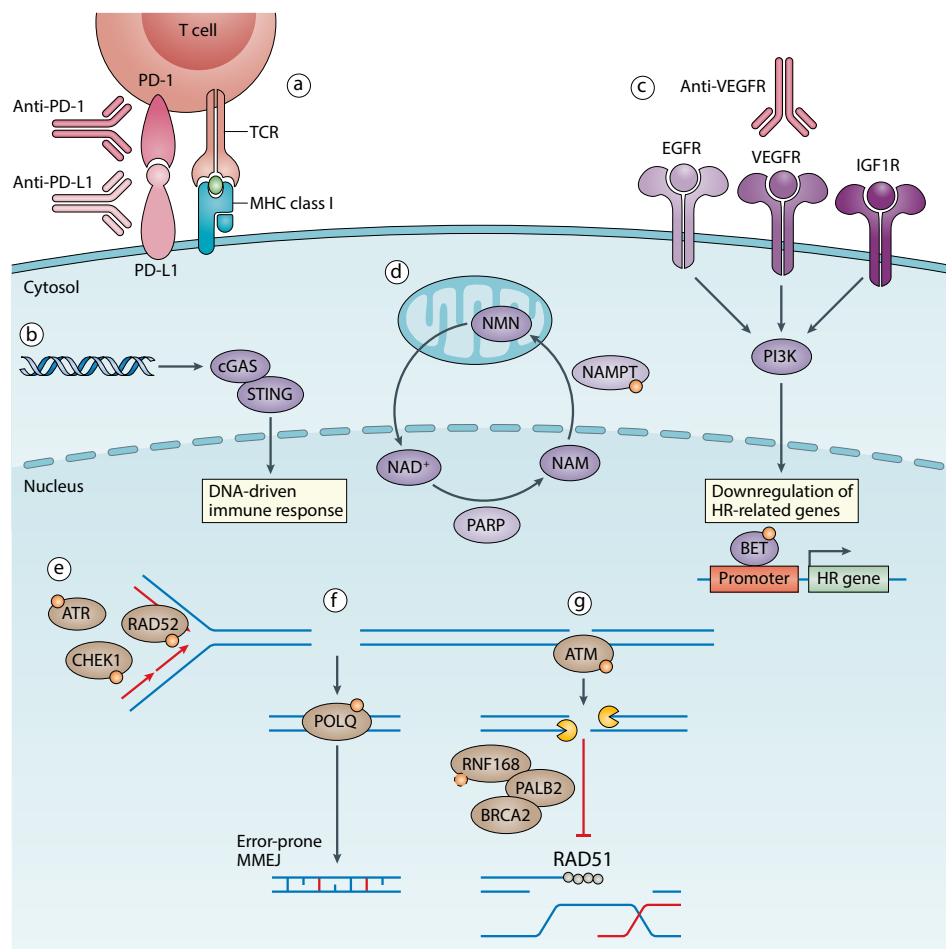


Figure 4 | Overcoming resistance to PARP inhibitors. Various combination strategies have been suggested to enhance the efficacy of poly(ADP-ribose) polymerase (PARP) inhibitors in treatment-resistant tumors. Immune-checkpoint inhibitors, such as anti-PD-1 or anti-CTLA4 antibodies, might be an alternative approach that is currently being assessed in the clinic given that homologous recombination (HR)-deficient tumours usually have high levels genomic instability and are thought to present an increased number of neoantigens on their surfaces (part **a**). Furthermore, PARP inhibitors have been shown to induce both PD-L1 expression as well as upregulation of cyclic GMP-AMP synthase (cGAS)-stimulator of interferon genes (STING) signaling, which might further boost the recruitment and/or activation of CD8+ T cells (part **b**). Reactivation of the HR pathway in tumors with acquired resistance to PARP inhibitors might be counteracted by treating patients with various tyrosine kinase inhibitors (such as VEGF-targeted therapies) or agents targeting epigenetic regulators of HR-related genes (such as bromodomain and extra-terminal domain (BET) inhibitors), or by targeting direct

mediators of HR, such as ATM or RNF168, which have been shown to promote HR in the absence of BRCA1 (parts **c**, **g**). NAD⁺ is the major substrate of PARP enzymes; therefore, inhibition of NAD⁺ synthesis might further enhance the cytotoxicity of PARP inhibitors through indirect inhibition of PARylation (part **d**). Multiple methods of suppressing restored replication fork protection in PARP inhibitor-resistant cells are currently being explored, such as inhibition of ATR or RAD52, which is thought to serve as a substitute for RAD51, as well as several cell cycle-related factors, such as CHEK1 (part **e**). Apart from combination therapy approaches, inhibition of microhomology-mediated end-joining (MMEJ) might be an alternative strategy because HR-deficient tumors are thought to depend on this pathway for DNA damage repair (part **f**); for example, inhibitors of the error-prone polymerase θ (POLQ) are currently being developed and are under consideration for use as single agents as well as in combination with PARP inhibitors. Inhibition of this mutagenic repair pathway might suppress or delay the onset of acquired resistance and reduce the extent of genomic instability of HR-deficient tumors.

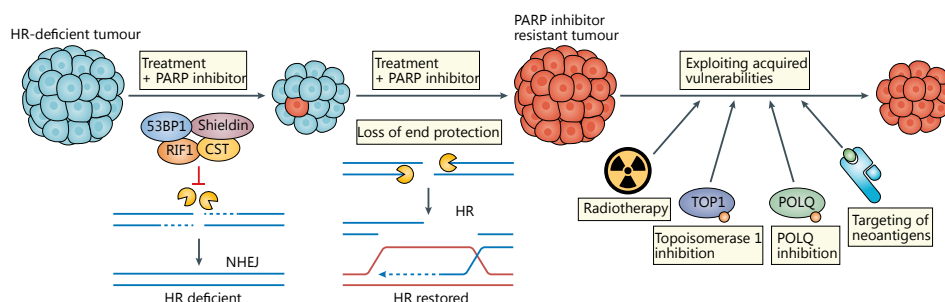


Figure 5 | Targeting acquired vulnerabilities of PARP inhibitor-resistant tumors. Acquired resistance to poly(ADP-ribose) polymerase (PARP) inhibitors often occurs through loss of additional DNA damage proteins, often resulting in the emergence of novel vulnerabilities that can be exploited therapeutically. For example, DNA-damaging agents such as radiotherapy or topoisomerase I inhibitors might be viable post-progression therapeutic strategies. Furthermore, inhibition of the error-prone DNA polymerase θ (POLQ) has been shown to be synthetic lethal with homologous recombination (HR) deficiency and might also delay the emergence of other resistance mechanisms. Depending on the type of resistance, tumors might also acquire and present tumour-specific neoantigens, which could potentially then be targeted using chimeric antigen receptor T cell therapies or immune-checkpoint inhibitors. CST, CTC1-STN1-TEN1; NHEJ, non-homologous end-joining.

Another factor that has become of increasing interest in the past years is the role of the DNA repair protein RAD52. Initial studies revealed only mild effects of RAD52 loss on viability *in vitro* as well as *in vivo*^{192,193}; however, co-depletion of RAD52 and BRCA1/2 was later reported to confer synthetic lethality, suggesting that RAD52 might serve as a backup pathway enabling RAD51 to gain access to resected DNA ends in the absence of BRCA1/2^{194,195}. Furthermore, evidence published over the past few years indicates that RAD52 might have a role in the repair of ssDNA at stalled replication forks as well as mediating fork reversal^{196,197}. The observed synthetic lethality might, therefore, be a combined effect of both functions of RAD52 rather than a consequence of one function. RAD52 inhibitors have been developed in the past years (reviewed elsewhere¹⁹⁸), and might provide an alternative method of targeting BRCA-deficient tumours. More research is needed to determine the *in vivo* efficacy of RAD52 inhibitors in both preclinical models and in patients, although results obtained thus far demonstrate a synergistic interaction between inhibitors of PARP and RAD52, leading to more potent cytotoxic effects on BRCA-deficient cells *in vitro* as well as *in vivo*¹⁹⁹.

Indirect inhibition of HR

To date, no direct inhibitors of proteins catalysing HR are available. An alternative strategy to inhibit HR restoration in patients receiving PARP inhibitors might be the use of drugs targeting actionable oncoproteins which, although not developed as HR inhibitors, interfere with gene expression, nuclear localization and/or the recruitment of HR factors, ultimately resulting in the indirect inhibition of HR (reviewed elsewhere³⁶). For example, therapies targeting VEGF or the PI3K–AKT pathway, have been reported to impair HR³⁶. In support of this notion, combining the VEGF antagonist bevacizumab with olaparib or niraparib improved the median PFS duration in two cohorts of women with ovarian cancer, even in those with HR-proficient tumours, relative to placebo or niraparib monotherapy^{200,201}. Furthermore, a phase I trial combining the AKT inhibitor capivasertib with olaparib revealed durable responses in patients with advanced-stage solid tumours, irrespective of *BRCA1/2* status²⁰², and another phase I trial combining the MEK inhibitor selumetinib with olaparib is currently ongoing (NCT03162627)²⁰³. However, the activity of these inhibitors might reflect impaired cell-cycle progression rather than direct inhibition of HR, suggesting that the effects observed for combination treatment may be additive rather than synergistic.

Indirect inhibition of HR might also be induced via pharmacological targeting of epigenetic regulators. For example, the bromodomain and extra-terminal domain (BET) protein BRD4 promotes global transcription by RNA polymerase II, and BET and/or BRD4 inhibitors have been shown to suppress the transcription of key DDR genes, including *CTIP*, *BRCA1*, *RAD51*, *TOPBP1* and *WEE1*, resulting in abrogation of HR and synergy with PARP inhibitors in preclinical investigations^{204–206}. Similarly, inhibition of histone deacetylases (HDACs) results in downregulation of HR and can be used to induce sensitivity to PARP inhibitors^{207–210}. Efficient suppression of HR and sensitization to PARP inhibitors has also been observed upon inhibition of cyclin-dependent kinases (CDKs), such as CDK1, which phosphorylates *BRCA1* and thus promotes HR repair²¹¹, and CDK12, which is a transcriptional regulator of several HR genes, including *BRCA1*^{212–214}. Furthermore, heat shock protein 90 (HSP90) promotes the stabilization of a subset of HR proteins, including *RAD51*, *BRCA1* and *BRCA2*, and targeted inhibition of this protein induces HR deficiency and promotes sensitivity to PARP inhibitors^{153,215,216}. The stability of these HR proteins can also be reduced by mild hyperthermia, which might be easily applicable in the clinic^{217,218}. Lastly, hypoxia has been reported to induce long-term epigenetic silencing of *BRCA1*, thereby also bestowing a vulnerability to PARP inhibitors that could potentially be exploited therapeutically²¹⁹. Importantly, all of these approaches can be used to enhance sensitivity to PARP inhibitors not only in tumours with restored HR, but also in those with hypomorphic or fully functional *BRCA* activity^{153,212,216}. However, for these reasons, combination strategies might also lead to substantial toxicities in nonmalignant proliferating cells, such as haematopoietic progenitors in the bone marrow.

Abrogation of cell-cycle checkpoint signalling

Data from several studies suggest that abrogation of cell-cycle checkpoint signalling might alleviate resistance to PARP inhibitors. ATM and ATR are the two major kinases controlling cell-cycle checkpoint activation and the ensuing arrest of cells in response to DNA damage. Several processes that cause resistance to PARP inhibitors in *BRCA1*-mutant cells, such as *BRCA1*-independent HR and fork protection, are dependent on ATR, which controls both processes by promoting RAD51 loading onto DSBs and stalled forks²²⁰. Thus, combinations comprising PARP inhibitors and ATR inhibitors are currently being investigated as potential methods of overcoming resistance to PARP inhibitors in *BRCA1*-deficient tumours with restored HR function or restored fork protection^{180,220–222}.

The chromatin remodelling enzyme ARID1A has been shown to regulate the DNA damage checkpoint via interactions with ATR, and loss of ARID1A leads to impaired cell-cycle checkpoint activation and sensitization of cells to PARP inhibitors¹⁰⁴. Similar to ATR, ATM kinase activity is required for the early stages of HR, and inhibition of ATM has been shown to resensitize cells with *BRCA1* and 53BP1 or *BRCA1* and REV7 deficiencies to PARP inhibitors^{134,142}.

PARP inhibitors have also been combined with WEE1 kinase inhibitors in preclinical models^{223–225}. WEE1 kinase regulates G2/M progression by inhibiting CDK1 and CDK2, thereby activating the G2/M cell-cycle checkpoint, resulting in cell-cycle arrest and providing time for DNA damage repair. The combination of PARP and WEE1 inhibitors aims to abrogate G2 arrest and induce mitotic catastrophe. A study using ovarian cancer xenograft models demonstrated that sequential rather than concurrent inhibition of PARP and WEE1 improves the tolerability of these drug combinations while still preserving antitumour activity²²⁵.

Multiple inhibitors of cell-cycle checkpoint kinases (such as ATR, ATM, CHK1 and WEE1) are being developed by pharmaceutical companies and are being tested in clinical trials designed to assess anticancer efficacy in combination with PARP inhibitors^{36,226}. The clinical applicability of these combinations will greatly depend on whether they are effective in patients with acquired resistance to PARP inhibitors without excessive toxic effects on nonmalignant tissues.

Targeting NAD⁺ metabolism

PARP1 uses oxidized NAD (NAD⁺) as a substrate for PARylation (BOX 1), which constitutes a major source of cellular NAD⁺ catabolic activity, resulting in NAD⁺ depletion to as low as 10–20% of its unstressed levels within minutes of induction of DNA damage²²⁷. Excessive PARP activation (for example, via oxidative stress or excessive DNA damage) effectively depletes the cellular pool of NAD⁺, leading to a progressive decline in ATP levels, energy loss and cell death^{228–230}. Thus, in order to maintain NAD⁺ levels, cells are reliant on salvage pathways. Functional genetic screens have shown that depletion of nicotinamide phosphoribosyltransferase (NAMPT), a rate-limiting enzyme in the NAD⁺ salvage pathway, enhances the cytotoxicity of PARP inhibitors in TNBC cells. Moreover, combining the NAMPT

inhibitor FK866 with olaparib resulted in more potent inhibition of the growth of TNBC xenografts *in vivo* than either agent alone²³¹. Neomorphic mutations in isocitrate dehydrogenase (IDH), which are common in gliomas and lead to decreased NAD⁺ levels through downregulation of the NAD⁺ salvage pathway enzyme nicotinate phosphoribosyltransferase (NAPRT1), render these tumours hypersensitive to NAD⁺ depletion²³². Importantly, mutant IDH also produces the oncometabolite D-2-hydroxyglutarate (D-2HG), which has been shown to inhibit HR and induce sensitivity to PARP inhibitors^{233,234}. Thus, neomorphic *IDH1/2* mutations might confer hypersensitivity to PARP inhibitors via two distinct mechanisms. Finally, the NAD⁺ derivative NADP⁺ can act as an endogenous PARP inhibitor that suppresses PARylation by competing for the NAD⁺ binding site of PARP. Consequently, cancer cells with high NADP⁺:NAD⁺ ratios have increased sensitivity to chemical PARP inhibition, irrespective of their *BRCA* mutation status²³⁵, which might reflect reduced PARylation rather than PARP trapping onto DNA.

Collectively, these studies suggest that the cytotoxicity of PARP inhibitors might be further enhanced by indirect inhibition of PARylation through targeted inhibition of NAD⁺ metabolism. More research is required in order to provide a deeper understanding of the interplay between cancer metabolism and (deficiencies in) HR repair, and how these interactions affect the efficacy of PARP inhibitors in patients with cancer. Ultimately, this knowledge might uncover new metabolic vulnerabilities of cancer cells exposed to PARP inhibitors that can be targeted to improve the efficacy of these agents.

Immunotherapy in BRCA-deficient cancers

The combination of PARP inhibitors with immune-checkpoint inhibitors, such as anti-PD-1 antibodies, is another potential approach to the treatment of patients with *BRCA1/2*-mutant cancers. Several observations have sparked a rapidly growing interest in such combinations. First, HR-deficient cancers are reported to have an increased mutational burden, possibly resulting in increased availability of tumour-specific neoantigens, including antigens originating from large genomic rearrangements²³⁶. Second, HR deficiencies might lead to the cytosolic accumulation of unrepaired DNA fragments, which can activate cyclic GMP–AMP synthase (cGAS)–stimulator of interferon genes (STING) signalling²³⁷. The recognition of extranuclear double-stranded DNA by cGAS triggers activation of the IRF3–type I interferon signalling pathway, which is an important mediator of systemic immune responses that induces the activation of several immune cell types²³⁸. Genomic rearrangements in *BRCA1/2*-deficient tumours might also disrupt chromatin boundaries and lead to the expression of repetitive RNAs which can activate innate immune signalling^{238,239}. Third, PARP inhibition induces both PD-L1 expression (via inactivation of GSK3 β) and cGAS–STING signalling, leading to increased CD8⁺ T cell infiltration and activation^{240,241,242,243}. However, whether PARP inhibitor-mediated activation of cGAS–STING signalling is dependent on the *BRCA* mutation status of the tumour is still a matter of debate. Data from one study suggest that cGAS–STING signalling is activated regardless of *BRCA* mutation status, while others found that activation

of this pathway occurs either solely or more potently in BRCA-deficient tumours^{240,241,191}.

In line with these findings, data from multiple studies indicate that PARP inhibition enhances the antitumour effects of anti-PD-1 antibodies in mouse models of breast and ovarian cancer^{240,241,242,243}. Several clinical trials are currently evaluating the effects of this combination in patients with these malignancies (reviewed elsewhere²⁴⁴). Initial clinical studies with PARP inhibitor–anti-PD-1 antibody combination have involved only small cohorts of patients and robust general conclusions therefore cannot be drawn, although certain interesting observations have already been reported. The combination of a PARP inhibitor with an anti-PD-1 antibody is generally well tolerated and seems to result in increased objective response rates when compared to monotherapies both in patients with ovarian cancer or breast cancer^{245–247}. However, the results of a phase I/II clinical trial involving women with platinum-resistant ovarian cancer found no significant differences in the objective response rate when comparing subgroups of patients with *BRCA1/2* mutations to those with wild-type *BRCA1/2*²⁴⁷. Of note, not all patients enrolled in this trial were tested for the presence of *BRCA1/2* mutations. Moreover, the mutation status of other HR genes was also not assessed. As mentioned above, the combination of immune-checkpoint inhibitors with PARP inhibitors remains an area of active investigation; therefore, whether patients with acquired resistance to PARP inhibitors might benefit from treatment with this combination has yet to be determined.

Targeting acquired vulnerabilities

Drug resistance often comes with a fitness cost that leads to acquired vulnerabilities, which can theoretically be targeted to improve the efficacy of subsequent therapies²⁴⁸ (**Fig. 5**). Several loss-of-function mutations that cause resistance to PARP inhibitors have been found to result in increased sensitivity to ionizing irradiation. For example, PARG inactivation, although detrimental to the efficacy of PARP inhibitors, results in increased sensitivity to ionizing radiation^{117,249}. In a similar fashion, loss of components of the 53BP1–RIF1–REV7–Shieldin or CST end-protection complexes, as well as PARP1 loss, have been demonstrated to result in hypersensitivity to ionizing radiation^{139,144,250–254}. As a consequence, radiotherapy might be a viable option for patients with BRCA-deficient tumours with acquired resistance to PARP inhibitors owing to loss of PARG, PARP1 or DSB end-protection.

Beyond sensitization to ionizing radiation, cells lacking in PARP1 activity also have increased susceptibility to the TOP I inhibitor camptothecin, owing to the role of PARP1 in the repair of TOP I cleavage sites²⁵⁵. Furthermore, PARG downregulation has also been shown to result in metabolic depletion of NAD⁺ and increased PARP1 trapping on chromatin, rendering such cells sensitive to the alkylating agent temozolomide^{256,257}.

Apart from the increased sensitivity of tumours with acquired resistance to PARP inhibitors to ionizing radiation, camptothecin or temozolomide, an alternative approach suggested in 2020 involves targeting tumours with acquired resistance to PARP inhibitors owing to genetic reversion¹³¹. Genetic reversion often does not restore the complete original amino

acid sequence of the protein and, therefore, most revertant proteins contain stretches of amino acids, often at the reversion junction, that are not encoded in the wild-type gene and might thus be presented on the cell surface as neoantigens and subsequently recognized by the immune system. Tumours harbouring such alterations could then be targeted using anticancer vaccines, chimeric antigen receptor T cell therapies and/or immune-checkpoint inhibitors¹³¹.

Despite the evidence described here, studies attempting to identify such acquired dependencies remain limited. A key approach to identify acquired vulnerabilities would be to perform pharmacological or genetic screens in different models of acquired resistance to PARP inhibitors. The identification of such dependencies might then enable specific targeting of PARP inhibitor-resistant tumours using therapies selected according to the underlying mechanism of resistance.

Preventing the emergence of resistance

Targeting drug-tolerant persisters

PARP inhibitors cause DNA damage specifically during the S and G2 phases of the cell cycle²⁵⁸ and thereby specifically target proliferating cells. Consequently, cell populations in G₀ or early G₁ phase might be unaffected by PARP inhibitors because neither HR nor replication forks are active during these phases. Indeed, continuous exposure to PARP inhibitors has been shown to induce senescence in ovarian cancer cell lines, which is reversed upon PARP inhibitor withdrawal, suggesting that senescent persister cells might be capable of contributing to further tumour growth²⁵⁹. Moreover, several processes, such as epigenetic reprogramming, transcriptional regulation as well as interactions with the tumour microenvironment might all delay cell growth and thereby make cells less responsive to therapy (reviewed elsewhere²⁶⁰). The persistence of drug-tolerant tumour cells provides a rationale for the use of long-term maintenance therapy, which might be able to kill residual dormant cellular populations once they enter the cell cycle.

Suppression of the mutator phenotype

In order to repair DNA DSBs in the absence of HR, BRCA1/2-deficient cells are able to upregulate microhomology-mediated end joining (MMEJ) as a compensatory mechanism, which is thought to have only a minor role in HR-proficient cells²⁶¹. MMEJ is an error-prone repair pathway, driven by the low-fidelity DNA polymerase θ (POLQ). POLQ joins two broken DNA strands based on short regions of sequence homology (>2 bp), which can be detected as an MMEJ-characteristic pattern of mutations in BRCA1/2-deficient tumours using whole-genome sequencing²⁶². Given that DSB repair in HR-deficient cancers is dependent on POLQ-mediated MMEJ, suppressing this error-prone DNA repair pathway might be another way to target these tumours. In line with this hypothesis, two groups have reported a synthetic lethal interaction between POLQ depletion and proteins involved in HR^{263,264}. Notably, POLQ inhibition suppresses the genomic instability arising from error-

prone MMEJ; therefore, this approach might be superior to PARP inhibition, which is thought to enhance genomic instability and thereby promote the emergence of HR-deficient cancers of a ‘mutator phenotype’. Inhibition of POLQ might therefore be effective not only in tumours with acquired resistance to PARP inhibitors, but also in preventing or attenuating the emergence of treatment resistance in PARP-inhibitor-naïve HR-deficient tumours.

The development of POLQ inhibitors is generating considerable research interest. The antibiotic novobiocin (NVB) is reported to inhibit the ATPase activity of POLQ²⁶⁵. In line with initial reports, inhibition of POLQ by NVB selectively kills HR-deficient tumours both *in vitro* as well as *in vivo*. Furthermore, NVB reduces tumour growth in a PDX model with combined loss of BRCA1 and 53BP1 function, suggesting that POLQ inhibition might also be a viable option for tumours with acquired resistance to PARP inhibitors owing to loss of DNA end-protection²⁶⁵. This study suggests that POLQ inhibition might be a promising strategy, either in combination with or as an alternative to PARP inhibitors. However, further research is needed to answer critical questions regarding the clinical use of POLQ inhibitors. For example, it remains to be determined (i) whether POLQ inhibition will be effective as monotherapy or only in combination with PARP inhibitors; (ii) whether all tumours that are resistant to PARP inhibitors will respond to POLQ inhibitors or whether sensitivity will be restricted to tumours that become resistant via certain mechanisms, such as the loss of DNA end-protection; (iii) whether tumours with genomic instability or mutations in HR-related genes other than *BRCA1* and *BRCA2* might be susceptible to inhibition of POLQ.

FUTURE DIRECTIONS

Over the past years, preclinical and clinical studies have substantially increased our knowledge of both the mechanism of action and possible sources of resistance to PARP inhibitors. PARP inhibitors are increasingly used clinically and their application is being expanded to indications beyond breast and ovarian cancer. Many mechanisms of resistance have been reported in cancer cell lines and mouse models, although the clinical relevance of most of these mechanisms remains unclear owing to the majority of the regulatory approvals of PARP inhibitors taking place in the past few years. Moreover, the mechanisms of resistance identified in preclinical studies might differ from those observed in patients given that most mature clinical data are from trials testing PARP inhibitors as second-line therapies. Tumour subclones in many of these patients might already have developed certain forms of resistance to previous treatments (such as taxanes or platinum-based chemotherapies) that confer cross-resistance to PARP inhibitors. Thus, determining whether improvements in PFS and, ultimately, in OS can be achieved by giving PARP inhibitors earlier in the course of treatment will be an important step. In comparison with second-line treatment regimens, first-line treatment with PARP inhibitors might not only further delay disease progression but could also postpone the onset of resistance and alter the underlying mechanisms of

resistance to these agents. For instance, PARP inhibitor resistance caused by genetic reversion mutations may result in cross resistance to second-line chemotherapy. In contrast, BRCA1-deficient tumours that have acquired resistance through loss of DNA end-protection may still respond to radiation therapy or POLQ inhibitors. It will therefore be important to determine how patients developed resistance to PARP inhibitors, so that cross resistance can be avoided in the second-line treatment.

Olaparib and niraparib have both been approved as first-line maintenance therapies and, with more patients likely to receive PARP inhibitors earlier in the course of disease, clinical trials of novel post-progression approaches are either planned or currently ongoing (for example NCT03106987). Molecular analysis of tumour biopsy samples and/or cell-free DNA samples (**Box 3**) obtained from these patients might provide more insight into the underlying mechanisms of resistance to PARP inhibitors as well as the mechanisms conferring cross-resistance between PARP inhibitors and other anticancer agents. Another key question is whether distinct or similar mechanisms drive disease recurrence after planned treatment cessation versus recurrence during maintenance therapy. Future studies will help to determine whether the recurring tumours might respond to re-challenge with PARP inhibitors.

Clinical attempts to determine which patients are most likely to benefit from PARP inhibitors and to identify the optimal treatment regimens are currently ongoing. Nonetheless resistance to PARP inhibitors might be an inevitable consequence of the genomic instability of these HR-deficient tumours. As mentioned above, targeted approaches designed to overcome resistance to PARP inhibitors remain limited. The systematic identification of the vulnerabilities of PARP inhibitor-resistant tumours will therefore be an important step. Data from *in vitro* as well as *in vivo* genetic screens will advance our understanding of the rewiring of treatment-resistant tumours, and pharmacological screens might also be used to identify compounds that specifically target these cancers. In order to study resistance to PARP inhibitors in settings more closely related to the clinic, genetically engineered mouse models that develop PARP inhibitor-resistant tumours might be of great value, as well as PDX models generated using samples from patients with acquired resistance. Conversely, in-depth analysis of tumours from patients with remarkably good responses to PARP inhibitors — so-called ‘exceptional responders’ — might be an alternative strategy to better identify novel molecular determinants of (hyper)sensitivity to these agents²⁶⁶. Finally, the establishment of single-cell omics technologies might facilitate more detailed investigations of patient-derived material, which is usually of limited availability.

Box 3| Detecting resistance in patients with cancer. Close monitoring of treatment response and the early detection of subclones that are likely to confer resistance to poly (ADP-ribose) polymerase (PARP) inhibitors are key to the success of a treatment regimen. However, standard tumor biopsy sampling is mostly invasive and thus often cannot be conducted on a regular basis. As a consequence, noninvasive methods of assessing tumor genomics using blood or plasma samples (liquid biopsies) are being intensively investigated as these can be performed serially and might provide a better indication of tumor heterogeneity. Several biomarkers can be detected within these biopsy samples, although circulating tumor DNA (ctDNA) is currently believed to be the most promising marker for the assessment of treatment response and the extent of residual disease. ctDNA is thought to be released from cells undergoing apoptosis or necrosis and has been suggested to provide a 'real-time' picture of disease status, owing to its short half-life, ranging from 16–150 minutes²⁶³. Initial evidence suggests that analysis of ctDNA might be a suitable method of detecting resistance to PARP inhibitors in patients. A subset of genetic reversion events leading to resistance to PARP inhibitors in patients with BRCA-mutated cancers can be readily detected in ctDNA^{123,129,130,268}. Interestingly, the presence of polyclonal PARP inhibitor-resistant populations has also been described, some of which were already present before treatment initiation^{123,268}. These studies suggest that ctDNA provides a simple method that not only enables the monitoring of treatment response but also might enable earlier switching of treatments as resistant clones begin to emerge. Certain genetic reversion events might well be detectable in ctDNA¹⁰⁶, although other mechanisms of resistance to PARP inhibitors, such as restoration of HR or replication fork protection might be more challenging because these processes are often caused by genomic alterations, such as large deletions or breakpoints in introns, that are less likely to be detected using current sequencing approaches. Although further research is required, ctDNA assays might provide a fast and cost-effective way of screening patients for common and/or patient-specific alterations associated with PARP inhibitor resistance. Currently ongoing clinical trials aimed at assessing the predictive value of ctDNA screening (e.g., NCT03182634) might shed more light on the potential use of this approach.

CONCLUSIONS

In conclusion, PARP inhibitors provide a promising treatment strategy that is potentially applicable to several stages of cancer progression. Multiple mechanisms of resistance to these agents have been identified and characterized over the past years and confirmation of the clinical relevance of these various mechanisms is urgently needed. Additionally, strategies designed to specifically target tumour cells with resistance to PARP inhibitors are still lacking. An improved understanding of the biology of HR-deficient cancers will facilitate the development of rational treatment strategies to prevent and/or delay the onset of resistance and will ultimately lead to improved long-term outcomes for patients.

ACKNOWLEDGEMENTS

Work in J.J.'s laboratory was funded by the Oncode Institute, which is partly financed by the Dutch Cancer Society. The work of M.P.D. is supported by the European Union's Horizon 2020 research and innovation programme under the Marie Skłodowska-Curie grant agreement No. 722729. The work of S.C.M. is supported by Boehringer Ingelheim Fonds. S.G. has received funding from the NCI (grants R01-CA243547, R01-CA202752 and 5P30CA072720-21), DOD, the Breast Cancer Research Foundation, Hugs for Brady, the Val Skinner Foundation, the Gertrude Fogarty Trust and AHEPA.

AUTHOR CONTRIBUTIONS

M.P.D. and S.C.M. made substantial contributions to researching data for this article and discussions of content. All authors contributed to writing the article and reviewing/editing of the manuscript before submission.

REFERENCES

1. Bryant, H. E. *et al.* Specific killing of BRCA2-deficient tumours with inhibitors of poly(ADP-ribose) polymerase. *Nature* **434**, 913–917 (2005).
2. Farmer, H. *et al.* Targeting the DNA repair defect in BRCA mutant cells as a therapeutic strategy. *Nature* **434**, 917–21 (2005).
3. Bai, P. & Cantó, C. The Role of PARP-1 and PARP-2 Enzymes in Metabolic Regulation and Disease. *Cell Metab.* **16**, 290–295 (2012).
4. Hanzlikova, H. *et al.* The Importance of Poly(ADP-Ribose) Polymerase as a Sensor of Unligated Okazaki Fragments during DNA Replication. *Mol. Cell* **71**, 319–331.e3 (2018).
5. Ray Chaudhuri, A. & Nussenzweig, A. The multifaceted roles of PARP1 in DNA repair and chromatin remodelling. *Nat. Rev. Mol. Cell Biol.* **18**, 610–621 (2017).
6. Chen, C., Feng, W., Lim, P. X., Kass, E. M. & Jasin, M. Homology-Directed Repair and The Role of BRCA1 , BRCA2 , and Related Proteins in Genome Integrity and Cancer. *Annu. Rev. Cancer Biol.* **2**, 313–336 (2017).
7. Scully, R., Panday, A., Elango, R. & Willis, N. A. DNA double-strand break repair-pathway choice in somatic mammalian cells. *Nat. Rev. Mol. Cell Biol.* **20**, 698–714 (2019).
8. Schlacher, K. *et al.* Double-strand break repair-independent role for BRCA2 in blocking stalled replication fork degradation by MRE11. *Cell* **145**, 529–542 (2011).
9. Schlacher, K., Wu, H. & Jasin, M. A Distinct Replication Fork Protection Pathway Connects Fanconi Anemia Tumor Suppressors to RAD51-BRCA1/2. *Cancer Cell* **22**, 106–116 (2012).
10. Nik-Zainal, S. *et al.* Landscape of somatic mutations in 560 breast cancer whole-genome sequences. *Nature* **534**, 47–54 (2016).
11. Patch, A. M. *et al.* Whole-genome characterization of chemoresistant ovarian cancer. *Nature* **521**, 489–494 (2015).
12. Armenia, J. *et al.* The long tail of oncogenic drivers in prostate cancer. *Nat. Genet.* **50**, 645–651 (2018).
13. Pritchard, C. C. *et al.* Inherited DNA-repair gene mutations in men with metastatic prostate cancer. *N. Engl. J. Med.* **375**, 443–453 (2016).
14. Robinson, D. *et al.* Integrative clinical genomics of advanced prostate cancer. *Cell* **161**, 1215–1228 (2015).
15. Waddell, N. *et al.* Whole genomes redefine the mutational landscape of pancreatic cancer. *Nature* **518**, 495–501 (2015).
16. Ashworth, A. & Lord, C. J. Synthetic lethal therapies for cancer: what's next after PARP inhibitors? *Nature Reviews Clinical Oncology* **15**, 564–576 (2018).
17. Bhattacharyya, A., Ear, U. S., Koller, B. H., Weichselbaum, R. R. & Bishop, D. K. The Breast Cancer susceptibility gene BRCA1 is required for subnuclear assembly of Rad51 and survival following treatment with the DNA cross-linking agent cisplatin. *J. Biol. Chem.* **275**, 23899–23903 (2000).
18. Treszezamsky, A. D. *et al.* BRCA1- and BRCA2-deficient cells are sensitive to etoposide-induced DNA double-strand breaks via topoisomerase II. *Cancer Res.* **67**, 7078–7081 (2007).
19. Evers, B. *et al.* A high-throughput pharmaceutical screen identifies compounds with specific toxicity against BRCA2-deficient tumors. *Clin. Cancer Res.* **16**, 99–108 (2010).
20. Gibson, B. A. & Kraus, W. L. New insights into the molecular and cellular functions of poly(ADP-ribose) and PARPs. *Nature Reviews Molecular Cell Biology* **13**, 411–424 (2012).
21. Pascal, J. M. & Ellenberger, T. The rise and fall of poly(ADP-ribose): An enzymatic perspective. *DNA Repair (Amst.)* **32**, 10–16 (2015).
22. Amé, J.-C. *et al.* PARP-2, A Novel Mammalian DNA Damage-dependent Poly(ADP-ribose) Polymerase. *J. Biol. Chem.* **274**, 17860–17868 (1999).
23. Hanzlikova, H., Gittens, W., Krejčíková, K., Zeng, Z. & Caldecott, K. W. Overlapping roles for PARP1 and PARP2 in the recruitment of endogenous XRCC1 and PNKP into oxidized chromatin. *Nucleic Acids Res.* **45**, 2546–2557 (2017).
24. Grundy, G. J. *et al.* PARP3 is a sensor of nicked nucleosomes and monoribosylates histone H2B Glu2. *Nat. Commun.* **7**, 1–12 (2016).
25. Rulten, S. L. *et al.* PARP-3 and APLF function together to accelerate nonhomologous end-joining. *Mol. Cell* **41**, 33–45 (2011).
26. Langelier, M. F., Riccio, A. A. & Pascal, J. M. PARP-2 and PARP-3 are selectively activated by 5' phosphorylated DNA breaks through an allosteric regulatory mechanism shared with PARP-1. *Nucleic Acids Res.* **42**, 7762–7775 (2014).
27. Mueller-Dieckmann, C. *et al.* The structure of human ADP-ribosylhydrolase 3 (ARH3) provides insights into the reversibility of protein ADP-ribosylation. *Proc. Natl. Acad. Sci. U. S. A.* **103**, 15026–15031 (2006).
28. Abplanalp, J. *et al.* Proteomic analyses identify ARH3 as a serine mono-ADP-ribosylhydrolase. *Nat. Commun.* **8**, 2055 (2017).
29. Barkauskaite, E. *et al.* Visualization of poly(ADP-ribose) bound to PARG reveals inherent balance between exo-

- and endo-glycohydrolase activities. *Nat. Commun.* **4**, 2164 (2013).
30. Liu, C., Wu, J., Paudyal, S. C., You, Z. & Yu, X. CHFR is important for the first wave of ubiquitination at DNA damage sites. *Nucleic Acids Res.* **41**, 1698–1710 (2013).
 31. Slade, D. PARP and PARG inhibitors in cancer treatment. *Genes Dev.* **34**, 360–394 (2020).
 32. Roy, R., Chun, J. & Powell, S. N. BRCA1 and BRCA2: Different roles in a common pathway of genome protection. *Nat. Rev. Cancer* **12**, 68–78 (2012).
 33. Harbeck, N. *et al.* Breast cancer. *Nat. Rev. Dis. Prim.* **5**, 1–31 (2019).
 34. Xia, B. *et al.* Control of BRCA2 Cellular and Clinical Functions by a Nuclear Partner, PALB2. *Mol. Cell* **22**, 719–729 (2006).
 35. Rahman, N. *et al.* PALB2, which encodes a BRCA2-interacting protein, is a breast cancer susceptibility gene. *Nat. Genet.* **39**, 165–167 (2007).
 36. Pilié, P. G., Tang, C., Mills, G. B. & Yap, T. A. State-of-the-art strategies for targeting the DNA damage response in cancer. *Nat. Rev. Clin. Oncol.* **16**, 81–104 (2019).
 37. Mateo, J. *et al.* A decade of clinical development of PARP inhibitors in perspective. *Ann. Oncol.* **30**, 1437–1447 (2019).
 38. Curtin, N. J. & Szabo, C. Poly(ADP-ribose) polymerase inhibition: past, present and future. *Nat. Rev. Drug Discov.* **19**, 711–736 (2020).
 39. Helleday, T. The underlying mechanism for the PARP and BRCA synthetic lethality: Clearing up the misunderstandings. *Mol. Oncol.* **5**, 387–393 (2011).
 40. Ström, C. E. *et al.* Poly (ADP-ribose) polymerase (PARP) is not involved in base excision repair but PARP inhibition traps a single-strand intermediate. *Nucleic Acids Res.* **39**, 3166–3175 (2011).
 41. Patel, A. G., Sarkaria, J. N. & Kaufmann, S. H. Nonhomologous end joining drives poly(ADP-ribose) polymerase (PARP) inhibitor lethality in homologous recombination-deficient cells. *Proc. Natl. Acad. Sci. U. S. A.* **108**, 3406–3411 (2011).
 42. Zahradka, P. & Ebisuzaki, K. A shuttle mechanism for DNA-protein interactions. The regulation of poly(ADP-ribose) polymerase. *Eur. J. Biochem.* **127**, 579–85 (1982).
 43. Murai, J. *et al.* Stereospecific PARP trapping by BMN 673 and comparison with olaparib and rucaparib. *Mol. Cancer Ther.* **13**, 433–443 (2014).
 44. Murai, J. & Pommier, Y. PARP Trapping Beyond Homologous Recombination and Platinum Sensitivity in Cancers. *Annu. Rev. Cancer Biol.* **3**, 131–150 (2019).
 45. Murai, J. *et al.* Trapping of PARP1 and PARP2 by clinical PARP inhibitors. *Cancer Res.* **72**, 5588–5599 (2012).
 46. Shen, Y. *et al.* BMN673, a novel and highly potent PARP1/2 inhibitor for the treatment of human cancers with DNA repair deficiency. *Clin. Cancer Res.* **19**, 5003–5015 (2013).
 47. Zandarashvili, L. *et al.* Structural basis for allosteric PARP-1 retention on DNA breaks. *Science (80-.).* **368**, eaax6367 (2020).
 48. Brown, J. S., Kaye, S. B. & Yap, T. A. PARP inhibitors: the race is on. *Br. J. Cancer* **114**, 713–715 (2016).
 49. Carney, B. *et al.* Target engagement imaging of PARP inhibitors in small-cell lung cancer. *Nat. Commun.* **9**, 1–13 (2018).
 50. Pommier, Y., O'Connor, M. J. & De Bono, J. Laying a trap to kill cancer cells: PARP inhibitors and their mechanisms of action. *Science Translational Medicine* **8**, (2016).
 51. LaFargue, C. J., Dal Molin, G. Z., Sood, A. K. & Coleman, R. L. Exploring and comparing adverse events between PARP inhibitors. *Lancet Oncol.* **20**, e15–e28 (2019).
 52. Zimmermann, M. *et al.* CRISPR screens identify genomic ribonucleotides as a source of PARP-trapping lesions. *Nature* **559**, 285–289 (2018).
 53. Schoonen, P. M. *et al.* Progression through mitosis promotes PARP inhibitor-induced cytotoxicity in homologous recombination-deficient cancer cells. *Nat. Commun.* **8**, 1–13 (2017).
 54. Maya-Mendoza, A. *et al.* High speed of fork progression induces DNA replication stress and genomic instability. *Nature* **559**, 279–284 (2018).
 55. Xiong, Y. *et al.* Pamiparib is a potent and selective PARP inhibitor with unique potential for the treatment of brain tumor. *Neoplasia (United States)* **22**, 431–440 (2020).
 56. Zejula | European Medicines Agency. Available at: <https://www.ema.europa.eu/en/medicines/human/EPAR/zejula>. (Accessed: 15th February 2022)
 57. Talzenna | European Medicines Agency. Available at: <https://www.ema.europa.eu/en/medicines/human/EPAR/talzenna>. (Accessed: 15th February 2022)
 58. Lynparza | European Medicines Agency. Available at: <https://www.ema.europa.eu/en/medicines/human/EPAR/lynparza>. (Accessed: 15th February 2022)
 59. Rubraca | European Medicines Agency. Available at: <https://www.ema.europa.eu/en/medicines/human/EPAR/rubraca>. (Accessed: 15th February 2022)
 60. Wahlberg, E. *et al.* Family-wide chemical profiling and structural analysis of PARP and tankyrase inhibitors. *Nat. Biotechnol.* **30**, 283–288 (2012).
 61. Halford, S. E. R. *et al.* Results of the OPARATIC trial: A phase I dose escalation study of olaparib in combination

- with temozolomide (TMZ) in patients with relapsed glioblastoma (GBM). *J. Clin. Oncol.* **35**, 2022 (2017).
62. Daniel, R. A. *et al.* Central nervous system penetration and enhancement of temozolomide activity in childhood medulloblastoma models by poly(ADP-ribose) polymerase inhibitor AG-014699. *Br. J. Cancer* **103**, 1588–1596 (2010).
63. Sun, K. *et al.* A comparative pharmacokinetic study of PARP inhibitors demonstrates favorable properties for niraparib efficacy in preclinical tumor models. *Oncotarget* **9**, 37080–37096 (2018).
64. Kizilbash, S. H. *et al.* Restricted delivery of talazoparib across the blood–brain barrier limits the sensitizing effects of PARP inhibition on temozolomide therapy in glioblastoma. *Mol. Cancer Ther.* **16**, 2735–2746 (2017).
65. Werner, T. L. *et al.* Safety and pharmacokinetics of veliparib extended-release in patients with advanced solid tumors: a phase I study. *Cancer Med.* **7**, 2360–2369 (2018).
66. Pothuri, B. *et al.* Phase I and pharmacokinetic study of veliparib, a PARP inhibitor, and pegylated liposomal doxorubicin (PLD) in recurrent gynecologic cancer and triple negative breast cancer with long-term follow-up. *Cancer Chemother. Pharmacol.* **85**, 741–751 (2020).
67. Wang, L. *et al.* Pharmacologic characterization of fluzoparib, a novel poly(ADP-ribose) polymerase inhibitor undergoing clinical trials. *Cancer Sci.* **110**, 1064–1075 (2019).
68. Kaufman, B. *et al.* Olaparib monotherapy in patients with advanced cancer and a germline BRCA1/2 mutation. *J. Clin. Oncol.* **33**, 244–50 (2015).
69. Kim, G. *et al.* FDA Approval Summary: Olaparib Monotherapy in Patients with Deleterious Germline BRCA-Mutated Advanced Ovarian Cancer Treated with Three or More Lines of Chemotherapy. *Clin. Cancer Res.* **21**, 4257–4261 (2015).
70. Ledermann, J. *et al.* Olaparib Maintenance Therapy in Platinum-Sensitive Relapsed Ovarian Cancer. *N. Engl. J. Med.* **366**, 1382–1392 (2012).
71. Balasubramaniam, S. *et al.* FDA Approval Summary: Rucaparib for the Treatment of Patients with Deleterious BRCA Mutation–Associated Advanced Ovarian Cancer. *Clin. Cancer Res.* **23**, 7165–7170 (2017).
72. Swisher, E. M. *et al.* Rucaparib in relapsed, platinum-sensitive high-grade ovarian carcinoma (ARIEL2 Part 1): an international, multicentre, open-label, phase 2 trial. *Lancet Oncol.* **18**, 75–87 (2017).
73. Kristeleit, R. S. *et al.* Clinical activity of the poly(ADP-ribose) polymerase (PARP) inhibitor rucaparib in patients (pts) with high-grade ovarian carcinoma (HGOC) and a BRCA mutation (BRCAmut): Analysis of pooled data from Study 10 (parts 1, 2a, and. *Ann. Oncol.* **27**, 296–312 (2016).
74. Moore, K. N. *et al.* QUADRA: A phase 2, open-label, single-arm study to evaluate niraparib in patients (pts) with relapsed ovarian cancer (ROC) who have received ≥ 3 prior chemotherapy regimens. *J. Clin. Oncol.* **36**, 5514–5514 (2018).
75. Moore, K. N. *et al.* Niraparib monotherapy for late-line treatment of ovarian cancer (QUADRA): a multicentre, open-label, single-arm, phase 2 trial. *Lancet Oncol.* **20**, 636–648 (2019).
76. Ledermann, J. *et al.* Olaparib maintenance therapy in patients with platinum-sensitive relapsed serous ovarian cancer: a preplanned retrospective analysis of outcomes by BRCA status in a randomised phase 2 trial. *Lancet Oncol.* **15**, 852–861 (2014).
77. Pujade-Lauraine, E. *et al.* Olaparib tablets as maintenance therapy in patients with platinum-sensitive, relapsed ovarian cancer and a BRCA1/2 mutation (SOLO2/ENGOT-Ov21): a double-blind, randomised, placebo-controlled, phase 3 trial. *Lancet Oncol.* **18**, 1274–1284 (2017).
78. Mirza, M. R. *et al.* Niraparib Maintenance Therapy in Platinum-Sensitive, Recurrent Ovarian Cancer. *N. Engl. J. Med.* **375**, 2154–2164 (2016).
79. Pujade-Lauraine, E. *et al.* Olaparib tablets as maintenance therapy in patients with platinum-sensitive, relapsed ovarian cancer and a BRCA1/2 mutation (SOLO2/ENGOT-Ov21): a double-blind, randomised, placebo-controlled, phase 3 trial. *Lancet Oncol.* **18**, 1274–1284 (2017).
80. Coleman, R. L. *et al.* Rucaparib maintenance treatment for recurrent ovarian carcinoma after response to platinum therapy (ARIEL3): a randomised, double-blind, placebo-controlled, phase 3 trial. *Lancet* **390**, 1949–1961 (2017).
81. Moore, K. *et al.* Maintenance Olaparib in Patients with Newly Diagnosed Advanced Ovarian Cancer. *N. Engl. J. Med.* **379**, 2495–2505 (2018).
82. González-Martín, A. *et al.* Niraparib in patients with newly diagnosed advanced ovarian cancer. *N. Engl. J. Med.* **381**, 2391–2402 (2019).
83. Robson, M. *et al.* Olaparib for metastatic breast cancer in patients with a germline BRCA mutation. *N. Engl. J. Med.* **377**, 523–533 (2017).
84. Litton, J. K. *et al.* Talazoparib in Patients with Advanced Breast Cancer and a Germline BRCA Mutation. *N. Engl. J. Med.* **379**, 753–763 (2018).
85. Golan, T. *et al.* Maintenance olaparib for germline BRCA-mutated metastatic pancreatic cancer. *N. Engl. J. Med.* **381**, 317–327 (2019).
86. de Bono, J. *et al.* Olaparib for Metastatic Castration-Resistant Prostate Cancer. *N. Engl. J. Med.* **382**, 2091–2102 (2020).
87. Ganesan, S. & Garber, J. Poly (ADP-Ribose) Polymerase Inhibitor Activity in Prostate Cancers Harboring Mutations

- in DNA Repair Genes: Who Benefits? *JCO Precis. Oncol.* 1034–1037 (2020). doi:10.1200/PO.20.00269
88. Abida, W. *et al.* Rucaparib in Men With Metastatic Castration-Resistant Prostate Cancer Harboring a BRCA1 or BRCA2 Gene Alteration. *J. Clin. Oncol.* JCO2001035 (2020). doi:10.1200/JCO.20.01035
 89. Lickliter, J. D. *et al.* A phase I dose-escalation study of BGB-290, a novel PARP1/2 selective inhibitor in patients with advanced solid tumors. *J. Clin. Oncol.* **34**, e17049–e17049 (2016).
 90. Lickliter, J. *et al.* Dose escalation/expansion study to investigate the safety, pharmacokinetics, food effect, and antitumor activity of BGB-290 in patients with advanced solid tumors. *Ann. Oncol.* **28**, v123 (2017).
 91. Ledermann, J. A. *et al.* Overall survival in patients with platinum-sensitive recurrent serous ovarian cancer receiving olaparib maintenance monotherapy: an updated analysis from a randomised, placebo-controlled, double-blind, phase 2 trial. *Lancet Oncol.* **17**, 1579–1589 (2016).
 92. Friedlander, M. L. *et al.* 234O Maintenance olaparib for patients (pts) with newly diagnosed, advanced ovarian cancer (OC) and a BRCA mutation (BRCAm): 5-year (y) follow-up (f/u) from SOLO1. *Ann. Oncol.* **31**, S1334 (2020).
 93. Poveda, A. *et al.* Olaparib tablets as maintenance therapy in patients with platinum-sensitive relapsed ovarian cancer and a BRCA1/2 mutation (SOLO2/ENGOT-Ov21): a final analysis of a double-blind, randomised, placebo-controlled, phase 3 trial. *Lancet Oncol.* **2045**, 1–12 (2021).
 94. Coleman, R. L. *et al.* Veliparib with first-line chemotherapy and as maintenance therapy in ovarian cancer. *N. Engl. J. Med.* **381**, 2403–2415 (2019).
 95. Ray-Coquard, I. *et al.* Olaparib plus Bevacizumab as First-Line Maintenance in Ovarian Cancer. *N. Engl. J. Med.* **381**, 2416–2428 (2019).
 96. McCabe, N. *et al.* Deficiency in the repair of DNA damage by homologous recombination and sensitivity to poly(ADP-ribose) polymerase inhibition. *Cancer Res.* **66**, 8109–8115 (2006).
 97. Hodgson, D. R. *et al.* Candidate biomarkers of PARP inhibitor sensitivity in ovarian cancer beyond the BRCA genes. *Br. J. Cancer* **119**, 1401–1409 (2018).
 98. Mateo, J. *et al.* DNA-Repair Defects and Olaparib in Metastatic Prostate Cancer. *N. Engl. J. Med.* **373**, 1697–1708 (2015).
 99. Abida, W. *et al.* Non-BRCA DNA Damage Repair Gene Alterations and Response to the PARP Inhibitor Rucaparib in Metastatic Castration-Resistant Prostate Cancer: Analysis From the Phase II TRITON2 Study. *Clin. Cancer Res.* **26**, 2487–2496 (2020).
 100. Tung, N. M. *et al.* TBCRC 048: A phase II study of olaparib monotherapy in metastatic breast cancer patients with germline or somatic mutations in DNA damage response (DDR) pathway genes (Olaparib Expanded). *J. Clin. Oncol.* **38**, 1002 (2020).
 101. Grellety, T. *et al.* Dramatic response to PARP inhibition in a PALB2-mutated breast cancer: moving beyond BRCA. *Ann. Oncol.* **31**, 822–823 (2020).
 102. Kondrashova, O. *et al.* Secondary somatic mutations restoring RAD51C and RAD51D associated with acquired resistance to the PARP inhibitor rucaparib in high-grade ovarian carcinoma. *Cancer Discov.* **7**, 984–998 (2017).
 103. Bang, Y. J. *et al.* Olaparib in combination with paclitaxel in patients with advanced gastric cancer who have progressed following first-line therapy (GOLD): a double-blind, randomised, placebo-controlled, phase 3 trial. *Lancet Oncol.* **18**, 1637–1651 (2017).
 104. Shen, J. *et al.* ARID1A Deficiency Impairs the DNA Damage Checkpoint and Sensitizes Cells to PARP Inhibitors. *Cancer Discov.* **5**, 752–767 (2015).
 105. Ismail, I. H. *et al.* Germline mutations in BAP1 impair its function in DNA double-strand break repair. *Cancer Res.* **74**, 4282–4294 (2014).
 106. Parrotta, R. *et al.* A Novel BRCA1-Associated Protein-1 Isoform Affects Response of Mesothelioma Cells to Drugs Impairing BRCA1-Mediated DNA Repair. *J. Thorac. Oncol.* **12**, 1309–1319 (2017).
 107. Sulkowski, P. L. *et al.* Krebs-cycle-deficient hereditary cancer syndromes are defined by defects in homologous-recombination DNA repair. *Nat. Genet.* **50**, (2018).
 108. Sulkowski, P. L. *et al.* Oncometabolites suppress DNA repair by disrupting local chromatin signalling. *Nature* **582**, 586–591 (2020).
 109. Pietanza, M. C. *et al.* Randomized, double-blind, phase II study of temozolomide in combination with either veliparib or placebo in patients with relapsed-sensitive or refractory small-cell lung cancer. *J. Clin. Oncol.* **36**, 2386–2394 (2018).
 110. Sen, T., Gay, C. M. & Byers, L. A. Targeting DNA damage repair in small cell lung cancer and the biomarker landscape. *Transl. Lung Cancer Res.* **7**, 50–68 (2018).
 111. Miller, R. E. *et al.* ESMO recommendations on predictive biomarker testing for homologous recombination deficiency and PARP inhibitor benefit in ovarian cancer. *Ann. Oncol.* **31**, 1606–1622 (2020).
 112. Jaspers, J. E. *et al.* BRCA2-deficient sarcomatoid mammary tumors exhibit multidrug resistance. *Cancer Res.* **75**, 732–741 (2015).
 113. Rottenberg, S. *et al.* High sensitivity of BRCA1-deficient mammary tumors to the PARP inhibitor AZD2281 alone and in combination with platinum drugs. *Proc. Natl. Acad. Sci. U. S. A.* **105**, 17079–17084 (2008).
 114. Vaidyanathan, A. *et al.* ABCB1 (MDR1) induction defines a common resistance mechanism in paclitaxel- and

- olaparib-resistant ovarian cancer cells. *Br. J. Cancer* **115**, 431–441 (2016).
115. Pettitt, S. J. *et al.* Genome-wide and high-density CRISPR-Cas9 screens identify point mutations in PARP1 causing PARP inhibitor resistance. *Nat. Commun.* **9**, 1849 (2018).
116. Pettitt, S. J. *et al.* A Genetic Screen Using the PiggyBac Transposon in Haploid Cells Identifies Parp1 as a Mediator of Olaparib Toxicity. *PLoS One* **8**, 1–10 (2013).
117. Gogola, E. *et al.* Selective Loss of PARG Restores PARylation and Counteracts PARP Inhibitor-Mediated Synthetic Lethality. *Cancer Cell* **33**, 1078–1093.e12 (2018).
118. Edwards, S. L. *et al.* Resistance to therapy caused by intragenic deletion in BRCA2. *Nature* **451**, 1111–1115 (2008).
119. Sakai, W. *et al.* Secondary mutations as a mechanism of cisplatin resistance in BRCA2-mutated cancers. *Nature* **451**, 1116–1120 (2008).
120. Ter Brugge, P. *et al.* Mechanisms of therapy resistance in patient-derived xenograft models of brca1-deficient breast cancer. *J. Natl. Cancer Inst.* **108**, 1–12 (2016).
121. Kondrashova, O. *et al.* Methylation of all BRCA1 copies predicts response to the PARP inhibitor rucaparib in ovarian carcinoma. *Nat. Commun.* **9**, (2018).
122. Afghahi, A. *et al.* Tumor BRCA1 reversion mutation arising during neoadjuvant platinum-based chemotherapy in triple-negative breast cancer is associated with therapy resistance. *Clin. Cancer Res.* **23**, 3365–3370 (2017).
123. Weigelt, B. *et al.* Diverse BRCA1 and BRCA2 reversion mutations in circulating cell-free DNA of therapy-resistant breast or ovarian cancer. *Clin. Cancer Res.* **23**, 6708–6720 (2017).
124. Barber, L. J. *et al.* Secondary mutations in BRCA2 associated with clinical resistance to a PARP inhibitor. *J. Pathol.* **229**, 422–429 (2013).
125. Norquist, B. *et al.* Secondary somatic mutations restoring BRCA1/2 predict chemotherapy resistance in hereditary ovarian carcinomas. *J. Clin. Oncol.* **29**, 3008–3015 (2011).
126. Domchek, S. M. Reversion Mutations with Clinical Use of PARP Inhibitors: Many Genes, Many Versions. *Cancer Discov.* **7**, 937–939 (2017).
127. Lin, K. K. *et al.* BRCA Reversion Mutations in Circulating Tumor DNA Predict Primary and Acquired Resistance to the PARP Inhibitor Rucaparib in High-Grade Ovarian Carcinoma. *Cancer Discov.* **9**, 210–219 (2019).
128. Pishvaian, M. J. *et al.* BRCA2 secondary mutation-mediated resistance to platinum and PARP inhibitor-based therapy in pancreatic cancer. *Br. J. Cancer* **116**, 1021–1026 (2017).
129. Quigley, D. *et al.* Analysis of Circulating Cell-Free DNA Identifies Multiclonal Heterogeneity of BRCA2 Reversion Mutations Associated with Resistance to PARP Inhibitors. *Cancer Discov.* **7**, 999–1005 (2017).
130. Goodall, J. *et al.* Circulating cell-free DNA to guide prostate cancer treatment with PARP inhibition. *Cancer Discov.* **7**, 1006–1017 (2017).
131. Pettitt, S. J. *et al.* Clinical BRCA1/2 Reversion Analysis Identifies Hotspot Mutations and Predicted Neoantigens Associated with Therapy Resistance. *Cancer Discov.* **10**, 1475–1488 (2020).
132. Ang, J. E. *et al.* Efficacy of chemotherapy in BRCA1/2 mutation carrier ovarian cancer in the setting of PARP inhibitor resistance: A multi-institutional study. *Clin. Cancer Res.* **19**, 5485–5493 (2013).
133. Bouwman, P. *et al.* 53BP1 loss rescues BRCA1 deficiency and is associated with triple-negative and BRCA-mutated breast cancers. *Nat. Struct. Mol. Biol.* **17**, 688–695 (2010).
134. Bunting, S. F. *et al.* 53BP1 Inhibits Homologous Recombination in Brca1-Deficient Cells by Blocking Resection of DNA Breaks. *Cell* **141**, 243–254 (2010).
135. Cao, L. *et al.* A selective requirement for 53BP1 in the biological response to genomic instability induced by Brca1 deficiency. *Mol. Cell* **35**, 534–541 (2009).
136. Di Virgilio, M. *et al.* Rlf1 Prevents Resection of DNA Breaks and Promotes Immunoglobulin Class Switching. *Science (80-. J.)* **339**, 711–715 (2013).
137. Feng, L., Fong, K. W., Wang, J., Wang, W. & Chen, J. RIF1 counteracts BRCA1-mediated end resection during DNA repair. *J. Biol. Chem.* **288**, 11135–11143 (2013).
138. Escribano-Díaz, C. *et al.* A cell cycle-dependent regulatory circuit composed of 53BP1-RIF1 and BRCA1-CtIP controls DNA repair pathway choice. *Mol. Cell* **49**, 872–83 (2013).
139. Chapman, J. R. *et al.* RIF1 is essential for 53BP1-dependent nonhomologous end joining and suppression of DNA double-strand break resection. *Mol. Cell* **49**, 858–71 (2013).
140. Zimmermann, M., Lottersberger, F., Buonomo, S. B., Sfeir, A. & de Lange, T. 53BP1 Regulates DSB Repair Using Rlf1 to Control 5' End Resection. *Science (80-. J.)* **339**, 700–704 (2013).
141. Boersma, V. *et al.* MAD2L2 controls DNA repair at telomeres and DNA breaks by inhibiting 5' end resection. *Nature* **521**, 537–40 (2015).
142. Xu, G. *et al.* REV7 counteracts DNA double-strand break resection and affects PARP inhibition. *Nature* **521**, 541–544 (2015).
143. Noordermeer, S. M. *et al.* The shieldin complex mediates 53BP1-dependent DNA repair. *Nature* **560**, 117–121 (2018).
144. Dev, H. *et al.* Shieldin complex promotes DNA end-joining and counters homologous recombination in BRCA1-null cells. *Nat. Cell Biol.* **20**, 954–965 (2018).

145. Ghezraoui, H. *et al.* 53BP1 cooperation with the REV7–shieldin complex underpins DNA structure-specific NHEJ. *Nature* **560**, 122–127 (2018).
146. Gupta, R. *et al.* DNA Repair Network Analysis Reveals Shieldin as a Key Regulator of NHEJ and PARP Inhibitor Sensitivity. *Cell* **173**, 972–988.e23 (2018).
147. Gao, S. *et al.* An OB-fold complex controls the repair pathways for DNA double-strand breaks. *Nat. Commun.* **9**, 1–10 (2018).
148. Findlay, S. *et al.* SHLD2/FAM35A co-operates with REV7 to coordinate DNA double-strand break repair pathway choice. *EMBO J.* **37**, (2018).
149. Tomida, J. *et al.* FAM35A associates with REV7 and modulates DNA damage responses of normal and BRCA1-defective cells. *EMBO J.* **37**, e99543 (2018).
150. Jaspers, J. E. *et al.* Loss of 53BP1 Causes PARP Inhibitor Resistance in *Brca1* -Mutated Mouse Mammary Tumors. *Cancer Discov.* **3**, 68–81 (2013).
151. Cruz, C. *et al.* RAD51 foci as a functional biomarker of homologous recombination repair and PARP inhibitor resistance in germline BRCA-mutated breast cancer. *Ann. Oncol.* **29**, 1203–1210 (2018).
152. Waks, A. G. *et al.* Reversion and non-reversion mechanisms of resistance to PARP inhibitor or platinum chemotherapy in BRCA1/2-mutant metastatic breast cancer. *Ann. Oncol.* **31**, 590–598 (2020).
153. Johnson, N. *et al.* Stabilization of mutant BRCA1 protein confers PARP inhibitor and platinum resistance. *Proc. Natl. Acad. Sci. U. S. A.* **110**, 17041–17046 (2013).
154. Barazas, M. *et al.* The CST Complex Mediates End Protection at Double-Strand Breaks and Promotes PARP Inhibitor Sensitivity in BRCA1-Deficient Cells. *Cell Rep.* **23**, 2107–2118 (2018).
155. Mirman, Z. *et al.* 53BP1–RIF1–shieldin counteracts DSB resection through CST- and Polα-dependent fill-in. *Nature* **560**, 112–116 (2018).
156. Tkáč, J. *et al.* HELB Is a Feedback Inhibitor of DNA End Resection. *Mol. Cell* **61**, 405–418 (2016).
157. He, Y. J. *et al.* DYNLL1 binds to MRE11 to limit DNA end resection in BRCA1-deficient cells. *Nature* **563**, 522–526 (2018).
158. Becker, J. R. *et al.* The ASCIZ-DYNLL1 axis promotes 53BP1-dependent non-homologous end joining and PARP inhibitor sensitivity. *Nat. Commun.* **9**, 5406 (2018).
159. Olivieri, M. *et al.* A Genetic Map of the Response to DNA Damage in Human Cells. *Cell* **182**, 481–496.e21 (2020).
160. Francica, P. *et al.* Functional Radiogenetic Profiling Implicates ERCC6L2 in Non-homologous End Joining. *Cell Rep.* **32**, 108068 (2020).
161. Drané, P. *et al.* TIRR regulates 53BP1 by masking its histone methyl-lysine binding function HHS Public Access. *Nature* **543**, 211–216 (2017).
162. Clairmont, C. S. *et al.* TRIP13 regulates DNA repair pathway choice through REV7 conformational change. *Nat. Cell Biol.* **22**, 87–96 (2020).
163. Choi, Y. E. *et al.* Platinum and PARP Inhibitor Resistance Due to Overexpression of MicroRNA-622 in BRCA1-Mutant Ovarian Cancer. *Cell Rep.* **14**, 429–439 (2016).
164. Ray Chaudhuri, A. *et al.* Replication fork stability confers chemoresistance in BRCA-deficient cells. *Nature* **535**, 382–387 (2016).
165. Ying, S., Hamdy, F. C. & Helleday, T. Mre11-dependent degradation of stalled DNA replication forks is prevented by BRCA2 and PARP1. *Cancer Res.* **72**, 2814–2821 (2012).
166. Schlacher, K., Wu, H. & Jasin, M. A Distinct Replication Fork Protection Pathway Connects Fanconi Anemia Tumor Suppressors to RAD51-BRCA1/2. *Cancer Cell* **22**, 106–116 (2012).
167. Schlacher, K. *et al.* Double-strand break repair-independent role for BRCA2 in blocking stalled replication fork degradation by MRE11. *Cell* **145**, 529–542 (2011).
168. Guillemette, S. *et al.* Resistance to therapy in BRCA2 mutant cells due to loss of the nucleosome remodeling factor CHD4. *Genes Dev.* **29**, 489–494 (2015).
169. Taglialatela, A. *et al.* Restoration of Replication Fork Stability in BRCA1- and BRCA2-Deficient Cells by Inactivation of SNF2-Family Fork Remodelers. *Mol. Cell* **68**, 414–430.e8 (2017).
170. Kolinjivadi, A. M. *et al.* Smarcal1-Mediated Fork Reversal Triggers Mre11-Dependent Degradation of Nascent DNA in the Absence of Brca2 and Stable Rad51 Nucleofilaments. *Mol. Cell* **67**, 867–881.e7 (2017).
171. Dugrawala, H. *et al.* RADX Promotes Genome Stability and Modulates Chemosensitivity by Regulating RAD51 at Replication Forks. *Mol. Cell* **67**, 374–386.e5 (2017).
172. Rondinelli, B. *et al.* EZH2 promotes degradation of stalled replication forks by recruiting MUS81 through histone H3 trimethylation. *Nat. Cell Biol.* **19**, 1371–1378 (2017).
173. Lai, X. *et al.* MUS81 nuclease activity is essential for replication stress tolerance and chromosome segregation in BRCA2-deficient cells. *Nat. Commun.* **8**, 1–13 (2017).
174. Lemaçon, D. *et al.* MRE11 and EXO1 nucleases degrade reversed forks and elicit MUS81-dependent fork rescue in BRCA2-deficient cells. *Nat. Commun.* **8**, (2017).
175. Ding, X. *et al.* Synthetic viability by BRCA2 and PARP1/ARTD1 deficiencies. *Nat. Commun.* **7**, (2016).
176. Zoppoli, G. *et al.* Putative DNA/RNA helicase Schlafen-11 (SLFN11) sensitizes cancer cells to DNA-damaging agents. *Proc. Natl. Acad. Sci. U. S. A.* **109**, 15030–15035 (2012).

177. Stewart, C. A. *et al.* Dynamic variations in epithelial-to-mesenchymal transition (EMT), ATM, and SLFN11 govern response to PARP inhibitors and cisplatin in small cell lung cancer. *Oncotarget* **8**, 28575–28587 (2017).
178. Lok, B. H. *et al.* PARP Inhibitor Activity Correlates with SLFN11 Expression and Demonstrates Synergy with Temozolomide in Small Cell Lung Cancer. *Clin. Cancer Res.* **23**, 523–535 (2017).
179. Barretina, J. *et al.* The Cancer Cell Line Encyclopedia enables predictive modelling of anticancer drug sensitivity. *Nature* **483**, 603–607 (2012).
180. Murai, J. *et al.* Resistance to PARP inhibitors by SLFN11 inactivation can be overcome by ATR inhibition. *Oncotarget* **7**, 76534–76550 (2016).
181. Murai, J. *et al.* SLFN11 Blocks Stressed Replication Forks Independently of ATR. *Mol. Cell* **69**, 371–384.e6 (2018).
182. Zhou, Y., Caron, P., Legube, G. & Paull, T. T. Quantitation of DNA double-strand break resection intermediates in human cells. *Nucleic Acids Res.* **42**, e19–e19 (2014).
183. Polato, F. *et al.* CtIP-mediated resection is essential for viability and can operate independently of BRCA1. *J. Exp. Med.* **211**, 1027–1036 (2014).
184. Reczek, C. R., Szabolcs, M., Stark, J. M., Ludwig, T. & Baer, R. The interaction between CtIP and BRCA1 is not essential for resection-mediated DNA repair or tumor suppression. *J. Cell Biol.* **201**, 693–707 (2013).
185. Cruz-García, A., López-Saavedra, A. & Huertas, P. BRCA1 accelerates CtIP-mediated DNA-end resection. *Cell Rep.* **9**, 451–459 (2014).
186. Nacson, J. *et al.* BRCA1 Mutation-Specific Responses to 53BP1 Loss-Induced Homologous Recombination and PARP Inhibitor Resistance. *Cell Rep.* **24**, 3513–3527.e7 (2018).
187. Nakada, S., Yonamine, R. M. & Matsuo, K. RNF8 regulates assembly of RAD51 at DNA double-strand breaks in the absence of BRCA1 and 53BP1. *Cancer Res.* **72**, 4974–4983 (2012).
188. Luijsterburg, M. S. *et al.* A PALB2-interacting domain in RNF168 couples homologous recombination to DNA break-induced chromatin ubiquitylation. *Elife* **6**, (2017).
189. Zong, D. *et al.* BRCA1 Haploinsufficiency Is Masked by RNF168-Mediated Chromatin Ubiquitylation. *Mol. Cell* **73**, 1267–1281.e7 (2019).
190. Belotserkovskaya, R. *et al.* PALB2 chromatin recruitment restores homologous recombination in BRCA1-deficient cells depleted of 53BP1. *Nat. Commun.* **11**, 819 (2020).
191. Callen, E. *et al.* 53BP1 Enforces Distinct Pre- and Post-resection Blocks on Homologous Recombination. *Mol. Cell* **77**, 26–38.e7 (2020).
192. Rijkers, T. *et al.* Targeted inactivation of mouse RAD52 reduces homologous recombination but not resistance to ionizing radiation. *Mol. Cell. Biol.* **18**, 6423–9 (1998).
193. Yamaguchi-Iwai, Y. *et al.* Homologous Recombination, but Not DNA Repair, Is Reduced in Vertebrate Cells Deficient in RAD52. *Mol. Cell. Biol.* **18**, 6430–6435 (1998).
194. Feng, Z. *et al.* Rad52 inactivation is synthetically lethal with BRCA2 deficiency. *Proc. Natl. Acad. Sci. U. S. A.* **108**, 686–691 (2011).
195. Lok, B. H., Carley, A. C., Tchang, B. & Powell, S. N. RAD52 inactivation is synthetically lethal with deficiencies in BRCA1 and PALB2 in addition to BRCA2 through RAD51-mediated homologous recombination. *Oncogene* **32**, 3552–3558 (2013).
196. Malacaria, E. *et al.* Rad52 prevents excessive replication fork reversal and protects from nascent strand degradation. *Nat. Commun.* **10**, 1–19 (2019).
197. Sotiropoulos, S. K. *et al.* Mammalian RAD52 Functions in Break-Induced Replication Repair of Collapsed DNA Replication Forks. *Mol. Cell* **64**, 1127–1134 (2016).
198. Hengel, S. R., Spies, M. A. & Spies, M. Small-Molecule Inhibitors Targeting DNA Repair and DNA Repair Deficiency in Research and Cancer Therapy. *Cell Chem. Biol.* **24**, 1101–1119 (2017).
199. Sullivan-Reed, K. *et al.* Simultaneous Targeting of PARP1 and RAD52 Triggers Dual Synthetic Lethality in BRCA-Deficient Tumor Cells. *Cell Rep.* **23**, 3127–3136 (2018).
200. Ray-Coquard, I. *et al.* Olaparib plus Bevacizumab as First-Line Maintenance in Ovarian Cancer. *N. Engl. J. Med.* **381**, 2416–2428 (2019).
201. Mirza, M. R. *et al.* Niraparib plus bevacizumab versus niraparib alone for platinum-sensitive recurrent ovarian cancer (NSGO-AVANOV2/ENGOT-ov24): a randomised, phase 2, superiority trial. *Lancet Oncol.* **20**, 1409–1419 (2019).
202. Yap, T. A. *et al.* Phase I trial of the parp inhibitor olaparib and akt inhibitor capivasertib in patients with brca1/2- and non-brca1/2-mutant cancers. *Cancer Discov.* **10**, 1528–1543 (2020).
203. Kurnit, K. C. *et al.* Abstract CT020: Phase I dose escalation of olaparib (PARP inhibitor) and selumetinib (MEK Inhibitor) combination in solid tumors with Ras pathway alterations. *Cancer Res.* **79**, CT020 LP-CT020 (2019).
204. Sun, C. *et al.* BRD4 Inhibition Is Synthetic Lethal with PARP Inhibitors through the Induction of Homologous Recombination Deficiency. *Cancer Cell* **33**, 401–416.e8 (2018).
205. Yang, L. *et al.* Repression of BET activity sensitizes homologous recombination-proficient cancers to PARP inhibition. *Sci. Transl. Med.* **9**, (2017).
206. Karakashev, S. *et al.* BET Bromodomain Inhibition Synergizes with PARP Inhibitor in Epithelial Ovarian Cancer.

- Cell Rep.* **21**, 3398–3405 (2017).
207. Min, A. *et al.* Histone deacetylase inhibitor, suberoylanilide hydroxamic acid (SAHA), enhances anti-tumor effects of the poly (ADP-ribose) polymerase (PARP) inhibitor olaparib in triple-negative breast cancer cells. *Breast Cancer Res.* **17**, 33 (2015).
 208. Konstantinopoulos, P. A., Wilson, A. J., Saskowski, J., Wass, E. & Khabele, D. Suberoylanilide hydroxamic acid (SAHA) enhances olaparib activity by targeting homologous recombination DNA repair in ovarian cancer. *Gynecol. Oncol.* **133**, 599–606 (2014).
 209. Chao, O. S. & Goodman, O. B. Synergistic loss of prostate cancer cell viability by coinhibition of HDAC and PARP. *Mol. Cancer Res.* **12**, 1755–1766 (2014).
 210. Marijon, H. *et al.* Co-targeting poly(ADP-ribose) polymerase (PARP) and histone deacetylase (HDAC) in triple-negative breast cancer: Higher synergism in BRCA mutated cells. *Biomed. Pharmacother.* **99**, 543–551 (2018).
 211. Johnson, N. *et al.* Compromised CDK1 activity sensitizes BRCA-proficient cancers to PARP inhibition. *Nat. Med.* **17**, 875–882 (2011).
 212. Johnson, S. F. *et al.* CDK12 Inhibition Reverses De Novo and Acquired PARP Inhibitor Resistance in BRCA Wild-Type and Mutated Models of Triple-Negative Breast Cancer. *Cell Rep.* **17**, 2367–2381 (2016).
 213. Joshi, P. M., Sutor, S. L., Huntoon, C. J. & Karnitz, L. M. Ovarian cancer-associated mutations disable catalytic activity of CDK12, a kinase that promotes homologous recombination repair and resistance to cisplatin and poly(ADP-ribose) polymerase inhibitors. *J. Biol. Chem.* **289**, 9247–9253 (2014).
 214. Bajrami, I. *et al.* Genome-wide profiling of genetic synthetic lethality identifies CDK12 as a novel determinant of PARP1/2 inhibitor sensitivity. *Cancer Res.* **74**, 287–297 (2014).
 215. Choi, Y. E. *et al.* Sublethal concentrations of 17-AAG suppress homologous recombination DNA repair and enhance sensitivity to carboplatin and olaparib in HR proficient ovarian cancer cells. *Oncotarget* **5**, 2678–2687 (2014).
 216. Jiang, J. *et al.* Ganetespib overcomes resistance to PARP inhibitors in breast cancer by targeting core proteins in the DNA repair machinery. *Invest. New Drugs* **35**, 251–259 (2017).
 217. Krawczyk, P. M. *et al.* Mild hyperthermia inhibits homologous recombination, induces BRCA2 degradation, and sensitizes cancer cells to poly (ADP-ribose) polymerase-1 inhibition. *Proc. Natl. Acad. Sci. U. S. A.* **108**, 9851–9856 (2011).
 218. van den Tempel, N. *et al.* Heat-induced BRCA2 degradation in human tumours provides rationale for hyperthermia-PARP-inhibitor combination therapies. *Int. J. Hyperth.* **34**, 407–414 (2018).
 219. Lu, Y., Chu, A., Turker, M. S. & Glazer, P. M. Hypoxia-induced epigenetic regulation and silencing of the BRCA1 promoter. *Mol. Cell. Biol.* **31**, 3339–50 (2011).
 220. Yazinski, S. A. *et al.* ATR inhibition disrupts rewired homologous recombination and fork protection pathways in PARP inhibitor-resistant BRCA-deficient cancer cells. *Genes Dev.* **31**, 318–332 (2017).
 221. Kim, H. *et al.* Targeting the ATR/CHK1 axis with PARP inhibition results in tumor regression in BRCA-mutant ovarian cancer models. *Clin. Cancer Res.* **23**, 3097–3108 (2017).
 222. Kim, H. *et al.* Combining PARP with ATR inhibition overcomes PARP inhibitor and platinum resistance in ovarian cancer models. *Nat. Commun.* **11**, 3726 (2020).
 223. Parsels, L. A. *et al.* PARP1 Trapping and DNA Replication Stress Enhance Radiosensitization with Combined WEE1 and PARP Inhibitors. *Mol. Cancer Res.* **16**, 222–232 (2018).
 224. Lallo, A. *et al.* The combination of the PARP inhibitor olaparib and the WEE1 Inhibitor AZD1775 as a new therapeutic option for small cell lung cancer. *Clin. Cancer Res.* **24**, 5153–5164 (2018).
 225. Fang, Y. *et al.* Sequential Therapy with PARP and WEE1 Inhibitors Minimizes Toxicity while Maintaining Efficacy. *Cancer Cell* **35**, 851–867.e7 (2019).
 226. Pilié, P. G., Gay, C. M., Byers, L. A., O'Connor, M. J. & Yap, T. A. PARP inhibitors: Extending benefit beyond BRCA-mutant cancers. *Clin. Cancer Res.* **25**, 3759–3771 (2019).
 227. Houtkooper, R. H., Cantó, C., Wanders, R. J. & Auwerx, J. The secret life of NAD⁺: An old metabolite controlling new metabolic signaling pathways. *Endocrine Reviews* **31**, 194–223 (2010).
 228. Virag, L. The Therapeutic Potential of Poly(ADP-Ribose) Polymerase Inhibitors. *Pharmacol. Rev.* **54**, 375–429 (2002).
 229. Eliasson, M. J. L. *et al.* Poly(ADP-ribose) polymerase gene disruption renders mice resistant to cerebral ischemia. *Nat. Med.* **3**, 1089–1095 (1997).
 230. Zong, W.-X. Alkylating DNA damage stimulates a regulated form of necrotic cell death. *Genes Dev.* **18**, 1272–1282 (2004).
 231. Bajrami, I. *et al.* Synthetic lethality of PARP and NAMPT inhibition in triple-negative breast cancer cells. *EMBO Mol. Med.* **4**, 1087–1096 (2012).
 232. Tateishi, K. *et al.* Extreme Vulnerability of IDH1 Mutant Cancers to NAD⁺ Depletion. *Cancer Cell* **28**, 773–784 (2015).
 233. Lu, Y. *et al.* Chemosensitivity of IDH1-mutated gliomas due to an impairment in PARP1-mediated DNA repair. *Cancer Res.* **77**, 1709–1718 (2017).
 234. Sulkowski, P. L. *et al.* 2-Hydroxyglutarate produced by neomorphic IDH mutations suppresses homologous

- recombination and induces PARP inhibitor sensitivity. *Sci. Transl. Med.* **9**, (2017).
235. Bian, C. *et al.* NADP⁺ is an endogenous PARP inhibitor in DNA damage response and tumor suppression. *Nat. Commun.* **10**, 693 (2019).
236. Strickland, K. C. *et al.* Association and prognostic significance of BRCA1/2-mutation status with neoantigen load, number of tumor-infiltrating lymphocytes and expression of PD-1/PD-L1 in high grade serous ovarian cancer. *Oncotarget* **7**, 13587–13598 (2016).
237. Parkes, E. E. *et al.* Activation of STING-dependent innate immune signaling by s-phase-specific DNA damage in breast cancer. *J. Natl. Cancer Inst.* **109**, 1–10 (2017).
238. Motwani, M., Pesiridis, S. & Fitzgerald, K. A. DNA sensing by the cGAS–STING pathway in health and disease. *Nat. Rev. Genet.* **20**, 657–674 (2019).
239. Zhu, Q. *et al.* BRCA1 tumour suppression occurs via heterochromatin-mediated silencing. *Nature* **477**, 179–184 (2011).
240. Shen, J. *et al.* PARP1 triggers the STING-dependent immune response and enhances the therapeutic efficacy of immune checkpoint blockade independent of BRCANess. *Cancer Res.* **79**, 311–319 (2019).
241. Ding, L. *et al.* PARP Inhibition Elicits STING-Dependent Antitumor Immunity in Brca1-Deficient Ovarian Cancer. *Cell Rep.* **25**, 2972–2980.e5 (2018).
242. Jiao, S. *et al.* PARP inhibitor upregulates PD-L1 expression and enhances cancer-associated immunosuppression. *Clin. Cancer Res.* **23**, 3711–3720 (2017).
243. Pantelidou, C. *et al.* PARP Inhibitor Efficacy Depends on CD8⁺ T-cell Recruitment via Intratumoral STING Pathway Activation in BRCA-Deficient Models of Triple-Negative Breast Cancer. *Cancer Discov.* **9**, 722–737 (2019).
244. Li, A. *et al.* Prospects for combining immune checkpoint blockade with PARP inhibition. *J. Hematol. Oncol.* **12**, 1–12 (2019).
245. Friedlander, M. *et al.* Pamiparib in combination with tislelizumab in patients with advanced solid tumours: results from the dose-escalation stage of a multicentre, open-label, phase 1a/b trial. *Lancet Oncol.* **20**, 1306–1315 (2019).
246. Domchek, S. M. *et al.* Olaparib and durvalumab in patients with germline BRCA-mutated metastatic breast cancer (MEDIOLA): an open-label, multicentre, phase 1/2, basket study. *Lancet Oncol.* **21**, 1155–1164 (2020).
247. Konstantinopoulos, P. A. *et al.* Single-Arm Phases 1 and 2 Trial of Niraparib in Combination with Pembrolizumab in Patients with Recurrent Platinum-Resistant Ovarian Carcinoma. *JAMA Oncol.* **5**, 1141–1149 (2019).
248. Leite de Oliveira, R., Wang, L. & Bernards, R. With great power comes great vulnerability. *Mol. Cell. Oncol.* **5**, 1–3 (2018).
249. Ame, J.-C. *et al.* Radiation-induced mitotic catastrophe in PARG-deficient cells. *J. Cell Sci.* **122**, 1990–2002 (2009).
250. Callen, E. *et al.* 53BP1 Mediates Productive and Mutagenic DNA Repair through Distinct Phosphoprotein Interactions. *Cell* **153**, 1266–1280 (2013).
251. Ward, I. M., Minn, K., van Deursen, J. & Chen, J. p53 Binding Protein 53BP1 Is Required for DNA Damage Responses and Tumor Suppression in Mice. *Mol. Cell. Biol.* **23**, 2556–2563 (2003).
252. Barazas, M. *et al.* Radiosensitivity Is an Acquired Vulnerability of PARP1-Resistant BRCA1-Deficient Tumors. *Cancer Res.* **79**, 452–460 (2019).
253. Eke, I. *et al.* 53BP1/RIF1 signaling promotes cell survival after multifractionated radiotherapy. *Nucleic Acids Res.* **48**, 1314–1326 (2020).
254. Feng, F. Y. *et al.* Targeted radiosensitization with PARP1 inhibition: Optimization of therapy and identification of biomarkers of response in breast cancer. *Breast Cancer Res. Treat.* **147**, 81–94 (2014).
255. Murai, J. *et al.* Rationale for poly(ADP-ribose) polymerase (PARP) inhibitors in combination therapy with camptothecins or temozolomide based on PARP trapping versus catalytic inhibition. *J. Pharmacol. Exp. Ther.* **349**, 408–416 (2014).
256. Tentori, L. *et al.* Poly(ADP-ribose) glycohydrolase inhibitor as chemosensitizer of malignant melanoma for temozolomide. *Eur. J. Cancer* **41**, 2948–2957 (2005).
257. Nagashima, H. *et al.* Poly(ADP-ribose) Glycohydrolase Inhibition Sequesters NAD⁺ to Potentiate the Metabolic Lethality of Alkylating Chemotherapy in IDH-Mutant Tumor Cells. *Cancer Discov.* **10**, 1672–1689 (2020).
258. Michelena, J. *et al.* Analysis of PARP inhibitor toxicity by multidimensional fluorescence microscopy reveals mechanisms of sensitivity and resistance. *Nat. Commun.* **9**, (2018).
259. Fleury, H. *et al.* Exploiting interconnected synthetic lethal interactions between PARP inhibition and cancer cell reversible senescence. *Nat. Commun.* **10**, (2019).
260. Shen, S., Vagner, S. & Robert, C. Persistent Cancer Cells: The Deadly Survivors. *Cell* **183**, 860–874 (2020).
261. Chang, H. H. Y., Pannunzio, N. R., Adachi, N. & Lieber, M. R. Non-homologous DNA end joining and alternative pathways to double-strand break repair. *Nat. Rev. Mol. Cell Biol.* **18**, 495–506 (2017).
262. Nik-Zainal, S. *et al.* Mutational processes molding the genomes of 21 breast cancers. *Cell* **149**, 979–993 (2012).
263. Ceccaldi, R. *et al.* Homologous-recombination-deficient tumours are dependent on Polθ-mediated repair. *Nature* **518**, 258–262 (2015).

264. Mateos-Gomez, P. A. *et al.* Mammalian polymerase θ promotes alternative NHEJ and suppresses recombination. *Nature* **518**, 254–257 (2015).
265. Zhou, J. *et al.* Polymerase Theta Inhibition Kills Homologous Recombination Deficient Tumors. *bioRxiv* 2020.05.23.111658 (2020). doi:10.1101/2020.05.23.111658
266. Wheeler, D. A. *et al.* Molecular Features of Cancers Exhibiting Exceptional Responses to Treatment. *Cancer Cell* **39**, 38–53.e7 (2021).
267. Wan, J. C. M. *et al.* Liquid biopsies come of age: Towards implementation of circulating tumour DNA. *Nat. Rev. Cancer* **17**, 223–238 (2017).
268. Vidula, N. *et al.* Routine Plasma-Based Genotyping to Comprehensively Detect Germline, Somatic, and Reversion BRCA Mutations among Patients with Advanced Solid Tumors. *Clin. Cancer Res.* **26**, 2546–2555 (2020).
269. Colombo, N. *et al.* ESMO-ESGO consensus conference recommendations on ovarian cancer: Pathology and molecular biology, early and advanced stages, borderline tumours and recurrent disease. *Ann. Oncol.* **30**, 672–705 (2019).
270. Cardoso, F. *et al.* 5th ESO-ESMO international consensus guidelines for advanced breast cancer (ABC 5). *Ann. Oncol.* **31**, 1623–1649 (2020).

SUPPLEMENTARY MATERIAL

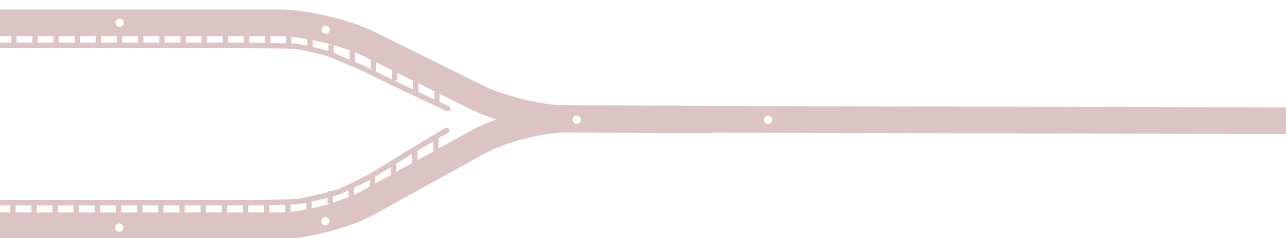
Supplementary table 1 | Clinically approved PARP inhibitors.

Cancer type	Drug	Indication	Agency	Specific restrictions
Ovarian cancer ²⁶⁹	Olaparib	First-line Maintenance: BRCA1/2-mutated, advanced-stage cancer, in CR or PR after first-line platinum-based chemotherapy	FDA, 2018	BRCA1/2 mutation detected using FDA-approved companion diagnostic ^a
			EMA, 2019	High-grade cancers only
		First-line Maintenance with Bevacizumab: advanced-stage cancer, in CR or PR after first-line platinum-based chemotherapy, associated with HRD-positive status defined by BRCA1/2 mutation and/or genomic instability	FDA, 2020	HRD status detected using FDA-approved companion diagnostic ^a
			EMA, 2020	High-grade cancers only, CR or PR after first-line platinum-based chemotherapy in combination with bevacizumab
		Second-line Maintenance: advanced-stage, recurrent cancer, in CR or PR to platinum-based chemotherapy	FDA, 2017	No specific restrictions
			EMA, 2018	High-grade cancers only, BRCA1/2 mutation
Rucaparib		Pre-treated Monotherapy: BRCA1/2-mutated, advanced-stage cancer, refractory to ≥ 3 prior lines of therapy	FDA, 2014	BRCA1/2 mutation detected using FDA-approved companion diagnostic ^a
		Second-line Maintenance: advanced-stage, recurrent cancer, in CR or PR to platinum-based chemotherapy	FDA, 2018	No specific restrictions
			EMA, 2019	High-grade cancers only
		Pre-treated Monotherapy: BRCA1/2-mutated, advanced-stage cancer, refractory to ≥ 2 prior lines of therapy	FDA, 2016	BRCA1/2 mutation detected using FDA-approved companion diagnostic ^a
			EMA, 2018	High-grade, platinum-sensitive cancers only, unable to tolerate further platinum therapy
		First-line Maintenance: advanced-stage cancer, in CR or PR after first-line platinum-based chemotherapy	FDA, 2020	No specific restrictions
Niraparib		Second-line Maintenance: advanced-stage, recurrent cancer, in CR or PR to platinum-based chemotherapy	EMA, 2020	High-grade cancers only
			FDA, 2017	No specific restrictions
		Pre-treated Monotherapy: advanced-stage cancer, refractory to ≥ 3 prior lines of therapy, associated with HRD-positive status defined by BRCA1/2 mutation and/or genomic instability	EMA, 2017	High-grade cancers only
			FDA, 2019	Progressed >6 months after response to the last platinum-based chemotherapy; HRD status detected using FDA-approved companion diagnostic ^a

Supplementary table 1 | Continued

Cancer type	Drug	Indication	Agency	Specific restrictions
Breast cancer ²⁷⁰	Olaparib	Pre-treated Monotherapy: BRCA1/2-mutated, HER2-negative, locally advanced or metastatic cancer; patients with hormone receptor-positive cancer should also have progressed on or after prior endocrine therapy, or be considered unsuitable for endocrine therapy	FDA, 2018	Previously treated with chemotherapy in the (neo)adjuvant or metastatic setting; BRCA1/2 mutation detected using FDA-approved companion diagnostic ^a
			EMA, 2019	Previously treated with an anthracycline and a taxane in the (neo)adjuvant or metastatic setting, unless patients were not suitable for these treatments
	Talazoparib	Pre-treated Monotherapy: BRCA1/2-mutated, HER2-negative, locally advanced or metastatic cancer	FDA, 2018	BRCA1/2 mutation detected using FDA-approved companion diagnostic ^a
			EMA, 2019	Previously treated with an anthracycline and a taxane in the (neo)adjuvant or metastatic setting, unless patients were not suitable for these treatments; patients with hormone receptor-positive cancer should also have progressed on or after prior endocrine therapy, or be considered unsuitable for endocrine therapy
Prostate cancer	Olaparib	Pre-treated Monotherapy: Metastatic, castration-resistant prostate cancer	FDA, 2020	HR gene-mutated, progressed following prior treatment with enzalutamide, or abiraterone; HR gene mutation detected using FDA-approved companion diagnostic ^a
			EMA, 2020	BRCA1/2-mutated, progressed following prior therapy that included a new hormonal agent
Pancreatic adenocarcinoma	Rucaparib	Pre-treated Monotherapy: BRCA1/2-mutated, metastatic, castration-resistant prostate cancer, previously treated with androgen receptor-directed therapy and taxane-based chemotherapy	FDA, 2020 ^b	BRCA1/2 mutation detected using FDA-approved companion diagnostic ^a
			FDA, 2019	BRCA1/2 mutation detected using FDA-approved companion diagnostic ^a
	Olaparib	First-line Maintenance: BRCA1/2-mutated, metastatic cancer who have not progressed on ≥ 16 weeks of a first-line platinum-based chemotherapy regimen	FDA, 2019	BRCA1/2 mutation detected using FDA-approved companion diagnostic ^a
			EMA, 2020	No specific restrictions

FDA, food and drug administration; EMA, European medicines agency; CR, complete remission; PR, partial remission; HRD, homologous recombination deficiency; HER2, human epidermal growth factor receptor 2; HR, homologous recombination; a, See <https://www.fda.gov/medical-devices/vitrodiagnostics/list-cleared-or-approved-companion-diagnostic-devices-vitro-and-imaging-tools> for details on FDA-approved companion diagnostics; b, accepted under accelerated approval.



Chapter 3

Multi-omics analysis reveals distinct non-reversion mechanisms of PARPi resistance in BRCA1- versus BRCA2-deficient mammary tumors

Jinhyuk Bhin*, Mariana Paes Dias*, Ewa Gogola*, Frank Rolfs, Sander R. Piersma, Roebi de Bruijn, Julian R. de Ruiter, Bram van den Broek, Alexandra A. Duarte, Wendy Sol, Ingrid van der Heijden, Lara Bakker, Taina S. Kaiponen, Cor Liefstink, Ben Morris, Roderick L. Beijersbergen, Marieke van de Ven, Connie R. Jimenez, Lodewyk F. A. Wessels, Sven Rottenberg and Jos Jonkers

**equal contribution*

ABSTRACT

BRCA1 and BRCA2 both function in DNA double-strand break repair by homologous recombination (HR). Due to their HR-defect, BRCA1/2-deficient cancers are sensitive to poly(ADP-ribose) polymerase inhibitors (PARPi) but they eventually acquire resistance. Preclinical studies yielded several PARPi resistance mechanisms that do not involve BRCA1/2 reactivation, but their relevance in the clinic remains elusive. To investigate which BRCA1/2-independent mechanisms drive spontaneous resistance in vivo, we combined molecular profiling with functional analysis of the HR status of matched PARPi-naïve and PARPi-resistant mouse mammary tumors harboring large intragenic deletions that prevent functional restoration of BRCA1/2. We observed restoration of HR in 64% of PARPi-resistant BRCA1-deficient tumors but none in the PARPi-resistant BRCA2-deficient tumors. Moreover, we found that 53BP1 loss is the prevalent resistance mechanism in HR-proficient BRCA1-deficient tumors, whereas resistance in BRCA2-deficient tumors is mainly induced by the loss of PARG. Our combined multi-omics analysis catalogued additional genes and pathways potentially involved in modulating PARPi response.

INTRODUCTION

The observation that many oncogenic events render cancer cells reliant on specific and druggable biological pathways is a premise of targeted therapies for personalized cancer treatment. Unfortunately, the selective pressure that initially kills cancer cells is also a driving force in selecting cells which acquired drug resistance. A better understanding of the recurrent molecular patterns of resistance in specific genetic contexts is therefore instrumental to improve clinical outcomes.

One example of cancer dependencies that can be exploited therapeutically is the defect in the repair of DNA double-strand breaks (DSBs) through homologous recombination (HR) due to BRCA1 or BRCA2 inactivation^{1,2}. Unlike the other DSB repair pathways, HR enables the accurate repair of DNA lesions as it uses the newly replicated sister chromatid as a template. Both BRCA1 and BRCA2 are essential in this process. While BRCA1 is required for the initiation of HR by promoting end-resection of the DSB, BRCA2 acts further downstream and, together with PALB2, stimulates the recruitment of RAD51 recombinase to the resected single-stranded DNA³. The HR defect resulting from the loss of BRCA1/2 can be targeted through the inhibition of poly(ADP-ribose) polymerase (PARP) enzymes PARP1 and PARP2^{1,2}. PARP1/2 have been implicated in several DNA damage response (DDR) pathways, including the repair of DNA single strand breaks (SSBs), DSBs and stabilization of replication forks (RFs)⁴. Catalytic inhibition as well as trapping of PARP1/2 on the DNA by PARP inhibitors (PARPi) leads to replication-coupled DSBs formation, which in turn requires HR for error-free repair⁵. BRCA1/2-defective cells can only employ error-prone repair to resolve the DSBs caused by PARPi treatment, resulting in accumulation of chromosomal aberrations and cell death by mitotic catastrophe⁶. The success of this approach resulted in the clinical approval of four different PARPi for the treatment of several types of cancers with HR defects⁷.

Despite the clinical benefit, sustained antitumor responses to PARPi are often hampered by the emergence of resistance. Previous studies have delineated several mechanisms by which BRCA1/2-deficient tumors evade PARPi toxicity⁷. Independently of HR, PARPi resistance may be induced through (i) cellular extrusion of PARPi by upregulation of the drug efflux transporter P-gp⁸; (ii) partial restoration of catalytic PARP activity through loss of poly(ADP-ribose) glycohydrolase (PARG)⁹; (iii) PARP1 downregulation/inactivation as well as mutations that abolish PARP1 trapping^{5,10,11}; and (iv) restoration of RF stability^{12–14}. All these mechanisms result in PARPi resistance by limiting PARPi-induced DNA damage, rather than restoring the capacity of BRCA1/2-deficient cells to efficiently repair DSBs. In contrast, HR restoration as result of secondary (epi)genetic events that lead to reactivation of functional BRCA1/2 may fully cancel the initial susceptibility to PARPi. In addition, genetic screens and *in vivo* studies in preclinical models demonstrated that inactivation of the 53BP1-RIF1-shieldin DSB end-protection pathway, which inhibits HR and is antagonized by BRCA1 during S phase, partially restores HR and confers PARPi resistance in BRCA1-deficient cells^{15–30}.

While multiple mechanisms of acquired PARPi resistance have been reported in preclinical *in vitro* models, their clinical relevance remains unclear. To date, the best clinically documented mechanism of resistance is restoration of BRCA1/2 function by secondary (epi)genetic events (e.g., reversion mutations)³¹. However, these results might be biased by the fact that PARPi were initially approved for second-line maintenance therapy following first-line treatment with platinum- based chemotherapies. Since (epi)genetic reactivation of BRCA1/2 function has been shown to be the main mechanism of platinum resistance in *BRCA1/2*-mutated tumors, it is plausible that some of these patients might have already developed BRCA-proficient, and therefore PARPi-resistant, tumor clones as a result of a first-line treatment^{32–35}. Moreover, reactivation of BRCA1/2 function is not found in all patients with refractory tumors^{33,36}, suggesting that BRCA1/2-independent PARPi resistance is relevant in the clinic.

The PARPi olaparib and niraparib have recently been approved as first-line maintenance therapies and clinical trials have started to test PARPi as single-agent neoadjuvant therapy³⁷. With more patients likely to receive PARPi earlier in the course of disease, it is important to understand which are the most frequent mechanisms of acquired PARPi resistance, and if these differ between *BRCA1*- and *BRCA2*-mutated tumors, in order to predict PARPi response and to develop strategies to overcome resistance. In the absence of available clinical data, we sought to answer these questions by combining functional analysis of HR status with molecular profiling of a unique collection of matched PARPi-naïve and PARPi-resistant mouse mammary tumors which harbor large intragenic deletions of *Brca1* or *Brca2* genes that cannot be spontaneously restored. Overall, our study shows that functional differences between BRCA1 and BRCA2 in the repair of DSBs also impact the resistance patterns in PARPi-treated tumors. While HR restoration accounted for the majority of BRCA1-deficient tumors, it did not occur in BRCA2-deficient tumors, suggesting that HR cannot be restored in *Brca2*-mutated tumors that cannot undergo BRCA2 reactivation. Moreover, among the previously reported resistance mechanisms, loss of 53BP1 and loss of PARG were the most dominant alterations in PARPi-resistant BRCA1-deficient and BRCA2-deficient tumors, respectively. Dysregulation of other known resistance factors was only sporadically observed, suggesting 53BP1 and PARG as potential biomarkers of acquired PARPi resistance. Additionally, our analysis yielded a list of potential genes and pathways involved in PARPi response and provides evidence that tumor-intrinsic alterations in pathways regulating the tumor microenvironment may influence PARPi efficacy.

RESULTS

HR restoration drives PARPi resistance in BRCA1-deficient tumors

To study the contribution of BRCA1/2-independent PARPi resistance mechanisms in BRCA1/2-deficient tumors, we used two genetically engineered mouse models (GEMMs) of BRCA1-associated breast cancer, *K14cre;Brca1^{F/F};Trp53^{F/F}* (KB1P) and *K14cre;Brca1^{F/}*

F;Trp53^{F/F};Mdr1a/b^{-/-} (KB1PM) as well as a GEMM of BRCA2-associated breast cancer, *K14cre;Brca2^{F/F};Trp53^{F/F}* (KB2P)^{8,9,38–40} (**Fig. 1A**). In these models, long-term treatment of mammary tumors with PARPi leads to spontaneous induction of resistance, which is preserved upon tumor passaging^{38,41}. Importantly, the tumors arising in these models harbor large intragenic deletions in the *Brca1* or *Brca2* genes^{39,40} and thus resistance to PARPi cannot be acquired via reactivation of BRCA1/2 function. Moreover, we eliminated the possibility of P-glycoprotein (Pgp)-mediated resistance to the PARPi olaparib by either the genetic inactivation of Pgp (*Mdr1a/b*) in the KB1PM model, or by treating Pgp-proficient KB1P and KB2P tumors with the PARPi AZD2461, which is a poor substrate for this transporter^{38,42} (**Fig. 1A**).

HR deficiency is the basis for sensitivity to PARPi and thus we hypothesized that HR restoration is the most likely way for tumors to acquire resistance to PARPi. We therefore assessed the HR status of matched PARPi-naïve and PARPi-resistant tumors by measuring their capacity to form ionizing radiation-induced RAD51 foci (RAD51-IRIF)^{23,43} (**Fig. 1B**). As a positive control for this assay, we used a HR-proficient mammary tumor derived from the *K14cre;Trp53^{F/F}* (KP) model and observed the highest accumulation of RAD51 foci 2 hours after induction of DNA damage (**Supplementary Fig. 1A-D**). Of note, all tumors exhibited high growth rates prior to irradiation, suggesting that differences in cell cycle distribution between the samples are negligible (**Supplementary Fig. 1E,F**). As expected, we did not detect any RAD51-IRIF formation in any of the PARPi-naïve tumors (**Fig. 1C,D**), confirming that the *Brca1/2* deletions induced in our models completely abolish HR-mediated repair. Consistent with this, whole-exome sequencing of DNA from PARPi-resistant tumors confirmed the complete Cre-mediated deletion of the floxed *Brca1/2* exons, thus no emerging resistance could be attributed to the selection of clones that retained wild-type BRCA proteins (**Supplementary Fig. 1G,H**). Analysis of the 45 PARPi-resistant BRCA1-deficient (BRCA1-KO) tumors revealed that 64% (29/45) of the tumors had restored the capacity to form RAD51 foci, including one tumor with a mixed pattern (RAD51-IRIF positive and negative areas) (**Fig. 1E**). These results indicate that HR recovery is the predominant mechanism of PARPi resistance in the KB1P(M) models, albeit not the only one. In contrast, none of the 26 PARPi-resistant BRCA2-deficient tumors exhibited RAD51-IRIF (**Fig. 1E**)⁹. Given that PARPi treatment is a potent trigger of HR restoration in the KB1P(M) models, lack of RAD51-IRIF in the BRCA2-deficient cohort strongly indicates that BRCA2 is indispensable for HR repair.

Alterations in previously reported PARPi resistance factors

To understand how prolonged PARPi treatment reshapes BRCA1/2-deficient tumors, we performed whole-exome sequencing (WE-seq), low-coverage whole-genome sequencing (LCWG-seq), and RNA sequencing (RNA-seq) on the collection of matched PARPi-naïve and PARPi-resistant KB1P(M) and KB2P tumors and identified alterations specific to each resistant tumor compared to the matched naïve tumor.

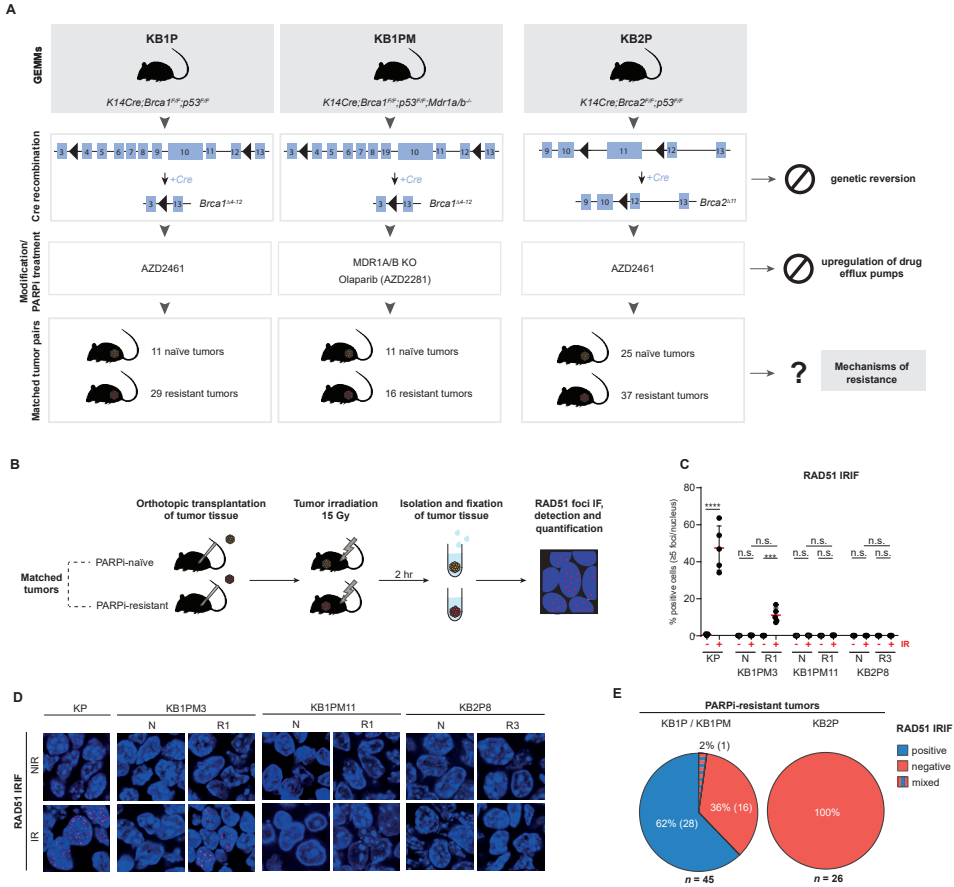


Figure 1 | HR restoration drives PARPi resistance in BRCA1-deficient tumors. A | Outline of the generation of matched PARPi-naïve and PARPi-resistant KB1P(M) and KB2P tumors and of the experimental approach. **B |** Schematic representation of the RAD51 IRIF formation assay. Cryopreserved PARPi-naïve and PARPi-resistant tumors were orthotopically transplanted into syngeneic recipient mice and, upon outgrowth to 500 mm³, DNA damage was inflicted by locally applied ionizing radiation (IR) at a dose of 15 Gy. 2 hr post-irradiation, tumors were isolated and fixed tissues were used for RAD51 immunofluorescence imaging. **C-D |** Quantification (C) and representative images (D) of the RAD51 IRIFs for the different matched KB1P(M) and KB2P tumor pairs and control KP tumors; IR – irradiated, NIR – non irradiated; scale bar, 100 μ m; data in (C) represented as percentage of positive cells (≥ 5 foci/nucleus) per imaged area (single data point, typically 100-200 cells/area); **** $p < 0.0001$, *** $p < 0.001$, ** $p < 0.01$ (two-tailed Mann-Whitney U test). **E |** Pie charts showing the outcome of the RAD51 IRIF assay in PARPi-resistant KB1P(M) and KB2P tumor cohorts; percentages and numbers of individual tumors analyzed are indicated; n – total number of individual tumors analyzed from the indicated models. $p = 0.0001$ (two-tailed Fisher's exact test).

We first interrogated if we could find genetic and transcriptional alterations in factors previously associated with PARPi resistance (Fig. 2A). To this end, we selected 25 genes reported to drive PARPi resistance due to BRCA-independent HR restoration, restoration of fork stability or modulation of PARP signaling/trapping⁷ (Supplementary table 1). We examined alterations in these genes in the different PARPi-resistant tumor groups with

informed HR status, i.e., (1) RAD51-positive KB1P(M), (2) RAD51-negative KB1P(M) and (3) KB2P tumors. Of the 25 genes, 23 have been reported to drive PARPi resistance upon loss of function, whereas 2 genes drive resistance as a result of gain of function. Globally, we found alterations in all known factors analyzed, which occurred at different frequencies in the different PARPi-resistant tumor groups. Nearly eighty percent (55/71) of all resistant tumors harbored deleterious mutations, copy number variations, and/or gene expression changes in at least one known factor. *Shld2*, *Parg*, *Rif1*, *Trp53bp1*, *Rev7*, *Ezh2*, *Mre11a*, *Mll3* and *Mll4* were amongst the most frequently altered genes ($\geq 10\%$ of all tumors) (**Fig. 2A**).

We next asked whether certain genes were preferentially altered within the three different PARPi-resistant tumor groups. We found that *Trp53bp1*, one of the best-studied PARPi-resistance factors involved in HR restoration via loss of DSB end-protection, was specifically altered in RAD51-positive KB1P(M) tumors (41%) as compared to RAD51-negative KB1P(M) (7%) and KB2P (3%) tumors (**Fig. 2A-D**). In contrast, *Shld2* and *Parg* were preferentially altered by copy number loss in KB2P tumors compared to KB1P(M) tumors (**Fig. 2A,C**). Previously, we reported that loss of PARG causes PARPi resistance independently of BRCA1/2 by restoring PAR formation and restoring the recruitment of DNA repair factors downstream of PARP1⁹. While we expected *Parg* to be equally altered in both KB1P(M) and KB2P tumors, we found that *Parg* was more frequently lost in KB2P tumors (44%) (**Fig. 2A,C**) than in RAD51-positive (18%) and RAD51-negative KB1P(M) tumors (27%) (**Fig. 2B**). The genomic location of *Shld2* is proximal to *Parg* (chr14qB) and thus copy number loss of *Parg* is often accompanied by concomitant loss of *Shld2* (**Fig. 2A**). Moreover, depletion of SHLD2 has been reported to drive PARPi resistance via HR restoration in BRCA1-deficient cells but not in BRCA2-deficient cells. Hence, loss of *Shld2* in KB2P tumors is most likely a consequence of *Parg* copy number loss rather than driving resistance to PARPi. In support of this, CRISPR/Cas9-mediated inactivation of SHLD2 did not drive resistance in cultured KB2P tumor cells (**Supplementary Fig. 2A,B**). MRE11 downregulation or copy loss was only found in KB2P and RAD51-negative KB1P(M) tumors, suggesting MRE11 is specifically lost in RAD51-negative PARPi-resistant tumors (**Fig. 2A,D**). This is in line with its key role in HR and suggests that loss of MRE11 may induce PARPi resistance by promoting RF protection.

We also applied Detection of Imbalanced Differential Signal (DIDS) analysis specifically designed for the detection of subgroup markers in heterogeneous populations⁴⁴. This tool is particularly useful for identifying drug resistance factors in a tumor group with multiple resistance mechanisms by detecting genes with outlying expression in the subset of resistant tumors compared to all naïve tumors^{9,45}. DIDS analysis additionally identified *Rev7* to be significantly downregulated in RAD51-positive PARPi-resistant KB1P(M) tumors, which is consistent with its role in the 53BP1-RIF1-shieldin pathway involved in DSB end-protection, and with the observation that REV7 loss promotes HR and PARPi resistance in BRCA1-deficient cells^{17,18,23,24,30} (**Fig. 2E,F**). *Ezh2*, which was previously shown to promote

fork stability and PARPi resistance when depleted, was also identified by DIDS analysis to be downregulated in PARPi-resistant KB2P tumors, in accordance with the previous findings that loss of EZH2 impairs response to PARPi in BRCA2-deficient cells but not in BRCA1-deficient cells⁴⁶ (**Fig. 2E,G**). Surprisingly, *Rif1* was significantly downregulated in PARPi-resistant KB2P tumors, suggesting RIF1 might have 53BP1-RIF1-shieldin-independent functions that could drive resistance in BRCA2-deficient tumors (**Fig. 2E,H**).

To confirm that PARPi resistance mediated by 53BP1 loss is enriched in RAD51-positive PARPi-resistant tumors, we evaluated the functional impairment of 53BP1 in KB1P(M) and KB2P tumors by analyzing 53BP1-IRIF formation (**Supplementary Fig. 2C,D**). We found that loss of 53BP1-IRIF was only detected in RAD51-positive or mixed PARPi-resistant KB1P(M) tumors, whereas PARPi-resistant KB2P tumors as well as PARPi-naïve KB1P(M) or KB2P tumors did not show loss of 53BP1-IRIF (**Fig. 2I and Supplementary Fig. 2E**). Consistently, tumors with loss of 53BP1-IRIF showed lower *Trp53bp1* expression levels than other tumors, suggesting good concordance between the omics data and the functional assay (**Fig. 2J**). Altogether, our analysis revealed multiple known factors significantly altered in RAD51-positive KB1P(M) and in KB2P tumors; however, none were found to specifically explain PARPi resistance in RAD51-negative PARPi-resistant KB1P(M) tumors.

HR-deficient PARPi-resistant BRCA1-KO tumors show increased immune cell infiltration

We then systematically characterized the three resistant tumor groups beyond the known resistance factors using our genomic and transcriptomics data. To identify recurrent focal genomic alterations between resistant and matched naïve tumors, we performed copy number analysis using RUBIC⁴⁷. The majority of the significantly recurrent alterations identified in PARPi-resistant tumors were focal deletions (**Supplementary Fig. 3A-C**), including loss of the regions encoding *Rev7* in RAD51-positive KB1P(M) tumors and *Parg* in KB2P tumors, respectively (**Supplementary Fig. 3A, C**). In PARPi-resistant RAD51-negative KB1P(M) tumors, we could not identify recurrent focal events, with the exception of one amplified locus on chromosome 8 (**Supplementary Fig. 3B**). Several genes encoded within the recurrently amplified/deleted loci in PARPi-resistant KB1P(M) and KB2P tumors are associated with DDR pathways (**Supplementary Fig. 3D**). Gene set analysis (GSA) demonstrated that genes involved in cell cycle/proliferation were depleted in PARPi-resistant RAD51-positive KB1P(M) tumors, whereas genes involved in positive regulation of immune cell activation were amplified in PARPi-resistant RAD51-negative KB1P(M) tumors (**Supplementary Fig. 3E-G**).

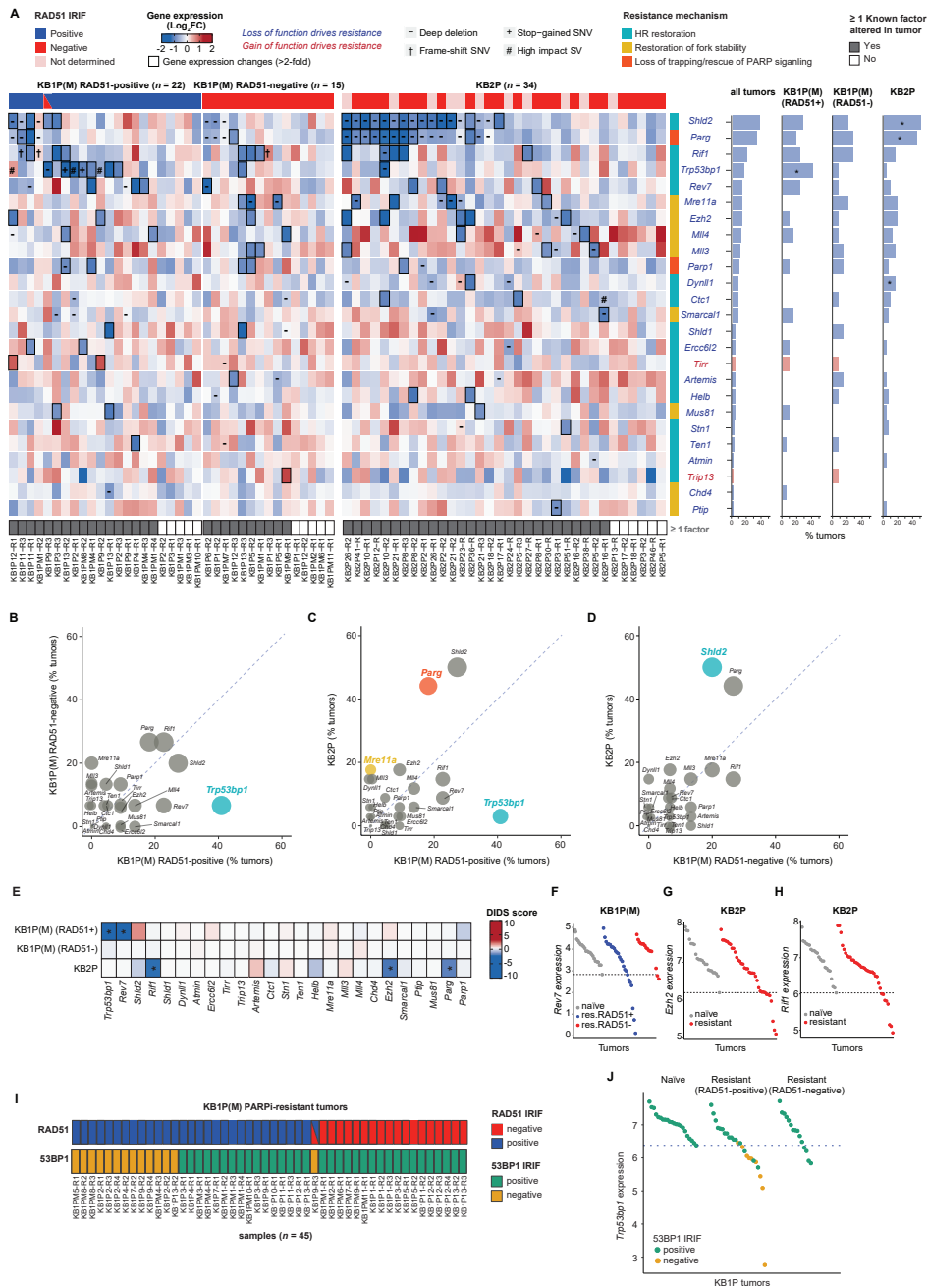


Figure 2 | Alterations in previously reported PARPi resistance factors. A | Heatmap (left) of gene expression changes between matched resistant vs naïve KB1P(M) and KB2P tumors for the previously reported PARPi resistance genes 7. Genes for which loss or gain of function have been reported to drive resistance are indicated in blue or red, respectively. In the heatmap, genomic are marked by different symbols (-: copy

number deletion, +: stop-gained SNV, †: frame-shift SNV, #: loss of function SV). The resistant tumors with transcriptional alterations (lower or higher than 2-fold compared to matched naïve tumors for each loss or gain of function drivers) are marked by thicker borderlines. The top panel of the heatmap indicates RAD51 IRIF status which is a proxy for HR status (positive - blue, negative - red, tumors with both positive and negative area - blue and red, tumors for which RAD51 IRIF was not determined, even though expected to be negative - pink). The bottom panel of the heatmap indicates the tumors with alterations in at least one known gene. Resistance mechanisms associated with each gene are categorized by different color bars (light green - HR restoration, purple - restoration of fork stability, light blue - PARP signaling). Frequencies for dysregulation of each gene (by either genomic or transcriptional alterations) are shown in the bar plots next to the heatmap (right). The genes preferentially altered in specific tumor types were assessed by the Fisher's exact test (asterisk, $P < 0.05$). **B-D** | Scatter plots comparing the alteration frequency of each PARPi resistance factor in the different resistant tumor types. The size of the circle is proportional to the sum of the alteration frequency of the two resistant tumor types compared and circles are colored if statistically significant (Fisher's exact test, $P < 0.05$). The color of the circle indicates the resistance mechanism associated with each resistance factor as mentioned in Figure 2A. **E** | DIDS outlier scores computed from gene expression data for known resistance factors. Red (positive score) and blue (negative score) indicate upregulation and downregulation of each factor in subset of resistant tumors compared to naïve tumors. The genes with significant DIDS scores are marked with asterisk (Permutation-based exact test, $P < 0.05$). **F-H** | Dot plots of *Rev7* gene expression in KB1P(M) tumors (F) and *Ezh2* (G) and *Rif1* (H) gene expressions in KB2P tumors where significant DIDS scores were detected. **I** | RAD51 and 53BP1 IRIF status in KB1P(M) PARPi-resistant tumors measured by in situ IRIF assay. **J** | Dot plots of *Trp53bp1* gene expression in KB1P(M) tumors with 53BP1 IRIF status.

Next, we transcriptionally characterized the different PARPi-resistant tumor groups. Differential gene expression analysis by limma⁴⁸ between resistant and naïve tumors identified 26, 349 and 1058 genes in PARPi-resistant RAD51-positive KB1P(M), RAD51-negative KB1P(M) and KB2P tumors, respectively, including downregulation of *Trp53bp1*, *Parg* and *Shld2* (**Fig. 2A and Supplementary Fig. 3H-J**). No known resistance-associated factors were found to be differentially expressed in RAD51-negative KB1P(M) tumors (**Supplementary Fig. 3I**). GSA of the differentially expressed genes (DEGs) in each group of resistant tumors identified distinct sets of pathways. Interestingly, PARPi-resistant RAD51-negative KB1P(M) tumors showed upregulation of immune-related pathways, including antigen processing and presentation, T-cell receptor signaling and phagosome (**Fig. 3A**), which might be associated with the enrichment of immune cell regulators with focal amplification in these tumors (**Supplementary Fig. 3F**). Co-functionality network analysis of upregulated immune-associated genes using the GenetICA-Network framework⁴⁹ revealed several immune cell modules, such as T cells (e.g., CD3D, CD3G, CD247), B cells (e.g., CD22, CD72, CD79A) and antigen presentation (e.g., CD74, CIITA, H2-OB, H2-AA, H2-AB1, H2-EB1, H2DMA, H2-DMB1, H2-DMB2), suggesting an increase in immune cell infiltration (**Fig. 3B**). We validated these findings by carrying out immunohistochemical (IHC) analysis of markers of leucocytes (CD45), T cells (CD3), B cells (B220) and macrophages (F4/80), revealing increased expression of all these markers in PARPi-resistant KB1P(M) tumors when compared to naïve tumors, with RAD51-negative KB1P(M) tumors displaying a stronger increase compared to RAD51-positive KB1P(M) tumors (**Fig. 3C**). Therefore, our findings suggest that RAD51-negative PARPi-resistant KB1P(M) tumors have higher immune infiltration compared to PARPi-naïve and RAD51-positive PARPi-resistant KB1P(M) tumors. Altogether, these data demonstrate that PARPi-resistant tumors display distinct

genomic and transcriptomic features depending on BRCA1/2 loss and HR status.

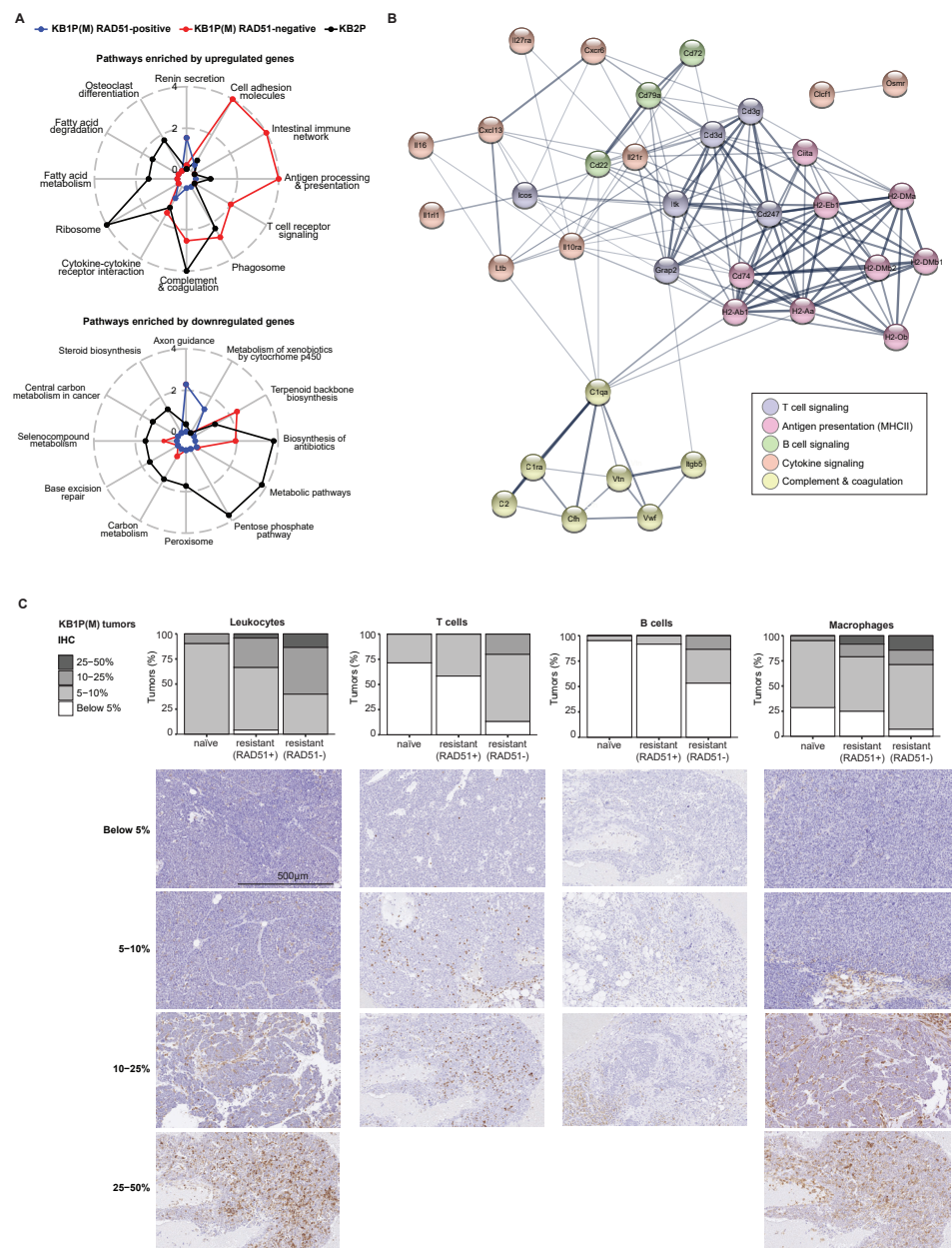


Figure 3 | HR-deficient PARPi-resistant BRCA1-KO tumors show increased immune cell infiltration. A | Radar chart showing pathways enriched by upregulated and downregulated genes in KB1P(M) and KB2P resistant tumors compared to naïve tumors based on gene expression data. **B** | Co-functionality network constructed by STRING⁶² for the immune-related genes that are significantly upregulated in RAD51-negative KB1P(M) resistant tumors compared to naïve tumors. The genes in the network were annotated by KEGG⁶² and colored depending on the annotated pathways. **C** | Quantification and representative images of IHC analysis of markers for different immune cells including leukocytes (CD45), T-cells (CD3), B-cells (B220), and macrophages (F4/80) in KB1P(M) tumors.

Multi-omics analysis identifies potential PARPi-resistance factors/pathways

To catalogue potential PARPi resistance factors, we identified genes displaying resistance-specific genomic (SNVs, INDELs, SVs, focal amplifications/deletions) and transcriptional (DEG sets) alterations in each group of resistant tumors by integrating WE-seq, LCWG-seq and RNA-seq data (**Fig. 4A**). Of note, we extended DEG sets to capture the genes with both homogeneous (by limma) and heterogenous behavior (by DIDS) between naïve and resistant tumors. Overall, we observed limited overlap between genomic and transcriptional alterations across all tumor groups, including several genes involved in DDR (**Fig. 4B and supplementary table 2**). Moreover, the overlap between genomic and transcriptional alterations was mostly derived from copy number alterations, with the exception of *Trp53bp1*, in which we found truncating SNVs and deleterious SVs leading to nonsense-mediated decay. The limited overlap between genomic and transcriptional alterations indicates that the genomic alterations do not always lead to gene expression changes. Nonetheless, several known resistance factors including *Trp53bp1*, *Rev7*, and *Parg* displayed both genomic and transcriptional alterations. We next explored biological pathways represented by the identified genes with resistance-specific genomic and transcriptional alterations (**Fig. 4C and supplementary table 3**). As described before, we found transcriptional upregulation of immune-associated pathways specifically in RAD51-negative KB1P(M) tumors, including upregulation of antigen processing and presentation, B and T cell receptor signaling, as well as immune checkpoint pathways (**Fig. 4C,D**). Interestingly, pathways associated with cell adhesion molecules and ECM-receptor interaction were transcriptionally downregulated in RAD51-positive KB1P(M) tumors, but upregulated in RAD51-negative KB1P(M) tumors (**Fig. 4C,D**). At the genomic level, loss-of-function alterations (mainly copy number loss or deleterious SNVs/SVs) were observed in pathways associated with signaling processes such as calcium and cAMP signaling pathways in RAD51-positive KB1P(M) tumors, and in metabolic pathways such as inositol phosphate and carbon metabolism in KB2P tumors (**Figures 4C and 4D**). In line with the limited overlap between genomic and transcriptional alterations (**Fig. 4B**), pathways enriched by genes with genomic alterations showed very limited overlap with those enriched in transcriptional alterations, with the exception of the phagosome pathway (**Fig. 4C**). Nonetheless, we found 46 genes that carried either genomic or transcriptional alterations in all three resistant tumor groups, including 8 genes (*Parp3*, *Gstm1*, *Il18*, *Padi4*, *Dnmt3b*, *Psrc1*, *Rif1* and *Ankrd26*) involved in DDR (**Fig. 4E,F**). Taken together, integration of genomics and transcriptomics data from PARPi-resistant versus PARPi-naïve tumors allowed us to catalogue genes and pathways potentially involved in modulating PARPi response.

To prioritize candidate resistance drivers, we identified genes with genomic alterations that had a significant impact on transcriptional changes in the protein-protein interaction network by carrying out driver analysis with DriverNet⁵⁰. We identified drivers in 25% of genes with resistance-specific mutations and in 23% of genes with copy number alterations (**Supplementary Fig. 4A**). Interestingly, DDR genes were more enriched in drivers compared

to non-drivers in all PARPi-resistant tumor groups, with the exception of drivers that were derived from copy number alterations in RAD51-negative KB1P(M) tumors (**Supplementary Fig. 4B-D**), supporting the previous findings that DDR pathways are strongly involved in governing PARPi response⁷.

***In vitro* loss-of-function screens fail to validate candidate drivers of *in vivo* PARPi resistance**

To identify causative drivers among the genes associated with PARPi resistance in KB1P(M) tumors, we performed functional genetic enrichment screens in human BRCA1-deficient cell lines. To obtain a comprehensive set of genes to be functionally tested in the screens, we generated global proteomics and phosphoproteomics data and identified proteins (DE-Prot) and phosphoproteins (DE-Phos) that were differentially expressed between naïve and resistant tumors. We combined the DE-Prot and DE-Phos with genes identified from WE-seq, LCWG-seq and RNA-seq analysis for all KB1P(M) tumors, including tumors whose RAD51-IRIF status was not determined, resulting in 3727 resistance-associated genes (**Supplementary Fig. 4E**). Plausible drivers were prioritized by recurrences in multiple datasets, associations with DDR, and potential as network drivers, yielding a final list of 891 putative PARPi resistance driving factors including 53BP1, REV7, HELB and PARG (**Supplementary Fig. 4F**).

We then generated a focused lentiviral shRNA library targeting the identified 891 candidate genes plus 133 non-essential genes as controls (**Supplementary table 5**). Given the strong effect of 53BP1 loss on PARPi resistance, we decided to exclude *Trp53bp1*-targeting shRNAs from the library to prevent them from obscuring less dominant hits. We introduced the lentiviral shRNA library in the human BRCA1-deficient cell lines SUM149PT and RPE1-hTERT-*BRCA1*^{-/-};*TP53*^{-/-}, which were subsequently selected with olaparib for three weeks (**Supplementary Fig. 4G**). REV7 behaved as a positive control and was identified as top hit in both cell lines, but no other common hits were found (**Supplementary Fig. 4H,I**). We identified RBMS1 as a hit in the screen carried out in SUM149PT cells (**Supplementary Fig. 4H**), but shRNA-mediated depletion of RBMS1 *in vivo* did not significantly affect survival of KB1P tumor-bearing mice (**Supplementary Fig. 4J**). Overall, these results suggest *in vitro* loss-of-function screens are insufficient to validate the candidate drivers of *in vivo* PARPi resistance arising from the multi-omics analysis.

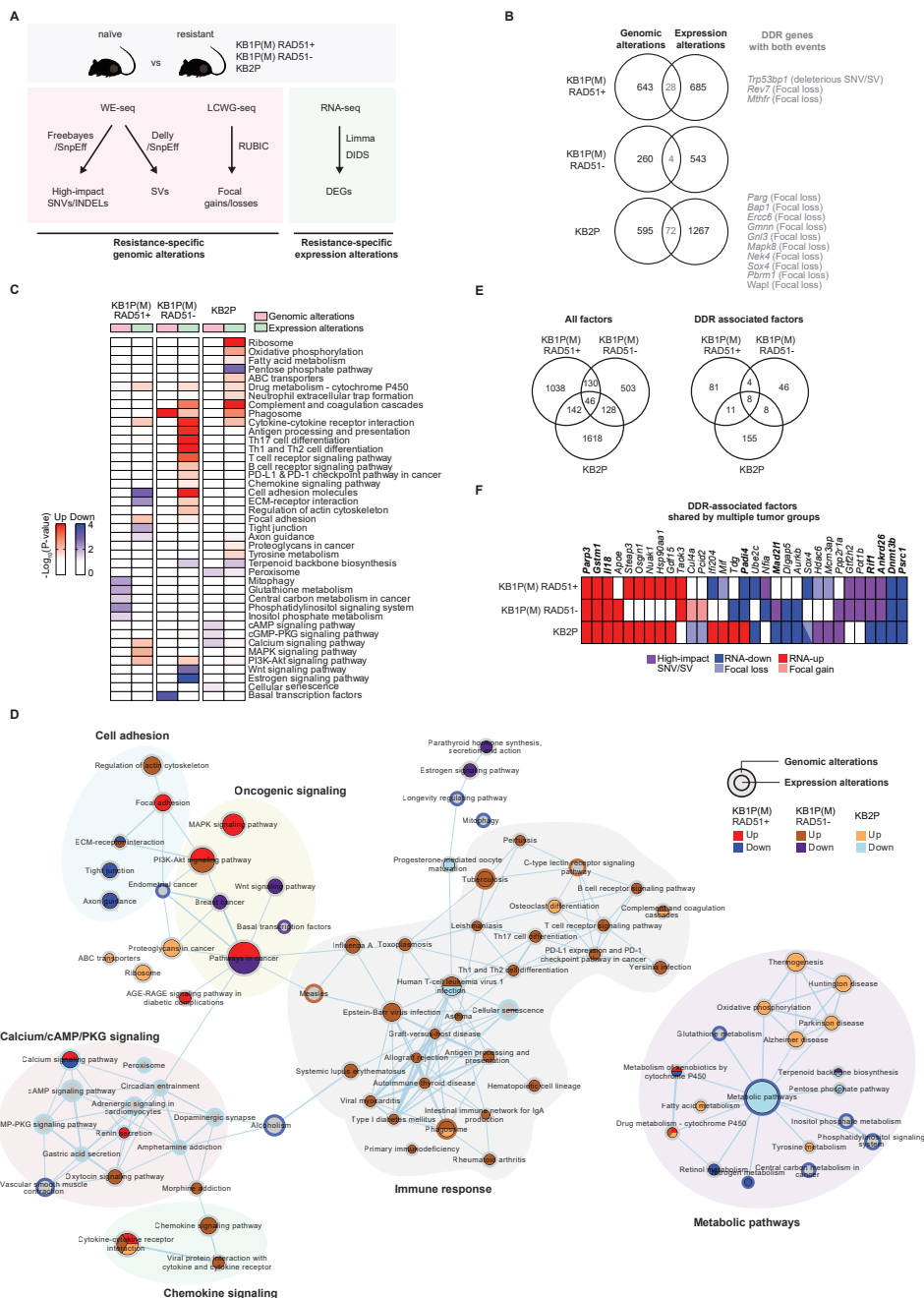


Figure 4 | Multi-omics analysis identifies potential PARPi-resistance factors/pathways. **A** | Schematic overview of the analysis to identify resistance-specific genomic and transcriptional alterations from WE-Seq, LCWG-Seq, and RNA-seq data. For each PARPi naïve and resistant RAD51-positive and RAD51-negative KB1P(M) and KB2P tumors, (1) deleterious SNVs, INDELs, SVs, and focal amplifications/deletions (resistance-specific genomic alterations) and (2) DEG sets identified by either limma or DIDS analysis (resistance-specific transcriptional alterations) were selected. DEG sets were extended to capture the genes with both

homogeneous (by limma) and heterogenous behavior (by DIDS) between naïve and resistant tumors. **B** | Venn diagrams showing the overlaps between the genes having resistance-specific genomic alterations (SNVs, INDELs, SVs, and copy number focal gains and losses) and transcriptional alterations (DEGs) in each resistant tumor type. **C** | Heatmap of pathways significantly enriched by the genes with resistance-specific genomic and transcriptional alterations. Enrichment, $-\log_{10}(\text{P-value})$ computed by fisher exact test, by upregulated and downregulated genes are represented by red and green in the heatmap, respectively. **D** | Pathway enrichment map for genes with resistance-specific genomic and transcriptional alterations constructed by EnrichmentMap⁶³. Node size represents size (number of genes) of gene sets (pathways) and edges represent mutual overlaps between the gene sets (minimum similarity score 0.3). Node and border represent enrichment by the genes with resistance-specific transcriptional and genomic alterations, respectively. **E** | Venn diagrams showing the overlaps of the genes having resistance-specific alterations with either genomic or transcriptional alterations across the three resistant tumor types. **F** | List of DDR-associated genes with resistance-specific alterations that were identified in multiple resistant tumor types.

DISCUSSION

In this study, we combined functional analysis of HR status with multi-omics analysis of a collection of matched PARPi-naïve and PARPi-resistant BRCA1-KO and BRCA2-KO mouse mammary tumors to classify the contribution of previously reported non-reversion resistance mechanisms in a preclinical “*in vivo* reality” of spontaneous acquired resistance. Overall, our analysis highlights the differences in resistance patterns between BRCA1- and BRCA2-deficient tumors and identifies HR restoration via loss of 53BP1 and restoration of PARP signaling via loss of PARG as the two dominant non-reversion resistance mechanisms in BRCA1- and BRCA2-deficient tumors, respectively. Additionally, our analysis generated a catalogue of candidate genes and pathways potentially involved in modulating PARPi response. Expanding the use of PARPi in the clinic should soon provide clinical specimens that will allow us to verify the relevance of our findings.

Functional differences between BRCA1 and BRCA2 impact PARPi resistance patterns

In our study we also used PARPi resistance as a tool to probe for different activities of BRCA1 and BRCA2 in DNA repair. BRCA1 and BRCA2 are often mentioned together, partly owing to their tumor suppressor activities and roles in HR repair. From a biological standpoint, however, BRCA1 and BRCA2 are not functionally redundant in HR. The epistatic relationship between BRCA1 and BRCA2 was first put forward in the context of embryonic lethality by Ludwig *et al.* almost 20 years ago⁵¹. Consistent with this relationship, previous work from our laboratory demonstrated that concomitant tissue-specific deletion of the *Brca1* and *Brca2* genes (KB1B2P) resulted in similar tumor development as single gene knockouts (KB1P and KB2P), indicating that BRCA1 and BRCA2 are epistatic in tumor suppression (Liu *et al.*, unpublished data). Our present analysis of PARPi resistance mechanisms reveals a clear functional distinction between BRCA1 and BRCA2 in DNA repair. While HR-deficiency and PARPi sensitivity of BRCA1-KO tumors could be largely suppressed by inactivation of the 53BP1-RIF1-shieldin pathway, BRCA2-KO tumors completely failed to rescue HR activity, as measured by RAD51 foci formation, underlying the essential role of BRCA2 in RAD51

loading during the HR process. Moreover, we found that the levels of the RAD51-IRIF in the PARPi-resistant KB1P(M) tumors were significantly lower than in BRCA-proficient controls, indicating partial restoration of HR activity in these samples (**Supplementary Fig. 1C**). This is consistent with previous DR-GFP-based HR reporter assays we performed in *Tp53bp1*- or *Rev7*-depleted KB1P cells²³. In addition, recent studies have suggested that whereas BRCA1 is dispensable for DNA end resection, its interaction with PALB2 and the resulting promotion of RAD51 loading cannot be fully compensated^{52,53}. It is therefore conceivable that inactivation of the 53BP1-RIF1-shieldin pathway in BRCA1-KO tumors rescues the DNA end resection defect, but fails to fully restore HR repair due to lack of BRCA1 activity downstream of resection. Altogether, these data show that BRCA1 and BRCA2 are not epistatic in the repair of DSBs by HR and that these differences impact the resistance patterns in PARPi-treated tumors.

Resistance mechanisms in HR-restored BRCA1-KO tumors

Loss of 53BP1 was the most frequent alteration in RAD51-positive PARPi-resistant KB1P(M) tumors, whereas all other DSB end-protection factors seemed to be only sporadic. In line with this, mice bearing *Shld1/2*- or *Ctc1*-mutated KB1P tumors exhibit only partial response to olaparib in comparison with mice bearing unmodified KB1P tumors, whereas mice bearing *Trp53bp1*-mutated tumors did not respond to PARPi treatment, resulting in survival curves identical to vehicle-treated mice^{17,54}. Moreover, loss of 53BP1 has also been observed in patient-derived tumor xenograft (PDX) models with acquired resistance to PARPi, and mutations in *TP53BP1* have been reported in tumor biopsies from patients with metastatic BRCA1-associated breast cancer receiving platinum chemotherapy or PARPi^{19,55,56}. Altogether, our results indicate that BRCA1-independent HR restoration driven by inactivation of 53BP1 may be the most common mechanism of PARPi resistance in patients with *BRCA1*-mutated tumors that do not undergo BRCA1 reactivation, and that 53BP1 may be a potential biomarker of PARPi response in *BRCA1*-mutated tumors.

Resistance mechanisms in HR-deficient BRCA1-KO tumors

More than one-third of all PARPi-resistant KB1P(M) tumors were RAD51-negative, indicating that they hadn't restored HR. Despite the fact that alterations in previously reported resistance factors were found sporadically in PARPi-resistant RAD51-negative KB1P(M) tumors, none of these factors were found significantly altered in any of the analyses carried out in this study. Moreover, alterations in these factors did not occur more frequently in PARPi-resistant RAD51-negative KB1P(M) tumors compared to PARPi-resistant RAD51-positive KB1P(M) or KB2P tumors. Nevertheless, gene set analysis of the DEGs identified in PARPi-resistant RAD51-negative KB1P(M) tumors yielded an enrichment in positive regulation of immune response which was in line with the increase in immune infiltration detected by IHC analysis. In line with this, organoids derived from one of the PARPi-resistant RAD51-negative KB1P(M) tumors (KB1PM7) failed to recapitulate PARPi resistance *in vitro*

but upheld PARPi resistance *in vivo*, suggesting PARPi resistance in this tumor may be driven via cell-extrinsic processes that can only be recapitulated *in vivo*⁵⁷. Moreover, these tumors preserve PARPi resistance following orthotopic transplantation of tumor fragments into syngeneic mice, indicating that the resistance phenotype is tumor-intrinsic.

Previous studies have reported that *BRCA1/2*-mutated tumors display increased immune infiltration upon treatment with PARPi, suggesting immune infiltration is required for PARPi antitumor efficacy⁵⁸. Interestingly, among the different pathways upregulated in PARPi-resistant RAD51-negative KB1P(M) tumors, we identified an enrichment in factors associated with upregulation of PD-L1 and PD-1 checkpoint pathway, which is in line with the previously reported upregulation of PD-L1 expression by PARPi⁵⁹. PARPi-resistant HR-deficient *BRCA1*-mutated tumors might therefore be treated with combinations of PARPi and immune-checkpoint inhibitors⁵⁹⁻⁶¹. Altogether, these data highlight the role of the tumor microenvironment in the response to PARPi.

Resistance mechanisms in BRCA2-KO tumors

PARG loss was undoubtedly the most frequent alteration in PARPi-resistant KB2P tumors and occurred significantly more often in KB2P tumors than in the other tumor groups, even though a few resistant KB1P(M) tumors carried copy number loss and/or downregulation of *Parg*. The strong selection for PARG loss in KB2P tumors could result from of the impossibility of HR restoration in these tumors. Even so, PARG loss was not more frequent in PARPi-resistant HR-negative KB1P(M) tumors compared to HR-positive KB1P(M) tumors.

Perturbations that occurred more frequently in PARPi-resistant BRCA2-KO tumors than in BRCA1-KO tumors were alterations associated with loss of PARP trapping or rescue of PARP signaling (44% in KB2P versus 32% in KB1P(M); mostly involving *Parg*) and alterations associated with restoration of replication fork stability (56% in KB2P versus 35% in KB1P(M); mostly involving sporadic alterations). Unlike PARG, perturbations in PARP1 were anecdotal in both KB1P and KB2P tumors, suggesting PARP1 activity is critical for the viability of BRCA1/2-deficient cells.

Overall, our data show that PARPi resistance cannot be achieved via HR restoration in BRCA2-deficient tumors that cannot undergo BRCA2 reactivation. Moreover, loss of PARG is the single most recurrent driver of acquired resistance in BRCA2-KO tumors, yielding PARG as a potential predictive marker of PARPi response in patients with *BRCA2*-mutated tumors.

Limitations of this study

Our tumor collection recapitulates BRCA1/2 loss-driven tumor formation and acquired PARPi resistance but does not capture the full complexity of the human cancer (e.g., metastatic disease, heterogeneity, hypomorphic mutations). Moreover, human genes do not always have mouse orthologs or play exactly the same functions across the two species. For example, the previously reported PARPi resistance factor SLFN11¹³ does not have a

mouse ortholog and that is why it was not included in our analysis.

This study relies on the comparison with naïve tumors but does not include the comparison with responsive tumors (before developing resistance). Such tumor cohort would allow to identify gene/pathways altered during PARPi treatment before the tumors develop resistance. Additionally, the multi-omics analysis carried out in this study does not include methylome data and thus we might miss epigenetic mechanisms of PARPi resistance. Nevertheless, changes in DNA-methylation are predicted to affect transcriptional activity and should therefore be visible in the RNA-seq data.

In this study we carried out *in vitro* loss-of-function screens in two human cell lines to validate candidate drivers of *in vivo* PARPi resistance, however this approach failed to yield common hits other than the already-known factor *REV7*. A limitation of this approach is that loss-of-function screens, such as shRNA-based screens, can only functionally validate candidate loss-of-function factors, which represent 40% (356/891) of all candidate drivers. Additionally, PARPi resistance in tumors without alterations in known resistance genes could be driven by the additive effect of multiple alterations rather than a single event. Finally, resistance could be driven by genes that modulate the tumor microenvironment, which cannot be adequately modeled in *in vitro* screens.

ACKNOWLEDGMENTS

We thank the members of the Preclinical Intervention Unit of the Mouse Clinic for Cancer and Ageing (MCCA) at the NKI for their technical support with the animal studies. We also thank the following NKI core facilities for their excellent service: Animal Pathology facility, Digital Microscopy facility, Genomics Core facility and Animal facility. We would like to thank Piet Borst (NKI, Amsterdam) for scientific discussions. This work was funded by Oncode Institute, the Dutch Cancer Society (KWF 2011-5220 and 2014-6532), the Netherlands Organization for Scientific Research (VICI 91814643), the Netherlands Genomics Initiative (93512009), the Swiss National Science Foundation (310030_179360), the Swiss Cancer League (KLS-4282-08-2017), the Wilhelm-Sander Foundation (no. 2019.069.1) and the European Research Council (ERC-2019-AdG-883877, SyG-319661).

AUTHOR CONTRIBUTIONS

Conceptualization, J.B., M.P.D., E.G., S.R., J.J.; Methodology, J.B., M.P.D., E.G., F.R., S.R.P.; Investigation, J.B., M.P.D., E.G., F.R., A.A.D., W.S., I.v.d.H., L.B., T.S.K., B.M.; Software Analysis, J.B., E.G., F.R., B.v.d.B., J.R.d.R., R.d.B., R.L.B., C.L.; Original Draft, Review & Editing – J.B., M.P.D., E.G., L.F.A.W., S.R., J.J.; Supervision, M.v.d.V., C.R.J., L.F.A.W., S.R., J.J.; Funding Acquisition, S.R. and J.J.

METHODS

EXPERIMENTAL MODEL AND SUBJECT DETAILS

Cell Lines and cell culture

KB1P (KB1P-G3)³⁸ and KB2P (KB2P-3.4)⁶⁴ mouse tumor-derived cell lines were previously described and were grown in DMEM/F12 (Gibco) supplemented with 10% FBS and 50 units/ml penicillin-streptomycin (Gibco), containing 5 µg/ml Insulin (Sigma), 5 ng/ml cholera toxin (Sigma) and 5 ng/ml murine epidermal growth-factor (Sigma), under low oxygen conditions (3% O₂, 5% CO₂ at 37°C). RPE1-hTERT *BRCA1*^{-/-};*TRP53*^{-/-} human cell line has been described before⁵³ and was grown in DMEM+GlutaMAX (Gibco) supplemented with 10% FBS and 50 units/ml penicillin-streptomycin (Gibco), under low oxygen conditions (3% O₂, 5% CO₂ at 37°C). SUM149PT (RRID:CVCL_3422) human cell line was grown in RPMI1640 (Gibco) medium supplied with 10% FBS and 50 units/ml penicillin-streptomycin (Gibco), under normal oxygen conditions (21% O₂, 5% CO₂, 37°C).

Mice

All animal experiments were approved by the Animal Ethics Committee of The Netherlands Cancer Institute (Amsterdam, the Netherlands) and performed in accordance with the Dutch Act on Animal Experimentation (November 2014). Parental FVB (FVB/NRj) and 129/Ola animals were purchased from Janvier Labs and Harlan Olac, respectively, and crossed at the NKI Animal Facility.

METHOD DETAILS

In situ RAD51-IRIF and 53BP1-IRIF assay

Cryopreserved material of PARPi-naïve or -resistant KB1P, KB1PM and KB2P tumors (KB1P(M): 23 naïve, 47 resistant; KB2P: 19 naïve, 26 resistant) was thawed and orthotopically engrafted into the right mammary fat pad of 6 week-old wild-type syngeneic female mice (KB1P(M) – FVB; KB2P – FVB:129/Ola(F1)). Tumor volume was monitored starting from two weeks after transplantations and calculated using the following formula: 0.5 x length x width². When tumors reached approximately 500 mm³ (100% relative tumor volume), they were locally irradiated using a CT-guided high precision cone beam micro-irradiator (X-RAD 225Cx) or left untreated (control). Two different factors were tested to optimize the assay: IR dosage (15 and 24 Gy) and post-irradiation incubation time (1-6 hr). We did not observe significant differences in RAD51 IRIF formation between the two IR dosages, and the highest accumulation of RAD51 foci was detected 2 hours after induction of DNA damage. Based on these results, we analyzed RAD51 IRIF in KB1P(M) and KB2P tumors 2 hr after irradiation with 15Gy. Post irradiation, tumors were isolated and part of the tissue was immediately fixed in 4% (w/v) solution of formaldehyde in PBS (remaining tissue was fresh frozen for the proteomic and phosphoproteomic analyses). 5 µm-thick FFPE (formalin-fixed paraffin embedded) tissue sections were then used for immunofluorescence. Following

deparaffinization (70°C, 20 min), tissues were rehydrated and cooked in DAKO Target Retrieval Solution pH 9 (#S236784, DAKO) for 20 min in microwave at ~600W, to allow antigen retrieval. Next, tissue permeabilization was achieved by incubating samples in 0.2% (v/v) Triton X-100 in PBS for 20 min and followed by 1 hr DNase (1,000 U/ml; #04536282001, Roche) treatment at 37°C. Blocking was done for 30 min in staining buffer (1% (w/v) BSA, 0.15% (w/v) glycine and 0.1% (v/v) Triton X-100 in PBS). Subsequent incubation with primary antibodies was carried out overnight at 4°C, and later with secondary antibodies for 1 hr at room temperature. The following antibodies (diluted in staining buffer) were used in this assay: rabbit polyclonal anti-RAD51 (kind gift from R. Kanaar, Erasmus MC, Rotterdam; 1:5,000), rabbit polyclonal anti-53BP1 (#ab21083, Abcam; 1:1,000), goat polyclonal anti-rabbit, Alexa Fluor® 658-conjugated (#A11011, Thermo Fisher Scientific; diluted 1:1,000). Samples were mounted with VECTASHIELD Hard Set Mounting Media with DAPI (#H-1500; Vector Laboratories). Images were taken with Leica SP5 (Leica Microsystems) confocal system equipped with a x100 objective and image stacks (~6 slices) were analyzed using an in-house developed ImageJ macro to automatically and objectively quantify IR-induced foci, as described before²³. Briefly, nuclei were segmented by thresholding the (median-filtered) DAPI signal, followed by a watershed operation to separate touching nuclei. For each z-stack the maximum-intensity projection of the foci signal was background-subtracted using a difference of gaussians method. Next, for every nucleus, foci candidates were identified as locations where the resulting pixel values exceeded the background by a factor (typically 25x) times the median standard deviation of all nuclei in the image. Additional filters for discriminating for foci size, nucleus size (to eliminate stromal cells) and absolute brightness were applied. Results were validated by visual inspection. Visualization as well as quantification of foci was done in a blinded fashion. For each sample, five random areas (246 x 246 µm; on average 125 cells per area) were imaged and analyzed. Cell was considered positive if contained >5 nuclear foci. KP tumor was used as a positive control in this assay.

53BP1 IHC

All IHC stainings were performed on FFPE material. For 53BP1 IHC, tissue sections were boiled for 30 min in citrate buffer pH 6.0 (#CBB 999, Scytek Laboratories) to facilitate antigen retrieval. Next, the stainings were carried out by using 3% (v/v) H₂O₂ solution in methanol for blocking endogenous peroxidase activity (20 min) and 4% BSA plus 5% normal goat serum (NGS) in PBS as a blocking buffer (30 min). Primary antibodies were diluted in 1.25% NGS plus 1% BSA in PBS, and applied on the samples overnight, at 4°C. Incubation with secondary antibodies (diluted in 1.25% NGS/1% BSA in PBS; 30 min, room temperature) (#E0433, DakoCytomation) was followed by incubation with streptavidin conjugated to horseradish peroxidase (1:200; 1.25% NGS/1% BSA in PBS; 30 min) (#P0397, DakoCytomation). For visualization DAB (#D5905, Sigma), H₂O₂ (#A-31642, Sigma, 1:1,250) and hematoxylin counterstaining were applied. IHC stainings were evaluated and scored (0 – negative, 1 – low expression, 2 – high expression) by a pathologist who was blinded regarding the identity

of the samples. Antibodies used in this protocol: rabbit polyclonal anti-53BP1 (#A300-272A, Bethyl Laboratories; 1:1,000), secondary donkey-anti-goat-Bio (#E0433, DakoCytomation; 1:200), secondary goat-anti-rabbit-Bio (#E0432, Dako Cytomation; 1:1,000).

Whole-exome sequencing (WE-seq)

Genomic DNA was isolated from fresh frozen tumor tissue using a standard Proteinase K and phenol:chloroform extraction and sheared to approximately 300 bp fragments using Covaris S2 sonicator. Next, 500-1000 ng of sheared DNA was used as a template for a 6-cycle PCR to construct a fragmented library using the KAPA HTP Library Preparation Kit (Roche). Exome enrichment was performed using SeqCap EZ Enrichment Kit (Roche) according to the manufacturer's protocol (SeqCap EZ Library SR User's Guide, v5.3). Samples were sequenced on an Illumina HiSeq2500 (Illumina). Adapters in the resulting reads were trimmed using Cutadapt⁶⁵ (version 1.12) and the trimmed reads were aligned to the GRCm38 reference genome using BWA (version 0.7.15)⁶⁶. The resulting alignments were sorted and marked for duplicates with Picard tools (version 2.5.0). Freebayes variant caller was used to identify SNVs and Indels for each sample with the mode of pooled-continuous (min-alternate-fraction = 0.1, min-alternate-count = 3, and min-coverage = 10)⁶⁷ and resulting variants were annotated by SnpEff⁶⁸. SNVs and Indels identified in FVB/NJ mice were obtained from Sanger Mouse Genome Project⁶⁹ and used to discard germline variants in our tumor samples. SNVs and Indels that were only identified in resistant tumors and predicted to be high-impact mutations by SnpEff were considered resistant tumor-specific alterations with functional effects and were used for downstream analysis. Structural variants were identified by delly (version 0.9.1) for each pair of resistant and matched naïve tumors and resulting variants were annotated by SnpEff. High-impact SVs predicted by SnpEff were used for downstream analysis.

Low-coverage whole-genome sequencing (LCWG-seq)

LCWG-seq data was generated as described before⁹. Briefly, genomic DNA was isolated from fresh-frozen tumor material using standard phenol:chloroform extraction. LCWG-seq was performed using double stranded DNA (dsDNA) and quantified with the Qubit® dsDNA HS Assay Kit (Invitrogen, #Q32851). Library preparation was performed with 1 µg of DNA and KAPA HTP Library Preparation Kit (KAPA Biosystems, #KK8234). Resulting reads (50 base single-end reads) were trimmed, sorted and marked for duplicates using the same pipeline as for the WES. The resulting alignments were analyzed to generate segmented profile differences between matched (naïve/resistant) samples derived from the same tumor donor using the QDNAseq and QDNAseq.mm10 R packages (bin size = 50K)⁷⁰. To identify regions with recurrent copy number difference (naïve vs resistant), we iteratively ran RUBIC with default cutoff for calling amplifications and deletions (focal threshold = 1e+08, min probes = 4, FDR < 0.25, amp.level and del.level = 0.1)⁴⁷.

RNA sequencing (RNA-seq)

RNA-seq data was generated as described before⁹. Briefly, fresh frozen tumor tissue were placed in 1 ml of TRIpure reagent (#BIO-38032, Bioline) and tissue lysis was achieved by high-speed shaking with stainless steel beads for 10 min, 50 Hz at room temperature (TissueLyser LT, Qiagen). Homogenized tissue lysates were further processed according to the TRIpure manufacturer's protocol. Strand-specific libraries were generated using the TruSeq Stranded mRNA sample preparation kit (Illumina Inc., San Diego, RS-122-2101/2) according to the manufacturer's instructions. The resulting reads (50 base single-end reads) were trimmed using Cutadapt⁶⁵ and aligned to the GRCm38 reference genome using STAR (version 2.5.2b)⁷¹. To identify differentially expressed (DE) genes, gene expression counts were first generated by featureCounts using gene definitions from Ensembl GRCm38 (version 76)⁷². Genes with counts per million (CPM) larger than one in at least 10% of samples were used for further analysis. Trimmed mean of M-value (TMM) normalization was applied to the data using edgeR⁷³ and Limma-voom was used to correct for the donor effect and identify the differentially expressed genes between naïve vs resistant tumors (FDR < 0.25 for KB1P and FDR<0.05 for KB2P, Log2 fold change>0.5)⁷⁴. Because of the intratumoral heterogeneity, we additionally applied DIDS (Detection of Imbalanced Differential Signal) for the detection of subgroup markers in resistant populations (P < 0.05)⁴⁴.

Selection of previously reported PARPi resistance factors

The list of resistance-associated factors was generated based on previous reports⁷. We excluded *SLFN11*¹³ which does not have a mouse ortholog and *Shld3* and *Radx* which were not expressed in our mouse cohort. In total, 25 genes were analyzed in our omics datasets (**Supplementary table 1**).

Selection of DNA damage response (DDR)-related genes

The DDR gene set was obtained from the previous study that was generated based by merging the gene lists from the previous papers and the NCBI search by terms of "DNA repair", "DNA damage response", "DNA replication", and "telomere-associated genes"⁹.

Gene set over-representation analysis

Gene set over-representation analysis was performed by DAVID⁷⁵ for genes with significant upregulation and downregulation (RNA-seq) and focal gains and losses (CNV-seq) in resistant tumors compared to naïve tumors. The significant gene sets were identified as the ones with P<0.05.

Driver gene analysis

For genes with resistant tumor-specific mutations and copy number variations as mentioned above, DriverNet was used to infer potential driver genes by assessing the impact of alterations on the expression network. Protein-protein interactome (PPI) to construct

expression network was obtained by orthologue mapping of human PPI merged from multiple PPI databases^{76–80}. The genes with more than 1.5-fold changes in expression were defined as genes showing outlying expression and used to assess the impact of mutations in the expression network. P-value was computed by gene-based randomization of 1000 times and genes with P-value <0.05 were selected as potential drivers.

Mass spectrometry (MS)-based proteomics

For the proteomic and phosphoproteomic analyses of KB1P(M) tumors, we used previously published proteomics dataset generated by MS (PRIDE accession code: PXD032007)⁸¹. For phosphoproteomic analysis, for phosphoproteomic analysis, MaxQuant phosphosite quantification data (Phospho (STY)Sites.txt) was log2-transformed, normalized on the median intensity of all identified phosphosites and replicates averaged favoring data presence. For global protein expression analysis, MaxQuant LFQ Intensity⁸² was log2-transformed and replicates were averaged. limma⁴⁸ was used for differential expression analysis.

Shld2 gene-editing

For CRISPR/Cas9-mediated genome editing of *Shld2*, sgRNA sequences (sgRNA#1: 5'-atcagtcagatccctgcgtt-3'; sgRNA#2: 5'-aacctgagtgatatgactag-3') were cloned into a modified version of the lentiCRISPR v2 backbone (RRID: Addgene_52961) in which a puromycin resistance ORF was cloned under the hPGK promoter, or into the pX330.puro backbone (Addgene #110403). Cloning of sgRNAs into the lentiCRISPR v2 backbone was carried out by melting the custom DNA oligos (Microsynth) at 95°C for 5 min, followed by annealing at RT for 2h and subsequently ligation with T4 ligase (NEB) into the BsmBI-digested (Fermantas) backbone. Cloning of sgRNAs into the pX330.puro backbone was performed similarly by ligating the previously annealed oligos into the BbsI-HF-digested backbone with T4 ligase (NEB). KB2P tumor-derived cells were transduced with the cloned lentiCRISPR v2 constructs and KB1P cells were transfected with the generated pX330.puro plasmids using a transfection reagent (TransIT-LT1 from Mirus) following the manufacturer's protocol. All constructs' sequences were verified by Sanger sequencing.

Lentiviral Transductions

Lentiviral stocks, pseudotyped with the VSV-G envelope, were generated by transient transfection of HEK293FT cells, as described before⁸³. Production of integration-deficient lentivirus (IDLV) stocks was carried out in a similar fashion, with the exception that the packaging plasmid contains a point mutation in the integrase gene (psPAX2, gift from Bastian Evers). Lentiviral titers were determined using the qPCR Lentivirus Titration Kit (Applied Biological Materials), following the manufacturer's instructions. Cells were incubated with lentiviral supernatants overnight in the presence of polybrene (8 µg/ml). Antibiotic selection was initiated 24h after transduction and was carried out for 3 consecutive days.

Long-Term Clonogenic Assays

Long-term clonogenic assays were always performed in 6-well plates. KB1P and KB2P tumor-derived cells were seeded at low density to avoid contact inhibition between the clones (4,000 and 3,000 cells/well, respectively). Control untreated plates were fixed with 4% formaldehyde between days 7 and 8 and treated plates between days 8 and 14. For the quantification, cells were stained with 0.1% crystal violet and analyzed in an automated manner using the ImageJ ColonyArea plugin previously described⁸⁴.

Functional Genetic Enrichment Screens

We have generated a focused shRNA library targeting the human candidate genes plus non-essential genes as controls, resulting in a total of 1025 genes. We selected 5 hairpins per gene, less when 5 weren't available, resulting in 5062 lentiviral hairpins (pLKO.1) from the Sigma Mission library (TRC 1.0 and 2.0) (**Supplementary table 5**). This library was then used to generate pools of lentiviral shRNAs which were then transduced in RPE1-hTERT *BRCA1*^{-/-};*TRP53*^{-/-} and SUM149PT human cells, as described in the section *Lentiviral Transductions*. Lentiviral transductions were carried out using a multiplicity of transduction (MOI) of 0.3, in order to ensure that each cell only gets incorporated with one only sgRNA. After transduction, the cells stably expressing integrated shRNA were selected with puromycin. After selection, cells were collected (T0) or seeded in the presence of PARPi (SUM149PT: 100.000 cells p/ 15 cm plate, 10nM olaparib; RPE1-hTERT *BRCA1*^{-/-};*TRP53*^{-/-}: 50.000 cells p/ 15 cm plate, 50nM olaparib). The total number of cells used in a single screen was calculated as following: library complexity x coverage (1000x). Triplicates were carried out for both cell lines. Cells were kept in culture for 3 weeks and medium was refreshed every 5 days. In the end of the screen, or at T0, cells were pooled and genomic DNA was extracted (QIAmp DNA Mini Kit, Qiagen). shRNA sequences were retrieved by a two-step PCR amplification, as described before²³. To maintain screening coverage, the amount of genomic DNA used as an input for the first PCR reaction was taken into account (6 µg of genomic DNA per 10⁶ genomes, 1 µg/PCR reaction). Resulting PCR products were purified using MiniElute PCR Purification Kit (Qiagen) and submitted for Illumina sequencing. Sequence alignment and dropout analysis was carried out using the algorithm MaGECK (Li et al., 2014).

DATA AND SOFTWARE AVAILABILITY

Sequencing of all functional genetic screens was performed at the Netherlands Cancer Institute and results will be made available upon request. The accession number for the raw data of WE-seq, LCWG-seq and RNA-seq reported in this chapter is European Nucleotide Archive (ENA): PRJEB25803.

REFERENCES

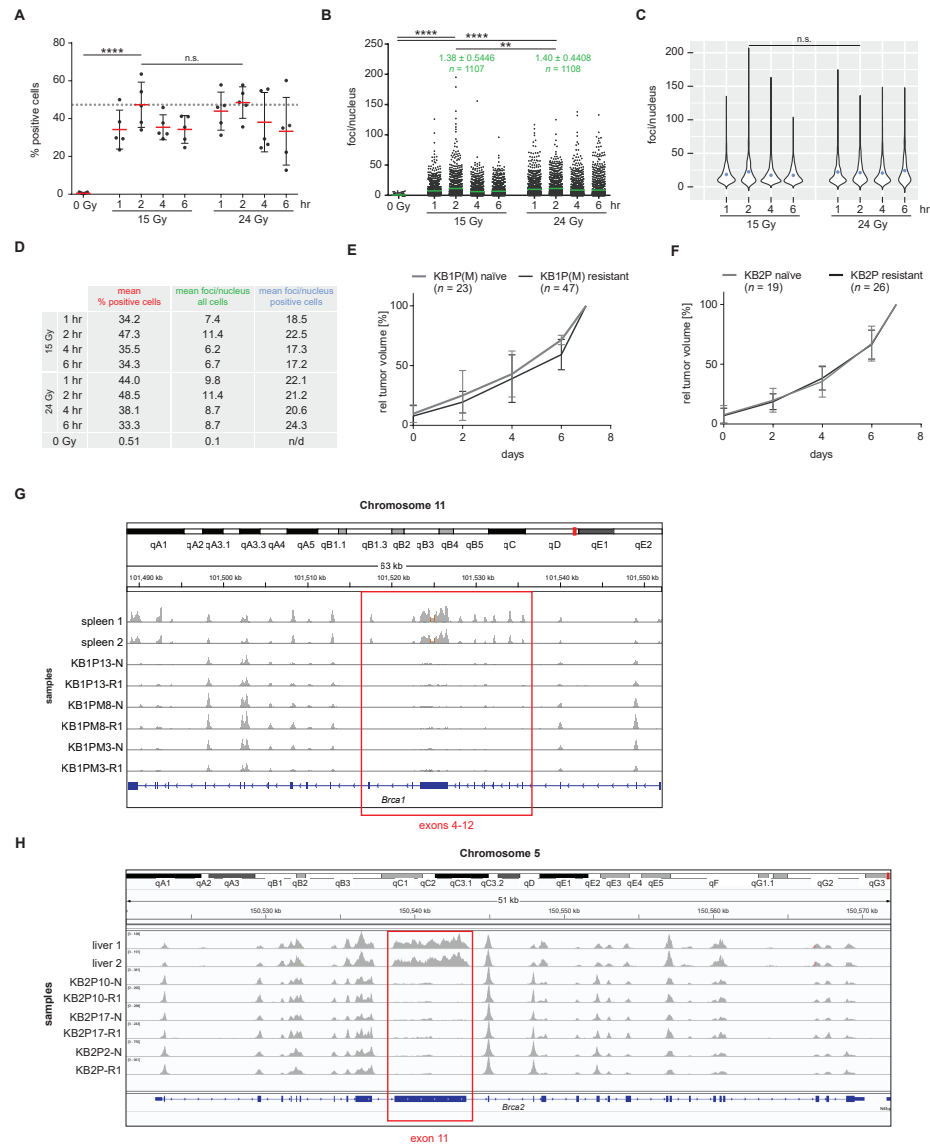
- Farmer, H. *et al.* Targeting the DNA repair defect in BRCA mutant cells as a therapeutic strategy. *Nature* **434**, 917–21 (2005).
- Bryant, H. E. *et al.* Specific killing of BRCA2-deficient tumours with inhibitors of poly(ADP-ribose) polymerase. *Nature* **434**, 913–917 (2005).
- Scully, R., Panday, A., Elango, R. & Willis, N. A. DNA double-strand break repair-pathway choice in somatic mammalian cells. *Nat. Rev. Mol. Cell Biol.* **20**, 698–714 (2019).
- Ray Chaudhuri, A. & Nussenzweig, A. The multifaceted roles of PARP1 in DNA repair and chromatin remodelling. (2017). doi:10.1038/nrm.2017.53
- Murai, J. *et al.* Trapping of PARP1 and PARP2 by clinical PARP inhibitors. *Cancer Res.* **72**, 5588–5599 (2012).
- Lupo, B. & Trusolino, L. Inhibition of poly(ADP-ribose)ylation in cancer: Old and new paradigms revisited. *Biochimica et Biophysica Acta - Reviews on Cancer* **1846**, 201–215 (2014).
- Paes Dias, M., Moser, S. C., Ganesan, S. & Jonkers, J. Understanding and overcoming resistance to PARP inhibitors in cancer therapy. *Nature Reviews Clinical Oncology* 1–19 (2021).
- Rottenberg, S. *et al.* Selective induction of chemotherapy resistance of mammary tumors in a conditional mouse model for hereditary breast cancer. *Proc. Natl. Acad. Sci. U. S. A.* **104**, 12117–12122 (2007).
- Gogola, E. *et al.* Selective Loss of PARG Restores PARylation and Counteracts PARP Inhibitor-Mediated Synthetic Lethality. *Cancer Cell* **33**, 1078–1093.e12 (2018).
- Pettitt, S. J. *et al.* A genetic screen using the PiggyBac transposon in haploid cells identifies Parp1 as a mediator of olaparib toxicity. *PLoS One* **8**, e61520 (2013).
- Pettitt, S. J. *et al.* Genome-wide and high-density CRISPR-Cas9 screens identify point mutations in PARP1 causing PARP inhibitor resistance. *Nat. Commun.* **9**, 1849 (2018).
- Murai, J. *et al.* SLFN11 Blocks Stressed Replication Forks Independently of ATR. *Mol. Cell* **69**, 371–384.e6 (2018).
- Murai, J. *et al.* Resistance to PARP inhibitors by SLFN11 inactivation can be overcome by ATR inhibition. *Oncotarget* **7**, 76534–76550 (2016).
- Cantor, S. B. & Calvo, J. A. Fork Protection and Therapy Resistance in Hereditary Breast Cancer. (2017).
- Bunting, S. F. *et al.* 53BP1 Inhibits Homologous Recombination in Brca1-Deficient Cells by Blocking Resection of DNA Breaks. *Cell* **141**, 243–254 (2010).
- Bouwman, P. *et al.* 53BP1 loss rescues BRCA1 deficiency and is associated with triple-negative and BRCA-mutated breast cancers. *Nat. Struct. Mol. Biol.* **17**, 688–695 (2010).
- Noordermeer, S. M. *et al.* The shieldin complex mediates 53BP1-dependent DNA repair. *Nature* **560**, 117–121 (2018).
- Gupta, R. *et al.* DNA Repair Network Analysis Reveals Shieldin as a Key Regulator of NHEJ and PARP Inhibitor Sensitivity. *Cell* **173**, 972–988.e23 (2018).
- Dev, H. *et al.* Shieldin complex promotes DNA end-joining and counters homologous recombination in BRCA1-null cells. *Nat. Cell Biol.* **20**, 954–965 (2018).
- Findlay, S. *et al.* SHLD 2/ FAM 35A co-operates with REV 7 to coordinate DNA double-strand break repair pathway choice. *EMBO J.* **37**, (2018).
- Gao, S. *et al.* An OB-fold complex controls the repair pathways for DNA double-strand breaks. *Nat. Commun.* **9**, 1–10 (2018).
- Tomida, J. *et al.* FAM 35A associates with REV 7 and modulates DNA damage responses of normal and BRCA1-defective cells. *EMBO J.* **37**, e99543 (2018).
- Xu, G. *et al.* REV7 counteracts DNA double-strand break resection and affects PARP inhibition. *Nature* **521**, 541–544 (2015).
- Boersma, V. *et al.* MAD2L2 controls DNA repair at telomeres and DNA breaks by inhibiting 5' end resection. *Nature* **521**, 537–40 (2015).
- Chapman, J. R. *et al.* RIF1 Is Essential for 53BP1-Dependent Nonhomologous End Joining and Suppression of DNA Double-Strand Break Resection. *Mol. Cell* **49**, 858–871 (2013).
- Feng, L. *et al.* Cell cycle-dependent inhibition of 53BP1 signaling by BRCA1. *Cell Discov.* **1**, 15019 (2015).
- Di Virgilio, M. *et al.* Rif1 prevents resection of DNA breaks and promotes immunoglobulin class switching. *Science (80-.)*. **339**, 711–715 (2013).
- Zimmermann, M., Lottersberger, F., Buonomo, S. B., Sfeir, A. & de Lange, T. 53BP1 Regulates DSB Repair Using Rif1 to Control 5' End Resection. *Science (80-.)*. **339**, 700–704 (2013).
- Escribano-Díaz, C. *et al.* A cell cycle-dependent regulatory circuit composed of 53BP1-RIF1 and BRCA1-CtIP controls DNA repair pathway choice. *Mol. Cell* **49**, 872–83 (2013).
- Ghezraoui, H. *et al.* 53BP1 cooperation with the REV7–shieldin complex underpins DNA structure-specific NHEJ. *Nature* **560**, 122–127 (2018).
- Ganesan, S. Tumor Suppressor Tolerance: Reversion Mutations in BRCA1 and BRCA2 and Resistance to PARP

- Inhibitors and Platinum. *JCO Precis. Oncol.* 1–4 (2018).
32. Barber, L. J. *et al.* Secondary mutations in BRCA2 associated with clinical resistance to a PARP inhibitor. *J. Pathol.* **229**, 422–9 (2013).
 33. Weigelt, B. *et al.* Diverse BRCA1 and BRCA2 Reversion Mutations in Circulating Cell-Free DNA of Therapy-Resistant Breast or Ovarian Cancer. *Clin. Cancer Res.* **23**, 6708–6720 (2017).
 34. Domchek, S. M. Reversion Mutations with Clinical Use of PARP Inhibitors: Many Genes, Many Versions. *Cancer Discov.* **7**, 937–939 (2017).
 35. Norquist, B. *et al.* Secondary somatic mutations restoring BRCA1/2 predict chemotherapy resistance in hereditary ovarian carcinomas. *J. Clin. Oncol.* **29**, 3008–3015 (2011).
 36. Ang, J. E. *et al.* Efficacy of chemotherapy in BRCA1/2 mutation carrier ovarian cancer in the setting of PARP inhibitor resistance: a multi-institutional study. *Clin. Cancer Res.* **19**, 5485–93 (2013).
 37. Litton, J. K. *et al.* Neoadjuvant Talazoparib for Patients With Operable Breast Cancer With a Germline BRCA Pathogenic Variant. *J. Clin. Oncol.* **38**, 388–394 (2020).
 38. Jaspers, J. E. *et al.* Loss of 53BP1 causes PARP inhibitor resistance in BRCA1-mutated mouse mammary tumors. *Cancer Discov.* **3**, 68–81 (2013).
 39. Jonkers, J. *et al.* Synergistic tumor suppressor activity of BRCA2 and p53 in a conditional mouse model for breast cancer. *Nat. Genet.* **29**, 418–425 (2001).
 40. Liu, X. *et al.* Somatic loss of BRCA1 and p53 in mice induces mammary tumors with features of human BRCA1-mutated basal-like breast cancer. *Proc. Natl. Acad. Sci.* **104**, 12111–12116 (2007).
 41. Ray Chaudhuri, A. *et al.* Replication fork stability confers chemoresistance in BRCA-deficient cells. *Nature* **535**, 382–387 (2016).
 42. Oplustil O'Connor, L. *et al.* The PARP Inhibitor AZD2461 Provides Insights into the Role of PARP3 Inhibition for Both Synthetic Lethality and Tolerability with Chemotherapy in Preclinical Models. *Cancer Res.* **76**, 6084–6094 (2016).
 43. Godin, S. K., Sullivan, M. R. & Bernstein, K. A. Novel insights into RAD51 activity and regulation during homologous recombination and DNA replication. *Biochem. Cell Biol.* **94**, 407–418 (2016).
 44. de Ronde, J. J., Rigail, G., Rottenberg, S., Rodenhuis, S. & Wessels, L. F. A. Identifying subgroup markers in heterogeneous populations. *Nucleic Acids Res.* **41**, e200–e200 (2013).
 45. Kas, S. M. *et al.* Transcriptomics and Transposon Mutagenesis Identify Multiple Mechanisms of Resistance to the FGFR Inhibitor AZD4547. *Cancer Res.* **78**, 5668–5679 (2018).
 46. Rondinelli, B. *et al.* EZH2 promotes degradation of stalled replication forks by recruiting MUS81 through histone H3 trimethylation. *Nat. Cell Biol.* **19**, 1371–1378 (2017).
 47. van Dyk, E., Hoogstraat, M., Ten Hoeve, J., Reinders, M. J. T. & Wessels, L. F. A. RUBIC identifies driver genes by detecting recurrent DNA copy number breaks. *Nat. Commun.* **7**, 12159 (2016).
 48. Ritchie, M. E. *et al.* limma powers differential expression analyses for RNA-sequencing and microarray studies. *Nucleic Acids Res.* **43**, e47–e47 (2015).
 49. Bhattacharya, A. *et al.* Transcriptional effects of copy number alterations in a large set of human cancers. *Nat. Commun.* **11**, 1–12 (2020).
 50. Bashashati, A. *et al.* DriverNet: uncovering the impact of somatic driver mutations on transcriptional networks in cancer. *Genome Biol.* **13**, R124–R124 (2012).
 51. Ludwig, T., Chapman, D. L., Papaioannou, V. E. & Efstratiadis, A. Targeted mutations of breast cancer susceptibility gene homologs in mice: lethal phenotypes of Brca1, Brca2, Brca1/Brca2, Brca1/p53, and Brca2/p53 nullizygous embryos. *Genes Dev.* **11**, 1226–1241 (1997).
 52. Nacson, J. *et al.* BRCA1 Mutation-Specific Responses to 53BP1 Loss-Induced Homologous Recombination and PARP Inhibitor Resistance. *Cell Rep.* **24**, 3513–3527.e7 (2018).
 53. Belotserkovskaya, R. *et al.* PALB2 chromatin recruitment restores homologous recombination in BRCA1-deficient cells depleted of 53BP1. *Nat. Commun.* **11**, 1–11 (2020).
 54. Barazas, M. *et al.* The CST Complex Mediates End Protection at Double-Strand Breaks and Promotes PARP Inhibitor Sensitivity in BRCA1-Deficient Cells. *Cell Rep.* **23**, 2107–2118 (2018).
 55. Cruz, C. *et al.* RAD51 foci as a functional biomarker of homologous recombination repair and PARP inhibitor resistance in germline BRCA-mutated breast cancer. *Ann. Oncol.* **29**, 1203–1210 (2018).
 56. Waks, A. G. *et al.* Reversion and non-reversion mechanisms of resistance to PARP inhibitor or platinum chemotherapy in BRCA1/2-mutant metastatic breast cancer. *Ann. Oncol.* **31**, 590–598 (2020).
 57. Duarte, A. A. *et al.* BRCA-deficient mouse mammary tumor organoids to study cancer-drug resistance. *Nat. Methods* **15**, 134–140 (2018).
 58. Pantelidou, C. *et al.* PARP Inhibitor Efficacy Depends on CD8 + T-cell Recruitment via Intratumoral STING Pathway Activation in BRCA-Deficient Models of Triple-Negative Breast Cancer. *Cancer Discov.* **9**, 722–737 (2019).
 59. Jiao, S. *et al.* PARP Inhibitor Upregulates PD-L1 Expression and Enhances Cancer-Associated Immunosuppression. *Clin. Cancer Res.* **23**, 3711–3720 (2017).
 60. Ding, L. *et al.* PARP Inhibition Elicits STING-Dependent Antitumor Immunity in Brca1-Deficient Ovarian Cancer.

- Cell Rep.* **25**, 2972–2980.e5 (2018).
61. Shen, J. *et al.* PARPi Triggers the STING-Dependent Immune Response and Enhances the Therapeutic Efficacy of Immune Checkpoint Blockade Independent of BRCAness. *Cancer Res.* **79**, 311–319 (2019).
 62. Szklarczyk, D. *et al.* The STRING database in 2021: customizable protein-protein networks, and functional characterization of user-uploaded gene/measurement sets. *Nucleic Acids Res.* **49**, D605–D612 (2021).
 63. Merico, D., Isserlin, R., Stueker, O., Emili, A. & Bader, G. D. Enrichment Map: A Network-Based Method for Gene-Set Enrichment Visualization and Interpretation. *PLoS One* **5**, e13984 (2010).
 64. Evers, B. *et al.* Selective Inhibition of BRCA2-Deficient Mammary Tumor Cell Growth by AZD2281 and Cisplatin. *Clin. Cancer Res.* **14**, 3916–3925 (2008).
 65. Martin, M. Cutadapt removes adapter sequences from high-throughput sequencing reads. *EMBnet.journal* **17**, 10 (2011).
 66. Li, H. Aligning sequence reads, clone sequences and assembly contigs with BWA-MEM. (2013).
 67. Garrison, E. & Marth, G. Haplotype-based variant detection from short-read sequencing. (2012).
 68. Cingolani, P. *et al.* A program for annotating and predicting the effects of single nucleotide polymorphisms, SnpEff: SNPs in the genome of *Drosophila melanogaster* strain w1118; iso-2; iso-3. *Fly (Austin)*. **6**, 80–92 (2012).
 69. Keane, T. M. *et al.* Mouse genomic variation and its effect on phenotypes and gene regulation. *Nat.* 2011 4777364 **477**, 289–294 (2011).
 70. Scheinin, I. *et al.* DNA copy number analysis of fresh and formalin-fixed specimens by shallow whole-genome sequencing with identification and exclusion of problematic regions in the genome assembly. *Genome Res.* **24**, 2022–2032 (2014).
 71. Dobin, A. *et al.* STAR: ultrafast universal RNA-seq aligner. *Bioinformatics* **29**, 15–21 (2013).
 72. Liao, Y., Smyth, G. K. & Shi, W. featureCounts: an efficient general purpose program for assigning sequence reads to genomic features. *Bioinformatics* **30**, 923–930 (2013).
 73. Robinson, M. D., McCarthy, D. J. & Smyth, G. K. edgeR: a Bioconductor package for differential expression analysis of digital gene expression data. *Bioinformatics* **26**, 139–140 (2010).
 74. Law, C. W., Chen, Y., Shi, W. & Smyth, G. K. voom: Precision weights unlock linear model analysis tools for RNA-seq read counts. *Genome Biol.* **15**, R29–R29 (2014).
 75. Prakash, R., Zhang, Y., Feng, W. & Jasin, M. Homologous recombination and human health: The roles of BRCA1, BRCA2, and associated proteins. *Cold Spring Harb. Perspect. Biol.* **7**, (2015).
 76. Stark, C. *et al.* BioGRID: a general repository for interaction datasets. *Nucleic Acids Res.* **34**, (2006).
 77. Xenarios, I. *et al.* DIP: the Database of Interacting Proteins. *Nucleic Acids Res.* **28**, 289 (2000).
 78. Goel, R., Harsha, H. C., Pandey, A. & Keshava Prasad, T. S. Human Protein Reference Database and Human Proteinpedia as Resources for Phosphoproteome Analysis. doi:10.1039/c1mb05340j
 79. Hermjakob, H. *et al.* IntAct: an open source molecular interaction database. *Nucleic Acids Res.* **32**, D452 (2004).
 80. Kotlyar, M., Pastrello, C., Sheahan, N. & Jurisica, I. Integrated interactions database: tissue-specific view of the human and model organism interactomes. *Nucleic Acids Res.* **44**, D536–D541 (2016).
 81. Zingg, D. *et al.* Truncated FGFR2 is a clinically actionable oncogene in multiple cancers. *Nat.* 2022 1–9 (2022).
 82. Cox, J. *et al.* Accurate proteome-wide label-free quantification by delayed normalization and maximal peptide ratio extraction, termed MaxLFQ. *Mol. Cell. Proteomics* **13**, 2513–2526 (2014).
 83. Follenzi, A., Ailles, L. E., Bakovic, S., Geuna, M. & Naldini, L. Gene transfer by lentiviral vectors is limited by nuclear translocation and rescued by HIV-1 pol sequences. *Nat. Genet.* **25**, 217–222 (2000).
 84. Guzmán, C., Bagga, M., Kaur, A., Westermarck, J. & Abankwa, D. ColonyArea: an ImageJ plugin to automatically quantify colony formation in clonogenic assays. *PLoS One* **9**, (2014).

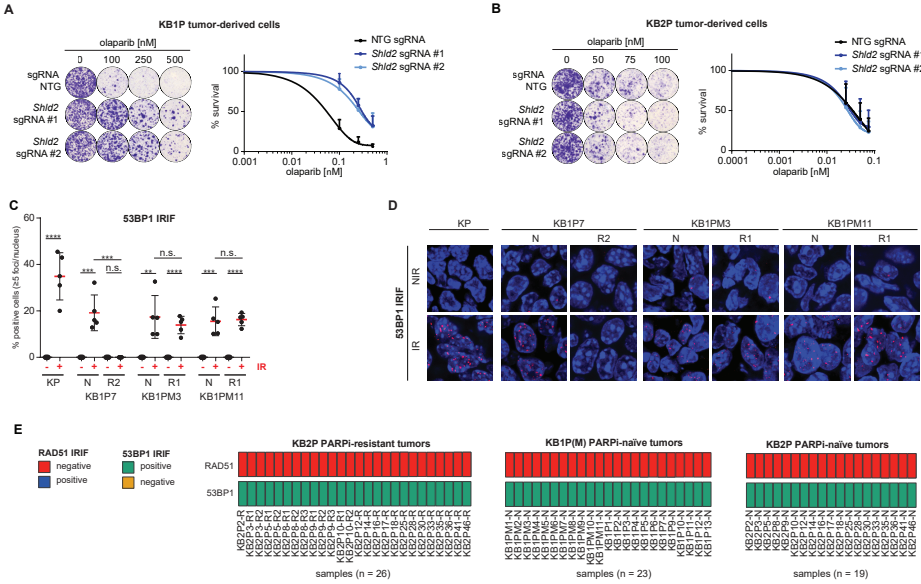
SUPPLEMENTARY FILES

Supplementary Tables 1-5 are available in the online version of the paper.

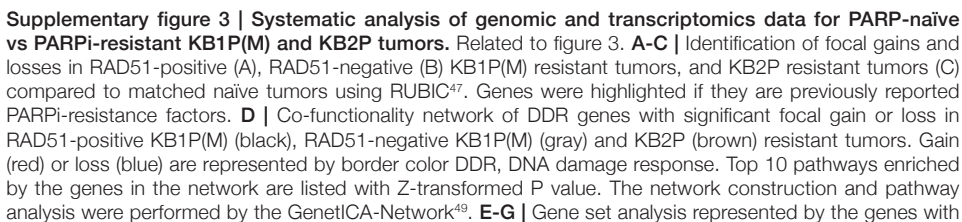


Supplementary figure 1 | Optimization of the RAD51 IRIF formation assay. Related to figure 1. A | Percentage of RAD51 positive cells (>5 foci/nucleus) per tumor area (single data point) in a KP tumor irradiated with 0, 15 or 24 Gy, 1-6 hr post-irradiation; **** $p < 0.0001$, n.s. not significant (two-tailed Mann-Whitney U test); data shown as mean (red line) \pm SD of a replicate, the experiment was repeated twice; grey dotted line indicates the mean value of a sample irradiated with 15 Gy and incubated for 2 hr. **B |** Number of foci per nucleus (single data point) quantified for the total tumor cell population of a KP described in (A); mean values are represented by green lines; ** $p < 0.01$, statistical analysis as in (A). **C |** Number of foci per nucleus quantified for positive cell population (>5 foci/nucleus) of a KP tumor described in (A), and represented as violin plots showing the density (width = frequency) of the data; mean values are represented by blue dots; statistical

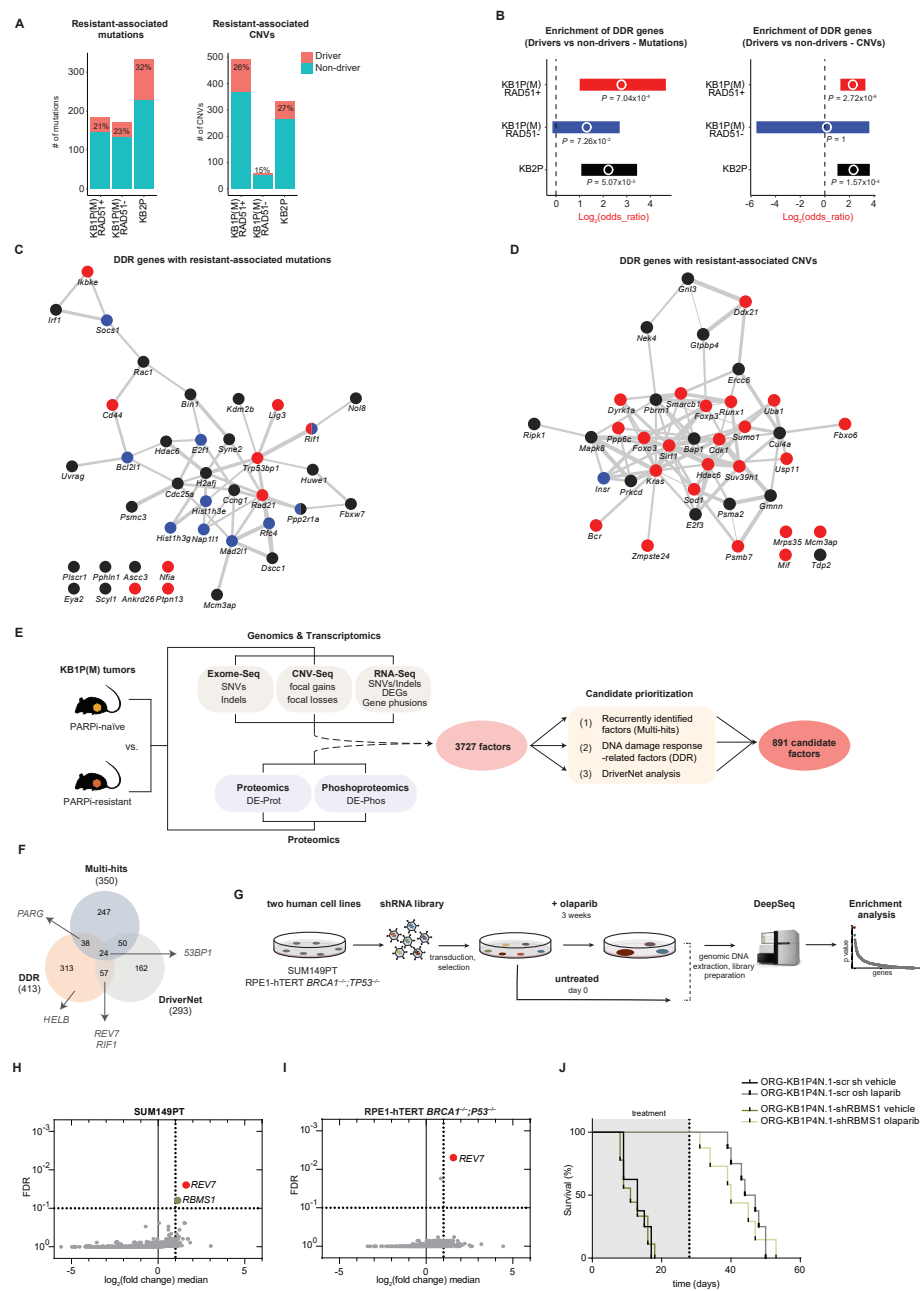
analysis as in (A). **D** | Summary of analyses represented in (A-C). **E-F** | Growth curves of KB1P(M) (E) and KB2P (F) tumors, samples were irradiated at day 7. **G-H** | Visualization of exome sequencing reads for the *Brca1* (G) and *Brca2* (H) genes in KB1P(M) and KB2P tumor samples, respectively; and normal tissues (spleen 1/2 and liver 1/2; controls), showing that deletions of specific exons (marked in red; *Brca1* – exons 4-12 (GRCm38, previously referred to as exons 5-13⁴⁰, *Brca2* – exon 11) are preserved in PARPi-naïve and PARPi-resistant tumor samples; data representative for the whole KB1P(M) and KB2P tumor panels.



Supplementary figure 2 | *Trp53bp1* gene expression correlates with 53BP1 IRIF. Related to figure 2. **A-B** | Representative images (left) and quantification (right) of clonogenic assays in the presence of olaparib in KB1P (A) and KB2P (B) tumor-derived cells modified by CRISPR-Cas9 with the indicated sgRNAs. Control untreated plates were harvested on day 7/8 and treated plates on day 14. Statistical analysis was performed using 2-way ANOVA followed by Dunnett's test. * $p < 0.05$, ** $p < 0.01$, *** $p < 0.001$. **C-D** | Representative images (A) and quantification (B) of 53BP1 IRIFs for the different matched KB1P(M) tumor pairs; IR – irradiated, NIR – non irradiated; scale bar, 100 μ m; data in (B) represented as percentage of positive cells (≥ 5 foci/nucleus) per imaged area (single data point, typically 100-200 cells/area); **** $p < 0.0001$, *** $p < 0.001$, ** $p < 0.01$, n.s. not significant (two-tailed Mann-Whitney U test). **E** | Outcome of the RAD51 and 53BP1 IRIF assays for PARPi-resistant KB2P tumors and for PARPi-naïve KB1P(M) and KB2P tumors; N – naïve; R – resistant.

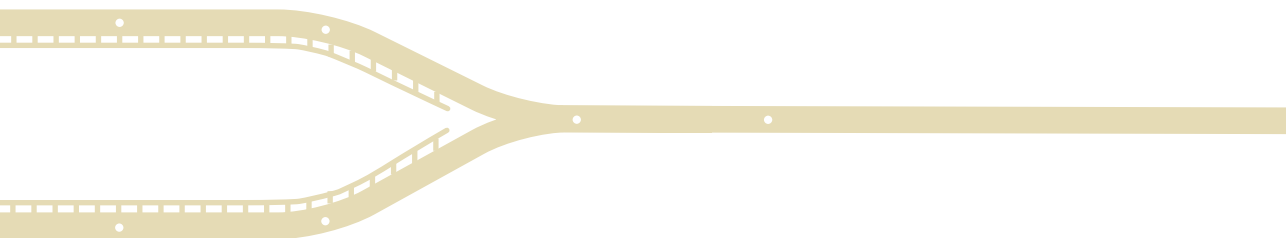


significant focal gain or loss in PARPi-resistant RAD51-positive KB1P(M) (E), RAD51-negative KB1P(M) (F) and KB2P (G) tumors, detected by RUBIC. Because only focal losses were detected in RAD51-positive KB1P(M) resistant tumors, gene set analysis was performed for the genes with focal losses (blue). For RAD51-negative KB1P(M) resistant tumors, only one focal gain was detected, gene set analysis was therefore performed only for the genes with focal gain (red). KB2P tumors showed three focal losses and one focal gain. The focal gain only encoded mostly for non-protein-coding genes with the exception of three genes and thus gene set analysis was performed only for the genes encoded by the areas of focal losses. The gene sets with $P < 0.01$ (fisher's exact test) were presented. **H-J** | Volcano plots of differentially expressed genes (DEGs) in PARPi-naïve vs PARPi-resistant RAD51-positive KB1P(M) (H), RAD51-negative KB1P(M) (I) and KB2P (J) tumors. Genes were highlighted if they are previously reported PARPi-resistance factors.



Supplementary figure 4 | In vitro loss-of-function screens fail to validate candidate drivers of in vivo PARPi resistance. Related to figure 4. **A** | Bar plot representing the number of driver and non-driver genes with high impact on expression of neighbors in a protein-protein interaction network. Driver potential was assessed for the genes with resistance-specific mutations (left) and copy number variations (right) by DriverNet⁵⁰. **B** | Enrichment of DDR genes in the identified drivers from each resistant tumor group. Log2 odd ratios (proportion of DDR genes in driver genes vs non-driver genes) were presented with 95% confidence intervals. P-values

were computed by fisher's exact test. **C-D** | DDR genes identified as drivers from resistance-associated mutations (C) and CNVs (D) were presented in the co-functionality networks. **E** | Schematic diagram showing the process of prioritizing candidate genes for functional screening. To enrich for plausible resistance driver genes, candidates were selected if (1) identified independently by at least two analyses ('multi-hits'), or (2) implicated in the DDR, or (3) identified as high-impact drivers in the protein-protein network using DriverNet⁵⁰. The latter identifies genes which impact the expression of interacting partners or factors that share the same biological pathway and was used to correct for the fact that frequency analyses integrating data across different omic platforms ('multi-hits') fails to identify events restricted to one biochemical domain (e.g., mutation or phosphorylation), but nonetheless important for driving resistance 50. WE-seq, LCWG-seq and RNA-seq analysis was included for all tumor collections, including tumors whose RAD51-IRIF status was not determined in KB1P(M) (68 for resistant and 43 for naïve tumors), and proteomics and phosphoproteomics data was generated for some of the KB1P(M) tumors (12 for resistant and 12 for naïve tumors). **F** | Venn diagram representing the number of genes identified in candidate prioritization analysis. Genes were highlighted if they are previously reported PARPi-resistance factors. **G** | Outline of functional genetic enrichment screen. Screen was performed in SUM149PT and RPE1-hTERT *BRCA1*^{-/-};*TP53*^{-/-} cells. Surviving cells were collected after 3 weeks and analysis and hit selection was performed using the MaGECK algorithm (Li et al., 2014). **H-I** | Plot of distribution log2ratio (fold change (treated versus untreated)) median for all genes versus false discovery rate (FDR) for the screen carried out in SUM149PT (H) and in RPE1-hTERT *BRCA1*^{-/-};*TP53*^{-/-} (I) cells. **J** | Kaplan–Meier survival curves of mice transplanted with ORG-KB1P4N.1 tumoroids lines modified with indicated shRNA and treated with 100 mg/kg olaparib. End of treatment (28 days) is indicated by a dotted line.



Chapter 4

Loss of nuclear DNA ligase III reverts PARP inhibitor resistance in BRCA1/53BP1 double-deficient cells by exposing ssDNA gaps

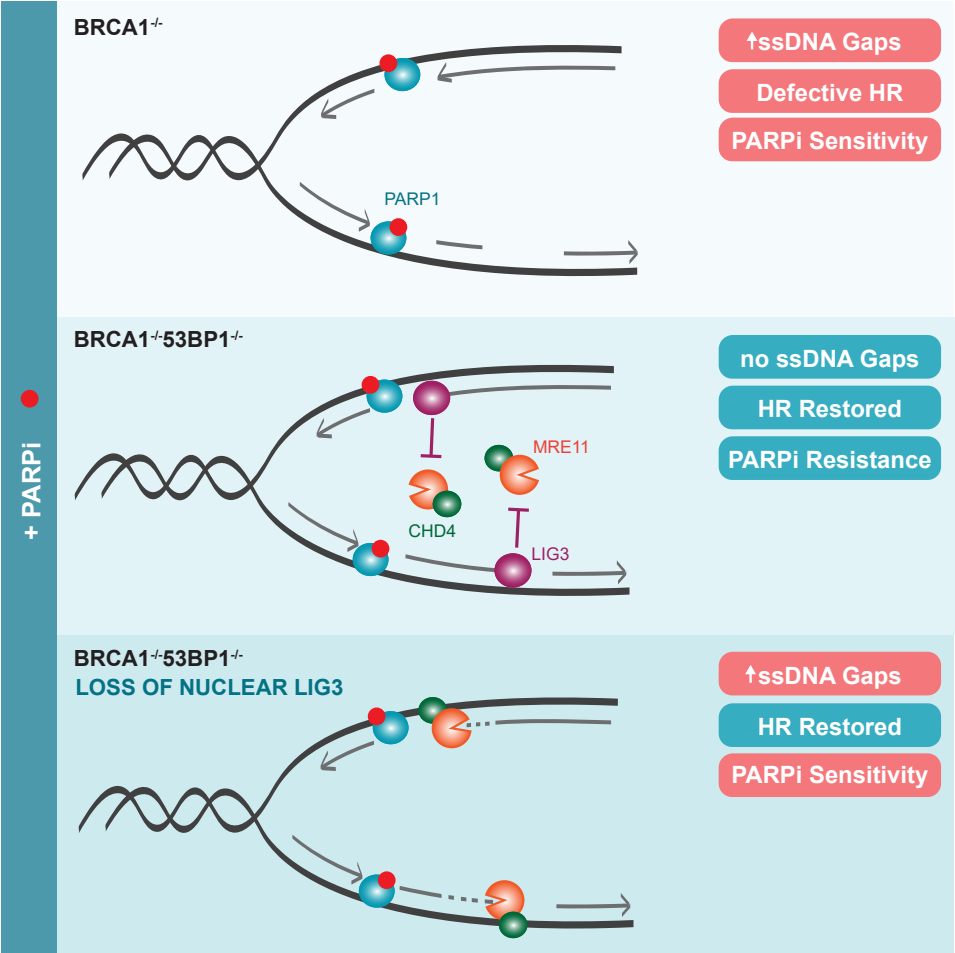
Mariana Paes Dias^{*}, Vivek Tripathi^{*}, Ingrid van der Heijden, Ke Cong, Eleni-Maria Manolika, Jinhyuk Bhin, Ewa Gogola, Panagiotis Galanos, Stefano Annunziato, Cor Liefink, Miguel Andujar-Sanchez, Sanjiban Chakrabarty, Graeme C.M. Smith, Marieke van de Ven, Roderick L. Beijersbergen, Jirina Bartkova, Sven Rottenberg, Sharon Cantor, Jiri Bartek, Arnab Ray Chaudhuri and Jos Jonkers

^{}equal contribution*

ABSTRACT

Inhibitors of poly(ADP-ribose) (PAR) polymerase (PARPi) have entered the clinic for the treatment of homologous recombination (HR)-deficient cancers. Despite the success of this approach, preclinical and clinical research with PARPi has revealed multiple resistance mechanisms, highlighting the need for identification of novel functional biomarkers and combination treatment strategies. Functional genetic screens performed in cells and organoids that acquired resistance to PARPi by loss of 53BP1 identified loss of LIG3 as an enhancer of PARPi toxicity in BRCA1-deficient cells. Enhancement of PARPi toxicity by LIG3 depletion is dependent on BRCA1 deficiency but independent of the loss of 53BP1 pathway. Mechanistically, we show that LIG3 loss promotes formation of MRE11-mediated post-replicative ssDNA gaps in BRCA1-deficient and BRCA1/53BP1 double-deficient cells exposed to PARPi, leading to an accumulation of chromosomal abnormalities. LIG3 depletion also enhances efficacy of PARPi against BRCA1-deficient mammary tumors in mice, suggesting LIG3 as a potential therapeutic target.

Graphical abstract



INTRODUCTION

Defects in DNA repair result in genome instability and thereby contribute to the development and progression of cancer. Alterations in high-fidelity DNA repair genes lead to a greater reliance on compensatory error-prone repair pathways for cellular survival. This does not only result in the accumulation of tumor-promoting mutations, but also provides cancer-specific vulnerabilities that can be exploited for targeted cancer therapy. The first example of such targeted approach was the use of poly(ADP-ribose) polymerase (PARP) inhibitors (PARPi) in the treatment of *BRCA1* or *BRCA2* deficient tumors defective in the error-free repair of DNA double-strand breaks (DSBs) through homologous recombination (HR)^{1,2}.

PARP1, which is the main target for PARPi is involved in various cellular processes, including the sensing of DNA single-strand breaks (SSBs), repair of DNA DSBs, stabilization of replication forks (RFs), chromatin remodeling (reviewed in ³) and the sensing of unligated Okazaki fragments during DNA replication⁴. Upon DNA damage, PARP1 is rapidly recruited to sites of DNA damage where it post-translationally modifies substrate proteins by synthesizing poly(ADP-ribose) (PAR) chains via PARylation. PARP1 itself is also a target of PARylation and the resulting PAR chains serve to recruit downstream repair factors. AutoPARylation of PARP1 also enhances its release from DNA, which is essential for various DNA repair processes⁵.

PARPi act not only through catalytic inhibition of PARP1, but also via trapping of PARP1 onto chromatin, resulting in RF collapse⁶⁻⁸. PARPi-treated *BRCA1/2*-defective cells can only employ error-prone repair to resolve DSBs caused by RF collapse, resulting in accumulation of chromosomal aberrations and cell death by mitotic catastrophe⁹. Successful clinical trials have resulted in approval of PARPi for treatment of patients with *BRCA1/2*-mutant ovarian and breast cancers¹⁰.

Despite the success of PARPi, multiple mechanisms of resistance have been identified, including upregulation of drug efflux transporters¹¹, PARP1 downregulation/inactivation/mutation¹², loss of PAR glycohydrolase¹³ or restoration of RF protection in the absence of *BRCA1/2*¹⁴. However, the best-studied PARPi resistance mechanisms involve restoration of HR activity via re-activation of *BRCA1/2* function or via loss of factors that govern DSB end-protection in *BRCA1*-deficient cells¹⁰. The latter may be achieved by loss of components of the 53BP1-RIF1-REV7-Shieldin complex¹⁵⁻²³.

Importantly, drug resistance often comes at a fitness cost due to collateral vulnerabilities which can be exploited therapeutically. For example, PARG inactivation causes PARPi resistance but results in increased sensitivity to ionizing radiation (IR) and temozolomide¹³. Similarly, *BRCA1*-deficient tumors that acquired PARPi resistance via 53BP1 loss are more radiosensitive²⁴. In this study, we identified DNA ligase III (LIG3), a known DNA repair factor²⁵⁻²⁸, as a collateral vulnerability of *BRCA1*-deficient cells with acquired PARPi resistance due to loss of DSB end-protection.

RESULTS

Functional genetic dropout screens identify LIG3 as a modulator of PARPi-resistance in BRCA1/53BP1 double-deficient cells

To identify acquired vulnerabilities in BRCA1-deficient cells which developed PARPi resistance via BRCA1-independent restoration of HR, we carried out functional genetic dropout screens in two types of cellular models deficient for BRCA1, p53 and 53BP1. The first screen was performed in genetically well-defined *Brca1*^{-/-};*Trp53*^{-/-};*Trp53bp1*^{-/-} mouse embryonic stem cells (ES-B1P.R mESCs) (**Supplementary Fig. 1A**). The second screen was performed in *Brca1*^{-/-};*Trp53*^{-/-};*Trp53bp1*^{-/-} tumor organoids (ORG-KB1P.R), derived from a *K14cre;Brca1*^{F/F};*Trp53*^{F/F} (KB1P) mouse mammary tumor that acquired resistance to PARPi *in vivo* due to loss of 53BP1 function²⁹ (**Supplementary Fig. 1A**). Both cellular models were transduced with a lentiviral library of 1,976 short hairpin RNA (shRNA) constructs targeting 391 DNA damage response (DDR) related genes^{13,15}. Cells were either mock treated or selected for 3 weeks in the presence of the PARPi olaparib (**Fig. 1A**). Olaparib selection was carried out at 25nM in ES-B1P.R mESCs and 50nM in ORG-KB1P.R organoids, concentrations which do not affect the viability of resistant cells, but are lethal to the corresponding PARPi-sensitive cells. Sequencing of the shRNAs in the surviving cells revealed a specific and reproducible dropout of hairpins targeting *Lig3* in the olaparib-treated cell population in both ES-B1P.R mESCs and ORG-KB1P.R organoids (**Fig. 1B**, **Supplementary Fig. 1B** and **Supplementary Tab. 1**). Furthermore, *Lig3* was observed to be the only common significant dropout gene identified across both screens (**Fig. 1C**). We therefore decided to investigate further whether LIG3 would constitute a useful target for the reversion of PARPi resistance in BRCA1-deficient cells.

Depletion of LIG3 increases the sensitivity to PARPi, independent of 53BP1 loss

To validate the findings of our shRNA screens, we carried out viability assays using shRNA-mediated depletion of LIG3 in ORG-KB1P.R organoids. LIG3 depletion significantly increased the sensitivity to olaparib when compared to the parental cells (**Fig. 1D** and **Supplementary Fig. 1C**). Increased sensitivity to olaparib was also observed upon depletion of LIG3 in PARPi-resistant KB1P.R cells, derived from an independent PARPi-resistant KB1P tumor with 53BP1 loss (Jaspers et al. 2013) (**Supplementary Fig. 1A,D,E**). These results confirm that depletion of LIG3 results in re-sensitization of BRCA1/53BP1 double-deficient cells to PARPi. Furthermore, depletion of LIG3 also reverted the resistance to olaparib in *Brca1*^{-/-};*Trp53*^{-/-} KB1P.S mammary tumor cells depleted of REV7, a downstream partner of 53BP1^{15,16} (**Supplementary Fig. 1A,F,G**), indicating that LIG3-mediated resistance is not exclusive for 53BP1-deficient cells.

We next asked whether LIG3 depletion would also increase the PARPi sensitivity of treatment-naïve BRCA1-deficient tumor cells with functional 53BP1. To test this, we used *Brca1*^{-/-};*Trp53*^{-/-} organoids, from here onwards refer to as ORG-KB1P.S, and KB1P.S cells

derived from independent PARPi-naïve KB1P tumors (**Supplementary Fig. 1A**)^{29,30}. In both cellular models, shRNA-mediated depletion of LIG3 resulted in increased sensitivity to olaparib (**Fig. 1E** and **Supplementary Fig. 1C,H,I**). Corroborating our findings, depletion of LIG3 also resulted in increased sensitivity to olaparib in the human *BRCA1*-mutant breast cancer cell line SUM149PT (**Supplementary Fig. 1J,K**). Importantly, our results were not restricted to olaparib, as LIG3 depletion also increased the sensitivity of KB1P.S cells to the PARPi talazoparib and veliparib (**Supplementary Fig. 1L**).

PARPi sensitization of cells by LIG3 depletion is dependent on BRCA1 status

Next, we sought to investigate whether the increased PARPi sensitivity of LIG3-depleted cells is BRCA1-dependent. shRNA-mediated depletion of LIG3 in *Trp53*^{-/-} organoids (ORG-KP), derived from *K14cre;Trp53^{F/F}* (KP) mouse mammary tumors (**Supplementary Fig. 1A**)²⁹, slightly increased the sensitivity to PARPi, but only at a high concentration of 10μM (**Fig. 1F** and **Supplementary Fig. 2A,B**). To corroborate these data, we validated the effect of LIG3 depletion in *R26^{creERT2};Brca1^{Sc0/-};Trp53^{-/-};Trp53bp1^{-/-}* mESCs (ES-P.R). Addition of 4-hydroxytamoxifen (4OHT) to ES-P.R mESCs induces cre-mediated deletion of the remaining *Brca1* allele, resulting in *R26^{creERT2};Brca1^{-/-};Trp53^{-/-};Trp53bp1^{-/-}* mESCs (ES-B1P.R), deficient for BRCA1 (**Fig. 1G** and **Supplementary Fig. 1A**)¹⁷. Since these mESCs are deficient for p53 and 53BP1, no difference in olaparib sensitivity was observed between the BRCA1-proficient ES-P.R and the BRCA1-deficient ES-B1P.R mESCs (**Fig. 1H** and **Supplementary Fig. 2C-F**). shRNA-mediated depletion of LIG3 did not affect cell proliferation in untreated ES-P or ES-B1P.R mESCs. However, LIG3 depletion did result in increased olaparib sensitivity in ES-B1P.R cells, compared to unmodified cells (**Fig. 1H** and **Supplementary Fig. 2E,F**). To investigate whether the effect was independent of the loss of 53BP1, we repeated this experiment in 53BP1-proficient *R26^{creERT2};Brca1^{Sc0/-};Trp53^{-/-}* mESCs (ES-P) (**Supplementary Fig. 1A** and **2C,D,G**). Depletion of LIG3 increased the sensitivity to PARPi in BRCA1-deficient ES-B1P.S cells but not in BRCA1-proficient ES-P cells (**Supplementary Fig. 2H-J**).

Additionally, we tested depletion of LIG3 in three isogenic human TERT-immortalized retinal pigment epithelial (RPE1) cell lines with engineered loss of *TP53* (RPE1-P), *TP53+BRCA1* (RPE1-B1P.S), or *TP53+BRCA1+TP53BP1* (RPE1-B1P.R) (**Supplementary Fig. 1A**). In line with the data observed in mouse cells, shRNA-mediated depletion of LIG3 only increased sensitivity to olaparib in RPE1-P cells at a higher concentration of 1μM, but rendered RPE1-B1P.R cells as sensitive to olaparib as the RPE1-B1P.S cells (**Fig. 1I** and **Supplementary Fig. 2K,L**). In addition, depletion of LIG3 further increased sensitivity of RPE1-B1P.S cells to olaparib (**Fig. 1I** and **Supplementary Fig. 2K,L**).

Finally, we asked if loss of LIG3 also results in hypersensitization of BRCA2-deficient cells to PARPi. To test this, we used *Brca2*^{-/-}; *Trp53*^{-/-} (KB2P) cells derived from a *K14cre;Brca2^{F/F};Trp53^{F/F}* (KB2P) mouse mammary tumor³¹ (**Supplementary Fig. 1A**). shRNA-mediated depletion of LIG3 in KB2P cells resulted in an increase in olaparib sensitivity that was modest

compared to the profound increase observed in KB1P cells (**Supplementary Fig. 2M,N**). In addition, we depleted LIG3 in BRCA2-proficient human DLD1 cells and an isogenic derivative in which *BRCA2* was deleted (DLD1-B2KO). We did not observe a significant increase in sensitivity to olaparib in the BRCA2-deficient DLD1-B2KO cells after depletion of LIG3 (**Supplementary Fig. 2O,P**). In line with the previous data, depletion of LIG3 in DLD1 cells only resulted in increased olaparib sensitivity at a high concentration of 2.5 μ M (**Supplementary Fig. 2O,Q**). Taken together, our data show that LIG3 is a strong modulator of PARPi response specifically in BRCA1-deficient cells and that LIG3 depletion enhances the toxicity of PARPi in BRCA1-deficient cells which acquired resistance due to loss of DSB end-protection.

PARPi toxicity in LIG3-depleted cells is dependent on PARP1

Most PARPi, in addition to blocking the catalytic activity of PARP1, also induce toxic PARP1-DNA complexes as a result of their trapping capacity^{6,7}. To test whether PARPi-mediated PARP1 trapping contributes to PARPi toxicity in LIG3-depleted cells, we generated *Parp1* knockout isogenic derivatives of ES-P.R mESCs and verified loss of PARP1 expression by western blot (**Supplementary Fig. 3A**). Compared to cells transduced with non-targeting sgRNA (ES-P.R sgNTG), ES-P.R-*Parp1*^{-/-} cells displayed decreased levels of PAR upon PARP inhibition and/or MMS treatment¹³, confirming functional loss of PARP1 (**Supplementary Fig. 3B**). We next exposed ES-P.R sgNTG and ES-P.R-*Parp1*^{-/-} cells to 4OHT to produce BRCA1-deficient ES-B1P.R sgNTG and ES-B1P.R-*Parp1*^{-/-} mESCs, which were tested for olaparib sensitivity with or without LIG3 depletion (**Supplementary Fig. 3C-F**). shRNA-mediated depletion of LIG3 did not affect viability of ES-B1P.R sgNTG or ES-B1P.R-*Parp1*^{-/-} cells (**Supplementary Fig. 3E**). In line with the notion that PARPi cytotoxicity is mediated by PARP1 trapping^{6,32}, elimination of PARP1 resulted in reduced sensitivity of ES-B1P.R cells to olaparib (**Supplementary Fig. 3F**). Importantly, elimination of PARP1 also reduced olaparib sensitivity in LIG3-depleted ES-B1P.R cells, indicating that the effect of LIG3 depletion on PARPi sensitivity in BRCA1-deficient cells is partially mediated by PARP1 trapping.

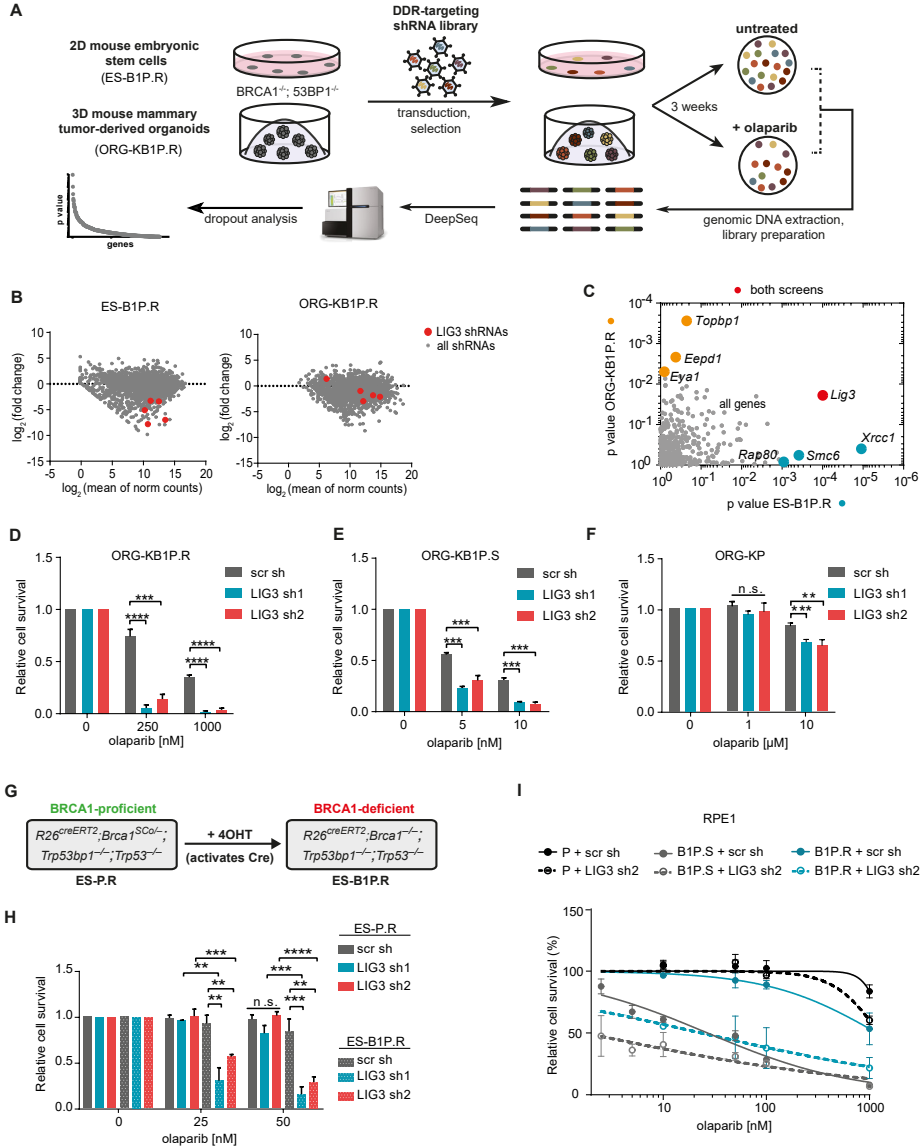


Figure 1 | Depletion of LIG3 increases sensitivity to PARPi in BRCA1-deficient cells, independent of 53BP1 loss. A | Outline of shRNA dropout screens. Screens were done at olaparib concentrations of 25 and 50 nM for ES-B1P.R and ORG-KB1P.R, respectively. **B |** Plot of log₂ ratio (fold change [treated versus untreated]) versus abundance (mean of normalized [norm] counts) of shRNAs extracted from ES-B1P.R mESCs and ORG-KB1P.R organoids treated with olaparib or left untreated for 3 weeks. To eliminate artifacts of significant cell death without PARPi, the analysis considered fold change between untreated and treated conditions and removed genes that were already depleted at T0 (day of seeding). Analyzed using MAGeCK. **C |** Comparison of the screening outcome between indicated cell lines. p value by MAGeCK. **D–F |** Quantification of long-term clonogenic assays with ORG-KB1P.R (D), ORG-KB1P.S (E), and ORG-KP organoids (F) treated with olaparib or left untreated. **G |** Schematic representation of the *Brca1* selectable conditional allele in *R26creERT2;Brca1^{SCA-/-};Trp53bp1^{-/-};Trp53^{-/-}* (ES-P.R) mESCs. Incubation of these cells with 4-hydroxytamoxifen (4OHT) induces CreERT2 recombinase, resulting in *R26creERT2;Brca1^{-/-};Trp53bp1^{-/-};Trp53^{-/-}* (ES-B1P.R) cells lacking BRCA1. **H |** Quantification of long-term clonogenic assay in ES-P.R and ES-B1P.R cells treated with olaparib. **I |** Quantification of long-term clonogenic

assays in RPE1-P, RPE1-B1P.S and RPE1-B1P.R cells treated with olaparib.

Data are represented as mean \pm SD. **p < 0.01, ***p < 0.001, and ****p < 0.0001; n.s., not significant (two-tailed t test).

Resistance to PARPi in 53BP1-deficient KB1P cells is mediated by nuclear LIG3

The *LIG3* gene encodes both mitochondrial and nuclear proteins³³. Importantly, mitochondrial LIG3 is essential for cellular viability as it ensures mtDNA integrity³⁴. Consequently, complete deletion of *Lig3* results in cellular death and early embryonic lethality in mice, whereas nuclear LIG3 has been shown to be dispensable for cell viability²⁸. We therefore asked whether the increased PARPi sensitivity of LIG3-depleted BRCA1-deficient cells resulted from loss of LIG3 activity in the nucleus or in the mitochondria. To test this, we generated nuclear *Lig3* knockout cells which only express the mitochondrial form of LIG3. To this end, we used 53BP1-deficient KB1P.R mouse tumor cells in which we introduced an ATG>CTC mutation in the internal translation initiation site that is required for expression of the nuclear LIG3 isoform but does not affect expression of mitochondrial LIG3 (**Fig. 2A**)³³. Western blot analysis of KB1P.R cells, one KB1P.R(LIG3^{mut/wt}) clone heterozygous for the ATG>CTC mutation (B1) and two KB1P.R(LIG3^{mut/mut}) clones with homozygous ATG>CTC mutation (A3, F5) showed that LIG3 is still expressed (**Fig. 2B**). However, immunofluorescence analysis of LIG3 in the same clones revealed that parental KB1P.R cells and the heterozygous KB1P.R(LIG3^{mut/wt}) B1 clone displayed LIG3 staining in both nucleus and mitochondria, whereas the homozygous KB1P.R(LIG3^{mut/mut}) A3 and KB1P.R(LIG3^{mut/mut}) F5 clones exhibited loss of nuclear LIG3 expression (**Fig. 2C**). Finally, we investigated whether the nuclear mutants of LIG3 displayed increased sensitivity to PARPi. Long-term clonogenic assays revealed that the nuclear LIG3-deficient KB1P.R(LIG3^{mut/mut}) A3 and KB1P.R(LIG3^{mut/mut}) F5 clones displayed hyper-sensitivity to olaparib when compared to the PARPi-resistant parental KB1P.R cells and the heterozygous KB1P.R(LIG3^{mut/wt}) B1 clone (**Fig. 2D and Supplementary Fig. 4A,B**).

Nuclear LIG3 consists of a N-terminal like zinc finger (ZnF) domain which is required for binding to DNA secondary structures³⁵ and a C-terminal BRCT domain required for interaction with other proteins such as XRCC1³⁶. To test the role of these domains in LIG3-mediated PARPi resistance, we generated overexpression constructs for wild-type human LIG3 (hLIG3^{WT}), carrying a mutation in the PARP-like ZnF domain (hLIG3^{R31L}) or a C-terminal $\Delta 774-922$ truncation (hLIG3 ^{$\Delta 774-922$}). We introduced these constructs in KB1P.R(LIG3^{mut/mut}) A3 cells - from here onwards referred to as KB1P.R(^{Δ nucLIG3}) - and carried out clonogenic assays (**Fig. 2E**). Whereas overexpression of hLIG3^{WT} rescued sensitivity to olaparib in KB1P.R(^{Δ nucLIG3}) cells, overexpression of either hLIG3 mutant failed to suppress olaparib sensitivity in KB1P.R(^{Δ nucLIG3}) cells (**Fig. 2F and Supplementary Fig. 4C**), indicating that both the DNA binding and BRCT domain are required for driving PARPi resistance in BRCA1 and 53BP1 double-deficient tumor cells.

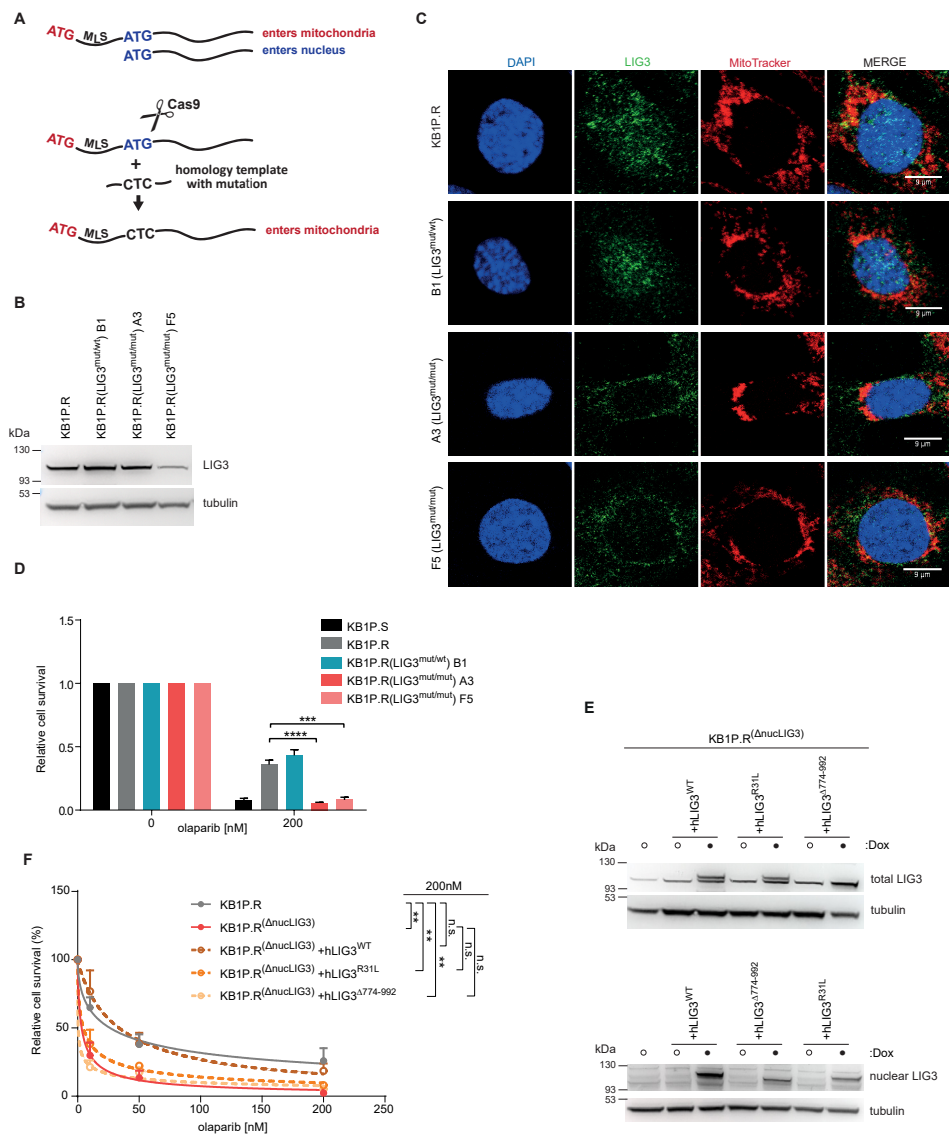


Figure 2 | Resistance to PARPi in 53BP1-deficient KB1P cells is mediated by nuclear LIG3. A | Generation of nuclear LIG3 mutants in KB1P.R cells. Lig3 contains two ATG translation initiation sites flanking a mitochondrial targeting sequence (MLS). Translation initiated at the upstream ATG site produces a mitochondrial protein, whereas translation from the downstream ATG site produces the nuclear form. Ablation of the downstream ATG allows cells to retain mitochondrial, but not nuclear LIG3 function. CRISPR-Cas9 was used to introduce in-frame ATG > CTC mutation in the nuclear ATG through delivery of a homology repair template. **B |** Western blot analysis of LIG3 in whole-cell lysates of KB1P.R, KB1P.R(LIG3^{mut/wt}) B1, KB1P.R(LIG3^{mut/mut}) A3, and KB1P.R(LIG3^{mut/mut}) F5 cells. **C |** LIG3 immunofluorescence and MitoTracker staining in nuclear LIG3 mutant cells. Scale bar, 9 μm. **D |** Quantification of long-term clonogenic assays with KB1P.S, KB1P.R cells, and nuclear LIG3 mutant clones B1, A3, and F5, treated with olaparib or untreated. **E |** Western blot analysis of total and nuclear LIG3 in KB1P.R and nuclear LIG3 mutant KB1P.R(ΔnucLIG3) cells. Expression of LIG3 constructs was induced with doxycycline (Dox) for 2 days prior to analysis. **F |** Quantification of long-term clonogenic assay with KB1P.R and nuclear LIG3 mutant KB1P.R(ΔnucLIG3) cells, treated with olaparib or untreated. Expression of LIG3 constructs was induced with doxycycline (Dox) starting 2 days before the assay and maintained for the duration of the assay. Data are represented as mean ± SD. **p < 0.01, ***p < 0.001, and ****p < 0.0001; n.s., not significant (two-tailed t test).

LIG3 is required at RFs in BRCA1-deficient cells treated with PARPi

Our data indicates that the increase in sensitivity to PARPi arising from LIG3 depletion is independent of the loss of DSB end-protection and therefore we hypothesized that this phenomenon could be independent of HR status. To test this hypothesis, we carried out RAD51 ionizing radiation-induced foci (RAD51 IRIF) in our mouse tumor-derived cell lines as a read-out of functional HR status¹⁵. As expected, BRCA1-deficient KB1P.S cells had significantly less IRIF per cell than the BRCA1-proficient KP cells (**Supplementary Fig. 1A**), while the BRCA1/53BP1 double-deficient KB1P.R cells displayed increased numbers of IRIF compared with KB1P.S (**Supplementary Fig. 5A**). Moreover, KB1P.R cells with shRNA-mediated depletion of LIG3 or with deletion of LIG3 nuclear isoform did not show a significant reduction of RAD51 IRIF (**Supplementary Fig. 5A**), corroborating our hypothesis that the sensitivity observed in LIG3-depleted cells is not a result of decreased HR in these cells.

LIG3 is also involved in the repair of DSBs by alternative end-joining (Alt-EJ) through its interaction with POLQ^{27,28}. It has been previously reported that HR-deficient tumors rely on POLQ for survival and that its depletion can enhance PARPi-response in both BRCA1-deficient cells and BRCA1/53BP1 double-mutant cells^{37–39}. Therefore, we hypothesized that, if the suppressive effect of LIG3 on PARPi sensitivity in BRCA1-deficient cells is dependent on its role in Alt-EJ, viability of LIG3-deficient cells should not be affected by inhibition of POLQ and that sensitivity of LIG3-deficient cells to olaparib would not be amplified by POLQ inhibition. To test this, we carried out both long-term clonogenic and short-term cytotoxicity assays with olaparib and the POLQ inhibitor ART558⁴⁰. Interestingly, inhibition of POLQ alone resulted in increased cell death in KB1P.R parental cells, as well as in nuclear LIG3 mutant KB1P.R^(ΔnucLIG3) cells (**Supplementary Fig. 5B,C**). Moreover, we observed a synergistic interaction between olaparib and ART558 in both cell lines (**Supplementary Fig. 5C**), suggesting that LIG3-mediated resistance is independent of its role in POLQ-mediated end-joining.

Data from recent studies indicate that LIG3 is present at RFs^{4,41–43}. Therefore, we next investigated whether LIG3 localizes to sites of DNA replication marked by 5-ethynyl-2'-deoxyuridine (EdU) incorporation, in the absence of DNA damage induction. To test this, we performed proximity ligation-based assays (PLA) to detect LIG3 binding to replicated DNA^{44,45}, in BRCA1-proficient KP, BRCA1-reconstituted KB1P.S+hB1²⁴, and in BRCA1-deficient KB1P.S cells. Interestingly, untreated KB1P.S cells showed significantly higher levels of LIG3-EdU PLA foci than KP or KB1P.S+hB1 cells (**Fig. 3A,B** and **Supplementary Fig. 5D,E**). We next tested if LIG3 localization at replication sites is affected by PARPi treatments which would trap PARP1 at RFs. Therefore, we carried out LIG3-EdU PLA after incubating cells with olaparib for 2hr. Quantification of LIG3-EdU PLA foci revealed that PARPi treatment did not induce any increase in the number of foci in KB1P.S+hB1 cells. In contrast, BRCA1-deficient KB1P.S cells displayed a striking increase in the number of PLA foci after olaparib treatment (**Fig. 3A** and **Supplementary Fig. 5D**). We next investigated whether LIG3 localization at replication sites is affected by the PARG inhibitor (PARGi) PDDX-001 which is known to increase PAR levels and to also result in an increase in chromatin-associated PARP1^{4,13,46}.

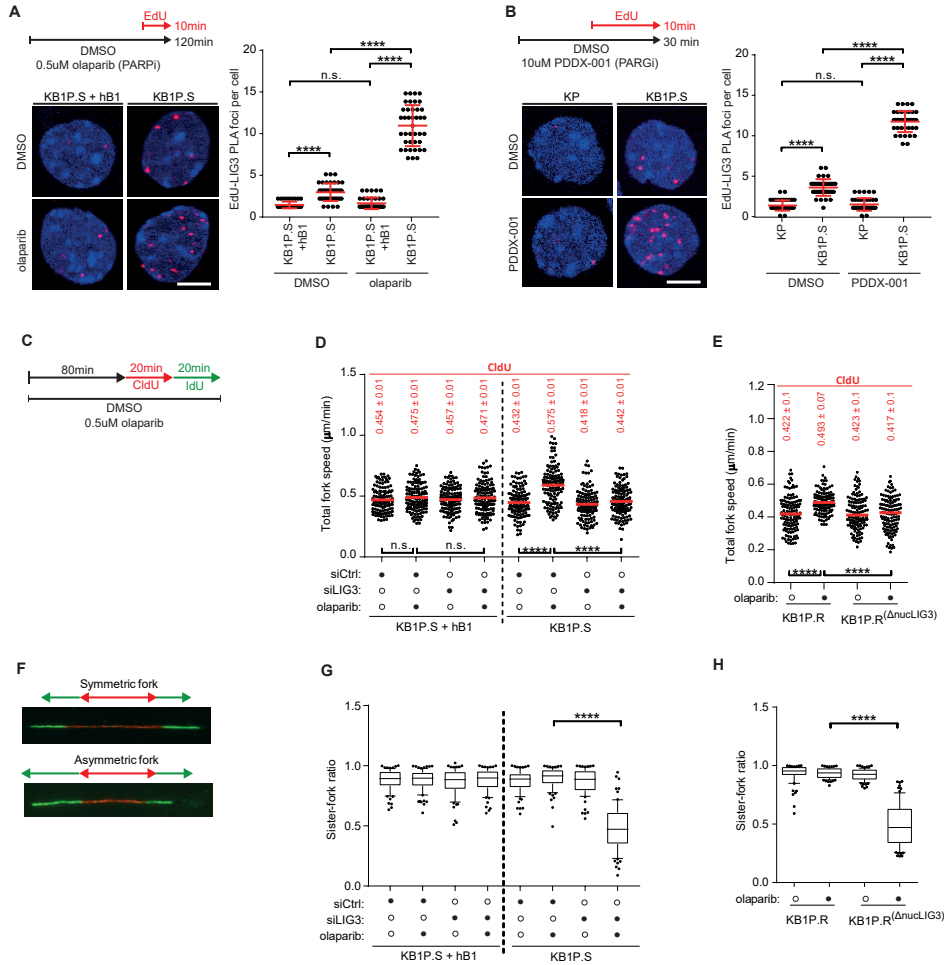


Figure 3 | LIG3 is required for replication forks in BRCA1-deficient cells treated with PARPi. A | Experimental setup, representative images, and quantification of LIG3-EdU proximity ligation assay (PLA) foci in KB1P.S+hB1 and KB1P.S cells incubated for 10 min with 20 mM EdU, in the absence or presence of olaparib. Scale bar, 5 mm. **B** | Experimental setup, representative images, and quantification of LIG3-EdU PLA foci in KP and KB1P.S cells incubated for 10 min with 20 mM EdU, in the absence or presence of PDDX-001. Scale bar, 5 mm. **C** | Experimental setup of DNA fiber assay. Cells were pre-incubated with 0.5 mM olaparib for 80 min, followed by sequential labeling with CldU (red) and IdU (green) in the presence of olaparib for 20 min each. RF progression was quantified by measuring tract lengths of CldU and IdU in micrometers. **D** | Quantification of RF speed in CldU tracks, following the indicated treatments, in KB1P.S+hB1 and KB1P.S cells after siRNA-mediated depletion of LIG3. **E** | Quantification of RF speed in CldU tracks, following the indicated treatments, in nuclear LIG3 mutant KB1P.R(Δ nucLIG3) cells. **F** | Representative images of symmetric and asymmetric RFs. **G** | Quantification of RF symmetry following the indicated treatments in KB1P.R cells. The box represents the 10th to 90th percentile range. **H** | Quantification of RF symmetry following the indicated treatments in KB1P.R and KB1P.R(Δ nucLIG3) cells. The box represents the 10th to 90th percentile range. Data are represented as mean. **** $p < 0.0001$; n.s., not significant (Mann-Whitney U test).

We therefore carried out LIG3-EdU PLA after incubating cells with PDDX-001 for 30 min. Similar to olaparib-treated cells, PDDX-001-treated BRCA1-deficient cells showed a strong increase in the number of LIG3-EdU PLA foci, while no significant changes were observed in KP cells (**Fig. 3B** and **Supplementary Fig. 5E**). Co-localization of LIG3 at EdU-marked replication sites after PDDX-001 treatment was also verified qualitatively by LIG3 immunostaining in KP, KB1P.S cells and KB1P.R cells (**Supplementary Fig. 5F**). Since we observe that both PARPi and PARGi treatment results in an increase in LIG3-EdU PLA foci, and that olaparib treatment results in a reduction of PAR levels while treatment with PDDX-001 results in an increase, we conclude that the upsurge in LIG3-EdU PLA is probably caused by PARP1 trapping, which is common to both inhibitors. Of note, untreated KB2P cells showed similar numbers of LIG3-EdU PLA foci as KP cells (**Supplementary Fig. 5G,H**). However, upon treatment with PDDX-001, KB2P cells showed more LIG3-EdU PLA foci than KP cells, but significantly less than KB1P.S cells (**Supplementary Fig. 5G,H**). These data support our previous findings that LIG3 depletion in BRCA2-deficient cells has a more modest effect on olaparib sensitivity than in BRCA1-deficient cells.

Since LIG3 seems to play a role at replication sites in BRCA1-deficient conditions, we asked whether depletion of LIG3 would affect RF progression in untreated and PARPi-treated BRCA1-deficient cells. To test this, we performed DNA fiber assay in BRCA1-deficient KB1P.S and BRCA1-reconstituted KB1P.S+hB1 cells. Cells were pre-incubated with olaparib for 80 min, followed by sequential labelling with CldU (red) and IdU (green) for 20 mins each in the presence of olaparib (**Fig. 3C**). Progression was measured by tract lengths of CldU and IdU. Analysis of RF speeds revealed no significant increase in BRCA1-proficient KB1P.S+hB1 cells after olaparib treatment (**Fig. 3D** and **Supplementary Fig. 5I,J**). In contrast, BRCA1-deficient KB1P.S cells exhibited an increase in RF speed upon olaparib treatment, in line with previous work⁴³. Surprisingly, while siRNA-mediated depletion of LIG3 did not affect RF speed in untreated cells, it significantly suppressed the PARPi-induced increase in RF speed in KB1P.S cells (**Fig. 3D** and **Supplementary Fig. 5I,J**). As observed in KB1P.S cells, olaparib treatment also resulted in increased RF speed in BRCA1/53BP1 double-deficient KB1P.R cells, which was rescued by siRNA-mediated LIG3 depletion or loss of nuclear LIG3 (**Fig. 3E** and **Supplementary Fig. 5I,K-M**). Similar data was also observed in BRCA1/53BP1 double-deficient RPE1-B1P.R cells treated with PARPi (**Supplementary Fig. 5N,O**). Since loss of LIG3 rescued the increase in RF speed in both BRCA1 and BRCA1/53BP1 double-deficient cells, we asked if this phenomenon was due to a restraint in RF speed or due to continuous RF stalling and restart and thus increased replication stress. We next analyzed RF symmetry in BRCA1-proficient and-deficient cells by measuring sister fork-ratio (**Fig. 3F,G**). While BRCA1-proficient KB1P.S+hB1 cells did not show any significant differences in RF symmetry across conditions, depletion of LIG3 induced a significant increase in sister fork asymmetry, indicative of RF stalling, in BRCA1-deficient KB1P.S cells exposed to olaparib (**Fig. 3G**). Similarly, loss of nuclear LIG3 in KB1P.R(^{ΔnucLIG3}) cells also resulted in RF asymmetry upon olaparib treatment (**Fig. 3H**). These

data corroborate our hypothesis that the lack of PARPi-induced RF acceleration observed in LIG3-depleted cells is a result of persistent RF stress upon loss of LIG3. Overall, our results support the notion that depletion of LIG3 in BRCA1-deficient cells exposed to PARPi leads to slower and asymmetric RFs.

Loss of LIG3 in BRCA1-deficient cells results in an increase in PARPi-mediated ssDNA regions

Recent studies have suggested that accumulation of post-replicative single-stranded DNA (ssDNA) gaps underlies BRCA deficiency and PARPi sensitivity^{43,47,48}. Since LIG3 is a DNA ligase and our data indicates that it is present at active RFs in BRCA1-deficient cells, we asked whether LIG3 depletion would result in an increase in S phase associated ssDNA. To test this, we cultured KB1P.S+hB1, KB1P.S and KB1P.R mouse tumor cells in medium supplemented with BrdU for 48hr followed by a 2hr-treatment with olaparib and quantification of native BrdU intensity by quantitative image-based cytometry (QIBC)⁴⁹ (**Fig. 4A**). As previously suggested, olaparib treatment did not result in an increase in ssDNA levels in BRCA1-proficient KB1P.S+hB1 cells nor in BRCA1/53BP1 double-deficient KB1P.R cells (**Fig. 4B,C** and **Supplementary Fig. 6A,B**). However, treatment with olaparib resulted in a significant increase in ssDNA levels in BRCA1-deficient KB1P.S cells during S-phase (**Fig. 4B,C**, and **Supplementary Fig. 6A,B**). These results were further confirmed in the RPE1 isogenic lines, showing PARPi-induced increase in ssDNA levels in RPE1-B1P.S cells but not in RPE1-P or RPE1-B1P.R cells (**Supplementary Fig. 6D**). Importantly, deletion of nuclear LIG3 in KB1P.R cells or shRNA-mediated LIG3 depletion in RPE1-B1P.R cells restored PARPi-induced ssDNA gaps accumulation (**Fig. 4D** and **Supplementary Fig. 6C,D**). LIG3 depletion also further increased PARPi-induced ssDNA gaps accumulation in RPE1-B1P.S cells (**Supplementary Fig. 6D**), suggesting that LIG3-mediated ssDNA gap suppression is HR-independent.

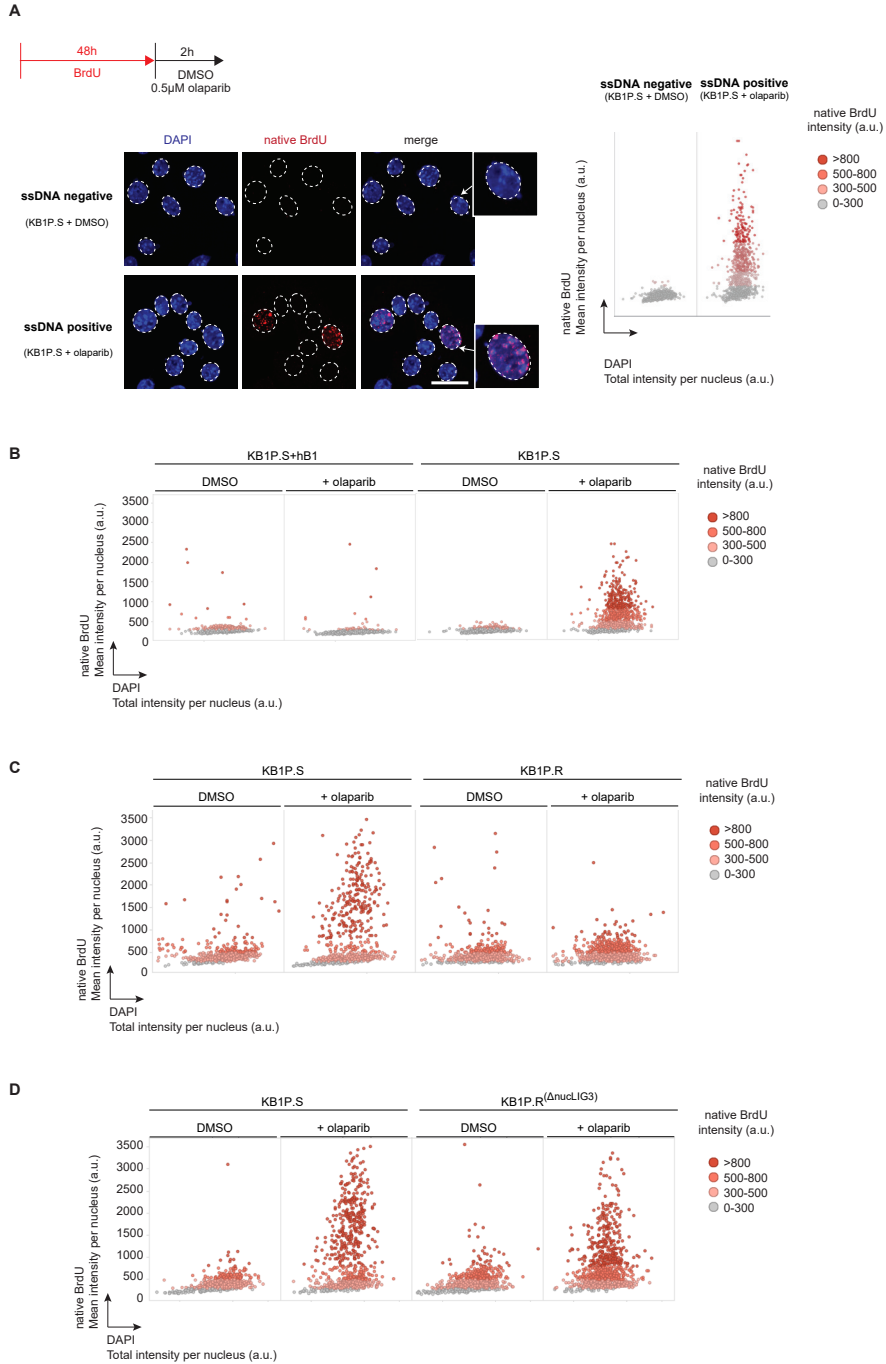


Figure 4 | Loss of LIG3 in BRCA1-deficient cells results in an increase in PARPi-mediated ssDNA regions.

A | Experimental setup to quantify amount of ssDNA gaps per nucleus by quantitative image-based cytometry (QIBC) analysis of mean intensity of native BrdU per nucleus. Cells were incubated with BrdU for 48 h followed by 2 h treatment with 0.5 mM olaparib or left untreated. Scale bar, 50 mm. **B–D** | QIBC analysis of ssDNA in KB1P.S+hB1 and KB1P.S cells (B), KB1P.S and KB1P.R cells (C), and KB1P.S and KB1P.R(Δ nucLIG3) cells (D).

Increase in ssDNA gaps results in increased genomic instability in *LIG3*-deficient cells

MRE11 has been shown to be involved in the processing of gaps at and behind RFs^{14,50,51}. Furthermore, the nucleosome remodeling factor CHD4 has been reported to be involved in the recruitment of MRE11 for nuclease processing at stressed RFs¹⁴. We therefore tested if the PARPi-induced increase in replication-associated ssDNA regions in KB1P.S and KB1P.R(*ΔnucLIG3*) cells was dependent on either MRE11 or CHD4. Both inhibition of MRE11 with mirin and siRNA-mediated depletion of CHD4 rescued the increase in replication-associated ssDNA regions in KB1P.R(*ΔnucLIG3*) cells treated with olaparib (**Fig. 5A** and **Supplementary Fig. 6E-G**). In contrast, neither treatment with mirin nor depletion of CHD4 rescued ssDNA exposure in parental KB1P.S cells (**Fig. 5A** and **Supplementary Fig. 6F,G**). To confirm if the observed increase of ssDNA was in the vicinity of RFs, we used electron microscopy (EM) to visualize the fine architecture of replication intermediates in KB1P.S, KB1P.R and KB1P.R(*ΔnucLIG3*) cells after 2hr-treatment with olaparib (**Fig. 5B,C**). In untreated conditions, a minority of the DNA molecules displayed ssDNA gaps behind the RF in all the three cell lines analyzed. However, olaparib treatment markedly enhanced the percentage of molecules displaying 1 or more post-replicative ssDNA gaps, specifically in KB1P.S and KB1P.R(*ΔnucLIG3*) but not in KB1P.R cells (**Fig. 5D**). Consistent with our QIBC data, we observed that the PARPi-induced post-replicative gaps in KB1P.S cells were not rescued upon inhibition of MRE11 whereas the post-replicative gaps in olaparib-treated KB1P.R(*ΔnucLIG3*) cells were dependent on MRE11-mediated processing (**Fig. 5D**). Of note, we did not observe an increase in RF reversal in any of the conditions (**Supplementary Fig. 6H**). Taken together, these data suggest that the PARPi-induced ssDNA regions in BRCA1-deficient and 53BP1-proficient cells are distinct in nature from the PARPi-induced gaps generated upon loss of *LIG3* in BRCA1/53BP1 double-deficient cells.

We next questioned if the suppression of post-replicative gaps observed upon either MRE11 inhibition or depletion of CHD4 could result in RF stability in KB1P.R(*ΔnucLIG3*) cells. To assess this, we performed DNA fiber assays to measure RF asymmetry in KB1P.R and KB1P.R(*ΔnucLIG3*) cells upon exposure to olaparib combined with either MRE11 inhibition or CHD4 depletion. Interestingly, our data revealed that the RF asymmetry observed in these cells upon treatments with olaparib was completely rescued upon MRE11 inhibition or depletion of CHD4 (**Fig. 5E**). However, MRE11 inhibition or CHD4 depletion did not result in an increase in RF speed in KB1P.R(*ΔnucLIG3*) cells exposed to olaparib as observed in KB1P.R cells, suggesting that the increase in RF speed is uncoupled from MRE11-mediated ssDNA gap exposure and from PARPi sensitivity (**Supplementary Fig. 6I,J**).

We next tested whether the increase in post-replicative ssDNA gaps upon *LIG3* depletion resulted in increased genomic instability. We analyzed chromosomal aberrations in metaphase spreads of KB1P.S+hB1, KB1P.S, KB1P.R and KB1P.R(*ΔnucLIG3*) cells after treatment with olaparib for 2hr. As expected, olaparib treatment resulted in increased numbers of chromosomal aberrations in KB1P.S cells but not in KB1P.S+hB1 and KB1P.R¹⁸ (**Fig. 5F** and **Supplementary Fig. 7K**). Interestingly, KB1P.R(*ΔnucLIG3*) cells showed a surge

in chromosomal aberrations when compared to KB1P.R cells (**Fig. 5F,G**). Interestingly, the aberrations in PARPi-treated KB1P.R(Δ nucLIG3) cells mainly consisted of chromosome and chromatid breaks, whereas PARPi-treated KB1P.S cells showed more radials (**Fig. 5G**). siRNA-mediated depletion of LIG3 further enhanced chromosomal aberrations in KB1P.S cells (**Supplementary Fig. 6K**). Of note, inhibition of MRE11 with mirin or siRNA-mediated depletion of CHD4 suppressed PARPi-induced genomic instability in KB1P.R(Δ nucLIG3) cells, indicating that PARPi-induced genomic instability in these cells is mediated by MRE11-dependent ssDNA gap exposure (**Fig. 5F,G** and **Supplementary Fig. 6L**). As expected, treatment with mirin or depletion of CHD4 did not rescue chromosomal aberrations in parental KB1P.S cells (**Fig. 5F,G**). Importantly, loss of LIG3 did not result in an increase in immediate DSBs following olaparib treatment, as assessed by pulsed-field gel electrophoresis (PFGE) of genomic DNA from KB1P.S+hB1, KB1P.S and KB1P.R cells and by immunofluorescence analysis of γ -H2AX foci in K.P, KB1P.S and KB1P.R cells (**Supplementary Fig. 7A,B**). Altogether, these data indicate that the increase in genomic instability induced by loss of nuclear LIG3 in BRCA1/53BP1 double-deficient cells exposed to PARPi is caused by post-replicative ssDNA gaps.

LIG3 depletion increases *in vivo* efficacy of PARPi

Our previous results established that LIG3 is a modulator of PARPi-response *in vitro*. To test whether our results could be recapitulated *in vivo*, we performed shRNA-mediated depletion of LIG3 in PARPi-naïve ORG-KB1P.S organoids (BRCA1-deficient) and PARPi-resistant ORG-KB1P.R organoids (BRCA1/53BP1 double-deficient) (**Fig. 6A** and **Supplementary Fig. 1A**). The modified organoid lines were transplanted into the mammary fat pad of syngeneic wild-type mice. Upon tumor outgrowth, mice were treated with olaparib or vehicle for 28 consecutive days, and mice were sacrificed when tumors progressed to a volume of ≥ 1500 mm³. LIG3 depletion did not affect tumor growth and all cohorts of vehicle-treated mice showed comparable survival (**Fig. 6B,C**). In contrast, LIG3 depletion significantly enhanced the anticancer efficacy of olaparib, resulting in increased survival of olaparib-treated mice bearing KB1P.S+shLIG3 tumors, compared to olaparib-treated mice with KB1P.S+shscr tumors (**Fig. 6B**). Importantly, LIG3 depletion also resensitized the PARPi-resistant KB1P.R tumors to olaparib. Whereas olaparib-treated and vehicle-treated mice with KB1P.R tumors showed comparable survival, olaparib treatment significantly prolonged the survival of mice bearing KB1P.R+shLIG3 tumors (**Fig. 6C**). Together, these data show that LIG3 also modulates PARPi response *in vivo*.

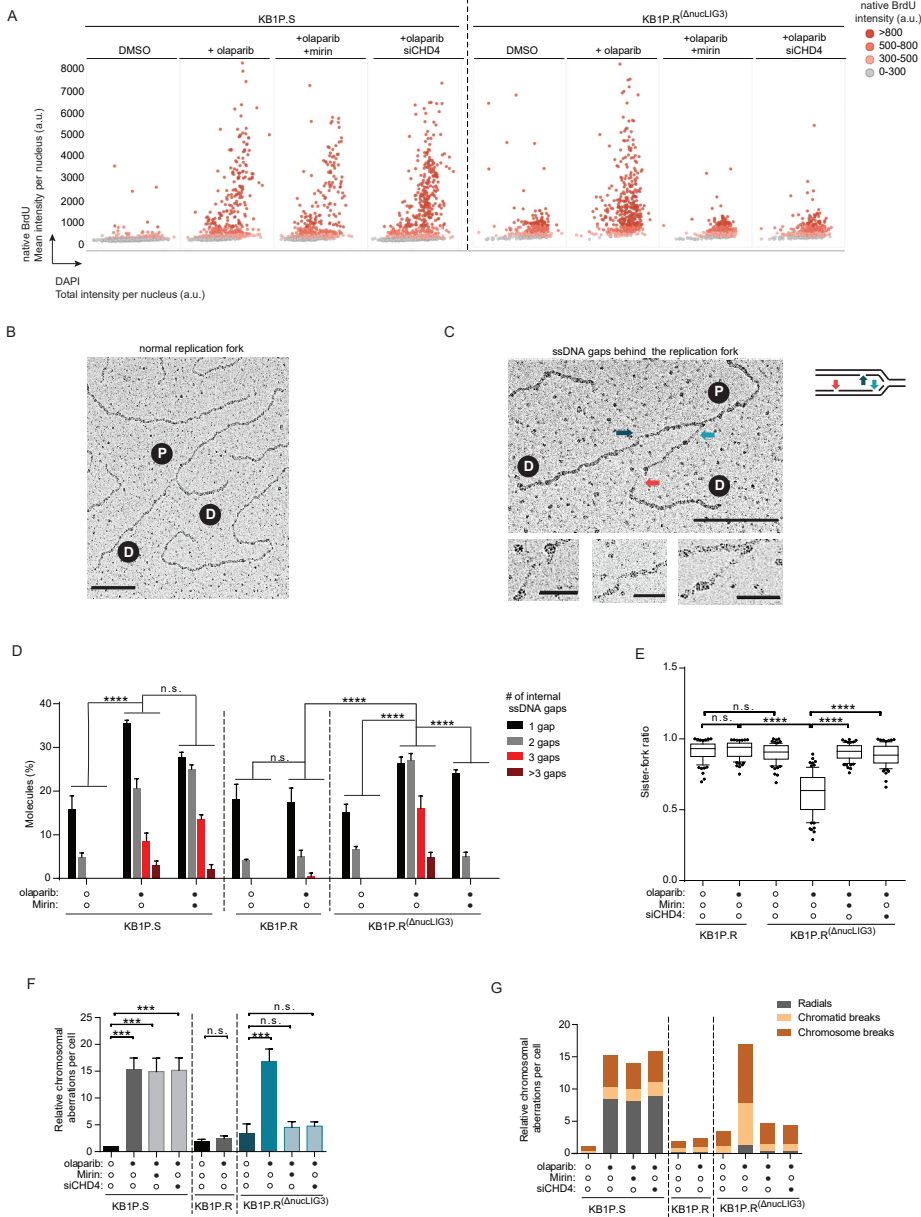


Figure 5 | Increase in ssDNA gaps results in increased genomic instability in LIG3-deficient cells. A | QIBC analysis of ssDNA gaps in KB1P.S and nuclear LIG3 mutant KB1P.R(Δ nucLIG3) cells. Cells were treated with 25 μ M mirin for 48hr prior to treatment with olaparib, or transfected with siRNA targeting CHD4. **B-C** | Representative electron micrographs of normal RF (B) and RF with internal ssDNA gaps behind the fork (C). Scale bar for large panels: 250nm = 1214bp; scale bar for small panels: 50nm = 242bp. P; parental strand. D; daughter strand. **D** | Quantification of internal ssDNA gaps behind RFs observed in KB1P.S, KB1P.R and KB1P.R(Δ nucLIG3) cells upon treatment with 0.5 μ M olaparib for 2hr. KB1P.S and KB1P.R(Δ nucLIG3) cells were additionally treated with 25 μ M mirin for 48hr prior to treatment with olaparib, or transfected with siRNA targeting CHD4. Data were acquired by electron microscopy. Data are represented as mean \pm SD. **** p <0.0001, n.s., not significant; two-way ANOVA. **E** | Quantification of RF symmetry in KB1P.R and KB1P.R(Δ nucLIG3) cells following indicated treatments. KB1P.R(Δ nucLIG3) cells were additionally treated with 25 μ M mirin for 48hr prior to treatment with olaparib, or transfected with siRNA

targeting CHD4. Data are represented as mean and the box represents 10-90 percentile range. **** $p < 0.0001$; n.s., not significant; Mann-Whitney U test. **F** | Quantification of chromosomal aberrations in KB1P.S, KB1P.R and KB1P.R(Δ nucLIG3) cells following 2 hr treatment with 0.5 μ M olaparib and recovery for 6 hr. KB1P.S and KB1P.R(Δ nucLIG3) cells were additionally treated with 25 μ M mirin for 48hr prior to treatment with olaparib, or transfected with siRNA targeting CHD4. Data are represented as mean \pm SD. *** $p < 0.001$, n.s., not significant; two-tailed t test. **G** | Quantification of the different types of chromosomal aberrations identified in (F).

Increased LIG3 expression in triple-negative breast and serous ovarian cancers

To assess the clinical relevance of LIG3, we determined LIG3 expression in sections of treatment-naïve tumors from a cohort of 86 women with triple-negative breast cancer (TNBC)¹³ and 51 women with high-grade serous ovarian carcinoma⁵², two clinically relevant groups of patient eligible for PARPi treatment. Immunohistochemistry (IHC) analysis revealed that, while LIG3 protein was expressed at normal levels in a majority of tumor cells in the biopsies, a substantial proportion of samples contained areas displaying aberrant expression of LIG3. Of the 87 TNBC cases analyzed, 32 (37.2%) and 17(19.8%) biopsies showed LIG3 overexpression in areas corresponding to >10% and >20% of the tumor, respectively (**Fig. 6D**). Similarly, 26 (51%) and 7 (13.7%) of the 51 ovarian cancer cases showed LIG3 overexpression in areas corresponding to >10% and >20% of the tumor, respectively (**Fig. 6E**). Conversely, LIG3-negative areas were observed in a small proportion of biopsies, with 2 (2.3%) and 1 (1.2%) of the 86 TNBC cases, and 2 (3.9%) and 4 (7.8%) of the 51 ovarian cancers displaying loss of LIG3 in areas corresponding to >10% and >20% of the tumor, respectively (**Fig. 6D,E**). These observations reveal that LIG3 expression is heterogeneous within and across TNBC and serous ovarian cancers, which might result in selective expansion of LIG3 overexpressing clones during PARPi treatment and thereby contribute to intratumoral and inter-patient differences in response to PARPi therapy

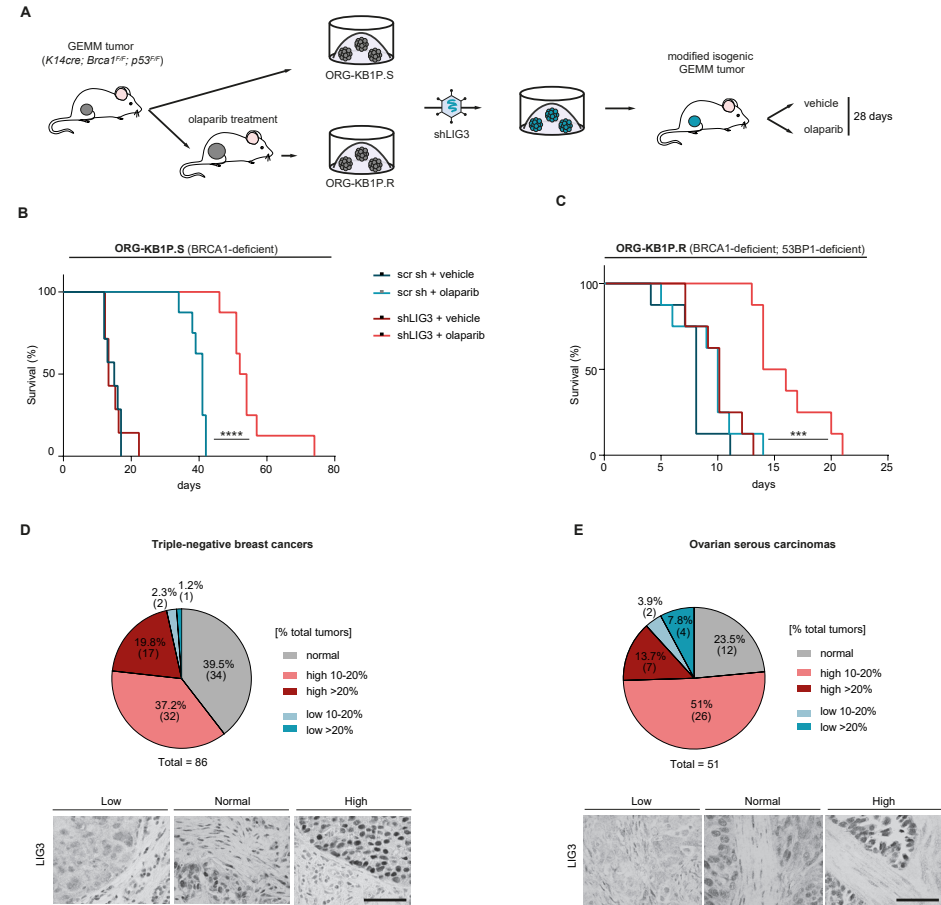


Figure 6 | LIG3 depletion increases *in vivo* efficacy of PARPi and is overexpressed in a fraction of human tumors. **A** | Outline of *in vivo* experimental set up. Organoids were modified *in vitro* and transplanted into the mammary fat pad of syngeneic, wild-type FVB/NRj mice. Upon tumor outgrowth, mice were treated with olaparib or vehicle for 28 consecutive days. **B-C** | Kaplan–Meier survival curves of mice transplanted with KB1P.S (B) or KB1P.R organoid lines (C), after *in vitro* shRNA-mediated depletion of LIG3. *** $p < 0.001$, **** $p < 0.0001$; Log-Rank (Mantel Cox). **D-E** | Summary and representative images of immunohistochemistry (IHC) analysis of LIG3 expression in triple-negative breast cancers (D) and ovarian serous carcinomas (E). Scale bar, 100 μm .

DISCUSSION

Molecular alterations that render cells resistant to targeted therapies may also cause synthetic dependencies, which can be exploited to design rational combination therapies. However, the pathways that can be targeted to exploit these vulnerabilities are poorly understood. In this study, we used shRNA dropout screens to identify synthetic dependencies of BRCA1-deficient cells which acquired resistance to PARPi treatment by restoration of HR due to loss 53BP1. We have identified LIG3 as a critical suppressor of PARPi toxicity in BRCA1/53BP1

double-deficient cells. Loss of LIG3 also enhances PARPi sensitivity of BRCA1-deficient cells with intact 53BP1, indicating that the role of LIG3 in BRCA1-deficient cells is independent of their 53BP1 status.

In this study, we show that the increase in sensitivity to PARPi observed upon LIG3 loss in BRCA1/53BP1 double-deficient cells results from an increase in post-replicative MRE11-dependent ssDNA gaps. This is in line with the notion that PARPi treatment results in accumulation of post-replicative ssDNA gaps and that exposure to these lesions is a key determinant of PARPi response^{43,48}. Moreover, our data show that exposure to post-replicative ssDNA gaps underlies PARPi cytotoxicity in both HR-deficient and HR-restored cells, indicating that LIG3-mediated PARPi resistance in BRCA1/53BP1 double-deficient cells is an HR-independent mechanism. Together, these data indicate that BRCA1/53BP1 double-deficient cells rely on LIG3 for suppression of PARPi-induced gaps, rendering LIG3 as a synthetic dependency of these cells. LIG3 depletion also increased sensitivity to PARPi in BRCA1/REV7 double-deficient cells, suggesting this synthetic dependency is common to BRCA1-deficient tumor cells that acquired PARPi resistance due to loss of end-protection.

We show that PARPi-induced ssDNA gaps in BRCA1-deficient cells are not substrates for MRE11-mediated degradation, indicating that PARPi-induced ssDNA gaps observed in LIG3-depleted BRCA1/53BP1 double-deficient cells are distinct from the gaps in BRCA1-deficient cells. Together, these data suggest existence of two different mechanisms of gap suppression in BRCA1-deficient cells, one dependent on loss of 53BP1 and another which is LIG3-dependent. In PARPi-sensitive BRCA1-deficient cells, 53BP1 drives the formation of post replicative ssDNA gaps upon PARPi treatment. Loss of LIG3 in these cells further enhances accumulation of PARPi-induced ssDNA gaps. On the other hand, PARPi-resistant BRCA1/53BP1 double-deficient cells are competent for HR and thus lack 53BP1-mediated gap formation, hence PARPi-induced ssDNA gaps only occur upon loss of LIG3 (**Fig. 7**).

53BP1-mediated gap induction in BRCA1-deficient cells exposed to PARPi may result from loss of recombinatorial gap repair⁵³ and/or defective Okazaki fragment processing (OFP) due to loss of the PARP1-XRCC1-LIG3 backup pathway^{4,42,43}. Cong et al. (2021)⁴³ have also suggested that PARPi resistance in BRCA1/53BP1 double-deficient cells is caused by restoration of the OFP backup pathway, evidenced by higher levels of chromatin-bound XRCC1 and LIG3 in these cells. While we find that the LIG3 BRCT domain, required for interaction with XRCC1, is critical for PARPi resistance in BRCA1/53BP1 double-deficient cells, we also find that PARPi-induced ssDNA gap formation in LIG3-depleted BRCA1/53BP1 double-deficient cells is fully rescued by MRE11 inhibition, indicating that LIG3 depletion in these cells does not impair OFP. Moreover, PARPi-induced ssDNA gaps in LIG3-depleted BRCA1/53BP1 double-deficient cells occur in both the newly replicated strands. Together, these data indicate that LIG3 is also involved in a separate, OFP-independent pathway of gap suppression.

Mechanistically, the LIG3-dependent gap suppression pathway might require repriming activities mediated by Pol α , PRIMPOL or another unknown primase, for bypass of lesions

such as PARPi-trapped PARP1 in BRCA1-deficient cells^{48,54–56}. These repriming activities could result in small gaps which require LIG3 to be filled. Loss of LIG3 in BRCA1-deficient and BRCA1/53BP1 double-deficient cells could thus result in the exposure of small ssDNA regions which would be a substrate for unscheduled MRE11-mediated processing. Subsequent processing of the small ssDNA regions could result in accumulation of longer stretches of post-replicative ssDNA, ultimately resulting in RF stalling, genomic instability and cell death (Fig. 7).

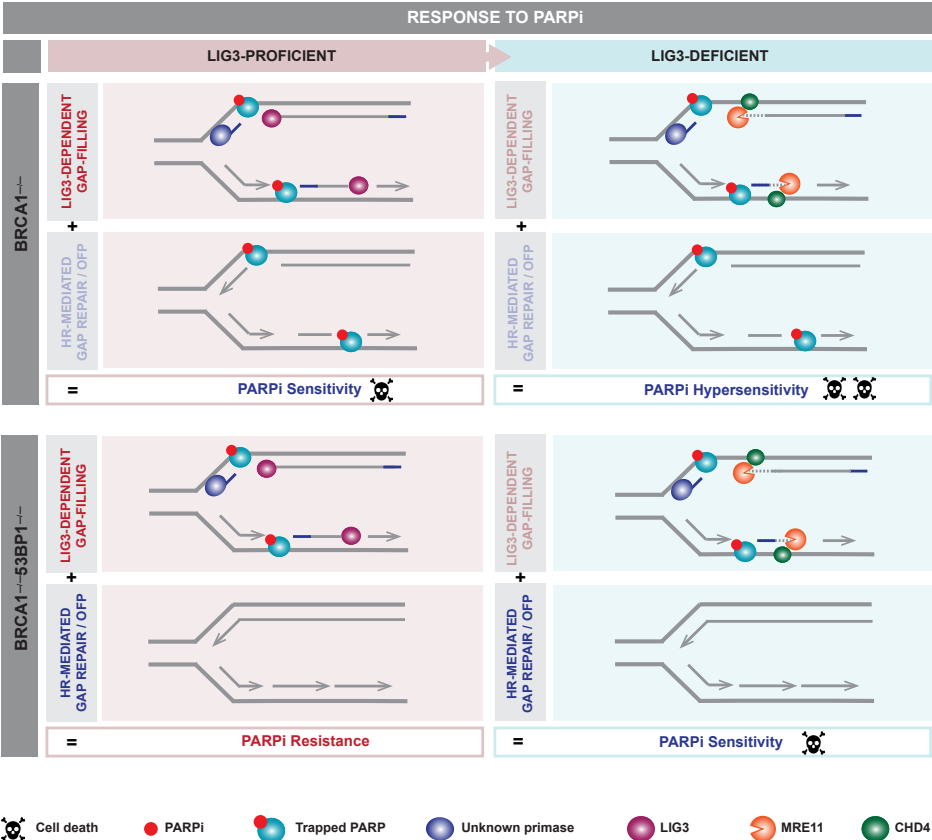


Figure 7 | Proposed model. BRCA1-deficient cells can bypass chromatin-trapped PARP1 lesions via two different mechanisms of gap suppression: one dependent on loss of 53BP1 and another which is LIG3-dependent. 53BP1-mediated ssDNA gap induction may result from loss of HR-mediated gap repair and/or defective Okazaki fragment processing. LIG3-mediated gap suppression might require repriming activities mediated by Polc, PRIMPOL or another unknown primase, resulting in small gaps which depend on LIG3 to be filled. Upon loss of LIG3, recruitment of MRE11 by CHD4 leads to unscheduled processing of the small gaps into longer stretches of post-replicative ssDNA, resulting in RF stalling and increased genomic instability. PARPi-sensitive BRCA1-deficient cells exhibit post-replicative PARPi-induced ssDNA gaps which are mediated by 53BP1. Accumulation of PARPi-induced post-replicative ssDNA gaps mediated by 53BP1 and by loss of LIG3 underlies PARPi hypersensitivity of BRCA1/LIG3 double-deficient cells. PARPi-resistant BRCA1/53BP1 double-deficient cells lack 53BP1-mediated gap formation, and PARPi-induced ssDNA gaps only occur upon loss of LIG3, resulting in accumulation of longer stretches of post-replicative ssDNA, RF stalling, genomic instability and PARPi sensitivity.

PARP1 has recently been implicated in restraining RF speed in cells⁵⁷. We indeed observe an increase of RF speed in BRCA1-deficient cells treated with low doses of PARPi. Importantly, the increase in speed was specific to cells deficient for BRCA1, contrasting with the previous reports where PARP inhibition increased RF speed in BRCA1-proficient cells⁵⁷, possibly reflecting the use of higher olaparib concentrations and longer periods of exposure to PARPi in the latter study. In addition, we observe that PARPi treatment induces faster RFs in PARPi-sensitive BRCA1-deficient cells as well as in PARPi-resistant BRCA/53BP1 double-deficient cells. Moreover, loss of LIG3 induces PARPi (hyper)sensitivity but suppresses PARPi-induced increase in RF speed in both BRCA1-deficient and BRCA1/53BP1 double-deficient cells. Together, these data show that PARPi-induced increase in RF speed in BRCA1-deficient cells is HR-independent and not causally related to PARPi sensitivity, in line with previous findings from Cong and colleagues⁴³.

Our findings might have therapeutic implications, as LIG3 depletion also increases the efficacy of PARPi *in vivo*, resulting in prolonged survival of mice bearing PARPi-sensitive BRCA1-deficient or PARPi-resistant BRCA1/53BP1 double-deficient mammary tumors. Furthermore, we find LIG3 to be overexpressed in a portion of TNBC and serous ovarian cancers, further suggesting that LIG3 could possibly be targeted in these cancers. Pharmacological inhibition of LIG3 might therefore be a potential strategy to combat resistance to PARPi. Taken together, our findings establish loss of LIG3 as a potent enhancer of PARPi synthetic lethality in BRCA1-deficient tumors, irrespective of their HR status, and provide insights into the role of LIG3 in restraining replication stress and genome instability induced by BRCA1 loss.

ACKNOWLEDGMENTS

We thank Peter Bouwman for sharing the mouse ESCs, Sylvie Noordermeer and Dan Durocher for the RPE1-TERT cells, and Madalena Tarsounas for the DLD1 isogenic cells. We thank Wei Zhao for helping with image analysis and to Hanneke van der Gulden, the NKI Preclinical Intervention Unit, Digital Microscopy facility, Genomics Core facility and Animal facility for technical assistance. This work was supported by grants from the European Union Horizon 2020 research and innovation program (agreement 722729); Dutch Research Council (Vici 91814643, Vidi 193.131); Dutch Cancer Society (KWF grant 11008); Oncode Institute; Swiss National Science Foundation (310030_179360); Swiss Cancer League (KLS-4282-08-2017); Danish Cancer Society (R204-A12617-B153, R167-A11068), Danish Council for Independent Research (DFF-7016-00313), Novo Nordisk Foundation (16854, 0060590), Danish National Research Foundation (DNRF 125), LundbeckFonden (R322-2019-2577); Swedish Research Council (VR-MH 2014-46602-117891-30); Swedish Cancer Foundation (170176); R01 CA254037.

AUTHOR CONTRIBUTIONS

Conceptualization – M.P.D., A.R.C. and J.J.; Methodology – M.P.D., I.v.d.H. and A.R.C.; Investigation – M.P.D., V.T., I.v.d.H., E.M., K.C., P.G., S.A., J. Bartkova, G.C.M.S. and M.A.S.; Supervision of *in vivo* experiments – M.v.d.V.; Data analysis – C.L., R.L.B, J.Bh. and S.Ch.; Writing of original draft, review & editing – M.P.D., A.R.C. and J.J.; Supervision – E.G., S.R., S.C., J. Bartek, A.R.C and J.J..

Supplementary Tables 1 and 2 are available in the online version of the paper.

METHODS

EXPERIMENTAL MODEL AND SUBJECT DETAILS

Cell Lines and cell culture

KP³¹, KB1P.S, KB1P.R³⁰ and KB1P.S+hB1²⁴ have been previously described. LIG3 nuclear mutants, KB1P.R-B1, KB1P.R-A3 and KB1P.R-F5, have been generated in this study. All these cell lines were cultured in DMEM/F12+GlutaMAX (Gibco) containing 5µg/ml Insulin (Sigma, #I0516), 5 ng/ml cholera toxin (Sigma, #C8052), 5 ng/ml murine epidermal growth-factor (EGF, Sigma, #E4127), 10% FBS and 50 units/ml penicillin-streptomycin (Gibco) and were cultured under low oxygen conditions (3% O₂, 5% CO₂ at 37°C). Mouse ES cells with a selectable conditional *Brca1* deletion (*R26Cre^{ERT2/wt};Brca1^{SCo/-}*) have been previously described (Bouwman et al. 2010). Additional knockout of *Trp53*, *Trp53bp1* and *Parp1* has been generated in this study. These cells were cultured on gelatin-coated plates in 60% buffalo red liver (BRL) cell conditioned medium, 0.1 mM β-mercaptoethanol (Merck) and 10³ U/ml ESGRO LIF (Millipore) and 50 units/ml penicillin-streptomycin (Gibco) under normal oxygen conditions (21% O₂, 5% CO₂, 37°C). SUM149PT (RRID: CVCL_3422) cells were grown in RPMI1640 (Gibco) medium supplied with 10% fetal calf serum and 50 units/ml penicillin-streptomycin (Gibco). RPE1-hTERT and DLD-1 cell lines were grown in DMEM+GlutaMAX (Gibco) supplemented with 10% FBS and 50 units/ml penicillin-streptomycin (Gibco). RPE1-P, RPE1-B1P.S and RPE1-B1P.R cells were generated by Noordermeer et al. 2018. HEK293FT (RRID: CVCL_6911) cells were cultured in IMDM+GlutaMAX-I (Gibco) supplemented with 10% FBS and 50 units/ml penicillin-streptomycin (Gibco). SUM149PT and DLD1 cell lines were cultured under normal oxygen conditions (21% O₂, 5% CO₂, 37°C). RPE1 cell lines were cultured under low oxygen conditions (3% O₂, 5% CO₂ at 37°C).

Tumor-Derived Organoids

All lines have been described before ²⁹. ORG-KB1P.S and ORG-KB1P.R tumor organoids were derived from a PARPi-naïve and PARPi-resistant *K14cre;Brca1^{F/F};Trp53^{F/F}* (KB1P) mouse mammary tumor, respectively. The ORG-KP tumor organoid line was derived from

a *K14cre;Trp53^{F/F};Abcb1a^{-/-};Abcb1b^{-/-}* (KPM) mouse mammary tumor. Cultures were embedded in Cultrex Reduced Growth Factor Basement Membrane Extract Type 2 (BME, Trevigen; 40 ml BME:growth media 1:1 drop in a single well of 24-well plate) and grown in Advanced DMEM/F12 (Gibco) supplemented with 1M HEPES (Gibco), GlutaMAX (Gibco), 50 units/ml penicillin-streptomycin (Gibco), B27 (Gibco), 125 mM N-acetyl-L-cysteine (Sigma) and 50 ng/ml murine epidermal growth factor (Sigma). Organoids were cultured under standard conditions (37°C, 5% CO₂) and regularly tested for mycoplasma contamination.

Mice

All animal experiments were approved by the Animal Ethics Committee of The Netherlands Cancer Institute (Amsterdam, the Netherlands) and performed in accordance with the Dutch Act on Animal Experimentation (November 2014). Organoid transplantation experiments were performed in syngeneic, wild-type F1 FVB (FVB/NRj) females, at the age of 6 weeks. Parental FVB animals were purchased from Janvier Labs. Animals were assigned randomly to the treatment groups and the treatments were supported by animal technicians who were blinded regarding the hypothesis of the treatment outcome.

Human Samples of TNBC and Ovarian Serous Carcinomas

Samples were previously described in¹³. Retrospective Triple Negative Breast Cancer (TNBCs) biopsies from 86 clinical high-risk patients (high-risk definition according to the Danish Breast Cooperative Group (www.dbcg.dk accessed 22.10.2009) that underwent mastectomy between 2003 and 2015 were selected and classified as being triple negative according to the criteria set in the ASCO/CAP guidelines (ER<1%, PR<1%, HER2 0, 1+ or 2+ but FISH/ CISH negative). The patients presented a unifocal tumor of an estimated size of more than 20 mm. None of the patients had previous surgery to the breast and did not receive preoperative treatment. This study was conducted in compliance with the Helsinki II Declaration and written informed consent was obtained from all participants and approved by the Copenhagen and Frederiksberg regional division of the Danish National Committee on Biomedical Research Ethics (KF 01-069/03). Paraffin-embedded material from the cohort of ovarian tumors was collected at the Department of Pathology, University Hospital, Las Palmas, Gran Canaria, Spain, from surgical operations performed in the period 1995-2005. For the purpose of the present study, only samples from serous ovarian carcinoma (the type approved for treatment by PARP inhibitors) were used from a larger cohort that was reported previously⁵², and included also other histological types of ovarian tumors. The use of long-term stored tissue samples in this study was in accordance with the Spanish codes of conduct (Ley de Investigación Biomédica) and was approved by the review board of the participating institution. Patients were informed that samples may be used for research purposes under the premise of anonymity.

METHOD DETAILS

Functional genetic screens

The DDR shRNA library was stably introduced into *Brca1^{-/-};Trp53^{-/-};Trp53bp1^{-/-}* mESCs and in KB1P4.R1 by lentiviral transduction using a multiplicity of transduction (MOI) of 1, in order to ensure that each cell only gets incorporated with one only sgRNA. mES cells and organoids were selected with puromycin, 3 µg/ml, for 3 days and then seeded in the presence of PARPi (ImES cells, 25nM olaparib; organoids, 50nM), left untreated or pelleted for the genomic DNA isolation (T0). The total number of cells used in a single screen was calculated as following: library complexity x coverage (5000x in mESc, 1000x in organoids). Cells were kept in culture for 3 weeks and passaged every 5 days (and seeded in single cells) while keeping the coverage at every passage. mES cells were seeded at a density of 2.5 million cells per 15 cm dish and organoids at a density of 50,000 cells/well, 24-well format. Screens were done in triplicate for each condition. In the end of the screen, cells were pooled and genomic DNA was extracted (QIAmp DNA Mini Kit, Qiagen). shRNA sequences were retrieved by a two-step PCR amplification, as described before¹⁵. To maintain screening coverage, the amount of genomic DNA used as an input for the first PCR reaction was taken into account (6 µg of genomic DNA per 10⁶ genomes, 1 µg/PCR reaction). Resulting PCR products were purified using MiniElute PCR Purification Kit (Qiagen) and submitted for Illumina sequencing. Sequence alignment and dropout analysis was carried out using the algorithms MAGeCK (Li et al., 2014) (FDR ≤ 0.1) and DESeq2⁵⁹ (FDR ≤ 0.05, log2Fc ≤ -2, baseMean ≥ 100, at least 3 hit shRNA in the depletion direction and none in the opposite direction). In order to reduce the noise level, we filtered out sgRNAs with low counts in the T0 sample: mESc, sum of the three T0 samples ≥ 10, organoids, mean over the three T0 samples ≥ 50. Gene ranking is generated automatically with MaGECK algorithm. To generate gene ranking based on DESeq2 algorithm, we calculated per gene the number of hit shRNAs and the mean of the log2FoldChange over those shRNAs. We then ranked the genes based on these two metrics.

Constructs

A collection of 1,976 lentiviral hairpins targeting 391 DDR-related mouse genes (pLKO.1; DDR library) was derived from the Sigma Mission library (TRCMm1.0) as described before¹⁵. Individual hairpin constructs used in the validation studies were selected from the TRC library: mouse LIG3 shRNA #1: TRCN0000070978, mouse LIG3 shRNA #2: TRCN0000070982, mouse REV7 shRNA: TRCN0000006570, human LIG3 shRNA #1: TRCN0000048498, human LIG3 shRNA #2: TRCN0000300259. For CRISPR/Cas9-mediated genome editing of *Parp1*, a sgRNAs was cloned into plentiGuide-Puro (lentiviral) as described previously⁶⁰. For the LIG3 overexpression constructs, human α-LIG3 wild type, human α-LIG3 carrying a mutation in the PARP-like ZnF domain (R31L), and human α-LIG3 with a C-terminal Δ774-922 truncation which includes the BRCT domain were cloned into PCW57.1 plasmid. All constructs were verified by Sanger sequencing.

Lentiviral transductions

Lentiviral stocks, pseudotyped with the VSV-G envelope, were generated by transient transfection of HEK293FT cells, as described before⁶¹. Production of integration-deficient lentivirus (IDLV) stocks was carried out in a similar fashion, with the exception that the packaging plasmid contains a point mutation in the integrase gene (psPAX2, gift from Bastian Evers). Lentiviral titers were determined using the qPCR Lentivirus Titration Kit (Applied Biological Materials), following the manufacturer's instructions. For all experiments the amount of lentiviral supernatant used was calculated to achieve an MOI of 50, except for the transduction of the lentiviral library for which a MOI of 1 was used, as described above. Cells were incubated with lentiviral supernatants overnight in the presence of polybrene (8 µg/ml). Tumor-derived organoids were transduced according to a previously established protocol²⁹. Antibiotic selection was initiated right after transduction for cells, 24h after transduction in organoids, and was carried out for 3 consecutive days.

Genome editing

For CRISPR/Cas9-mediated genome editing of *Trp53* in mESCs, *R26Cre^{ERT2/wt};Brca1^{SCo/-}* cells¹⁷ were transiently transfected with a modified pX330-U6-Chimeric-BB-CBh-hSpCas9 plasmid containing a puromycin resistance marker^{62,63} in which a sgRNA targeting *Trp53* was cloned. Knockout clones were selected under puromycin for 3 days and tested by TIDE and western blot.

For CRISPR/Cas9-mediated genome editing of *Trp53bp1* in mESCs, Cas9-expressing *R26Cre^{ERT2/Cas9};Brca1^{SCo/-};Trp53^{-/-}* cells⁶⁴ were incubated with lentiviral supernatants of pLentiGuide-Puro cloned with a sgRNA targeting *Trp53bp1*. After selection with puromycin for 3 days, surviving cells were subcloned and tested by TIDE and western blot.

For CRISPR/Cas9-mediated genome editing of *Parp1*, the Cas9-expressing *R26Cre^{ERT2/Cas9}; Brca1^{-/-};Trp53^{-/-};Trp53bp1^{-/-}* mESCs were incubated with lentiviral supernatants of pLentiGuide-Puro cloned with a sgRNA targeting *Parp1*. After selection with puromycin for 3 days, surviving cells were subcloned and tested by TIDE and western blot.

For the disruption of the starting codon encoding for nuclear LIG3, the desired mutation (ATG>CTC) was introduced in KB1P.R mouse tumor cells according to the Alt-R CRISPR-Cas9 System of IDT⁶⁵. Briefly, the crRNA targeting sequence and the homology template, a 120bp ssODN, were designed using CRISPR design tools of Benchling. While the sgRNA was designed to target the nuclear ATG, the homology template contains an ATG>CTC mutation, encoding a leucine instead of the original methionine. 10 µl tracrRNA (100 µM) and 10 µl crRNA (100 µM) were annealed in 80 µl nuclease free duplex buffer (IDT#11-05-01-03) to form a 10µM gRNA solution. The ssODN template was also annealed to form a 10µM solution. 6 µl of 10 µM sgRNA, 6 µl of 10 µM Cas9 protein, and 6 µl of 10 µM ssODN (Ultramer IDT) were mixed in optiMEM (Gibco), to final volume of 125 µl and incubated for 5 min at RT (Mix 1). Then, 3µl of Lipofectamine RNAiMAX (Invitrogen) were mixed with 122 µl with optiMEM (Mix 2). Mix 1 and mix 2 were mixed together and incubated at RT for 20

min. During these 20 min, 150.000 cells were trypsinized and collected in 750 μ l of medium. The 250 μ l Mix was then added to the cells in a 12-well for reverse transfection. Next day cells were expanded and 3 days after transfection the cells were harvested for analysis of the genomic DNA.

To assess modification rate, genomic DNA was extracted (Puregene Core Kit A, Qiagen) and 100 ng was used as an input for the PCR amplification of the targeted sequence. PCR reaction was performed with Thermo Scientific Phusion High-Fidelity PCR Master Mix (Thermo Scientific), according to manufacturer's instructions (3-step protocol: annealing - 60C for 5 s, extension time 30 s) and using primers listed in **Supplementary Tab. 2**. Resulting PCR products served as a template for the BigDye Terminator v3.1 reaction (Thermo Fisher). BigDye PCR reactions were performed with the same forward primers as in the preceding PCR reactions (no reverse primer used) and according to the BigDye manufacturer's protocol. For knockout, allele composition was determined with the TIDE analysis⁶⁶ by comparing sequences from modified and parental (transduced with non-targeting sgRNAs) cells. For knock-in, allele composition was determined with the TIDER analysis⁶⁷ by comparing sequences from modified and parental cells (transduced with non-targeting sgRNAs), and reference template. The later was generated with a simple two-step PCR protocol, with two complementary primers designed to carry the designed mutations as present in the donor template (Brinkman et al. 2018).

siRNA and transfections

Non-targeting siRNA and siRNA against mouse and human LIG3 were transfected into the cells using Lipofectamine RNAiMAX (Invitrogen) according to the manufacturer's instructions. All experiments were carried out between 48 and 72hr post-transfection.

Long-Term clonogenic assays

Long-term clonogenic assays were always performed in 6-well plates, with exception of organoids which were cultured in 24-well plated as described before, and to DLD-1 cells which was performed in a 12-well plate. Cells were seeded at low density to avoid contact inhibition between the clones (KB1P.S: 5,000 cells/well; KB1P.R: 2,500 cells/well; ORG-KB1P.S and ORG-KB1P.R: 50.000 cells/well; ES-B1P.R and ES-P.R: 3,000 cells/well; ES-B1P.S and ES-P: 5,000 cells/well; SUM149PT: 5,000 cells/well; RPE1-P: 3,000 cells/well, RPE1-B1P.S and RPE1-B1P.R: 5,000 cells/well; DLD-1: 3,500 cells/well; DLD-1 BRCA2 KO cells: 5,000) and cultured for 10-15 days. Media was refreshed once a week. For the quantification, cells were incubated with Cell-Titer Blue (Promega) reagent and later fixed with 4% formaldehyde and stained with 0.1% crystal violet. Drug treatments: cells were grown in the continuous presence of PARPi (olaparib, talazoparib or veliparib) at the indicated concentrations. mESCs with a selectable conditional *Brca1* deletion were treated with 0.5 μ M 4OHT for 3 days right before the start of the clonogenic assay, when indicated. PARPis were reconstituted in DMSO (10 mM) and 4OHT in EtOH (2.5 mM). Expression of

human LIG3 constructs was induced with treatment with 2 μ M Doxycycline for two days prior to the start of the assay and at the start of the assay.

Proliferation assay

Cells were imaged every 4h using IncuCyte®, for 1 week duration. Cells were seeded at low density and grown under normal oxygen conditions (21% O₂, 5% CO₂, 37°C). Data was analyzed using IncuCyte ZOOM 2018A software.

RT-qPCR

In order to determine gene expression levels, RNA was extracted from cultured cells using ISOLATE II RNA Mini Kit (Bioline) and used as a template to generate cDNA with Tetro cDNA Synthesis Kit (Bioline). Quantitative RT-PCR was performed using SensiMix SYBR Low-ROX Kit (Bioline; annealing temperature – 60°C) in a Lightcycler 480 384-well plate (Roche), and analyzed using Lightcycler 480 Software v1.5 (Roche). Mouse *Rps20* and human *HPRT* were used as house-keeping genes. The primer sequences used in this study are listed in **Supplementary table 2**.

Western Blot

Cells were trypsinized and then lysed in lysis buffer (20 mM Tris pH 8.0, 300 mM NaCl, 2% NP40, 20% glycerol, 10 mM EDTA, protease inhibitors (cOmplete Mini EDTA-free, Roche, 100x stock)), for 20 min. For PAR detection in PARP1 knockout mES cells, 10 μ M PARGi was added to the lysis buffer, when indicated. For P53 detection, cells were irradiated at 15 x 100 μ J/cm². The protein concentration was determined using Pierce BCA Protein Assay Kit (Thermo Scientific). SDS-Page was carried out with the Invitrogen NuPAGE SDS-PAGE Gel System (Thermo Fisher; for LIG3: 2-8% Tris-acetate gels were used, buffer Tris-Acetate; for all other proteins: 4–12% Bis-Tris gels were used, buffer: MOPS; input: 40 μ g protein), according to the manufacturer's protocol. Next, proteins were electrophoretically transferred to a nitrocellulose membrane (Biorad). Before blocking, membranes were stained with Ponceau S, followed by blocking in 5% (w/v) milk in TBS-T for 1 hr at RT. Membranes were incubated with primary antibody 4hrs at RT in 1% (w/v) milk in TBS-T (rabbit anti-PARP1, 1:1000; rabbit anti-H3, 1:5000; mouse anti-lig3, 1:500; rabbit anti-lig3, 1:1000; rabbit anti-tubulin, 1:1000; anti-PAR, 1:1000; mouse anti-P53, 1:1000). Horseradish peroxidase (HRP)-conjugated secondary antibody incubation was performed for 1 hr at RT (anti-mouse or anti-rabbit HRP 1:2000) in 1% (w/v) milk in TBS-T. Signals were visualized by ECL (Pierce ECL Western Blotting Substrate, Thermo Scientific).

Cytotoxicity assays

Cytotoxicity assays were carried in 96-well plates, for 3 days. Olaparib and POL θ inhibitor ART558 were used at the indicated concentrations. Olaparib was used at concentrations that wouldn't lead to lethality of LIG3-depleted cells when used as single agent in order

to allow a window to detect the effect of POLθ inhibition. KB1P.R and KB1P.R A3 cells were seeded at high density, 2,000 cells/well. For the quantification, cells were incubated with Cell-Titer Blue (Promega) reagent. The expected drug combination responses were calculated based on Bliss reference model using SynergyFinder⁶⁸.

Proximity ligation assay (PLA)

Protocol was carried out as mentioned previously ⁴⁵. On coverslips, cells were grown to a confluence of 60-70%. On the day of the experiment, cells were incubated with PARGi (10μM) for a total of 30 minutes or 0.5μM olaparib for 2hr and the final 10 minutes cells were incubated with EdU (20μM) during PARGi incubation to visualize S-phase cells. After EdU labeling cells were gently washed two times with PBS and fixed with 4% paraformaldehyde for 15 min at RT. PFA was discarded after fixation and slides were washed with cold PBS for 8 minutes each three times. Cells were next permeabilized by incubating the coverslips in PBS containing 0.5% Triton-X for 15 min at RT and subsequently washed in PBS twice for 5 min each. Freshly prepared click reaction mix (2mM of copper sulfate, 10 μM of biotin-azide and 100 mM of sodium ascorbate were added to PBS in that order and mixed well) was applied to the slides (30 μl/slide) in a humid chamber and incubated for 1 hr at RT. Slides were washed with PBS for 5 min after the click reaction and placed back in the humid chamber and blocked at room temperature for 1 hr with a blocking buffer (10% goat serum and 0.1% Triton X-100 in PBS). In combination with anti-biotin (1:1000), rabbit anti-LIG3 (1:150, Sigma-Aldrich, #HPA006723) primary antibody was diluted in a blocking solution, dispensed to slides (30 μl/slide) and incubated in a humid chamber at 4°C overnight. Slides were washed with wash buffer A (0.01 M Tris-HCl, 0.15 M NaCl, and 0.05 % Tween-20, pH 7.4) for 5 min each after overnight incubation. Duolink In Situ PLA probes, the anti-mouse plus and anti-rabbit minus were diluted 1:5 in the blocking solution (10% goat serum and 0.1% Triton X-100 in PBS), dispensed to slides (30 μl/well) and incubated at 37°C for 1 hr. Slides were washed three times with buffer-A, 5 min each. The ligation mix was prepared by diluting Duolink ligation stock (1:5) and ligase (1:40) in high purity water and was applied to slides (30 μl/well) and incubated at 37°C for 30 min. Slides were washed with buffer-A twice for 2 min each. Amplification mix was prepared by diluting Duolink amplification stock (1:5) and rolling circle polymerase (1:80) in high-purity water and applied to slides (30μl /well) and incubated for 100 min at 37°C in a humid chamber. Slides were washed with wash buffer-B solution (0.2 M Tris and 0.1 M NaCl) three times for 10 min each and one time in 0.01X diluted wash buffer-B solution for 1 min. Coverslips were incubated with DAPI for 5 min and mounted with ProLong Gold antifade reagent (Invitrogen) and imaged using confocal and analyzed using ImageJ software ⁶⁴.

Immunofluorescence

RAD51 IRIF

Cells were seeded on Millicell EZ slides (#PEZGS0816, Millipore) 24 hr prior the assay to achieve ~90% confluency. Cells were then irradiated using the Gammacell 40 Extractor

(Best Theratronics Ltd.) at the dose of 10 Gy and allowed to recover for 3 hr. Cells washed with PBS++ (PBS solution containing 1 mM CaCl₂ and 0.5 mM MgCl₂) and pre-extracted with 0.5% (v/v) Triton X-100 in PBS++ for 5 min. Next, cells were washed with PBS++ and fixed with 2% (v/v) paraformaldehyde solution in PBS for 20 min. Next, cells were permeabilized with ice-cold methanol/acetone solution (1:1) for 15 min. To minimize the background, cells were further incubated for 20 min in staining buffer (1% (w/v) BSA, 1% (v/v) FBS, 0.15% (w/v) glycine and 0.1% (v/v) Triton X-100 in PBS). Staining buffer was also used as a solvent for antibodies – primary antibody anti-RAD51, 1:1500, #ab133534, abcam; secondary antibody Alexa Fluor® 658-conjugated, 1:1000, A11011, Invitrogen. Incubation with primary and secondary antibodies was done for 2 hr and 1 hr, respectively. All incubations were performed at room temperature. Samples were mounted with VECTASHIELD Hard Set Mounting Media with DAPI (#H-1500; Vector Laboratories). Images were captured with Leica SP5 (Leica Microsystems) confocal system and analyzed using an in-house developed macro to automatically and objectively evaluate the DNA damage-induced foci¹⁵. As a positive and negative control for RAD51 staining, BRCA-proficient KP and BRCA1-deficient KB1P.S cells were used.

LIG3-EdU co-localization

Cells were incubated with 20 μM EdU for 1 hr to visualize cells in S-phase. In the last 20 min, 10 μM PARGi was added to the medium. Cells washed with PBS and pre-extracted with CSK50 buffer for 7 min (10 μM PARGi PDDX-001 was added to pre-extraction buffer). Cells were washed with PBS and fixed with 4% formaldehyde, followed by three washes with PBS and permeabilization with ice-cold methanol/acetone solution (1:1). EdU Click-iT reaction mix was added to each well and incubated at RT for 30 min. Fixed cells were washed three times with staining buffer (5% (v/v) FBS, 5% (w/v) BSA, and 0.05% (v/v) Tween-20 in PBS) and incubated with primary antibody anti-LIG3 (1:150, Sigma-Aldrich, #HPA006723) in staining buffer for 2 hr at RT. After three washes in staining buffer, cells were incubated with secondary antibody anti-rabbit Alexa Fluor 488 (1:500, A27034, Invitrogen) in staining buffer, followed by three last washes in staining buffer and one wash in PBS. Samples were mounted with VECTASHIELD Hard Set Mounting Media with DAPI (#H-1500; Vector Laboratories). Images were captured with Leica SP5 (Leica Microsystems) confocal system and analyzed with ImageJ software.

Native BrdU

Cells were labeled with 10 μM BrdU for 48 hr. When indicated, cells were incubated with Mirin (25 μM) for the same 48 hr. Upon treatment with the final 2 hr PARPi inhibitor (0.5 μM), the cells were washed with PBS and pre-extracted by CSK-buffer (PIPES 10 mM, NaCl 100 mM, Sucrose 300 mM, EGTA 250 mM, MgCl₂ 1 mM, DTT 1 mM and protease inhibitors cocktail) on ice for 5 minutes. Cells were then fixed using 4% formaldehyde (FA) for 15 min at RT, and then permeabilized by 0.5% Triton X-100 in CSK-buffer. Permeabilized cells were

then incubated with primary antibody against anti-BrdU antibody (Abcam 6326) at 37°C for 1 hr. Cells were washed and incubated with secondary antibodies (Alexa Fluor 594) for 1h at room temp. After the wash cells were incubated with DAPI (0.1µg/ml) for 5 minutes. For mouse tumor cells (high content imaging), DAPI and ssDNA signal, Z-stack of 6 stacks (1mm/stack) covering at least 75 fields were imaged. Results were analyzed using DAPI channel and filtered with roundness and size of the nucleus. The quantification of pixel intensities (mean, median and sum) for each nucleus was calculated in the DAPI and 594 nm channels. The quantified values obtained were exported to Tibco spotfire software (TIBCO Spotfire®) for the generation of scatter plots. For human RPE1 cells, images were collected by fluorescence microscopy (Axioplan 2 and Axio Observer, Zeiss) at a constant exposure time in each experiment. Representative images were processed by ImageJ software. Mean intensities of ssDNA in each nucleus were measured with Cell Profiler software version 3.1.5 from Broad Institute.

H2AX foci

Cells were incubated treated for 2hr with PARPi inhibitor (0.5µM). Cells were then washed with PBS and fixed with 4% formaldehyde, followed by three washes with PBS and permeabilization with ice-cold methanol/acetone solution (1:1). Fixed cells were washed three times with staining buffer (5% (v/v) FBS, 5% (w/v) BSA, and 0.05% (v/v) Tween-20 in PBS) and incubated with primary antibody anti-H2AX (Ser139) (1:1000, Cell Signaling, Cat#2577) in staining buffer for 2hr at RT. After three washes in staining buffer, cells were incubated with secondary antibody anti-rabbit Alexa Fluor 488 (1:500, A27034, Invitrogen) in staining buffer, followed by three last washes in staining buffer and one wash in PBS. Samples were mounted with VECTASHIELD Hard Set Mounting Media with DAPI (#H-1500; Vector Laboratories). Images were captured with Leica SP5 (Leica Microsystems) confocal system and analyzed with ImageJ software.

DNA Fiber assay

Mouse tumor cells

DNA fiber analysis was conducted in accordance with the previously described protocol⁶⁹. Briefly, cells were transfected for 48 hours followed by treatment with olaparib (0.5µM), or left untreated, for the final two hours. Cells were sequentially pulse-labelled with nucleotide analogues, 30µM CldU (c6891, Sigma-Aldrich) and 250µM IdU (I0050000, European Pharmacopoeia) for 20 min during the incubation of olaparib. After double labelling, cells were washed with PBS, harvested and resuspended in ice cold PBS to the final concentration 2.5×10^5 cells per ml. Labelled cells were mixed with unlabeled cells at 1:1 (v/v), and 2.5 µl of cell suspension was spotted at the end of the microscope slide. 8 µl of lysis buffer (200mM Tris-HCl, pH 7.5, 50mM EDTA, and 0.5% (w/v) SDS) was applied on the top of the cell suspension, then mixed by gently stirring with the pipette tip and incubated for 8 min. Following cell lysis, slides were tilted to 15–45° to allow the DNA fibers spreading

along the slide, air dried, fixed in 3:1 methanol/acetic acid overnight at 4 °C. Subsequently, fibers were denatured with 2.5 M HCl for 1 hr. After denaturation, slides were washed with PBS and blocked in blocking solution (0.2% Tween 20 in 1% BSA/PBS) for 40 min. After blocking, primary antibody solutions are applied, anti-BrdU antibody recognizing CldU (1:500, ab6326; Abcam) and IdU (1:100, B44, 347580; BD) for 2 hours in the dark at RT followed by 1h incubation with secondary antibodies: anti-mouse Alexa Fluor 488 (1:300, A11001, Invitrogen) and anti-rat Cy3 (1:150, 712-166-153, Jackson Immuno-Research Laboratories, Inc.). Finally, slides are washed with PBS and subsequently mounting medium is spotted and coverslips are applied by gently pressing down. Slides were sealed with nail polish and air dried. Fibers were visualized and imaged by Carl Zeiss Axio Imager D2 microscope using 63X Plan Apo1.4 NA oil immersion objective. Data analysis was carried out with ImageJ software⁶⁴.

RPE1-hTERT cells

These assays were performed as previously described^{43,70}. Briefly, cells were treated for 2 hr with 0.5μM olaparib or left untreated. During the last 40 min, cells were labeled by sequential incorporation of IdU and CldU into nascent DNA strand. Cells were then collected, washed, spotted, and lysed on positively charged microscope slides by 7.5 mL spreading buffer for 8 min at RT. Individual DNA fibers were released and spread by tilting the slides at 45°C. After air-drying, fibers were fixed by 3:1 methanol/acetic acid at RT for 3 min. Fibers were then rehydrated in PBS, denatured with 2.5 M HCl for 30 min, washed with PBS, and blocked with blocking buffer for 1 hr. Next, slides were incubated for 2.5 hr with primary antibodies diluted in blocking buffer (IdU, B44, 347580; BD; CldU, ab6326, Abcam), washed several times in PBS, and then incubated with secondary antibodies in blocking buffer for 1 hr (IdU, goat anti-mouse, Alexa 488; CldU, goat anti-rat, Alexa Fluor 594). After washing and air-drying, slides were mounted with Prolong (Invitrogen, P36930). Finally, fibers were visualized and imaged with Axioplan 2 imaging, Zeiss.

Metaphase spreads and telomere FISH

Metaphase spreads were carried out according to the standard protocol described previously⁴⁵. Briefly, exponentially growing cells (50–80 % confluence) were treated with 0.5μM olaparib for 2hr or left untreated, and recovered for 6 hr. Post treatment, drug treated medium was washed out and cells were allowed to grow in complete growth medium and exposed with colcemid for 8h. Metaphase spreads were prepared by conventional methods and check under the microscope before telomere labelling. Metaphase slides in coplin jar containing 2X SSC buffer (Sigma-S6639) were equilibrated at room temperature for 10 minutes. Proteins were digested by incubation of the slides in pre-warmed 0.01M HCl containing pepsin for 1.5 min at 37°C. Slides were washed twice with PBS 5 min each and then one time with 1 M MgCl₂ in 1X PBS for 5 min. After washing slides were placed in coplin jar containing 1% formaldehyde and fixed for 10 mins at RT without shaking. Slides

were washed with PBS and dehydrated in the ethanol series: 70%, 90% and 100% for 3 minutes each and air dried. Next, slides were denatured in 70% deionized formamide at 80°C for 1 min 15 sec and immediately placed in chilled ethanol series 70%, 90% and 100% for 3 minutes each and allowed slides for air dry. Pre-annealed telomere probes were added to the denatured slides and allowed for hybridization at 37°C in hybridization chamber for 40 minutes. After hybridization slides were washed sequentially 3 times each with 50% formamide in 2X SSC (preheated to 45°C), 0.1X SSC (preheated to 60°C), 4X SSC (0.1% Tween-20), and 2X SSC respectively. Slides were allowed to air dry and mounted using DAPI anti-fade. A minimum 60 metaphase images were captured using Carl Zeiss Axio Imager D2 microscope using 63x Plan Apo 1.4 NA oil immersion objective and analyzed with ImageJ software⁶⁴ for chromosomal aberrations.

Electron microscopy analysis

EM analysis was performed according to the standard protocol⁷¹. For DNA extraction, cells were lysed in lysis buffer and digested at 50 °C in the presence of Proteinase-K for 2hr. The DNA was purified using chloroform/isoamyl alcohol and precipitated in isopropanol and given 70% ethanol wash and resuspended in elution buffer (TE). Isolated genomic DNA was digested with PvuII HF restriction enzyme for 4 to 5 hr. Replication intermediates were enriched by using QIAGEN G-100 columns (as manufacture's protocol) and concentrated by an Amicon size-exclusion column. The benzyldimethylalkylammonium chloride (BAC) method was used to spread the DNA on the water surface and then loaded on carbon-coated nickel grids and finally DNA was coated with platinum using high-vacuum evaporator MED 010 (Bal Tec). Microscopy was performed with a transmission electron microscope FEI Talos, with 4 K by 4 K cmos camera. For each experimental condition, at least 70 RF intermediates were analyzed per experiment and ImageJ software⁶⁴ was used to process analyze the images.

DSB detection by PFGE

DSB detection by PFGE was done as reported previously⁷². Cells were casted into 0.8% agarose plugs (2.5x10⁵ cells/plug), digested in lysis buffer (100mM EDTA, 1% sodium lauryl sarcosine, 0.2% sodium deoxycholate, 1 mg/ml proteinase-K) at 37 °C for 36–40 h, and washed in 10mM Tris-HCl (pH 8.0)–100mM EDTA. Electrophoresis was performed at 14 °C in 0.9% pulse field-certified agarose (Bio-Rad) using Tris-borate-EDTA buffer in a Bio-Rad Chef DR III apparatus (9h, 120°, 5.5V/cm, and 30- to 18-s switch time; 6h, 117°, 4.5V/cm, and 18- to 9-s switch time; and 6h, 112°, 4V/cm, and 9- to 5-s switch time). The gel was stained with ethidium bromide and imaged on Uvidoc-HD2 Imager. Quantification of DSB was carried out using ImageJ software⁶⁴. Relative DSB levels were calculated by comparing the results in the treatment conditions to that of the DSB level observed in untreated controls.

In vivo studies

Tumor organoids were collected, incubated with TripLE at 37°C for 10 min, dissociated into single cells, resuspended in tumor organoid medium, filtered with 70µm nylon filters (Corning) and resuspended in complete mouse media/BME mixture (1:1). KB1P4.N1 and KB1P4.R1 organoid suspensions contained a total of 20.000 and 10.000 cells, respectively, per 40 µl of media/BME mixture, and were injected in the fourth right mammary fat pad of wild-type FVB/N mice. Mammary tumor size was determined by caliper measurements (length and width in millimeters), and tumor volume (in mm³) was calculated by using the following formula: $0.5 \times \text{length} \times \text{width}^2$. Upon tumor outgrowth to approximately 75 mm³, in mice injected with N1 organoids, and 40 mm³, in mice injected with R1 organoids, mice were treated with vehicle, or olaparib (50 mg/kg, mice injected with N1 organoids; 100 mg/kg, mice injected with R1 organoids) intraperitoneally for 28 consecutive days. Animals were sacrificed with CO₂ when the tumor volume reached 1,500 mm³.

Immunohistochemistry analysis

Five-µm tissue sections were cut from formalin-fixed, paraffin-embedded tissue blocks from a cohort of 86 TNBC¹³ and 51 human serous ovarian carcinomas⁵² and mounted on Super Frost Plus slides (Menzel-Glaser, Braunschweig, Germany), baked at 60°C for 60 min, deparaffinized, and rehydrated through graded alcohol rinses. Heat induced antigen retrieval was performed by immersing the slides in citrate pH 6.0 buffer and heating them in a 750 W microwave oven for 15 min. The sections were then stained with primary antibody anti-LIG3 (1: 250, Sigma-Aldrich, #HPA006723) overnight in a cold-room, followed by subsequent processing by the indirect streptavidin-biotin-peroxidase method using the Vectastain Elite kit (Vector Laboratories, Burlingame, CA, USA) and nickel-sulphate-based chromogen enhancement detection as previously described⁷³, without nuclear counterstaining. For negative controls, sections were incubated with non-immune sera. The results were evaluated by two experienced researchers, including a senior oncopathologist, and the data expressed as percentage of positive tumor cells within each lesion, while recording frequencies of cases with LIG3 overabundant (LIG3-high) or lost (LIG3-low) staining in 10-20% and in excess of 20% of the tumor cells (see Figure 6G for examples of staining patterns). Cases with over 90% of cancer cells showing a staining intensity comparable with surrounding stromal cells on the same section (internal control) were regarded as displaying a normal pattern of LIG 3 expression.

DATA AND SOFTWARE AVAILABILITY

Original western blot, agarose gel and microscopy images have been deposited at Mendeley and are publicly available as of the date of publication: <https://doi.org/10.17632/d2t837shk9.1>. Microscopy data reported in this paper is available from the lead contact upon request. This paper does not report original code. Any additional information required to reanalyze the data reported in this paper is available from the lead contact upon request.

REFERENCES

1. Farmer, H. *et al.* Targeting the DNA repair defect in BRCA mutant cells as a therapeutic strategy. *Nature* **434**, 917–21 (2005).
2. Bryant, H. E. *et al.* Specific killing of BRCA2-deficient tumours with inhibitors of poly(ADP-ribose) polymerase. *Nature* **434**, 913–917 (2005).
3. Ray Chaudhuri, A. & Nussenzweig, A. The multifaceted roles of PARP1 in DNA repair and chromatin remodelling. (2017). doi:10.1038/nrm.2017.53
4. Hanzlikova, H. *et al.* The Importance of Poly(ADP-Ribose) Polymerase as a Sensor of Unligated Okazaki Fragments during DNA Replication. *Mol. Cell* **71**, 319–331.e3 (2018).
5. Pascal, J. M. & Ellenberger, T. The rise and fall of poly(ADP-ribose): An enzymatic perspective. *DNA Repair (Amst)*. **32**, 10–16 (2015).
6. Murai, J. *et al.* Trapping of PARP1 and PARP2 by clinical PARP inhibitors. *Cancer Res.* **72**, 5588–5599 (2012).
7. Murai, J. *et al.* Stereospecific PARP trapping by BMN 673 and comparison with olaparib and rucaparib. *Mol. Cancer Ther.* **13**, 433–443 (2014).
8. Helleday, T. The underlying mechanism for the PARP and BRCA synthetic lethality: Clearing up the misunderstandings. *Molecular Oncology* **5**, 387–393 (2011).
9. Lupo, B. & Trusolino, L. Inhibition of poly(ADP-ribosylation) in cancer: Old and new paradigms revisited. *Biochimica et Biophysica Acta - Reviews on Cancer* **1846**, 201–215 (2014).
10. Paes Dias, M., Moser, S. C., Ganesan, S. & Jonkers, J. Understanding and overcoming resistance to PARP inhibitors in cancer therapy. *Nature Reviews Clinical Oncology* 1–19 (2021). doi:10.1038/s41571-021-00532-x
11. Rottenberg, S. *et al.* High sensitivity of BRCA1-deficient mammary tumors to the PARP inhibitor AZD2281 alone and in combination with platinum drugs. *Proc. Natl. Acad. Sci. U. S. A.* **105**, 17079–17084 (2008).
12. Pettitt, S. J. *et al.* Genome-wide and high-density CRISPR-Cas9 screens identify point mutations in PARP1 causing PARP inhibitor resistance. *Nat. Commun.* **9**, 1849 (2018).
13. Gogola, E. *et al.* Selective Loss of PARG Restores PARylation and Counteracts PARP Inhibitor-Mediated Synthetic Lethality. *Cancer Cell* **33**, 1078–1093.e12 (2018).
14. Ray Chaudhuri, A. *et al.* Replication fork stability confers chemoresistance in BRCA-deficient cells. *Nature* **535**, 382–387 (2016).
15. Xu, G. *et al.* REV7 counteracts DNA double-strand break resection and affects PARP inhibition. *Nature* **521**, 541–544 (2015).
16. Boersma, V. *et al.* MAD2L2 controls DNA repair at telomeres and DNA breaks by inhibiting 5' end resection. *Nature* **521**, 537–40 (2015).
17. Bouwman, P. *et al.* 53BP1 loss rescues BRCA1 deficiency and is associated with triple-negative and BRCA-mutated breast cancers. *Nat. Struct. Mol. Biol.* **17**, 688–695 (2010).
18. Bunting, S. F. *et al.* 53BP1 Inhibits Homologous Recombination in Brca1-Deficient Cells by Blocking Resection of DNA Breaks. *Cell* **141**, 243–254 (2010).
19. Chapman, J. R. *et al.* RIF1 Is Essential for 53BP1-Dependent Nonhomologous End Joining and Suppression of DNA Double-Strand Break Resection. *Mol. Cell* **49**, 858–871 (2013).
20. Escribano-Díaz, C. *et al.* A Cell Cycle-Dependent Regulatory Circuit Composed of 53BP1-RIF1 and BRCA1-CtIP Controls DNA Repair Pathway Choice. *Mol. Cell* **49**, 872–883 (2013).
21. Noordermeer, S. M. *et al.* The shieldin complex mediates 53BP1-dependent DNA repair. *Nature* **560**, 117–121 (2018).
22. Ghezraoui, H. *et al.* 53BP1 cooperation with the REV7–shieldin complex underpins DNA structure-specific NHEJ. *Nature* **560**, 122–127 (2018).
23. Dev, H. *et al.* Shieldin complex promotes DNA end-joining and counters homologous recombination in BRCA1-null cells. *Nat. Cell Biol.* **20**, 954–965 (2018).
24. Barazas, M. *et al.* Radiosensitivity Is an Acquired Vulnerability of PARPi-Resistant BRCA1-Deficient Tumors. *Cancer Res.* **79**, 452–460 (2019).
25. Caldecott, K. W., Aoufouchi, S., Johnson, P. & Shall, S. XRCC1 polypeptide interacts with DNA polymerase β and possibly poly (ADP-ribose) polymerase, and DNA ligase III is a novel molecular 'nick-sensor' in vitro. *Nucleic Acids Res.* **24**, 4387–4394 (1996).
26. Cappelli, E. *et al.* Involvement of XRCC1 and DNA ligase III gene products in DNA base excision repair. *J. Biol. Chem.* **272**, 23970–23975 (1997).
27. Wang, H. *et al.* DNA ligase III as a candidate component of backup pathways of nonhomologous end joining. *Cancer Res.* **65**, 4020–4030 (2005).
28. Simsek, D. *et al.* Crucial role for DNA ligase III in mitochondria but not in Xrcc1-dependent repair. *Nature* **471**, 245–8 (2011).
29. Duarte, A. A. *et al.* BRCA-deficient mouse mammary tumor organoids to study cancer-drug resistance. *Nat. Methods* **15**, 134–140 (2018).

30. Jaspers, J. E. *et al.* Loss of 53BP1 Causes PARP Inhibitor Resistance in *Brca1* -Mutated Mouse Mammary Tumors. *Cancer Discov.* **3**, 68–81 (2013).
31. Evers, B. *et al.* Selective Inhibition of BRCA2-Deficient Mammary Tumor Cell Growth by AZD2281 and Cisplatin. *Clin. Cancer Res.* **14**, 3916–3925 (2008).
32. Pettitt, S. J. *et al.* A genetic screen using the PiggyBac transposon in haploid cells identifies Parp1 as a mediator of olaparib toxicity. *PLoS One* **8**, e61520 (2013).
33. Lakshminpathy, U. & Campbell, C. The human DNA ligase III gene encodes nuclear and mitochondrial proteins. *Mol. Cell. Biol.* **19**, 3869–76 (1999).
34. Puebla-Osorio, N., Lacey, D. B., Alt, F. W. & Zhu, C. Early Embryonic Lethality Due to Targeted Inactivation of DNA Ligase III. *Mol. Cell. Biol.* **26**, 3935–3941 (2006).
35. Taylor, R. M., Whitehouse, C. J. & Caldecott, K. W. The DNA ligase III zinc finger stimulates binding to DNA secondary structure and promotes end joining. *Nucleic Acids Res.* **28**, 3558–3563 (2000).
36. Caldecott, K. W., McKeown, C. K., Tucker, J. D., Jungquist, S. & Thompson, L. H. An interaction between the mammalian DNA repair protein XRCC1 and DNA ligase III. *Mol. Cell. Biol.* **14**, 68–76 (1994).
37. Mateos-Gomez, P. A. *et al.* Mammalian polymerase θ promotes alternative NHEJ and suppresses recombination. *Nature* **518**, 254–7 (2015).
38. Ceccaldi, R. *et al.* Homologous recombination-deficient tumors are hyper- dependent on POLQ-mediated repair. *Nature* **518**, 258–262 (2015).
39. Zhou, J. *et al.* Polymerase Theta Inhibition Kills Homologous Recombination Deficient Tumors. *bioRxiv* 2020.05.23.111658 (2020).
40. Zatreanu, D. *et al.* Pol θ inhibitors elicit BRCA-gene synthetic lethality and target PARP inhibitor resistance. *Nat. Commun.* **12**, 3636 (2021).
41. Sriramachandran, A. M. *et al.* Genome-wide Nucleotide-Resolution Mapping of DNA Replication Patterns, Single-Strand Breaks, and Lesions by GLOE-Seq II Genome-wide Nucleotide-Resolution Mapping of DNA Replication Patterns, Single-Strand Breaks, and Lesions by GLOE-Seq. (2020).
42. Arakawa, H. & Iliakis, G. Alternative Okazaki Fragment Ligation Pathway by DNA Ligase III. *Genes (Base)*. **6**, 385–398 (2015).
43. Cong, K. *et al.* Replication gaps are a key determinant of PARP inhibitor synthetic lethality with BRCA deficiency. *Mol. Cell* (2021).
44. Tagliatalata, A. *et al.* Restoration of Replication Fork Stability in BRCA1- and BRCA2-Deficient Cells by Inactivation of SNF2-Family Fork Remodelers. *Mol. Cell* **68**, 414–430.e8 (2017).
45. Mukherjee, C. *et al.* RIF1 promotes replication fork protection and efficient restart to maintain genome stability. *Nat. Commun.* **10**, 3287 (2019).
46. James, D. I. *et al.* First-in-class chemical probes against poly(ADP-ribose) glycohydrolase (PARG) inhibit DNA repair with differential pharmacology to olaparib. *ACS Chem. Biol.* **11**, 3179–3190 (2016).
47. Panzarino, N. J. *et al.* Replication gaps underlie BRCA deficiency and therapy response. *Cancer Res.* **81**, 1388–1397 (2021).
48. Quinet, A. *et al.* PRIMPOL-Mediated Adaptive Response Suppresses Replication Fork Reversal in BRCA-Deficient Cells. *Mol. Cell* **77**, 461–474.e9 (2020).
49. Toledo, L. I. *et al.* ATR Prohibits Replication Catastrophe by Preventing Global Exhaustion of RPA. *Cell* **155**, 1088–1103 (2013).
50. Hashimoto, Y., Chaudhuri, A. R., Lopes, M. & Costanzo, V. Rad51 protects nascent DNA from Mre11-dependent degradation and promotes continuous DNA synthesis. *Nat. Struct. Mol. Biol.* **17**, 1305–1311 (2010).
51. Schlacher, K. *et al.* Double-strand break repair-independent role for BRCA2 in blocking stalled replication fork degradation by MRE11. *Cell* **145**, 529–542 (2011).
52. Moudry, P. *et al.* TOPBP1 regulates RAD51 phosphorylation and chromatin loading and determines PARP inhibitor sensitivity. *J. Cell Biol.* **212**, 281–288 (2016).
53. Branzei, D. & Szakal, B. DNA damage tolerance by recombination: Molecular pathways and DNA structures. *DNA Repair (Amst)*. **44**, 68–75 (2016).
54. Piberger, A. L. *et al.* PrimPol-dependent single-stranded gap formation mediates homologous recombination at bulky DNA adducts. *Nat. Commun.* **11**, (2020).
55. García-Gómez, S. *et al.* PrimPol, an Archaic Primase/Polymerase Operating in Human Cells. *Mol. Cell* **52**, 541 (2013).
56. Fumasoni, M., Zwicky, K., Vanoli, F., Lopes, M. & Branzei, D. Error-Free DNA Damage Tolerance and Sister Chromatid Proximity during DNA Replication Rely on the Pol α /Primase/Ctf4 Complex. *Mol. Cell* **57**, 812–823 (2015).
57. Maya-Mendoza, A. *et al.* High speed of fork progression induces DNA replication stress and genomic instability. *Nature* **559**, 279–284 (2018).
58. Bouwman, P. *et al.* A High-Throughput Functional Complementation Assay for Classification of BRCA1 Missense Variants. *Cancer Discov.* **3**, 1142–1155 (2013).
59. Love, M. I., Huber, W. & Anders, S. Moderated estimation of fold change and dispersion for RNA-seq data with

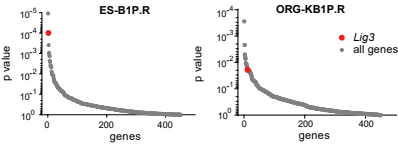
- DESeq2. *Genome Biol.* **15**, 550 (2014).
60. Sanjana, N. E., Shalem, O. & Zhang, F. Improved vectors and genome-wide libraries for CRISPR screening. *Nature Methods* **11**, 783–784 (2014).
 61. Follenzi, A., Ailles, L. E., Bakovic, S., Geuna, M. & Naldini, L. Gene transfer by lentiviral vectors is limited by nuclear translocation and rescued by HIV-1 pol sequences. *Nat. Genet.* **25**, 217–222 (2000).
 62. Cong, L. *et al.* Multiplex Genome Engineering Using CRISPR/Cas Systems. *Science (80-.)*. **339**, 819–823 (2013).
 63. Drost, R. *et al.* BRCA1185delAG tumors may acquire therapy resistance through expression of RING-less BRCA1. *J. Clin. Invest.* **126**, 2903–2918 (2016).
 64. Barazas, M. *et al.* The CST Complex Mediates End Protection at Double-Strand Breaks and Promotes PARP Inhibitor Sensitivity in BRCA1-Deficient Cells. *Cell Rep.* **23**, 2107–2118 (2018).
 65. Yoshimi, K. *et al.* ssODN-mediated knock-in with CRISPR-Cas for large genomic regions in zygotes. *Nat. Commun.* **7**, 10431 (2016).
 66. Brinkman, E. K., Chen, T., Amendola, M. & van Steensel, B. Easy quantitative assessment of genome editing by sequence trace decomposition. *Nucleic Acids Res.* **42**, e168–e168 (2014).
 67. Brinkman, E. K. *et al.* Easy quantification of template-directed CRISPR/Cas9 editing. *Nucleic Acids Res.* **46**, e58–e58 (2018).
 68. Ianevski, A., Giri, A. K. & Aittokallio, T. SynergyFinder 2.0: visual analytics of multi-drug combination synergies. *Nucleic Acids Res.* **48**, W488–W493 (2020).
 69. Ray Chaudhuri, A. *et al.* Topoisomerase i poisoning results in PARP-mediated replication fork reversal. *Nat. Struct. Mol. Biol.* **19**, 417–423 (2012).
 70. Peng, M. *et al.* Opposing Roles of FANCD1 and HLF Protect Forks and Restrain Replication during Stress. *Cell Rep.* **24**, 3251–3261 (2018).
 71. Zellweger, R. *et al.* Rad51-mediated replication fork reversal is a global response to genotoxic treatments in human cells. *J. Cell Biol.* **208**, 563–579 (2015).
 72. Cornacchia, D. *et al.* Mouse Rif1 is a key regulator of the replication-timing programme in mammalian cells. *EMBO J.* **31**, 3678–3690 (2012).
 73. Bartkova, J. *et al.* DNA damage response as a candidate anti-cancer barrier in early human tumorigenesis. *Nature* **434**, 864–870 (2005).

SUPPLEMENTARY FILES

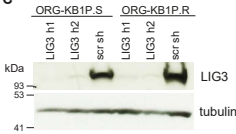
A

Cell line	Genotype	Cell line	Genotype
ORG-KB1P.R	<i>Brca1</i> ^{-/-} ; <i>Trp53</i> ^{-/-} ; <i>Trp53bp1</i> ^{-/-}	ES-P.R	<i>Brca1</i> ^{SCo} ; <i>Trp53</i> ^{-/-} ; <i>Trp53bp1</i> ^{-/-}
KB1P.R		ES-B1P.R	<i>Brca1</i> ^{-/-} ; <i>Trp53</i> ^{-/-} ; <i>Trp53bp1</i> ^{-/-}
ORG-KB1P.S		ES-P	<i>Brca1</i> ^{SCo} ; <i>Trp53</i> ^{-/-}
KB1P.S	<i>Brca1</i> ^{-/-} ; <i>Trp53</i> ^{-/-}	ES-B1P.S	<i>Brca1</i> ^{-/-} ; <i>Trp53</i> ^{-/-}
ORG-KP		RPE1-B1P.R	<i>BRCA1</i> ^{-/-} ; <i>TP53</i> ^{-/-} ; <i>TP53BP1</i> ^{-/-}
KP		RPE1-B1P.S	<i>BRCA1</i> ^{-/-} ; <i>TP53</i> ^{-/-}
KB2P	<i>Brca2</i> ^{-/-} ; <i>Trp53</i> ^{-/-}	RPE1-P	<i>TP53</i> ^{-/-}

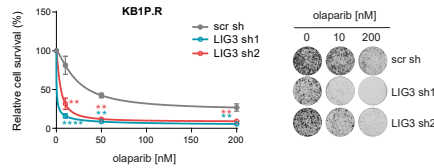
B



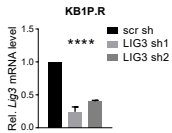
C



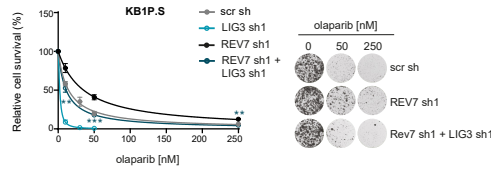
D



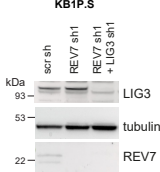
E



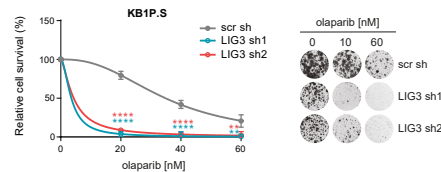
F



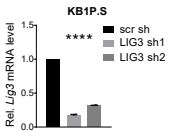
G



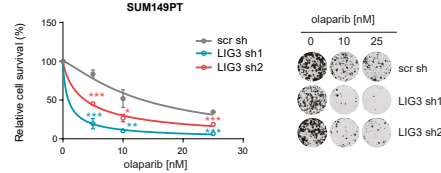
H



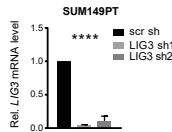
I



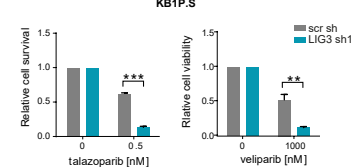
J



K

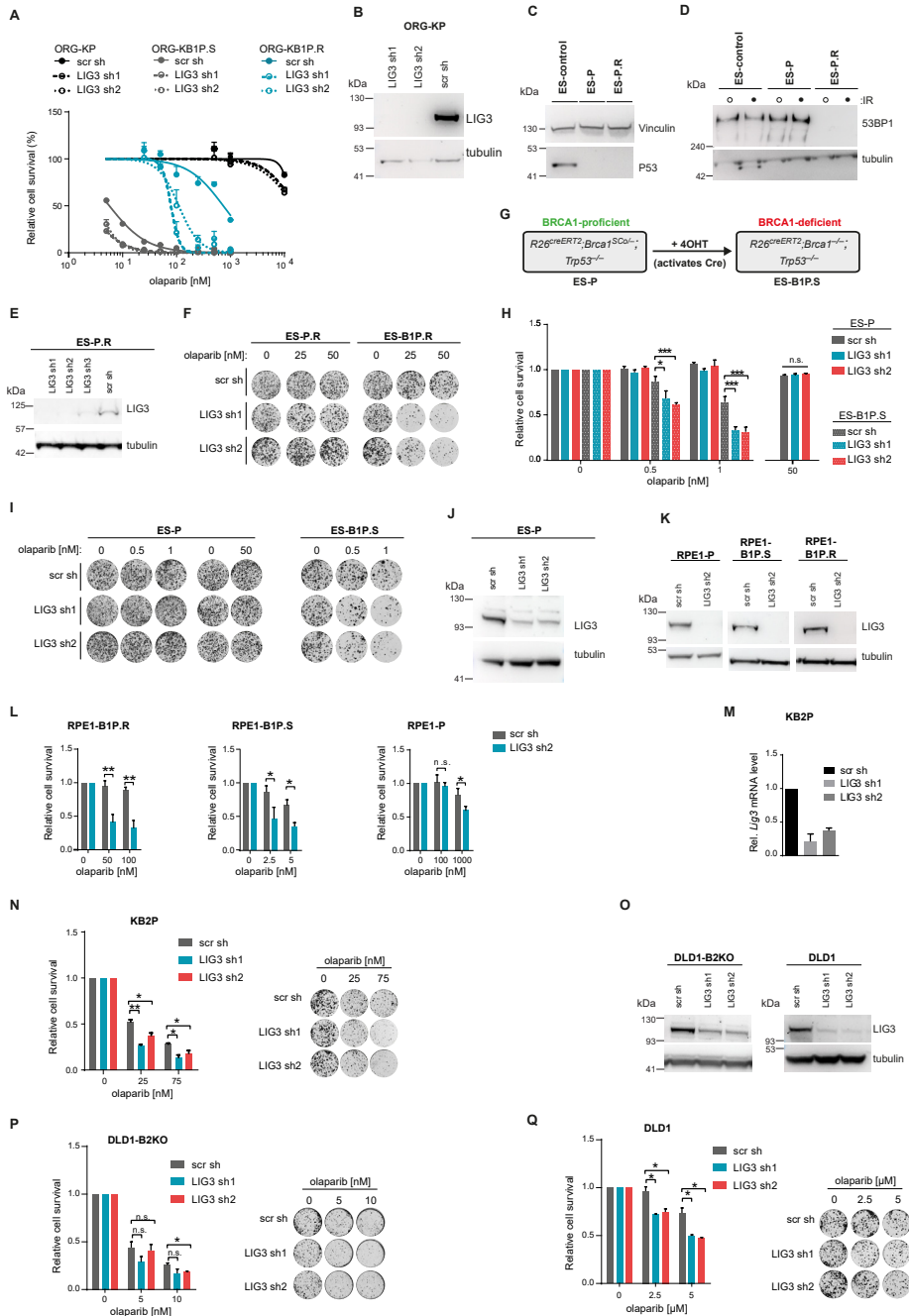


L



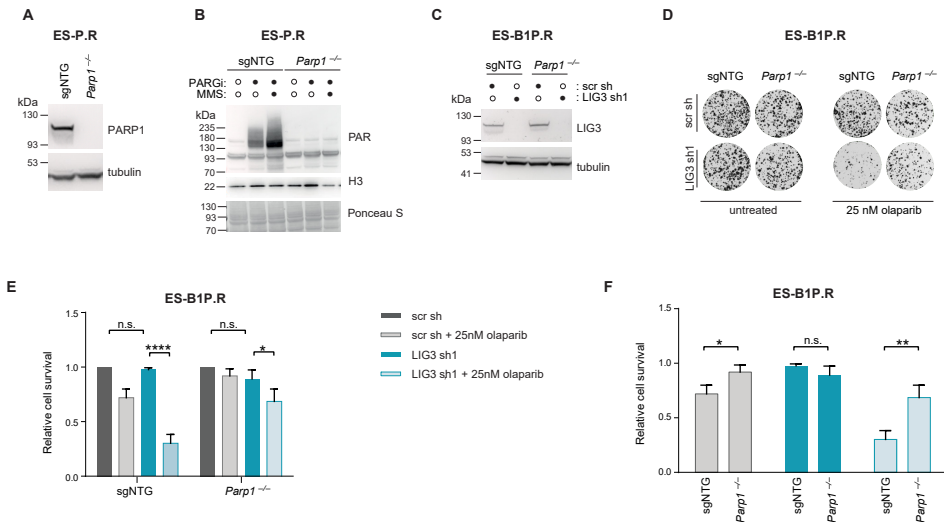
Supplementary Figure 1 | Depletion of LIG3 increases sensitivity to PARPi in HR-negative and HR-restored cells. Related to Figure 1. A | Summary table of cell line abbreviations and respective genotypes. B | Distribution of the one-sided p value (gene dropout) for all genes targeted by the shRNA-based library in mESCs (left) and in organoids (right), by MAGeCK. C | Western blot analysis of LIG3 in ORG-KB1P.S and

ORG-KB1P.R organoids, transduced with shRNA targeting LIG3. **D** | Quantification (left) and representative images (right) of long-term clonogenic assay with KB1P.R cells treated with olaparib or left untreated. **E** | RT-qPCR analysis of *Lig3* expression levels in KB1P.R cells expressing the indicated shRNAs. **F** | Quantification (left) and representative images (right) of long-term clonogenic assay with KB1P.S cells, treated with olaparib or left untreated. **G** | Western blot analysis of LIG3 and REV7 in KB1P.S cells expressing indicated shRNAs. **H** | Quantification (left) and representative images (right) of long-term clonogenic assay with KB1P.S cells, treated with olaparib or left untreated. **I** | RT-qPCR analysis of *Lig3* expression levels in KB1P.S cells expressing the indicated shRNAs. **J** | Quantification (left) and representative images (right) of long-term clonogenic assay with SUM149PT cells, treated with olaparib or left untreated. **K** | RT-qPCR analysis of *LIG3* expression levels in SUM149PT cells expressing the indicated shRNAs. **L** | Quantification of long-term clonogenic assay with KB1P.S cells, treated with the PARPi talazoparib (left) and veliparib (right). Data are represented as mean \pm SD. * $p < 0.05$, ** $p < 0.01$, *** $p < 0.001$, **** $p < 0.0001$, n.s., not significant; two-tailed t test.



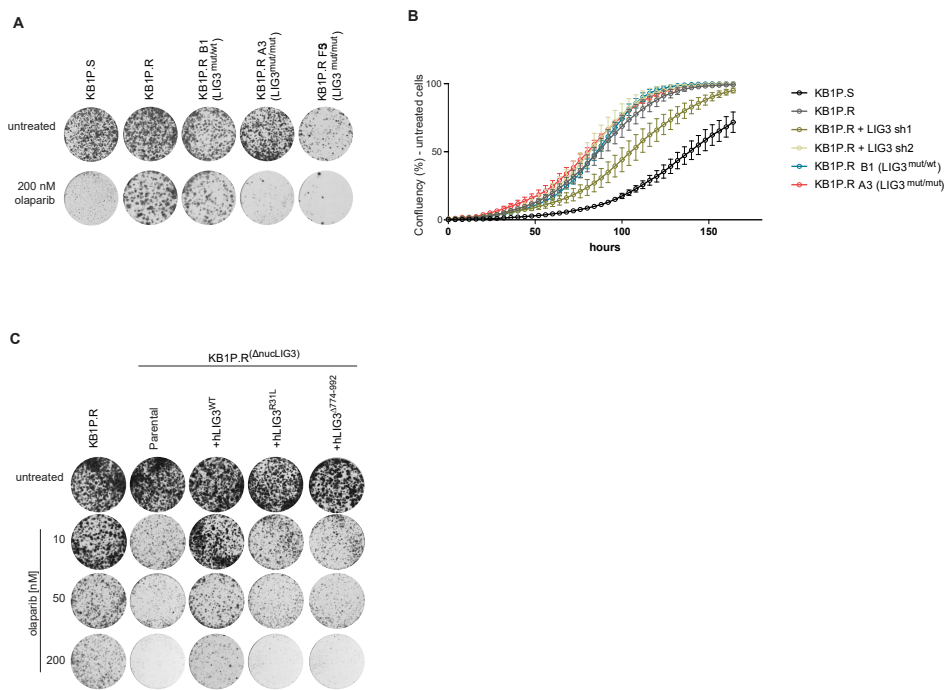
Supplementary Figure 2 | Lethality observed in Lig3-depleted cells is dependent on BRCA1 loss. Related to Figure 1. A | Quantification of long-term clonogenic assay with ORG-KB1P.R, ORG-KB1P.S, and ORG-KP organoids treated with olaparib. **B** | Western blot analysis of Lig3 in ORG-KP organoids, transduced with shRNA targeting Lig3. **C-D** | Western blot analysis of P53 (C) and 53BP1 (D) in ES-P.R and in ES-P mESCs. **E** | Western blot analysis of Lig3 in ES-P.R mESCs, transduced with shRNA targeting Lig3. **F** | Representative images of long-term clonogenic assay with ES-P.R and ES-B1P.R mESCs treated with olaparib or left untreated.

G | Schematic representation of the *Brca1* selectable conditional allele in *R26^{creERT2};Brca1^{SCo^{-/-}};Trp53^{-/-}* (ES-P). Incubation of these cells with 4-hydroxytamoxifen (4OHT) induces a CreERT2 recombinase fusion protein, resulting in *R26^{creERT2};Brca1^{-/-};Trp53^{-/-}* (ES-B1P.R) cells lacking BRCA1 protein expression. **H-I** | Quantification (H) and representative images (I) of long-term clonogenic assay with ES-P and ES-B1P.S mESCs treated with olaparib or left untreated. **J** | Western blot analysis of *Lig3* in ES-P mESCs, transduced with shRNA targeting *Lig3*. **K** | Western blot analysis of *Lig3* in RPE1-P, RPE1-B1P.S and RPE1-B1P.R cells transduced with shRNA targeting *Lig3*. **L** | Quantification of long-term clonogenic assay with RPE1-P, RPE1-B1P.S and RPE1-B1P.R cells treated with olaparib or left untreated. **M** | RT-qPCR analysis of *Lig3* expression levels in KB1P.R cells expressing indicated shRNAs. **N** | Quantification (left) and representative images (right) of long-term clonogenic assay with KB2P cells treated with olaparib or left untreated. **O** | Western blot analysis of BRCA2-deficient DLD1-B2KO cells and parental DLD1 cells transduced with *Lig3*-targeting shRNAs. **P-Q** | Quantification (left) and representative images (right) of long-term clonogenic assay with DLD1-B2KO (P) and parental DLD1 cells (Q) treated with olaparib or left untreated. Data are represented as mean \pm SD. * $p < 0.05$, ** $p < 0.01$, *** $p < 0.001$, **** $p < 0.0001$, n.s., not significant; two-tailed t test.

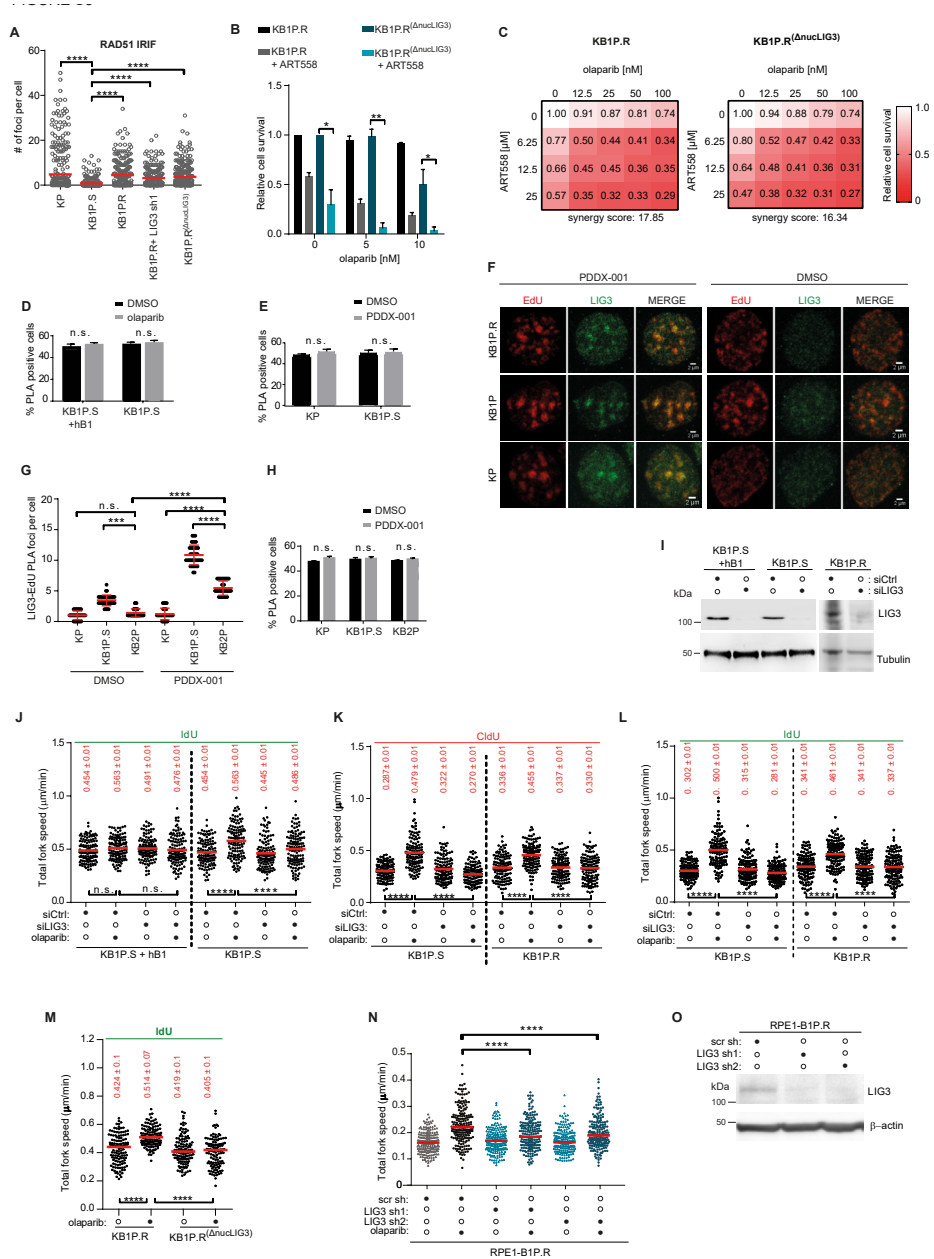


Supplementary Figure 3 | PARPi Toxicity in *Lig3*-depleted Cells is dependent on PARP1. Related to Figure 1. **A** | Western blot analysis of PARP1 in ES-P.R cells transduced with non-targeting single-guide RNA (ES-P.R sgNTG) and in ES-P.R *Parp1*^{-/-} cells. **B** | Western blot analysis of PAR in ES-P.R sgNTG and in ES-P.R *Parp1*^{-/-} cells, left untreated, or treated with PARGi (PDDX-001) and/or 0.01% MMS for 30 min. **C** | Western blot analysis of *Lig3* in ES-P.R sgNTG and ES-P.R *Parp1*^{-/-} cells, transduced with shRNA targeting *Lig3*. **D-F** | Representative images (D) and quantification (E,F) of long-term clonogenic assay in ES-B1P.R *Parp1*^{-/-} cells treated with olaparib and upon shRNA-mediated depletion of *Lig3*. Values were normalized to untreated scr sh for each line.

Data are represented as mean \pm SD. * $p < 0.05$, ** $p < 0.01$, *** $p < 0.001$, **** $p < 0.0001$, n.s., not significant; two-tailed t test.

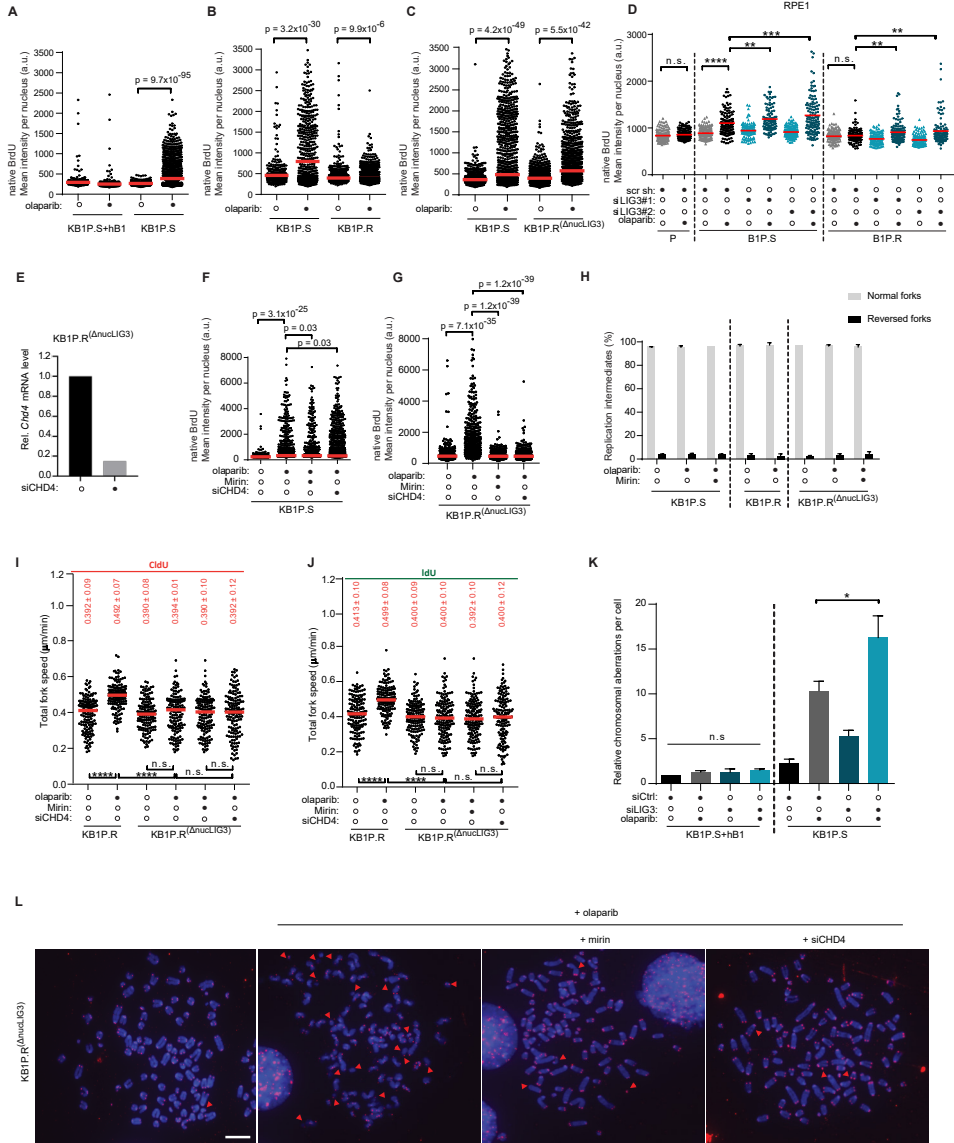


Supplementary Figure 4 | Resistance to PARPi in 53BP1-deficient KB1P cells is mediated by nuclear LIG3. Related to Figure 2. A | Representative images of long-term clonogenic assay with KB1P.S, KB1P.R, KB1P.R(LIG3^{mut/wt}) B1, KB1P.R(LIG3^{mut/mut}) A3 and KB1P.R(LIG3^{mut/mut}) F5 cells, treated with olaparib or left untreated. **B** | Quantification of proliferation assays in KB1P.S, KB1P.R, KB1P.R transduced with shRNAs targeting LIG3, KB1P.R(LIG3^{mut/mut}) A3 and KB1P.R(LIG3^{mut/wt}) B1. Cell confluency was measured every 4h with IncuCyte. **C** | Representative images of long-term clonogenic assay with KB1P.R and KB1P.R(ΔnucLIG3) nuclear LIG3 mutant cells (for which we selected KB1P.R(LIG3^{mut/mut}) clone A3), treated with olaparib or untreated. Expression of indicated LIG3 constructs was induced with Doxycycline 2 days before the assay and maintained for the duration of the assay.



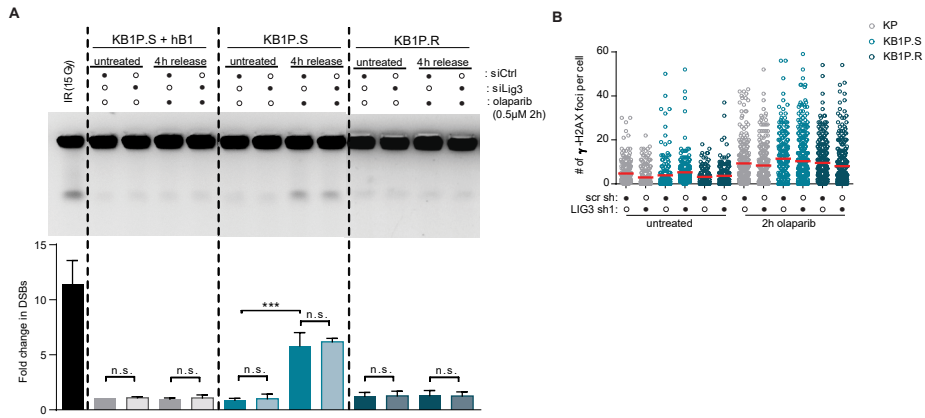
Supplementary Figure 5 | LIG3 is required at replication forks in BRCA1-deficient cells treated with PARPi. Related to Figure 3. A | Quantification of RAD51 IRIF after irradiation with 10Gy and 3 hr recovery, in KP, KB1P.S, KB1P.R, KB1P.R after shRNA-mediated LIG3 depletion, and nuclear LIG3 mutant KB1P.R(Δ nucLIG3) cells. Data are represented as mean. **** $p < 0.0001$, Unpaired T test. **B** | Quantification of long-term clonogenic assay in KB1P.R and nuclear LIG3 mutant KB1P.R(Δ nucLIG3) cells, left untreated or treated with olaparib and/or 25 μ M POL θ inhibitor ART558. Treatment with olaparib was carried out at concentrations not toxic to KB1P.R(Δ nucLIG3) cells so epistasis or absence of it could be observed. Data are represented as mean \pm SD. * $p < 0.05$, ** $p < 0.01$, n.s., not significant; two-tailed t test. **C** | Quantification of short-term cytotoxicity assay upon combination treatment with olaparib and POL θ inhibitor ART558, at the indicated concentrations, in KB1P.R and KB1P.R(Δ nucLIG3) cells. Treatment

with olaparib was carried out at concentrations not toxic to KB1P.R^(ΔnucLIG3) cells so epistasis or absence of it could be observed. Synergy scores were calculated based on Bliss reference model using SynergyFinder. **D** | Percentage of LIG3-EdU proximity ligation assay (PLA) positive cells corresponding to Figure 4A. **E** | Percentage of LIG3-EdU PLA positive cells corresponding to Figure 4B. **F** | Immunostaining of LIG3 in detergent-pre-extracted KB1P.R, KB1P.S and KP cells, incubated for 1 hr with 20μM EdU in the absence or presence of PARG inhibitor PDDX-001. Scale bar, 2μm. **G** | Quantification of LIG3-EdU PLA foci in KB2P cells incubated for 10 min with 20μM EdU, in the absence or presence of PDDX-001. ± SD, ***p<0.001 ****p<0.0001; n.s., not significant; Mann-Whitney U test. **H** | Percentage of LIG3-EdU PLA positive cells in (F). **I** | Western blot analysis of LIG3 in KB1P.S+hB1, KB1P.S and KB1P.R cells transfected with siRNA targeting LIG3, used for DNA fiber assays. **J** | Quantification of IdU tracks in KB1P.S+hB1 and KB1P.S cells, following the indicated treatments. Data are represented as mean. ****p<0.0001, n.s., not significant; Mann-Whitney U test. **K-L** | Quantification of CldU (J) and IdU tracks (K) in KB1P.S and KB1P.R cells, following the indicated treatments. Data are represented as mean. n.s., not significant, ****p<0.0001, Mann-Whitney U test. **M** | Quantification of IdU tracks in nuclear LIG3-mutant KB1P.R^(ΔnucLIG3) cells, following the indicated treatments. Data are represented as mean. ****p<0.0001, n.s., not significant; Mann-Whitney U test. **N** | Quantification of fork speed in RPE1-B1P.R cells transfected with shRNAs targeting LIG3, following the indicated treatments. Data are represented as mean. ****p<0.0001, Mann-Whitney U test. **O** | Western blot analysis of RPE1-B1P.R cells after shRNA-mediated depletion of LIG3.

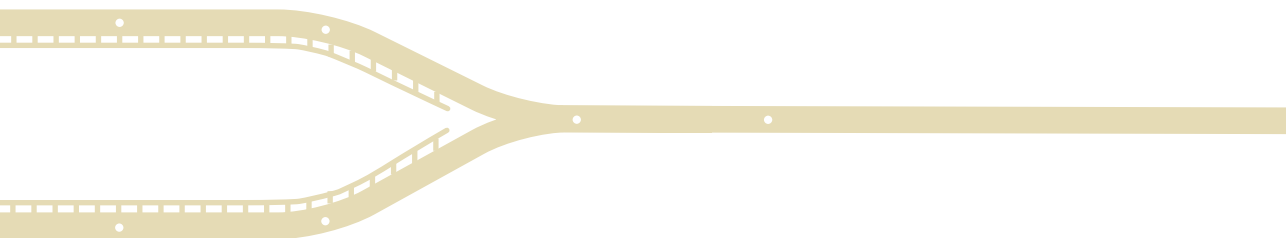


Supplementary Figure 6 | Ligase III depletion reverts PARPi resistance by increasing post-replicative MRE11-mediated ssDNA gaps. Related to Figures 4 and 5. **A-C** | Dot plot of native BrdU mean intensity per nucleus as shown in Figure 4B (A), in Figure 4C (B) and in Figure 4D (C). Data are represented as mean. Unpaired t test, p value was calculated using R. **D** | Quantification of immunofluorescence analysis of ssDNA gaps in RPE1 cells as shown in 4A. * $p < 0.05$, ** $p < 0.01$, *** $p < 0.001$, **** $p < 0.0001$, n.s., not significant; unpaired t test. **E** | RT-qPCR analysis of *Chd4* expression levels in nuclear Lig3 mutant KB1P.R(ΔnuclIG3) cell line transfected siRNA targeting CHD4. **F-G** | Dot plot of native BrdU mean intensity per nucleus shown in Figure 5D. Unpaired t test, p value was calculated using R. **H** | Quantification of normal and reversed forks in KB1P.S, KB1P.R and KB1P.R(ΔnuclIG3) cells. Data were acquired by electron microscopy. **I-J** | Quantification of CldU (I) and IdU tracks (J) in KB1P.R and KB1P.R(ΔnuclIG3) cells, following the indicated treatments. KB1P.R(ΔnuclIG3) cells were additionally treated with 25μM mirin or transfected with siRNA targeting CHD4, 48 hr prior to treatment with olaparib. Data are represented as mean. **** $p < 0.0001$, n.s., not significant; Mann-Whitney U test. **K** | Quantification of chromosomal aberrations in Lig3-proficient and Lig3-depleted KB1P.S+hB1 and KB1P.S cells following 2 hr treatment with 0.5μM olaparib

and recovery for 6 hr. **L** | Representative images of chromosomal aberrations in Figure 5F and 5G. Telomeres are labeled in red. Red arrowheads indicate chromosomal aberrations. Scale bar, 50µm.



Supplementary Figure 7 | **LIG3 depletion does not result in DSB formation. Related to Figure 6. A |** Representative image (top) and quantification (bottom) of pulsed-field gel electrophoresis (PFGE) analysis of DSBs in LIG3-proficient and LIG3-depleted KB1P.S+hB1, KB1P.S and KB1P.R cells, treated with 0.5µM olaparib for 2 hr and released for 4hr or left untreated. Data are represented as mean ± SD, ***p<0.001, n.s., not significant, two-tailed t test. **B |** γ-H2AX foci formation in LIG3-proficient and LIG3-depleted KP, KB1P.S and KB1P.R cells treated with 0.5µM olaparib for 2 hr or left untreated.



Chapter 4

Addendum

**Filling in the gaps in PARP
inhibitor-induced synthetic lethality**

Mariana Paes Dias & Jos Jonkers

ABSTRACT

Tumors with loss of BRCA1 are homologous recombination (HR) deficient and hypersensitive to poly(ADP-ribose) polymerase inhibitors (PARPi). However, these tumors may restore HR and acquire PARPi resistance via loss of end-protection of DNA double-strand breaks. We found that loss of nuclear DNA ligase III resensitizes HR-restored BRCA1-deficient cells to PARPi by exposing post-replicative single-stranded DNA (ssDNA) gaps. Our work, and that of others, identifies ssDNA gaps as a key determinant of PARPi response.

Developing targeted therapies is one of the main goals of current cancer research. The synthetic lethality of poly(ADP-ribose) (PAR) polymerase inhibitors (PARPi) in homologous recombination (HR)-deficient tumors provides an example of a targeted therapy that has been successfully translated into the clinic. Despite the success of this approach, drug resistance poses a major obstacle and combination treatment strategies are required to overcome PARPi resistance¹. One of the best-studied mechanisms of PARPi resistance involves restoration of HR in cells with defects in *BRCA1* via loss of DNA double-strand break (DSB) end-protection factors (e.g., 53BP1, MAD2L2 or shieldin complex subunits 1-3)¹. Recently, we have identified nuclear DNA ligase III (LIG3) as a critical mediator of PARPi resistance in *BRCA1*-deficient cells that have restored HR via loss of 53BP1². Depletion of LIG3 resensitizes *BRCA1*/53BP1 double-deficient cells to PARPi *in vitro* and *in vivo*, rendering LIG3 as a synthetic dependency of *BRCA1*/53BP1 double-deficient cells and a potential therapeutic target. Importantly, loss of nuclear LIG3 does not revert HR restoration but exposes cells to MRE11 mediated post-replicative single-stranded DNA (ssDNA) gaps upon treatment with PARPi, leading to accumulation of chromosomal abnormalities and cell death².

The synthetic lethality observed between PARPi and *BRCA1/2* mutations has long been attributed to the requirement of *BRCA1/2* for error-free repair of DSBs via HR and for replication fork protection (FP)¹. Recent work from Cong and colleagues shows that *BRCA1/2*-deficient cells accumulate ssDNA gaps upon exposure to PARPi, which is reverted in cells that acquired resistance to PARPi³. Our work recapitulates these findings and shows that it is possible to revert PARPi resistance in *BRCA1*/53BP1 double-deficient cells by reinstating ssDNA gap exposure via depletion of LIG3. Together, these observations indicate that exposure to post-replicative ssDNA gaps is a key determinant of PARPi cytotoxicity, which is independent of HR restoration. Moreover, it was shown that depletion of *BRCA1* interacting helicase 1 (BRIP1), which phenocopies loss of *BRCA1* in regards to its HR and FP functions, does not result in exposure to PARPi-induced ssDNA gaps, which goes in line with the (unexpected) lack of response of BRIP1-deficient cells to PARPi³. Altogether, these findings identify ssDNA gap exposure as novel predictor of PARPi sensitivity, in addition to defects in HR and FP.

In the presence of 53BP1, loss of LIG3 enhances PARPi sensitivity and ssDNA gap exposure in *BRCA1*-deficient cells but not in *BRCA1*-proficient cells, indicating that the increase in PARPi toxicity resulting from LIG3 depletion is dependent on *BRCA1* loss, but independent of 53BP1. Surprisingly, inhibition of MRE11 rescued the increase in PARPi-induced ssDNA gaps in LIG3-depleted *BRCA1*/53BP1 double-deficient cells but did not revert ssDNA gap exposure in *BRCA1*-deficient cells in the presence of LIG3². This indicates that the PARPi-induced ssDNA gaps observed upon LIG3 loss are distinct from the gaps in *BRCA1*-deficient cells when LIG3 is present. Hence, the additional increase in ssDNA gaps and subsequent hypersensitivity to PARPi observed in LIG3-depleted *BRCA1*-deficient cells is most likely due to ablation of two independent gap-suppression (or gap-filling) pathways.

ssDNA regions can originate upon DNA damage induced by e.g., ultraviolet radiation^{4,5}, and have been recently associated with chemotherapy response. Panzarino et al. suggested

that exposure to ssDNA gaps upon induction of replication stress underlies “BRCAness” and dictates response to cisplatin⁶. Further support for the existence of two independent gap suppression pathways is provided by Tirman et al., who showed two temporally distinct post-replicative repair mechanisms to fill primase and DNA directed polymerase (PRIMPOL) dependent ssDNA gaps generated in cisplatin-treated (BRCA1/2-proficient) cells with defective replication fork reversal due to PARP inhibition or loss of SMARCAL1 (SWI/SNF related, matrix-associated, actin-dependent regulator of chromatin, subfamily A-like 1)⁷. In line with our findings that one gap suppression mechanism is mediated by HR while another is dependent on LIG3 but HR-independent, they show that one pathway requires the RAD51 recombinase, whereas the other does not rely on recombination-mediated repair⁷. Moreover, they found that BRCA1/2 promotes gap filling by limiting MRE11 activity upon simultaneous cisplatin treatment and suppression of fork reversal. Together with our finding that MRE11 inhibition fails to rescue PARPi-induced ssDNA gaps in BRCA1-deficient cells, these results suggest that the role of BRCA1/2 in gap filling is context-dependent.

An increase in ssDNA gaps as a result of PRIMPOL-mediated repriming has also been shown to arise during unperturbed replication in HR-deficient tumors, which were shown to rely on error-prone translesion synthesis (TLS) for their repair, rendering TLS a synthetic dependency of HR-deficient cells⁸. Moreover, HR-restoration via 53BP1 depletion rescued the synthetic lethality between BRCA1-deficiency and loss of TLS repair, indicating that, in unperturbed conditions, BRCA1/53BP1 double-deficient cells do not rely on TLS for ssDNA gap repair⁸. While loss of nuclear LIG3 does not increase ssDNA gap exposure in unchallenged conditions, it remains to be tested if loss of LIG3 restores the need for TLS in BRCA1/53BP1 double-deficient cells. It also remains to be determined if repriming activities (e.g., by PRIMPOL) are responsible for the ssDNA gaps observed upon PARPi treatment. Of note, depletion of PRIMPOL did not rescue PARPi-induced ssDNA gaps in LIG3-depleted BRCA1/53BP1 double-deficient cells to the same extent as inhibition of MRE11 or depletion of CHD4 (² and unpublished data).

While the ssDNA gap model remains to be validated in the clinic, the identification of ssDNA gap exposure as a vulnerability in BRCA1/2-deficient cells and as a predictor of PARPi sensitivity creates new opportunities for designing combination therapies to improve response to PARPi. Novel therapeutic strategies to increase exposure to ssDNA gaps or block gap suppression might effectively counteract PARPi resistance and thereby improve progression-free survival of patients.

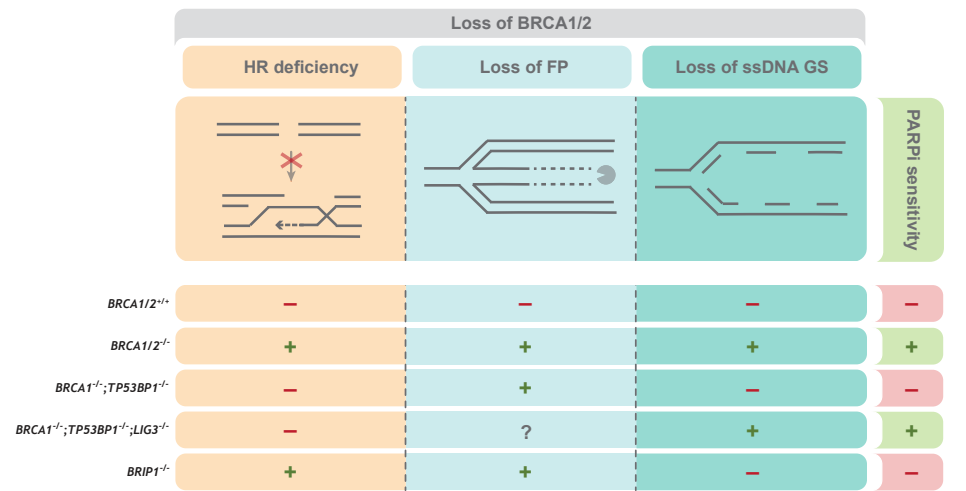


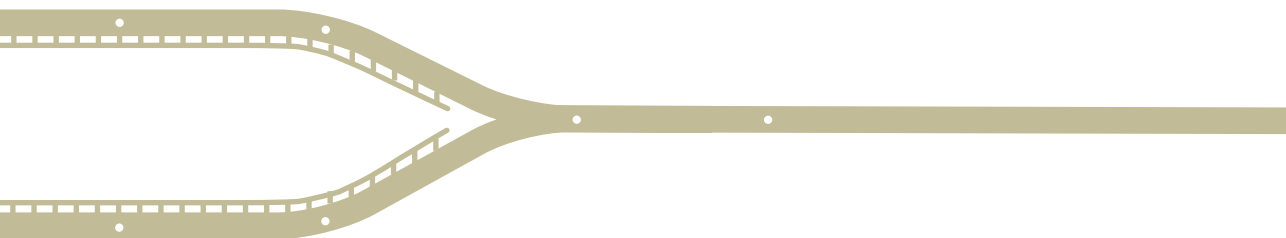
Figure 1 | Predictors of PARPi sensitivity in BRCA1/2-deficient cells. A | To date, three key determinants of response to poly(ADP-ribose) polymerase inhibitors (PARPi) have been identified: homologous recombination (HR) deficiency, loss of replication fork protection (FP) and loss of single-stranded DNA (ssDNA) gap suppression (GS). Cells with loss of BRCA1/2 display all three hallmarks, rendering these cells highly sensitive to PARP inhibition. Loss of 53BP1 in BRCA1-deficient cells restores HR and GS, hindering response to PARPi. Additional loss of nuclear DNA ligase III (LIG3) in BRCA1/53BP1 double-deficient cells restores ssDNA gap exposure and re-sensitizes these cells to PARPi. BRIP1-deficient cells show HR deficiency and loss of FP but maintain GS, which renders these cells resistant to PARPi.

ACKNOWLEDGMENTS

Our work is supported by grants from the European Union Horizon 2020 research and innovation program (agreement 722729) and Oncode Institute, which is partly financed by the Dutch Cancer Society (KWF).

REFERENCES

1. Paes Dias, M., Moser, S. C., Ganesan, S. & Jonkers, J. Understanding and overcoming resistance to PARP inhibitors in cancer therapy. *Nature Reviews Clinical Oncology* 1–19 (2021).
2. Paes Dias, M. *et al.* Loss of nuclear DNA ligase III reverts PARP inhibitor resistance in BRCA1/53BP1 double-deficient cells by exposing ssDNA gaps. *Mol. Cell* (2021).
3. Cong, K. *et al.* Replication gaps are a key determinant of PARP inhibitor synthetic lethality with BRCA deficiency. *Mol. Cell* (2021).
4. Hashimoto, Y., Chaudhuri, A. R., Lopes, M. & Costanzo, V. Rad51 protects nascent DNA from Mre11-dependent degradation and promotes continuous DNA synthesis. *Nat. Struct. Mol. Biol.* **17**, 1305–1311 (2010).
5. Lopes, M., Foiani, M. & Sogo, J. M. Multiple mechanisms control chromosome integrity after replication fork uncoupling and restart at irreparable UV lesions. *Mol. Cell* **21**, 15–27 (2006).
6. Panzarino, N. J. *et al.* Replication gaps underlie BRCA deficiency and therapy response. *Cancer Res.* **81**, 1388–1397 (2021).
7. Tirman, S. *et al.* Temporally distinct post-replicative repair mechanisms fill PRIMPOL-dependent ssDNA gaps in human cells. *Mol. Cell* **81**, 4026–4040.e8 (2021).
8. Tagliatela, A. *et al.* REV1-Pol ζ maintains the viability of homologous recombination-deficient cancer cells through mutagenic repair of PRIMPOL-dependent ssDNA gaps. *Mol. Cell* **81**, 4008–4025.e7 (2021).



Chapter 5

Genome-wide dropout screens in BRCA1/53BP1 double-deficient cells as an approach to identify vulnerabilities of PARPi-resistant cells

Mariana Paes Dias, Ingrid van der Heijden, Cor Liefink, Anna Khalizieva, Yvette Faas, Carmen Fonseca, Jinhyuk Bhin, Justin Sprengers, Natalie Proost, Zuzanna Nowicka, Fendler Wojciech, Marieke van de Ven, Sven Rottenberg, Arnab Ray Chaudhuri, Roderick L. Beijersbergen, Piet Borst, and Jos Jonkers

In preparation

ABSTRACT

Tumors with loss of BRCA1 are defective for homologous recombination (HR) repair and hypersensitive to poly(ADP-ribose) polymerase inhibitors (PARPi). However, these tumors may acquire PARPi resistance via loss of DNA double-strand break (DSB) end-protection factors, such as 53BP1, which results in restoration of HR. In this chapter, we carried out a genome-wide functional genetic dropout screen in BRCA1/53BP1 double-deficient cells in order to identify vulnerabilities that could be exploited therapeutically to improve PARPi response. This screen yielded an extensive list of candidate genes, including thirteen subunits from mitochondrial complex I (MCI) as well as four genes associated with DNA damage response (DDR) pathways. Candidate genes with an $FDR \leq 0.3$ were selected for focused library screens in BRCA1-proficient and BRCA1/53BP1 double-deficient cells in order to validate our previous findings and to find genes whose loss augments the cytotoxicity of PARPi more strongly in BRCA1-deficient cells than in BRCA1-proficient cells. In these screens, we identified sixteen hits associated with DDR, including recombination and meiosis genes such as *SWSAP1* and *GGNBP2*, suggesting that rewiring of the DDR may revert PARPi resistance in BRCA1/53BP1 double-deficient cells. While individual validation of MCI subunits was technically hard to achieve, we found that loss of *SWSAP1* enhances toxicity of PARPi, *in vitro* and *in vivo*. Overall, in this chapter we show that genome-wide screens are a promising approach to identify candidate targets to improve PARPi response.

INTRODUCTION

Error-free repair of DNA double-strand breaks (DSBs) is achieved by homologous recombination (HR). BRCA1 and BRCA2 are key players in HR repair and heterozygous germline mutations in *BRCA1* or *BRCA2* genes predispose to breast and ovarian cancers that show HR deficiency due to loss of the wild-type *BRCA1/2* allele. The HR defect of *BRCA1/2*-mutated tumors can be targeted by the use of poly (ADP-ribose) polymerase (PARP) inhibitors (PARPi)^{1,2}.

PARP1, which is the main target of PARPi, is involved in various cellular processes, including the sensing of DNA single-strand breaks (SSBs). Upon damage, PARP1 is rapidly recruited to sites of DNA damage and transfers negatively charged ADP-ribose groups from donor NAD⁺ onto target proteins in a process termed poly(ADP-ribose)ylation (PARylation), required for SSB repair and thought to be inhibited upon PARPi treatment. PARP1 itself is a prime target of PARylation and the resulting PAR chains serve as a platform for the recruitment of downstream repair factors and subsequent release of PARP1 from the DNA, which is essential for repair to take place³. PARPi were initially thought to act by preventing the repair of SSBs, which accumulate during the S phase of the cell cycle, posing a threat to replication fork progression^{1,2}. This model was later challenged since PARPi were shown to trap PARP1 at DNA lesions due to impaired autoPARylation, resulting in DNA-protein crosslinks⁴⁻⁷. These crosslinks then trigger the collapse of replication forks that encounter trapped PARP1, leading to an accumulation of DSBs during S phase. Cells are dependent on BRCA1/2-mediated HR repair to resolve DSBs in an error-free manner and thus PARPi can induce DNA lesions that are lethal to BRCA1/2-deficient tumor cells but not to wild-type non-tumor cells.

The success of this approach has so far led to the approval of four different PARPi for the treatment of several cancers^{8,9}. However, while clinical trials have demonstrated promising response rates among patients receiving PARPi, most patients will inevitably develop resistance, resulting in disease relapse. Preclinical and clinical data have revealed that acquired resistance to PARPi can develop via three general mechanisms: (i) drug target-related mechanisms, such as upregulation of drug efflux pumps or mutations in PARP1 or functionally related proteins; (ii) restoration of HR via reactivation of BRCA1/2 or rewiring of the DDR network; (iii) restoration of replication fork stability⁸. Nonetheless, most of the mechanisms of PARPi resistance and resistance-associated factors identified thus far lead to the reactivation of the HR pathway. *In vitro* studies have shown that, in the impossibility of BRCA1/2 functional reactivation, HR can be restored in BRCA1-deficient cells through the loss of components of the 53BP1-RIF1-Shieldin complex¹⁰⁻¹⁸. There are two major forms of repair that cells employ to repair DSBs: non-homologous end joining (NHEJ) and HR. The choice between the two pathways is regulated in the context of the cell cycle. While NHEJ promotes the direct ligation of the broken DNA ends, and it is active throughout the cell cycle while favored in the G1 phase, HR is restricted to the S/G2 phase,

when the sister chromatid is available as a template for repair¹⁹. The 53BP1-RIF1-Shieldin complex plays a key role in NHEJ by suppressing DSB end-resection. In the absence of BRCA1/2, end-resection and consequently HR cannot take place in S/G2 phase and cells use error-prone NHEJ to repair DSBs. However, loss of any of the factors from the 53BP1-RIF1-Shieldin complex in BRCA1-deficient cells restores end-resection and HR, rendering these cells resistant to PARPi^{10–18}. Additional evidence that loss of the 53BP1-RIF1-shieldin end-protection pathway mediates resistance to PARPi comes from *in vivo* studies in mouse models of BRCA1-deficient breast cancer in which BRCA1 functional reactivation is not possible. These studies showed that acquired resistance, resulting from prolonged exposure of mice to PARPi, was frequently associated with HR restoration and loss-of-function alterations of *Trp53bp1* (ref. 20 and our own unpublished data). Moreover, loss of 53BP1 and shieldin components has been observed in patient-derived tumor xenograft (PDX) models with acquired resistance to PARPi, and mutations in *TP53BP1* have been reported in tumor biopsies from patients with metastatic BRCA1-associated breast cancer receiving platinum chemotherapy or PARPi^{18,21,22}.

In this study, we used functional genetic screens in BRCA1/53BP1 double-deficient cells to identify acquired vulnerabilities and modulators of PARPi response, which could potentially be targeted to improve PARPi response. This approach has previously yielded DNA ligase III (LIG3), a known DNA repair factor, as a collateral vulnerability of BRCA1-deficient cells with acquired PARPi resistance due to loss of DSB end-protection²³. While the previous screen used a DNA damage response (DDR)-focused library, in this study we carried out a genome-wide screen to expand our search beyond previously reported DNA damage repair factors. This genome-wide screen yielded an extensive list of candidate genes, which was used to generate a focused library for secondary screens in BRCA1/53BP1 double-deficient cells and BRCA1-proficient cells. We identified multiple candidate targets, including many subunits from the mitochondrial respiratory complex I (MCI). However individual validation of these subunits was technically hard to achieve. In addition, our screening efforts yielded several hits associated DNA damage response (DDR), including recombination and meiosis genes, such as *SWSAP1* and *GGNBP2*. While further investigation is required, our results suggest *SWSAP1* as a potential therapeutic target for the treatment of BRCA1/2-deficient cancers.

RESULTS

Genetic dropout screens in BRCA1/53BP1 double-deficient cells identify candidate modulators of PARPi resistance

To identify acquired vulnerabilities in BRCA1-deficient cells that developed PARPi resistance via BRCA1-independent restoration of HR, we carried out functional genetic dropout screens in *Brca1*^{-/-};*Trp53*^{-/-};*Trp53bp1*^{-/-} mouse embryonic stem (mES) cells (ES-B1P.R). Cells were transduced with a lentiviral genome-wide CRISPR library consisting of

90,230 single-guide RNAs (sgRNAs) targeting 18,424 genes (5 sgRNAs/gene) and were subsequently either mock-treated or treated for 3 weeks with 25 nM of the PARPi olaparib²⁴, which does not affect the viability of PARPi-resistant ES-B1P.R cells but is lethal to the corresponding PARPi-sensitive *Brca1*^{-/-};*Trp53*^{-/-} (ES-B1P.S) cells (**Fig. 1A**). Sequencing and analysis of the sgRNAs in the surviving cells yielded seventeen hits, including the Shu complex factors *Swsap1* and *Zswim7*, the base excision repair factor *Polb* and the transcription-coupled nucleotide excision repair factor *Cops7a*, as well as several subunits of the MCI, including *Ndufa8*, *Ndufs7*, *Ndufb8*, *Ndufa2*, *Ndufa1*, *Ndufa5*, *Ndufs8*, *Ndufa3*, *Ndufs1*, *Ndufb4*, *Ndufb10*, *Ndufb7* and *Nubpl* (**Fig. 1B,C**, **Supplementary Fig. 1A and Supplementary table 1**). Analysis of the predicted protein-protein interactions of all genes with a false discovery rate (FDR) ≤ 0.3 using the STRING database (<https://string-db.org/>) identified several gene clusters associated with mitochondrial oxidative metabolism such as complex I and Coenzyme Q (CoQ) of the mitochondrial respiratory chain, as well as lipoic acid metabolism (**Supplementary Fig. 1B**). STRING analysis also identified a cluster of diverse DDR factors and a cluster of genes associated with RNA-binding and processing of RNA secondary structures (**Supplementary Fig. 1B,C**).

To further validate our screening results, we carried out focused screens in BRCA1-deficient and BRCA1-proficient mouse and human cells, for which we generated custom mouse and human sgRNA libraries that included all candidate genes with FDR ≤ 0.3 (**Supplementary table 2**). We used BRCA1-deficient ES-B1P.R mES cells and isogenic BRCA1-proficient ES-P.R cells, as well as two isogenic human TERT-immortalized retinal pigment epithelial (RPE1) cell lines with engineered loss of TP53 (RPE1-P) or TP53+BRCA1+TP53BP1 (RPE1-B1P.R)¹⁶ (**Supplementary Fig. 2A**). The focused candidate screen in ES-B1P.R cells identified thirty-one genes, including eighteen genes associated with recombination-mediated repair (e.g., *Swsap1*, *Zswim7*, *Pds5b*, *Mnd1*, *Psmc3ip* (*Hop2*), *Rad18*, *Chd1l*, *Swi5*, *Chd1l*, *Rad54l*, *Hsf2bp*, *Rnf8*) and other repair pathways (e.g., *Cops7a*, *Usp22*, *Sp1*, *Cks1b*, *Cand1*, *Trip*) (**Fig. 1D**).

Screening in BRCA1-proficient cells allowed us to identify several hits that were specifically or stronger depleted in BRCA1-deficient cells (e.g., *Ggnbp2*, *Mnd1* and *Swsap1* in mES cells, and *HELQ* in RPE1 cells) (**Fig. 1E-I and Supplementary Fig. 2B**). Additionally, our screens identified genes whose loss was synthetic lethal in BRCA1/53BP1 double-deficient cells, but not in BRCA1-proficient cells, such as *Rnf8* in RPE1 cells (**Fig. H and Supplementary Fig. 2D-F**). The focused screen in RPE1-B1P.R cells yielded fewer hits than the focused screen in ES-B1P.R mES cells, which is expected as the focused library was based on the genome-wide screen results carried out in the same mES cells (**Fig. 1F,G**). Nonetheless, the screens in RPE1-B1P.R cells identified several genes previously reported to suppress response to PARPi, such as *RNASEH2A*²⁵, *ATM*^{10,13}, and *CHD1L/ALC1*²⁶⁻²⁹. These genes were also identified as hits in the mES screens, although their context specificity (i.e., specific to BRCA1-deficient cells) varied between the two cell lines (**Fig. 1D-I and Supplementary Fig. 2B,C**).

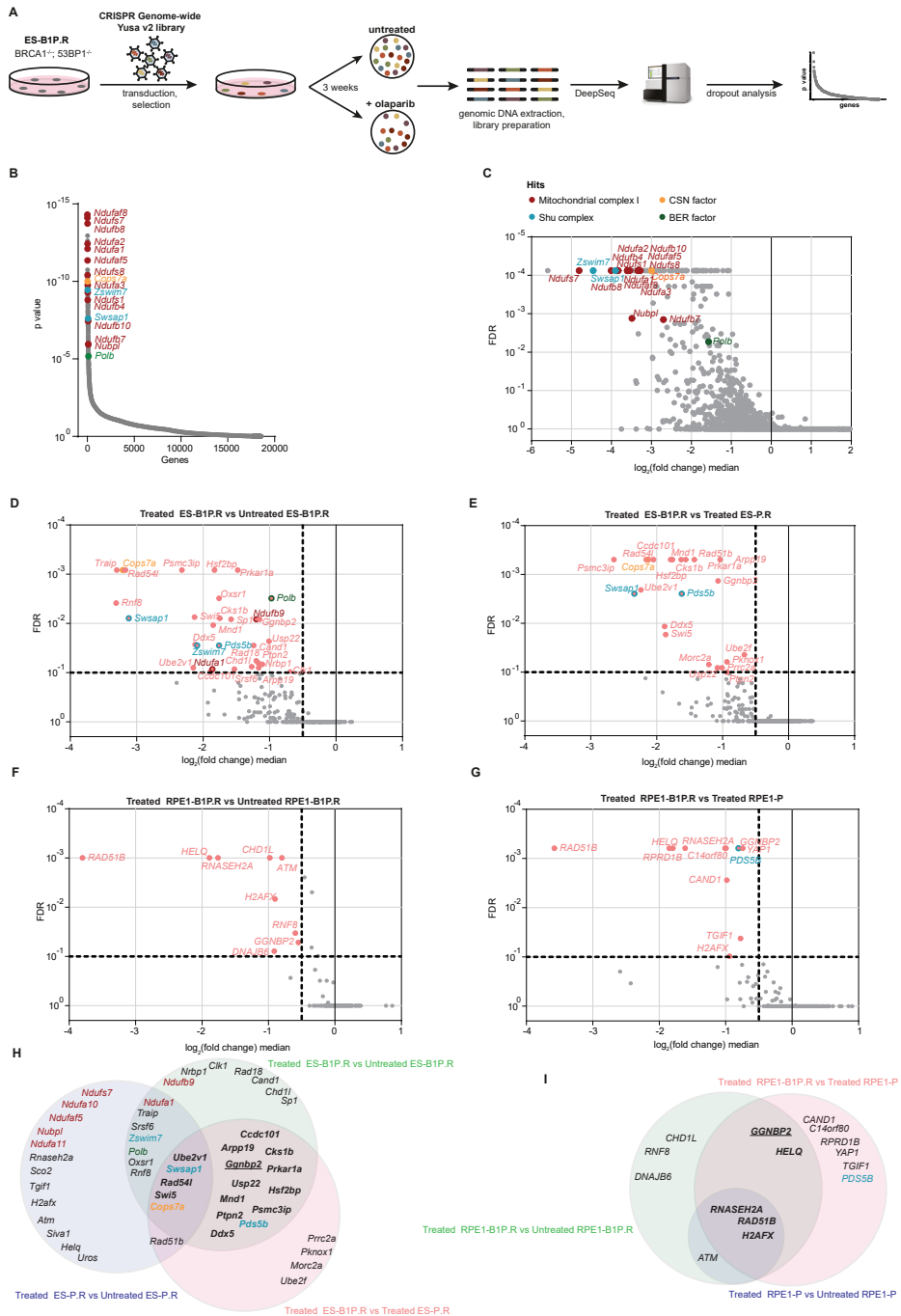


Figure 1 | Genetic dropout screens in BRCA1/53BP1 double-deficient cells identify candidate modulators of PARPi resistance. **A** | Outline of genome-wide dropout screen in ES-B1P.R cells, using mouse improved genome-wide knockout CRISPR library v2. Cells were treated with 25nM olaparib for three weeks or left untreated. **B** | Plot of distribution of the one-sided p value (gene dropout) for all genes targeted by the sgRNA library. **C** | Plot of distribution \log_2 ratio (fold change (treated versus untreated)) median for all genes versus false

discovery rate (FDR) of results from genome-wide screen in ES-B1P.R cells. **D** | Plot of distribution \log_2 ratio (fold change (treated versus untreated)) median for all genes versus FDR of results from screen using focused candidate library in ES-B1P.R cells. **E** | Plot of distribution \log_2 ratio (fold change (treated ES-B1P.R versus treated ES-P.R)) median for all genes versus false FDR of results from screen using focused candidate library in mES cells. **F** | Plot of distribution \log_2 ratio (fold change (treated versus untreated)) median for all genes versus FDR of results from screen using focused candidate library in RPE1-B1P.R cells. **G** | Plot of distribution \log_2 ratio (fold change (treated RPE1-B1P.R versus treated RPE1-P)) median for all genes versus FDR of results from screen using focused candidate library in human RPE1 cells. **H** | Venn diagram depicting significant genes in mES and RPE1 screens.

Loss of GGNBP2 was the only common hit in both mES and RPE1 cells to increase PARPi sensitivity in BRCA1/53BP1 double-deficient cells but not in BRCA1-proficient cells (**Fig. 1D-J and Supplementary Fig. 2B,C**). GGNBP2 (a.k.a. LCRG1) plays a key role in spermatogenesis and one study reported GGNBP2 to be involved DSB repair during meiotic progression^{30,31}. Preliminary data showed that CRISPR-mediated deletion of GGNBP2 moderately increases response to olaparib treatment (**Supplementary Fig. 2G**). Of note, working antibodies against GGNBP2 were not available and quantification of gene expression by RT-PCR revealed residual mRNA expression, suggesting that GGNBP2 was not completely lost (**Supplementary Fig. 2H**). Analysis of whole-genome sequencing data of metastatic solid tumors from 16 patients who received PARPi (olaparib or niraparib) as single or combination therapy³² showed that patients with tumors with lower *GGNBP2* copy number responded better to the treatment, whereas patients with tumors with higher *GGNBP2* copy number status had progressive disease (**Supplementary Fig. 2I**). While these data are limited, they indicate that *GGNBP2* copy number might correlate with response to PARPi in patients. Further investigation is required to conclusively determine the effect of GGNBP2 in PARPi response. Altogether, the screens carried out in this study yielded a list of potential candidate targets to increase response to PARPi.

Validation of mitochondrial complex I subunits

As mentioned above, our initial genome-wide screen yielded several subunits of the MCI (**Fig. 1B,C and Supplementary Fig. 1B,C**). While only *Ndutf8*, *Ndufs7*, *Ndufb8*, *Ndutf2*, *Ndutf1*, *Ndutf5*, *Ndufs8*, *Ndutf3*, *Ndufs1*, *Ndufb4*, *Ndufb10*, *Ndufb7* and *Nubpl* scored as hits using the strict hit selection criteria, almost all of the MCI subunits encoded in the nuclear DNA scored as significant (\log_2 ratio (fold change (treated versus untreated)) median for all genes ≤ -1 ; FDR ≤ 0.1) (**Fig. 2A**). Given that MCI is responsible for oxidation of NADH to NAD⁺, these results suggest that a block in this process might sensitize the cells to PARPi (**Fig. 2B**).

We hypothesized that disruption of MCI leads to a strong increase in the cellular NADH/NAD ratio, resulting in decreased amounts of NAD⁺ available as substrate for PARP1. This might lead to decreased residual PARP1 activity in the presence of PARPi, and thus to increased PARPi-mediated toxicity. To test our hypothesis, we transduced ES-B1P.R cells with sgRNAs targeting two of the best scoring MCI genes in the initial genome-wide

screen, *Ndufa2* and *Ndufaf8* (**Fig. 1B, C**). TIDE analysis revealed a Cas9 cutting efficiency of around 60% for both genes³³. To assess functional impairment of MCI, we quantified mitochondrial oxygen consumption rate (OCR) measured with the Seahorse Bioanalyzer XFe24. Both, *Ndufa2*- and *Ndufaf8*-disrupted pools showed a decrease of around 50% in OCR, when compared to cells transduced with a non-targeting sgRNA (sgNTG), suggesting that deletion of *Ndufa2* and *Ndufaf8* impairs MCI (**Fig. 2C and Supplementary Fig. 3A**). Unfortunately, we were unable to obtain *Ndufa2* and *Ndufaf8* knockout (KO) clones, as these cells grew gradually slower after three to four weeks in culture. In addition, *Ndufa2* and *Ndufaf8* KO cells induced fast acidification of the cell culture medium. We therefore decided to use shRNA-mediated depletion to validate our initial screen in ES-B1P.R cells. Since shRNAs targeting NDUFAF8 were not available, we tested shRNA-mediated depletion of NDUFA2 and NDUFS8. shRNA-mediated depletion of both MCI factors in ES-B1P.R cells resulted in increased PARPi toxicity, albeit moderate in cells with shRNA-mediated depletion of NDUFA2. Moreover, shRNA-mediated depletion of NDUFS8 resulted in impaired growth in untreated conditions (**Fig. 2D**). Similar results were observed in mouse-tumor derived BRCA1/53BP1 double-deficient KB1P.R cells, derived from a *K14cre;Brca1^{F/F};Trp53^{F/F}* (KB1P) mouse mammary tumor that acquired resistance to PARPi *in vivo* because of loss of 53BP1 function^{20,23}. shRNA-mediated depletion of NDUFA2 and NDUFS8 in KB1P.R cells resulted in growth defects in untreated conditions, even though depletion of NDUFA2 did result in increased sensitivity to olaparib (**Fig. 2E**). Short-term cytotoxic assays in ES-B1P.R cells with shRNA-mediated depletion of NDUFA2 and NDUFS8 showed similar results as in long-term clonogenic assays, suggesting seeding cells at higher density does not improve growth of MCI-deficient cells (**Fig. 2F**).

In the initial genome-wide screen, we didn't observe decreased growth of MCI-depleted ES-B1P.R cells in untreated conditions, as sgRNAs targeting MCI subunits did not show a reduction in reads among the total cell population, compared to the day of seeding (i.e. starting day of the screen) (**Supplementary table 1**). However, validation experiments using sgRNAs and shRNAs suggested the opposite. We hypothesized that faster medium acidification might contribute to the reduced growth of MCI-deficient cells, and that in the context of the genome-wide screen, MCI-proficient cells could compensate for the very minor proportion of MCI-deficient cells. To test if co-culture with parental cells could rescue the growth defect of MCI-depleted ES-B1P.R cells, we decided to carry out competition assays in which parental and MCI-depleted cells were mixed in different ratios, followed by treatment with olaparib for two weeks. As control, we included a condition where we mixed PARPi-sensitive ES-B1P.S cells with ES-B1P.R cells (**Fig. 2G**). According to the initial genome-wide screen results, we should expect an enrichment of the GFP-labeled parental cells in olaparib-treated conditions, whereas in untreated conditions the ratio of parental to shRNA-depleted cells should remain constant. However, while we observed progressive loss of NDUFA2-deficient and NDUFS8-deficient ES-B1P.R cells with increasing PARPi concentrations, the initial cell ratio was not maintained in untreated conditions, suggesting

that the tested co-culture ratios contained insufficient MCI-proficient cells to suppress the growth defect of MCI-depleted cells (**Fig. 2G**). Of note, cells with shRNA-mediated depletion of NDUFA2 showed only a mild growth defect and the ratios in untreated conditions were close to the ratios of the starting population, in line with the previous results (**Fig. 2D**). We next tested if chemical inhibition of MCI by rotenone, piericidin A or metformin could recapitulate the results observed in our initial screen. Treatment of ES-B1P.R cells with MCI inhibitors resulted in impaired growth and rapid medium acidification. Nevertheless, combined treatment with olaparib and MCI inhibitors tended to induced stronger growth inhibition than either of the single-agent treatments (**Fig. 2H-J**). Overall, we were unable to validate the results of our genome-wide screen and to conclusively establish that loss of MCI subunits increases response to PARPi.

Effect of pyruvate supplementation in MCI-deficient cells

Several studies have shown that supplementation with uridine and pyruvate/aspartate enables cells to grow without a functional respiratory chain^{25,34–36}. It has been suggested that glycolysis can provide sufficient ATP when the respiratory chain is compromised; however, NAD⁺ regenerated during respiration is also required for production of aspartate via the malate-aspartate shuttle^{34,36}. In turn, aspartate is a key precursor for both purines and pyrimidines. Since aspartate levels in blood are low and most cells are unable to take up aspartate from the environment, respiratory chain-compromised cells need additional electron acceptors for carbon biosynthesis, such as aspartate and nucleotide base synthesis, to maintain proliferation^{34,36}. Indeed, it has been shown that the anti-proliferative effects of the MCI inhibitors metformin, rotenone and piericidin A can be suppressed by supplementation with pyruvate³⁵ (**Supplementary Fig. 3B**).

We therefore decided to test if supplementation with pyruvate would rescue the growth defects of our MCI-deficient cells. Preliminary data suggested that ES-B1P.R *Ndudaf8* KO cells require pyruvate for proliferation, as addition of pyruvate, alone or in combination with lactate, improved growth of these cells when compared with medium supplemented with lactate only (**Supplementary Fig. 3C,D**). Also, the growth defect of ES-B1P.R cells in which MCI was impaired via shRNA-mediated depletion of NDUFA2 or NDUFS8 could be rescued by supplementation with pyruvate (**Supplementary Fig. 3D**). The effect of pyruvate on the MCI-depleted cells was striking, as they seemed to proliferate even better than the parental cells with pyruvate supplementation, although NDUFS8-deficient cells seemed to reach a plateau earlier. On the contrary, supplementation with lactate did not improve proliferation of MCI-depleted cells and impaired proliferation of parental cells to levels comparable with MCI-depleted cells, suggesting that the proliferation defect in MCI-depleted cells is, at least in part, due to increased lactate levels, which would explain the rapid medium acidification. Further experiments will be required to confirm these preliminary data.

Figure 2

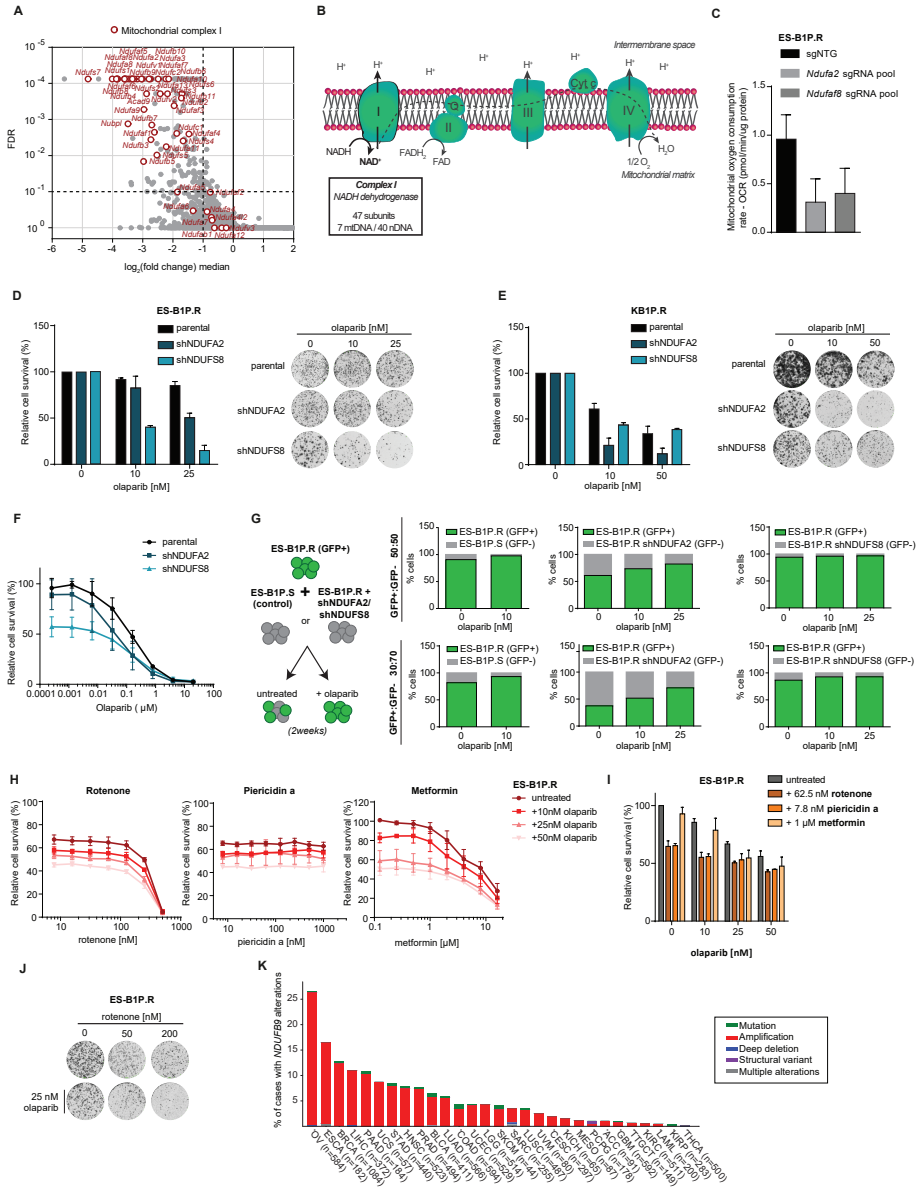


Figure 2 | Validation of mitochondrial complex I subunits. A | Plot of distribution \log_2 ratio (fold change) (treated versus untreated) median for all genes versus false discovery rate (FDR) of results from genome-wide screen in ES-B1P.R cells displaying all MCI genes included in the screen. **B** | Oxidative phosphorylation depicting complex I, II, III and IV. MCI is composed by 47 subunits, 7 encoded in mitochondrial DNA and 40 encoded in nuclear DNA, and is responsible for oxidation of mitochondrial NADH to NAD^+ . **C** | Quantification of mitochondrial oxygen consumption rate (OCR) measured with the Seahorse Bioanalyzer XFe24 in ES-B1P.R transduced with sgRNA non-targeting (sgNTG) or with sgRNA targeting the genes *Ndufa2* and *Ndufa8*. **D-E** | Quantification and representative images of long-term clonogenic assays in ES-B1P.R (D) and in KB1P.R (E) cell lines, treated with olaparib. Cells were treated for the whole extent of the assay. **F** | Quantification of short-term cytotoxicity assay in ES-B1P.R cells treated with olaparib. **G** | Competition assay with parental and MCI-deficient cells mixed in

different ratios (50:50% and 30:70%). ES-B1P.S were used as control. Cells were treatment with PARPi for 2 weeks and passaged twice a week. Measurement of GFP-positive cells was done by FACS. **H-I** | Quantification of short-term cytotoxicity assay in ES-B1P.R cells treated with olaparib in combination with the indicated MCI inhibitors. **J** | Representative images of long-term clonogenic assay in ES-B1P.R cells treated with olaparib and rotenone. **K** | An overview of the frequency of alterations of the *NDUFB9* gene across all available Cancer Genome Atlas (TCGA) PanCancer Atlas cohorts with at least one samples altered.

The MCI subunit *NDUFB9* is frequently amplified in human cancers

The focused candidate screen in ES-B1P.R cells failed to identify as many MCI subunits as in the original screen in the same cell line, with the exception of *Ndufa1* and *Ndufb9*. Moreover, sgRNAs targeting *Ndufa1*, *Ndufb9* and other MCI factors were depleted in untreated conditions, in line with our validation experiments but in contrast to the initial screen (**Supplementary Fig. 2D**). Notably, in the Cancer Genome Atlas (TCGA) PanCancer Atlas, containing over 10,000 primary tumors encompassing 33 different cancer types (www.cbioportal.org), *NDUFB9* was found amplified in several cancer types that are treated with PARPi, including ovarian cancer (27%), breast cancer (13%), pancreatic cancer (11%) and prostate cancer (8%) (**Fig. 2K**). *Ndufa1*, *Ndufs7*, *Ndufa10*, *Ndufaf5*, *Nubpl* and *Ndufa11* were also identified as hits in the BRCA1-proficient ES-P.R cells, suggesting that the increase in PARPi-mediated toxicity upon MCI impairment is BRCA1-independent. In line with this, shRNA-mediated depletion of *NDUFA2* and *NDUFS8* in BRCA1-proficient KP cells derived from a *K14cre;Trp53^{F/F}* (KP) mouse mammary tumor, increased response to olaparib (**Supplementary Fig. 2B,E and 3E**)³⁷. Of note, none of the MCI subunits scored as hits in the focused screens carried out in RPE1 cells. This could possibly be a result of differences in oxygen availability, since the screens in mES cells were carried out in normal oxygen conditions, while RPE1 cells were cultured in low oxygen (3%).

Validation of Shu complex factors

Our genome-wide dropout screen also identified two members of the Shu complex, *Swsap1* and *Zswim7* (a.k.a. *Sws1*) (**Fig. 1B,C and supplementary Fig. 1B**). The Shu complex is a recently identified complex that is critical for promoting the assembly of both RAD51 and its meiotic counterpart, DMC1, nucleoprotein filaments at resected DNA ends during meiotic HR^{38,39}. SWSAP1 was identified in human cells through its association with SWS1 and is considered to be a novel RAD51 paralog since, like RAD51 and the canonical RAD51 paralogs, it contains Walker A and B motifs predicted to be important for nucleotide binding/hydrolysis³⁹. Recent investigation of the human Shu complex revealed SPIDR and PDS5B as additional factors of the Shu complex^{40,41}. While *Pds5b* and *Spidr* did not score as hits with the strictest selection criteria in our genome-wide screen (**Supplementary Fig. 1A**), both genes had an FDR <0.3 and were therefore included in the focused library (**Supplementary Fig. 1B**).

In our focused library screen in ES-B1P.R cells, sgRNAs targeting *Swsap1* were found to be eight-fold depleted in olaparib-treated cells compared to untreated cells (**Fig. 1C,D**). sgRNAs targeting *Zswim7* and *Pds5b* were four-fold depleted in olaparib-treated cells

compared to untreated cells, whereas sgRNAs targeting *Spidr* were not significantly lost (**Fig. 1D**). *Swsap1* and *Zswim7* were also identified as hits our focused library screen in BRCA1-proficient ES-P.R cells, although depletion of *Swsap1*-targeting sgRNAs was four-fold stronger in PARPi-treated ES-B1P.R cells than in ES-P.R cells, suggesting that SWSAP1 loss augments the cytotoxicity of PARPi more strongly in ES-B1P.R cells than in ES-P.R cells (**Fig. 1E,H and supplementary Fig. 2B**). Interestingly, while most of the Shu complex factors did not score in RPE1 cells, shRNAs targeting *PDS5B* were significantly depleted in BRCA1-deficient RPE1-B1P.R compared to BRCA1-proficient RPE1-P cells (**Fig. 1F,G,I and supplementary Fig. 2C**).

Loss of SWSAP1 enhances *in vitro* efficacy of PARPi

Given the strong effect of SWSAP1 loss on PARPi-mediated toxicity in ES-B1P.R cells, we decided to investigate whether SWSAP1 would constitute a useful target for reversing PARPi resistance in BRCA1/53BP1 double-deficient cells. We therefore generated *Swsap1* KO clones in PARPi-resistant KB1P.R cells and in KB1P.S-53BP1KO cells, in which 53BP1 was deleted using CRISPR/Cas9. In line with our screening results, deletion of *Swsap1* rendered cells as responsive to olaparib as the PARPi-sensitive KB1P.S cells (**Fig. 3A,B and Supplementary Fig. 4A**). Loss of SWSAP1 also enhanced the toxicity of olaparib in PARPi-sensitive KB1P.S cells, suggesting enhanced response to PARPi mediated by SWSAP1 loss is not dependent on 53BP1 loss (**Fig. 3C and Supplementary Fig. 4A**). According to our screens, loss of SWSAP1 also increases PARPi response in BRCA1-proficient cells, albeit to a lesser extent than in BRCA1-deficient or BRCA1/53BP1 double-deficient cells. To test whether the effects of SWSAP1 loss on PARPi sensitivity are BRCA1-dependent, we used BRCA1-proficient KP cells and KB1P.S cells that were reconstituted with human BRCA1 (KB1P.S+hBRCA1). In both cell lines, *Swsap1* deletion increased olaparib-mediated toxicity in comparison to the non-modified cells, consistent with our screening results⁴² (**Fig. 3C and Supplementary Fig. 4A**). Of note, increased response of *Swsap1*-deleted KP cells to olaparib was only observed at much higher drug concentrations (above 1 μ M). Deletion of *Swsap1* in the mouse tumor cell lines also resulted in mild proliferation defects in untreated conditions (**Fig. 3A-D**). We next tested if deletion *SWSAP1* augments the response to PARPi in the isogenic RPE1-P and RPE1-B1P.R cell lines used for the focused candidate screens. Contrary to what was observed in the screen, deletion of *SWSAP1* enhanced response to olaparib in RPE1-B1P.R cells, although it also impaired proliferation (**Supplementary Fig. 4B**). Nonetheless, the proliferation defect observed upon deletion of *SWSAP1* was milder in RPE1-P cells, as well as the effect in PARPi-response (**Supplementary Fig. 4C**). Lastly, we investigated if deletion of *Swsap1* also increases PARPi response in BRCA2-deficient KB2P cells derived from a *K14cre;Brca2^{F/F};Trp53^{F/F}* (KB2P) mouse mammary tumor, as well as in BRCA2-reconstituted KB2P+hBRCA2 cells. While SWSAP1 loss had no effect on PARPi response in KB2P cells, we did observe an increased response to olaparib in

Swsap1-deleted KB2P+hBRCA2 cells, albeit milder than the increase observed in *Swsap1*-deleted KB1P.S+hBRCA1 cells (**Fig.3F,G**). Altogether, these results suggest that loss of SWSAP1 enhances PARPi response independently of BRCA1/2, although the strongest effect is observed in cells that originate from BRCA1-deficient tumors.

53BP1 loss and consequent restoration of HR activity has previously been shown to reduce the hypersensitivity of BRCA1-deficient cells to other DNA-damaging agents, such as topoisomerase I (TOP1) inhibitors²⁰. Hence, we decided to test if our *Swsap1*-deleted cells showed improved response to the TOP1 inhibitor camptothecin. Similar to olaparib, response to camptothecin was enhanced by SWSAP1 loss in all KB1P.R, KB1P.S and KB1P.S+hBRCA1 cell lines (**Fig. 3H,I**).

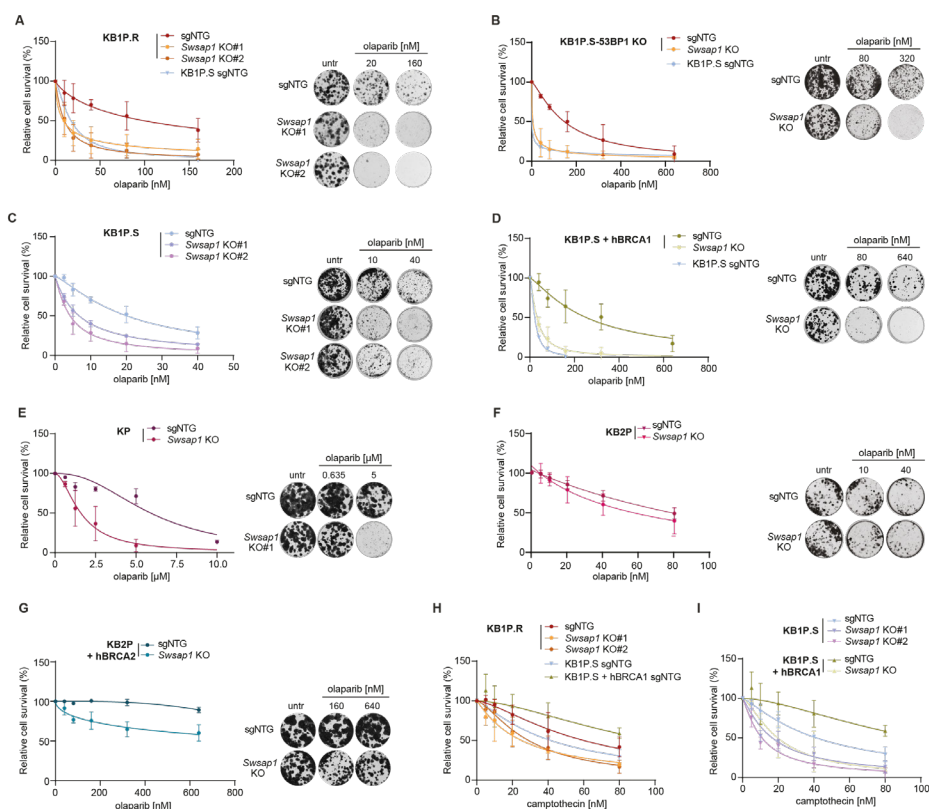


Figure 3 | Loss of SWSAP1 enhances in vitro efficacy of PARPi. A-F | Quantification and representative images of long-term clonogenic assays in KB1P.R (A), *Trp53bp1* deleted KB1P.S (KB1P.S-53BP1KO) (B), KB1P.S (C), KB1P.S reconstituted with human BRCA1 (KB1P.S+hBRCA1) (D), KP (E), KB2P (F) and KB2P reconstituted with human BRCA2 (KB2P+hBRCA2) (G) cell lines; treated with olaparib. Cells were treated for the whole extent of the assay. **H |** Quantification of long-term clonogenic assay in KB1P.R, KB1P.S and KB1P.S+hBRCA1 cell lines; treated with camptothecin for 6 hours the day after seeding. **I |** Quantification of long-term clonogenic assay in KB1P.S and KB1P.S+hBRCA1 cell lines, treated with camptothecin for 6 hours the day after seeding.

Effects of SWSAP1 loss on RAD51 loading and replication

We next tested if the *Swsap1*-deleted mouse mammary tumor cells displayed defective loading of RAD51, as previously suggested^{39–41}. To this end, we quantified the foci formation kinetics of RAD51 in KP cells exposed to ionizing radiation (IR) (10Gy), olaparib (500nM for 2 hours) or camptothecin (60nM for 4 hours). RAD51 foci formation was consistently delayed and reduced in *Swsap1*-deleted KP cells in response to all three damage-inducing agents (**Fig. 4A**). However, while loss of RAD51 loading could potentially explain increased response to PARPi in *Swsap1*-deleted KP, KB1P.S-53BP1KO and KB1P.S+hBRCA1 cells, it does not explain the increased response in KB1P.S cells, since these cells are already HR-deficient.

Several recent investigative advances have suggested that non-canonical RAD51 paralogs also play a role during DNA replication⁴³. We therefore measured replication fork progression in KB1P.S and KB1P.S+hBRCA1 cells in untreated conditions and observed that deletion of *Swsap1* resulted in longer tracks in KB1P.S but not in KB1P.S+hBRCA1 cells, suggesting that replication forks progressed faster in *Swsap1*-deleted BRCA1-deficient cells (**Fig. 4B,C**). We next looked at replication fork protection in the presence of hydroxyurea (HU), which results in replication stress by depleting the dNTP pool (**Fig. 4B**). In line with the known role of BRCA1 in replication fork protection, KB1P.S cells displayed shorter tracks in comparison to KB1P.S+hBRCA1; however, loss of SWSAP1 rescued fork protection in KB1P.S cells (**Fig. 4D**)⁴⁴. Since fork protection does not directly result in increased sensitivity to PARPi, but rather the opposite, suppression of fork degradation upon is not the reason for the increased sensitivity of SWSAP1-deficient cells to PARPi and topoisomerase II inhibitors. Further experiments will therefore be required to understand the mechanism(s) behind the increase drug sensitivity of *Swsap1*-deleted cells.

Loss of SWSAP1 enhances *in vivo* efficacy of PARPi in mice bearing BRCA1/2-deficient tumors

We next tested the effect of SWSAP1 loss *in vivo*. To this end, we orthotopically transplanted *Swsap1*-deleted KB1P.S and KB1P.S-53BP1KO cells, along with the corresponding non-modified lines, into the mammary fat pads of NMRI nude mice. Upon tumor outgrowth, mice were treated with olaparib or vehicle for 28 consecutive days, or with topotecan from days 0-14 and sacrificed when tumors progressed to a volume of 1,500 mm³. Olaparib-treated mice bearing *Swsap1*-deleted KB1P.S-53BP1KO tumors had increased survival compared with mice bearing unmodified PARPi-resistant KB1P.S-53BP1KO tumors (**Fig. 5A**). However, *Swsap1*-deleted tumors displayed slower growth and untreated mice had similar survival as the olaparib-treated ones, which challenges our *in vitro* observations (**Fig. 5A**). Also in PARPi-sensitive KB1P.S tumors, *Swsap1*-deletion further augmented the *in vivo* response to lower doses of olaparib, although the survival of some untreated mice bearing *Swsap1*-deleted KB1P.S tumors was similar to the survival of olaparib-treated mice due to slower growth of these tumors (**Fig. 5B**). Although the *in vivo* data do not exactly correlate

with what was observed *in vitro*, they suggest that SWSAP1 modulates growth of BRCA1-deficient tumors. Additional tumor intervention studies will be required to determine if loss of SWSAP1 improves the *in vivo* response of BRCA1/53BP1 double-deficient tumors to PARPi and if the slower growth and improved PARPi response of *Swsap1*-deleted tumors is independent of BRCA1 loss. Of note, mRNA expression of *Swsap1*, *Zswim7*, *Pds5b* and *Spidr* was significantly increased in KB1P and/or KB2P compared to KP tumors, suggesting that BRCA1/2-deficient tumors might display increased dependency on the Shu complex (Supplementary Fig. 4E-H).

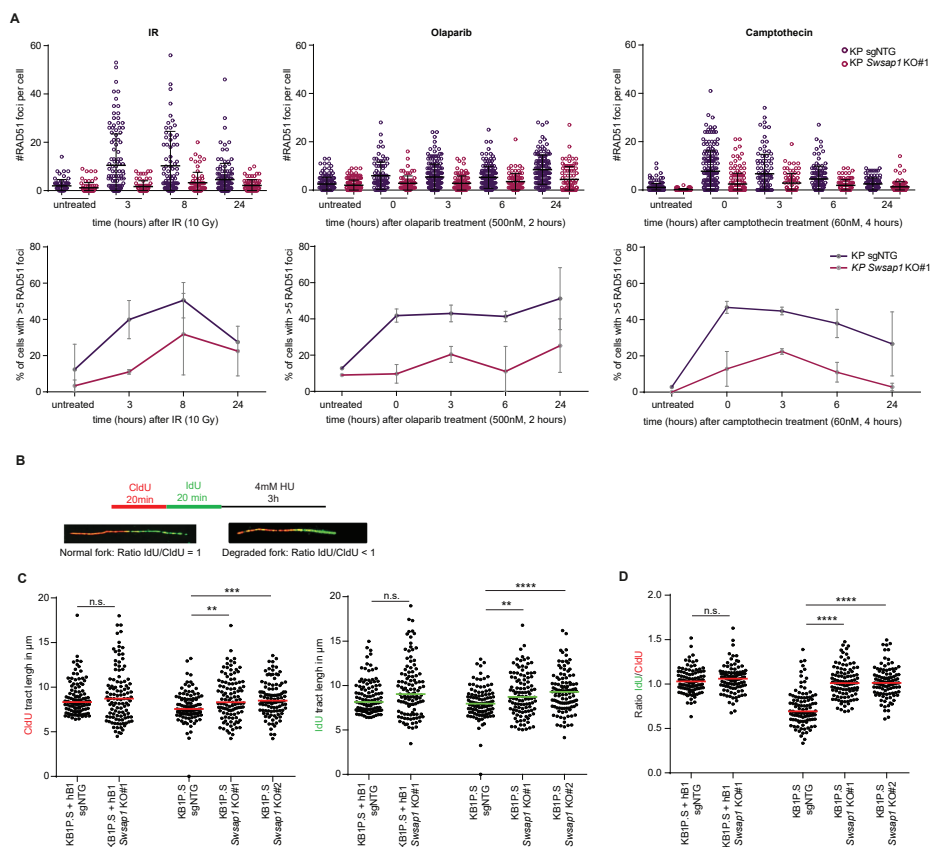


Figure 4 | Effects of SWSAP1 loss on RAD51 loading and replication. A | Quantification of RAD51 foci formation in KP cells, in response to ionizing radiation (IR) (10Gy), olaparib (500nM for 2 hours) and camptothecin (60nM for 4 hours), and following indicated recovery time. **B** | Experimental outline and representative images of normal and degraded replication forks. **C-D** | Quantification of fork progression (C) and fork degradation (D) in KB1P.S and KB1P.S+hBRCA1 cells. Data are represented as mean. ** $p < 0.01$, *** $p < 0.001$, **** $p < 0.0001$, n.s., not significant; Mann-Whitney U test.

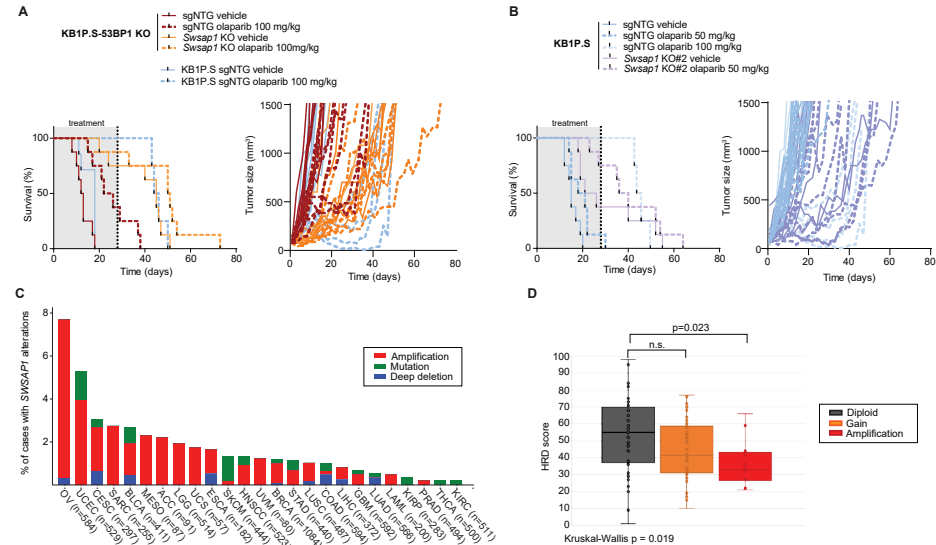


Figure 5 | Loss of SWSAP1 enhances in vivo efficacy of PARPi in mice bearing BRCA1/2-deficient tumors and SWSAP1 amplification is found in human cancers. A | Kaplan-Meier survival curves (left) and tumor growth curves (right) of mice transplanted with KB1P.S-53BP1KO cells. Upon tumor outgrowth, mice were treated with 100 mg/kg olaparib for 28 days as is indicated by a dotted line. Curves corresponding to mice transplanted with KB1P.S cells are displayed as control. **B |** Kaplan-Meier survival curves (left) and tumor growth curves (right) of mice transplanted with KB1P.S cells. Upon tumor outgrowth, mice were treated with 50 mg/kg olaparib for 28 days as is indicated by a dotted line. Curves corresponding to mice transplanted with KB1P.S cells and treated with 100 mg/kg are displayed as control. **C |** An overview of the frequency of alterations of the *SWSAP1* gene across all available Cancer Genome Atlas (TCGA) PanCancer Atlas cohorts with at least one samples altered. **D |** Association between *SWSAP1* amplification and homologous recombination deficiency (HRD) score, which is the sum of scores for telomeric-allelic imbalance, large-scale transition, and loss-of-heterozygosity.

DISCUSSION

Molecular alterations that lead to resistance to targeted therapies often result in acquired vulnerabilities which could be exploited to design rational combination therapies and selectively kill unresponsive cancer cells. In this study, we carried out functional genetic loss-of-function screens in PARPi-resistant BRCA1/53BP1 double-deficient cells to identify specific dependencies of these cells that could be exploited to overcome PARPi resistance. In the initial genome-wide screen, we identified several hits associated with DDR and with oxidative phosphorylation, including multiple subunits of the MCI, whereas the hits from the follow-up focused screens were mostly associated with recombination-associated DNA repair. In line with this, we identified SWSAP1, part of the Shu complex and involved in meiotic recombination, as a modulator of PARPi response and show that loss of SWSAP1 enhances toxicity of PARPi, *in vitro* and *in vivo*. Altogether, this study generated an extensive list of potential modulators of PARPi response and shows that genome-wide functional genomic screens are a promising approach to identify candidate therapeutic targets to overcome resistance.

Mitochondrial Complex I

The MCI consists of forty-seven subunits, with forty of them encoded in the nuclear DNA. The genome-wide screen carried out in this study identified thirteen of these subunits as hits, and almost all were significantly depleted in olaparib-treated conditions ($\log_2FC \leq -1$; $FDR \leq 0.1$). However, validation of the effects of MCI loss on PARPi sensitivity proved difficult as cells didn't seem to tolerate MCI loss as well as in the initial screen. While most of our data are preliminary, our results indicate that modulation of PARPi response by MCI activity may be dependent on the tissue culture medium and on the surrounding cells/environment, suggesting that *in vitro* cultures may not be the best approach to validate our findings. Hence, one could envision experiments where the effect of shRNA-mediated depletion of MCI on PARPi response is tested *in vivo*, as previously described^{23,48}. In addition, as maintaining MCI-depleted cells over time proved to be technically difficult, it was not possible to test our hypothesis that MCI disruption results in a decrease in the NAD^+ available as substrate for PARP1, which in turn leads to decreased residual PARylation in the presence of PARPi, and consequently in increased PARP1 trapping and PARPi-mediated toxicity.

Nonetheless, the concept that residual PARylation levels modulate response to PARPi has already been suggested by previous work from our lab, which shows that PARG depletion and subsequent increase in PARylation leads to resistance to PARPi⁴⁶. Moreover, depletion of nicotinamide phosphoribosyltransferase (NAMPT), a rate-limiting enzyme in the NAD^+ salvage pathway, has been shown to enhance the cytotoxicity of PARPi in triple-negative breast cancer cells⁴⁹. Another study has suggested that increased levels of the NAD^+ derivative $NADP^+$ can act as endogenous PARPi by competing for the NAD^+ binding site of PARP1 and thereby suppressing PARylation. Consequently, cancer cells with high $NADP^+$ to NAD^+ ratios have increased sensitivity to PARPi, irrespective of their *BRCA1/2* mutation status, which might reflect reduced PARylation rather than PARP1 trapping onto DNA⁵⁰. Together with our preliminary data, these studies suggest that reduction of NAD^+ availability can impair PARylation which, in the presence of PARPi, can eliminate residual PARylation and enhance the toxicity of PARPi.

Oxidative metabolism has also been identified as a vulnerability of HR-deficient tumors. A recent study suggested that HR-deficient ovarian and breast cancers rely on oxidative metabolism to supply NAD^+ for PARP-dependent DNA repair mechanisms⁵¹. In addition, they show that metformin significantly affected PAR levels in both p53-deficient and *BRCA2/p53* double-deficient cells, although depletion was stronger in *BRCA2*-deficient cells. Surprisingly, combination of PARPi with MCI inhibitors impaired response to PARPi, contrary to our results. Further studies will be required to conclusively test if a block in the oxidation of NADH to NAD^+ eliminates residual PARylation and enhances PARPi response, and if it also affects other NAD^+ -using enzymes.

SWSAP1

RAD51 is crucial for HR and thus inhibiting alternative pathways of RAD51 loading might

sensitize cells to PARPi and help to combat resistance to PARPi. Our genome-wide and focused screens identified several members of the Shu complex as modulators of PARPi-mediated toxicity. *Swsap1* was the strongest hit from the Shu complex and further validation showed that deletion of *Swsap1* increases response to PARPi and topoisomerase II inhibitors, suggesting SWSAP1 could be a potential therapeutic target to improve drug response. Of note, the strongest effects of SWSAP1 loss on the response to PARPi (i.e., re-sensitization to drug doses similar or lower than KB1P.S cells) were observed in cells that originated from HR-deficient BRCA1-deficient tumors, even if HR had subsequently been restored via 53BP1 loss or BRCA1 re-expression (e.g., KB1P.R, KB1P.S-53BP1KO and KB1P.S+hBRCA1 cells). Weaker effects of SWSAP1 loss on PARPi response were observed in cells that always expressed wild-type BRCA1 (such as KP, KB2P+hBRCA2 and RPE1-p53-KO cells). Further validation in additional isogenic BRCA1/2-deficient and -proficient human cancer cell lines is required to understand if SWSAP1 is a specific vulnerability of BRCA1/2-deficient cells.

Additional evidence that SWSAP1 could be a potential therapeutic target in cancer therapy arises from the fact that survival data from genome-scale RNAi and CRISPR-Cas9 screens (<https://depmap.org/portal>) show that all four Shu complex factors (SWSAP1, ZSWIM7, PDS5B and SPIDR) are non-essential. Hence, toxicity associated with pharmacological inhibition of SWSAP1 in normal cells might be limited. In support of this, SWSAP1 is dispensable for mouse viability, albeit essential for male and female fertility^{38,41,52}. Similar knockout phenotypes were observed for ZWIM7 and SPIDR. In contrast, other RAD51 paralogs such as RAD51B, RAD51C, RAD51D, and XRCC2 are essential for embryonic survival.

To investigate if SWSAP1 might be a potential therapeutic target, we tested the effect of *Swsap1* deletion *in vivo* by orthotopically transplanting *Swsap1*-deleted KB1P.S and KB1P.S-53BP1KO cells into the mammary fat pad of NMRI nude mice. Deletion of *Swsap1* slowed tumor growth in untreated conditions in 6/8 KB1P.S-53BP1KO tumors and in 3/8 KB1P.S tumors, comparable to what was observed *in vitro*. Moreover, we observed an increased olaparib response in *Swsap1*-deleted KB1P.S tumors, but not in *Swsap1*-deleted BRCA1/53BP1 double-deficient tumors. The latter contrasts with the *in vitro* data and might be due to the slow growth of the *Swsap1*-deleted KB1P.S-53BP1KO tumors. Further *in vivo* studies are required to test the effect of prolonged olaparib treatment (e.g., 56 days instead of 28 days) on these tumors. Additionally, testing the effect of *Swsap1* deletion in BRCA1-proficient mammary tumors will be required to determine whether the impaired tumor growth and increased PARPi sensitivity caused by SWSAP1 loss are a specific vulnerability of BRCA1-deficient tumor cells.

Recent studies suggest the SWSAP1-ZSWIM7-SPIDR complex is critical for inter-homolog HR but dispensable for mitotic intra-chromosomal HR, explaining why patients and mice with loss-of-function mutations in this complex are viable⁴¹. In this study, we showed SWSAP1 is also important for the proliferation of BRCA1-deficient and BRCA1/53BP1

double-deficient tumor cells, and for their response to DNA damage-inducing agents like PARPi and topoisomerase II inhibitors. Similar to previous studies, we observed lower levels of DNA damage-induced nuclear RAD51 foci in *Swsap1*-deleted KP tumor cells, suggesting loss of Shu complex may impair HR repair in mitotic cells^{39–41}. Impaired HR could explain the increased sensitivity of *Swsap1*-deleted HR-proficient and HR-restored cells to PARPi and topoisomerase II inhibitors, but it does not explain the increased response of *Swsap1*-deleted HR-negative KB1P cells, suggesting that other mechanisms may underlie the effect of SWSAP1 loss on response to these DNA damage-inducing agents. Recent studies suggested non-canonical RAD51 paralogs also play a role during DNA replication stress and thus defects in replication stress response might explain the increased drug sensitivity of *Swsap1*-deleted HR-negative BRCA1/2-deficient cells⁴³. In line with this, KB1P.S cells showed faster replication fork progression, and replication fork protection was restored in KB1P.S cells. Fork protection reduces sensitivity to PARPi and thus suppression of fork degradation cannot explain the increased drug sensitivity of *Swsap1*-deleted cells. Additional experiments such as analysis of replication fork restart, fork asymmetry and induction of post-replicative single-stranded DNA (ssDNA) gaps will help understanding if replication stress is causal to the increased PARPi sensitivity of SWSAP1-deficient cells. Importantly, the Shu complex has also been reported to be important for the removal of alkylation adducts in ssDNA during replication and for the regulation of RAD52 localization during rDNA repair, and thus the role of these pathways in the response to PARPi should also be investigated^{43,54–56}.

Intriguingly, *SWSAP1* is frequently amplified in multiple cancer types (www.cbioportal.org), including ovarian cancer (7%) and breast cancer (1%), and ovarian cancers with amplified *SWSAP1* show lower HR-deficiency (HRD) scores. It would therefore be interesting to test if overexpression of SWSAP1 in BRCA1/2-deficient cells causes (partial) restoration of HR and RAD51 loading, and a reduced response to PARPi.

In sum, our screening efforts identified a comprehensive list of potential therapeutic targets that might be exploited to improve PARPi response. The majority of the hits arising from the secondary screens were associated with DDR and recombination, suggesting that rewiring of DDR is the most promising approach of reverting PARPi resistance in BRCA1/53BP1 double-deficient cells. However, screens in models which better represent physiological conditions (e.g., *in vivo* screens) will be important to determine if the non-DDR pathways identified by our screening efforts (e.g., oxidative phosphorylation) may also play a role in mediating PARPi resistance.

ACKNOWLEDGMENTS

We thank Peter Bouwman for sharing the mouse ES cells, Sylvie Noordermeer and Dan Durocher for the RPE1-TERT cells, and Roebi de Bruijn for the analysis of tumor RNA-seq. We thank Hanneke van der Gulden, the NKI Preclinical Intervention Unit, Digital Microscopy facility, Genomics Core facility and Animal facility for technical assistance. The underlying study have been made possible partly on the basis of the data that the Hartwig Medical Foundation (HMF, Utrecht, the Netherlands) and the Center of Personalized Cancer Treatment (CPCT, Rotterdam, the Netherlands). This work was supported by grants from the European Union Horizon 2020 research and innovation program (agreement 722729), Dutch Research Council (Vici 91814643, Vidi 193.131) and Onco Institute.

AUTHOR CONTRIBUTIONS

Conceptualization: M.P.D., P.B. and J.J.; Methodology: M.P.D., I.v.d.H., A.R.C and P.B.; Investigation: M.P.D., I.v.d.H., C.F., Y.F., A.K.; Animal studies: J.S., N.P., and M.v.d.V.; Data analysis: C.L., R.L.B. and J.B.; Writing of original draft, review & editing: M.P.D., P.B. and J.J.; Supervision: S.R., A.R.C and J.J.

METHODS

EXPERIMENTAL MODEL AND SUBJECT DETAILS

Cell Lines and cell culture

KP³⁷, KB1P.S, KB1P.R⁵⁷ and KB1P.S+hB1⁴² have been previously described.⁵³BP1KO KB1P.S cells as well as all *Swsap1* KO lines have been generated in this study. All these cell lines were cultured in DMEM/F12+GlutaMAX (Gibco) containing 5 µg/ml Insulin (Sigma), 5 ng/ml murine epidermal growth-factor (EGF, Sigma), 10% FBS and 50 units/ml penicillin-streptomycin (Gibco) and were cultured under low oxygen conditions (3% O₂, 5% CO₂ at 37°C). Mouse ES cells with a selectable conditional *Brca1* deletion (*R26Cre^{ERT2}/wt*; *Brca1^{SCo/-}*) have been previously described^{12,23}. These cells were cultured under normal oxygen conditions (21% O₂, 5% CO₂, 37°C), on gelatin-coated plates in 60% buffalo red liver (BRL) cell conditioned medium, 0.1 mM β-mercaptoethanol (Merck) and 10³ U/ml ESGRO LIF (Millipore) and 50 units/ml penicillin-streptomycin (Gibco); except when pyruvate supplementation was tested, for what we used DMEM+GlutaMAX without previous supplementation with pyruvate (GIBCO), supplemented with 10% FBS and 50 units/ml penicillin-streptomycin (Gibco). *Brca1* deletion in these cells was induced by incubation with 4-hydroxytamoxifen for three days. RPE1-hTERT cell lines were grown in DMEM+GlutaMAX (Gibco) supplemented with 10% FBS and 50 units/ml penicillin-streptomycin (Gibco),

under low oxygen conditions (3% O₂, 5% CO₂ at 37°C). RPE1-P, RPE1-B1P.S and RPE1-B1P.R cells were previously generated and the *SWSAP1* KO lines were established in this study¹⁶. HEK293FT (RRID: CVCL_6911) cells were cultured in IMDM+GlutaMAX-I (Gibco) supplemented with 10% FBS and 50 units/ml penicillin-streptomycin (Gibco), under normal oxygen conditions (21% O₂, 5% CO₂, 37°C).

Mice

All animal experiments were approved by the Animal Ethics Committee of The Netherlands Cancer Institute (Amsterdam, the Netherlands) and performed in accordance with the Dutch Act on Animal Experimentation (November 2014). Cell line transplantation experiments were performed in NMRI nude females, at the age of 6 weeks. NMRI nude animals were purchased from Janvier Labs. Animals were assigned randomly to the treatment groups and the treatments were supported by animal technicians who were blinded regarding the hypothesis of the treatment outcome.

METHOD DETAILS

Drugs

Olaparib (Syncom), camptothecin (Sigma), rotenone (Sigma) and piericidin a (Sandbio) were dissolved in DMSO. Metformin hydrochloride (Sigma) was dissolved in water. All dissolved compounds were stored at -20°C.

Functional Genetic Screens

Genome-wide screen

Mouse improved genome-wide knockout CRISPR library v2 was stably introduced into *Brca1*^{-/-}; *Trp53*^{-/-}; *Trp53bp1*^{-/-} mESCs by lentiviral transduction using a multiplicity of transduction (MOI) of 0.3, in order to ensure that each cell only gets incorporated with one only sgRNA. mES cells and organoids were selected with puromycin, 3 µg/ml, for 3 days and then seeded in the presence of 25nM olaparib, left untreated or pelleted for the genomic DNA isolation (T0). The total number of cells used in a single replicate was calculated as following: library complexity x coverage (500x). Cells were seeded at a density of 2.5 million cells per 15 cm dish and were kept in culture for 3 weeks and passaged every 7 days (and seeded in single cells) while keeping the coverage at every passage. Triplicates were performed for each condition. In the end of the screen, cells were pooled and genomic DNA was extracted (QIAmp DNA Mini Kit, Qiagen). sgRNA sequences were retrieved by a two-step PCR amplification, as described before⁴⁸. To maintain screening coverage, the amount of genomic DNA used as an input for the first PCR reaction was taken into account (6 µg of genomic DNA per 10⁶ genomes, 1 µg/PCR reaction). Resulting PCR products were purified using MiniElute PCR Purification Kit (Qiagen) and submitted for Illumina sequencing. Sequence alignment and dropout analysis was carried out using the algorithms MAGeCK (Li et al., 2014) and DESeq2^{58,59}. Gene ranking is generated automatically with MaGECK

algorithm. To generate gene ranking based on DESeq2 algorithm, we calculated per gene the number of hit sgRNAs and the mean of the \log_2 FoldChange over those sgRNAs. We then ranked the genes based on these two metrics.

Focused screen

For the design of the custom sgRNA library the BROAD GPP sgRNA design portal (<https://portals.broadinstitute.org/gppx/crispick/public>) was used. The sgRNA sequences targeting the candidate genes (**Supplementary table 2**), essential, non-essential, safe-haven regions (non-coding) and non-targeting genes were ordered as pool of oligonucleotides (TWIST Biosciences) with flanking sequences to enable PCR amplification and Gibson assembly into pLentiGuide-Puro (pLG, addgene #52963). The sgRNA library was generated as described previously, with modifications⁶⁰. The oligo library was amplified with KAPA® HiFi HotStart Polymerase (Roche, Catalog #KK2502) according to manufacturer protocol using 1x KAPA HiFi Fidelity buffer, 0.3mM each dNTP, 0.4 ng/ul oligo pool, 0.3uM pLG_U6_forward (5'- GGCTTTATATATCTTGTGGAAAGGACGAAACACCG-3'), 0.3uM pLG-TRACR_Reverse (5'-GACTAGCCTTATTTAACTTGCTATTTCTAGCTCTAAAAC-3'), 0.5 U KAPA HiFi HotStart DNA polymerase in a total volume of 25ul with the PCR conditions: 98°C, 3 min; denature 98°C, 30 sec; anneal 62°C, 15 sec; extend 72 °C 10, sec; 15 cycles followed by 10 min at 72°C. Purification of the PCR product was performed with the Isolate II PCR and Gel kit (Bioline, cat. BIO-52060) according to the manufacturer's directions. The linearized pLentiGuide plasmid backbone was extracted from gel using the Isolate II PCR and Gel kit (Bioline, cat no. BIO-52060) according to the manufacturer's directions. For Gibson assembly, each reaction contained 100ng purified digested plasmid and 5ng purified PCR product. The Gibson reaction were precipitated as as described previously and 100ng of the pooled sgRNA library was transformed in 25ul Endura Electrocompetent cells according to the manufacturer's instructions⁶⁰. After transformation and overnight colony growth, bacteria were collected by scraping in LB and plasmid DNA was isolated using Nucleobond Xtra Midi (Macherey-Nagel cat#740410). The representation of the sgRNA library was verified by next generation sequencing. Focused candidate screens were carried out similarly to genome-wide screen: ES-B1P.R cells were treated with 25nM olaparib for two weeks or left untreated; RPE1-P and RPE1-B1P.R were treated with 100nM olaparib for two weeks or left untreated. Triplicates were performed for each condition. DNA extraction and library preparation was carried out as in genome-wide screen.

Oxygen consumption rate (OCR)

OCR was measured using Seahorse Bioscience XFe24 Analyzer (Agilent). Cells were seeded 24hr before the assay in XF24 Seahorse Cell Culture microplates (Agilent) (sgNTG, 90,000 cells/well; sgNDUFA2, 100,000 cells/well; sgNDUFAF8, 120,000 cells/well). For OCR measurements, the following reagents were added: oligomycin (1 μ M), FCCP (0.4 μ M), and rotenone (1 μ M) and antimycin A (1 μ M). All results were normalized to protein content.

Briefly, cells were washed with PBS and then lyzed with RIPA buffer for 20 min. The protein concentration was then determined using Pierce BCA Protein Assay Kit (Thermo Scientific).

Long-Term Clonogenic Assays

Long-term clonogenic assays were performed in 6-well plates for the validation of MCI and in 12-well plates for validation of the Shu complex. Cells were seeded at low density to avoid contact inhibition between the clones (6-well: ES-B1P.R, 3,000 cells/well; KB1P.R, 2,500 cells/well; KP, 1,000 cells/well; 12-well: KB1P.S, 2,000 cells/well; KB1P.R, 1,000 cells/well; KB1P.S-53BP1KO, 1,000 cells/well; KB1P.S+hBRCA1, 500 cells/well; KB2P, 2,000 cells/well; KB2P+hBRCA2, 500 cells/well; KP, 500 cells/well; RPE1-P, 800 cells/well, RPE1-B1P.R, 1,000 cells/well) and cultured for 7-10 days. For the quantification of Shu complex experiments, cells were incubated with Cell-Titer Blue (Promega) reagent to measure cell viability and later fixed with 4% formaldehyde and stained with 0.1% crystal violet to generate representative images of the experiment. Because Cell-Titer Blue assay relies on cellular metabolic capacity, we decided not to use this tool to measure cell viability in the MCI experiments. Hence, at the end of the assay, cells were directly fixed with 4% formaldehyde and stained with 0.1% crystal violet and quantification was carried out by diluting (extraction) crystal violet with 1% acetic acid and absorbance was measured at 590 nm wavelength.

Short-term Cytotoxicity Assays

Cells were seeded in 96-well plates (parental and NDUFA2-depleted cells, 1,000 cells/well; NDUFS8-depleted cells, 2,000 cells/well) and the indicated drugs were added the next day and left for three days. At the end of the assay, plates were fixed with cold TCA (50 %) and left in the fridge for one hour, washed with water five times, and then airdried. For quantification, Sulforhodamine B (SRB) was added for 30 min. Plates were then washed three times with 1% acetic acid and left to airdry. 10mM TRIS solution was added to the dry plates for a short period to dissolve the SRB and absorbance was measured at 540 nm wavelength.

Competition assays

GFP-labeled parental cells and MCI-depleted cells were mixed at the indicated different ratios and treatment with olaparib for two weeks. At the end of the assay, cells were collected and FACS was performed using the BD LSRFortessa Cell Analyzer (BD Biosciences) equipped with the BD FACSDiva Software (v.8.0.2, BD Biosciences). Data were analyzed using FlowJo (v.10.7.1, BD Biosciences).

Proliferation assay

Cells were seeded at low density in 96-well plates (4,000 cells/well) and imaged every 4h using IncuCyte®, for 1 week duration. Cells were grown under normal oxygen conditions (21% O₂, 5% CO₂, 37°C), in the presence or absence of 1 mM pyruvate or 1 mM lactate.

Data was analyzed using IncuCyte ZOOM 2018A software.

Western Blot

Cells were trypsinized and then lysed in RIPA buffer for 20 min. The protein concentration was determined using Pierce BCA Protein Assay Kit (Thermo Scientific). SDS-Page was carried out with the Invitrogen NuPAGE SDS-PAGE Gel System (Thermo Fisher 4–12% Bis-Tris gels were used) buffer: MOPS; input: 40µg protein, according to the manufacturer's protocol. Next, proteins were electrophoretically transferred to a nitrocellulose membrane (Biorad). Before blocking, membranes were stained with Ponceau S, followed by blocking in 5% (w/v) milk in TBS-T for 1hr at RT. Membranes were incubated with primary antibody 4hrs at RT in 1% (w/v) milk in TBS-T (rabbit anti-SWSAP1, 1:500, antibody produced for this study). Horseradish peroxidase (HRP)-con-jugated secondary antibody incubation was performed for 1 hr at RT (anti-rabbit HRP 1:2000) in 1% (w/v) milk in TBS-T. Signals were visualized by ECL (Pierce ECL Western Blotting Substrate, Thermo Scientific).

RT-qPCR

In order to determine gene expression levels, RNA was extracted from cultured cells using ISOLATE II RNA Mini Kit (Bioline) and used as a template to generate cDNA with Tetro cDNA Synthesis Kit (Bioline). Quantitative RT-PCR was performed using SensiMix SYBR Low-ROX Kit (Bioline; annealing temperature – 60°C). *Swsap1_forward* (5'- GCTCCAGAAGGTTCTGTTTCCA -3'), *Swsap1_reverse* (5'- TCCAGAAGCAATGCAGCCAA -3'), *Ggnbp2_forward* (5'- GAG-GAGTTCCCCTTCGAGAG -3'), *Ggnbp2_reverse* (5'- GCACCATTATTCTGATGCCCAT -3').

RAD51 Foci Immunofluorescence

Cells were seeded on coverslips 24 hr prior the assay to achieve ~90% confluency. Cells were then EITHER irradiated using the Gammacell 40 Extractor (Best Theratronics Ltd.) at the dose of 10 Gy, treated with 500nM olaparib for 2 hr, or TREATED with 60nM camptothecin for 4 hr, and allowed to recover for the indicated times. Cells washed with PBS++ (PBS solution containing 1 mM CaCl₂ and 0.5 mM MgCl₂) and pre-extracted with 0.5% (v/v) Triton X-100 in PBS++ for 5 min. Next, cells were washed with PBS++ and fixed with 2% (v/v) paraformaldehyde solution in PBS for 20 min. cells were then permeabilized with ice-cold methanol/acetone solution (1:1) for 15 min. To minimize the background, cells were further incubated for 20 min in staining buffer (1% (w/v) BSA, 1% (v/v) FBS, 0.15% (w/v) glycine and 0.1% (v/v) Triton X-100 in PBS). Staining buffer was also used as a solvent for antibodies – primary antibody rabbit anti-RAD51, 1:1000, #70-002, Bioacademia; secondary antibody Alexa Fluor® 658-conjugated, 1:1000, A11011, Invitrogen. Incubation with primary and secondary antibodies was done for 2 hr and 1 hr, respectively. All incubations were performed at room temperature. Samples were mounted with VECTASHIELD Hard Set Mounting Media with DAPI (#H-1500; Vector Laboratories). Images were captured with Leica SP5 (Leica Microsystems) confocal system and analyzed using an in-house developed macro to

automatically and objectively evaluate the DNA damage-induced foci ¹⁰.

DNA Fiber Assay

DNA fiber analysis was conducted in accordance with the previously described protocol⁶¹. Cells were sequentially pulse-labelled with nucleotide analogues, 30µM CldU (c6891, Sigma-Aldrich) and 250µM IdU (I0050000, European Pharmacopoeia) for 20 min. After double labelling, cells were washed with PBS and either treated with 4mM HU for 3 hr or left untreated. Then, cells were harvested and resuspended in ice cold PBS to the final concentration 2.5 × 10⁵ cells per ml. Labelled cells were mixed with unlabeled cells at 1:1 (v/v), and 2.5 µl of cell suspension was spotted at the end of the microscope slide. 8 µl of lysis buffer (200mM Tris-HCl, pH 7.5, 50mM EDTA, and 0.5% (w/v) SDS) was applied on the top of the cell suspension, then mixed by gently stirring with the pipette tip and incubated for 8 min. Following cell lysis, slides were tilted to 15–45° to allow the DNA fibers spreading along the slide, air dried, fixed in 3:1 methanol/acetic acid overnight at 4 °C. Subsequently, fibers were denatured with 2.5 M HCl for 1 hr. After denaturation, slides were washed with PBS and blocked in blocking solution (0.2% Tween 20 in 1% BSA/PBS) for 40 min. After blocking, primary antibody solutions are applied, anti-BrdU antibody recognizing CldU (1:500, ab6326; Abcam) and IdU (1:100, B44, 347580; BD) for 2 hours in the dark at RT followed by 1h incubation with secondary antibodies: anti-mouse Alexa Fluor 488 (1:300, A11001, Invitrogen) and anti-rat Cy3 (1:150, 712-166-153, Jackson Immuno-Research Laboratories, Inc.). Finally, slides are washed with PBS and subsequently mounting medium is spotted and coverslips are applied by gently pressing down. Slides were sealed with nail polish and air dried. Fibers were visualized and imaged by Carl Zeiss Axio Imager D2 microscope using 63X Plan Apo1.4 NA oil immersion objective. Data analysis was carried out with ImageJ software⁶⁴.

In vivo Studies

Mouse tumor-derived cells were dissociated into single cells and collected in medium, filtered with 70µm nylon filters (Corning) and resuspended in complete media/BME mixture (1:1). All cell line suspensions contained a total of 500.000 cells per 40 µl of media/BME mixture, and were injected in the fourth right mammary fat pad of wild-type mice. Mammary tumor size was determined by caliper measurements (length and width in millimeters), and tumor volume (in mm³) was calculated by using the following formula: 0.5 × length × width². Upon tumor outgrowth to approximately 75 mm³, mice were treated with either vehicle or olaparib for 28 consecutive days. Animals were sacrificed with CO₂ when the tumor volume reached 1,500 mm³.

Correlation between GGNBP2 Copy Number Status and PARPi Response in HMF Cohort

Processed whole genome sequencing data on metastatic solid tumors were obtained from the Hartwig Medical Foundation (HMF) (data access request DR-184) and analyzed

based on their bioinformatic pipeline (<https://github.com/hartwigmedical/pipeline>) designed to detect all types of somatic alterations including structural variations and copy number aberrations as previously described⁶². Patients who received olaparib or niraparib as single or combination therapy were used to investigate the association between GGNBP2 copy number status and clinical response to PARP inhibitors. First RECIST response evaluated 8-12 weeks after the treatment was used to define clinical response.

TCGA Data Analysis and Comparison of HRD Score between Samples with SWSAP1 Gain/ Amplification and Samples with Wild-type (diploid) SWSAP1

Genomic data of OV cohort generated by The Cancer Genome Atlas (TCGA) consortium. Copy number and gene expression (as z-scores relative to all samples) data were downloaded from cBioPortal (<http://www.cbioportal.org/>) on 22 June 2022. Scores for telomeric-allelic imbalance (TAI), large-scale transition (LST), loss-of-heterozygosity (HRD LOH) and Homologous Recombination Deficiency (HRD) were downloaded from TCGA DDR Data Resources available under <https://gdc.cancer.gov/about-data/publications/PanCan-DDR-2018>. TAI represents the number of subchromosomal regions with allelic imbalance extending to the telomere, LST is the number of chromosomal breaks between adjacent regions of at least 10Mb, HRD LOH is the number of loss-of-heterozygosity regions of intermediate size (< 15Mb but < whole chromosome in length) and HRD Score is calculated from the three scores (TAI + LST + HRD LOH). HRD score and its components were compared between samples with different SWSAP1 copy number using Kruskal-Wallis test (global test) and post-hoc comparisons were made based on multiple comparisons of mean ranks of all group pairs (Siegel, Castellan, 1988, p. 213-215).

DATA AND SOFTWARE AVAILABILITY

Sequencing of all functional genetic screens was performed at the Netherlands Cancer Institute and results will be made available upon request. WGS data from HMF can be obtained through standardized procedures and request forms at <https://www.hartwigmedicalfoundation.nl>. The TCGA ovarian cancer dataset used in this study is available with informed consent under the authorization of local Institutional Review Boards (<https://www.cancer.gov/about-nci/organization/ccg/research/structural-genomics/tcga>). Copy number data used for this manuscript are deposited by the GDC (<https://gdc.cancer.gov/about-data/publications/pancanatlas>).

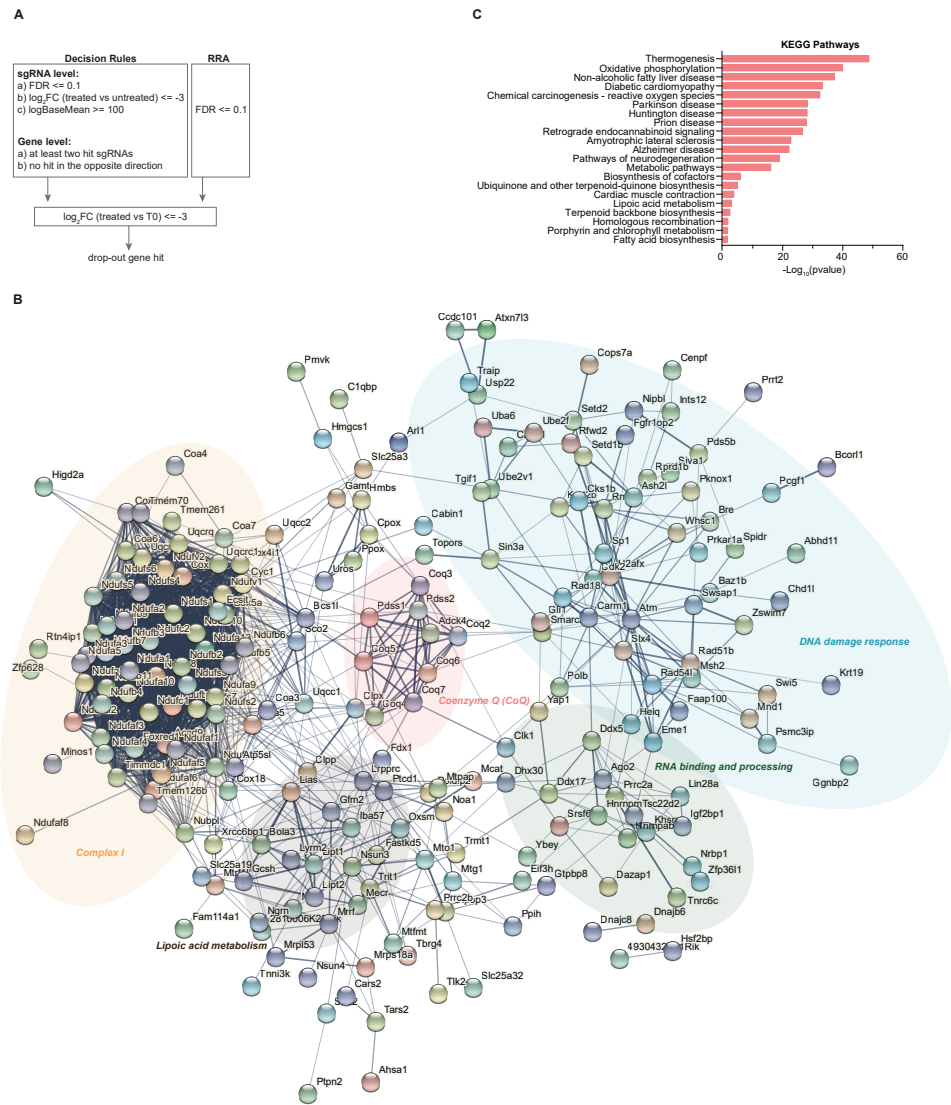
REFERENCES

1. Farmer, H. *et al.* Targeting the DNA repair defect in BRCA mutant cells as a therapeutic strategy. *Nature* **434**, 917–21 (2005).
2. Bryant, H. E. *et al.* Specific killing of BRCA2-deficient tumours with inhibitors of poly(ADP-ribose) polymerase. *Nature* **434**, 913–917 (2005).
3. Pascal, J. M. & Ellenberger, T. The rise and fall of poly(ADP-ribose): An enzymatic perspective. *DNA Repair (Amst)*. **32**, 10–16 (2015).
4. Helleday, T. The underlying mechanism for the PARP and BRCA synthetic lethality: Clearing up the misunderstandings. *Molecular Oncology* **5**, 387–393 (2011).
5. Ström, C. E. *et al.* Poly (ADP-ribose) polymerase (PARP) is not involved in base excision repair but PARP inhibition traps a single-strand intermediate. *Nucleic Acids Res.* **39**, 3166–3175 (2011).
6. Murai, J. *et al.* Trapping of PARP1 and PARP2 by clinical PARP inhibitors. *Cancer Res.* **72**, 5588–5599 (2012).
7. Murai, J. *et al.* Stereospecific PARP trapping by BMN 673 and comparison with olaparib and rucaparib. *Mol. Cancer Ther.* **13**, 433–443 (2014).
8. Paes Dias, M., Moser, S. C., Ganesan, S. & Jonkers, J. Understanding and overcoming resistance to PARP inhibitors in cancer therapy. *Nature Reviews Clinical Oncology* 1–19 (2021). doi:10.1038/s41571-021-00532-x
9. Mateo, J. *et al.* A decade of clinical development of PARP inhibitors in perspective. *Ann. Oncol.* **30**, 1437–1447 (2019).
10. Xu, G. *et al.* REV7 counteracts DNA double-strand break resection and affects PARP inhibition. *Nature* **521**, 541–544 (2015).
11. Boersma, V. *et al.* MAD2L2 controls DNA repair at telomeres and DNA breaks by inhibiting 5' end resection. *Nature* **521**, 537–40 (2015).
12. Bouwman, P. *et al.* 53BP1 loss rescues BRCA1 deficiency and is associated with triple-negative and BRCA-mutated breast cancers. *Nat. Struct. Mol. Biol.* **17**, 688–695 (2010).
13. Bunting, S. F. *et al.* 53BP1 Inhibits Homologous Recombination in Brca1-Deficient Cells by Blocking Resection of DNA Breaks. *Cell* **141**, 243–254 (2010).
14. Chapman, J. R. *et al.* RIF1 Is Essential for 53BP1-Dependent Nonhomologous End Joining and Suppression of DNA Double-Strand Break Resection. *Mol. Cell* **49**, 858–871 (2013).
15. Escobedo-Díaz, C. *et al.* A Cell Cycle-Dependent Regulatory Circuit Composed of 53BP1-RIF1 and BRCA1-CtIP Controls DNA Repair Pathway Choice. *Mol. Cell* **49**, 872–883 (2013).
16. Noordermeer, S. M. *et al.* The shieldin complex mediates 53BP1-dependent DNA repair. *Nature* **560**, 117–121 (2018).
17. Ghezraoui, H. *et al.* 53BP1 cooperation with the REV7–shieldin complex underpins DNA structure-specific NHEJ. *Nature* **560**, 122–127 (2018).
18. Dev, H. *et al.* Shieldin complex promotes DNA end-joining and counters homologous recombination in BRCA1-null cells. *Nat. Cell Biol.* **20**, 954–965 (2018).
19. Scully, R., Panday, A., Elango, R. & Willis, N. A. Stalled replication forks DNA double-strand break repair-pathway choice in somatic mammalian cells D N A D A m A g e. doi:10.1038/s41580-019-0152-0
20. Jaspers, J. E. *et al.* Loss of 53BP1 causes PARP inhibitor resistance in BRCA1-mutated mouse mammary tumors. *Cancer Discov.* **3**, 68–81 (2013).
21. Cruz, C. *et al.* RAD51 foci as a functional biomarker of homologous recombination repair and PARP inhibitor resistance in germline BRCA-mutated breast cancer. *Ann. Oncol.* **29**, 1203–1210 (2018).
22. Waks, A. G. *et al.* Reversion and non-reversion mechanisms of resistance to PARP inhibitor or platinum chemotherapy in BRCA1/2-mutant metastatic breast cancer. *Ann. Oncol.* **31**, 590–598 (2020).
23. Paes Dias, M. *et al.* Loss of nuclear DNA ligase III reverts PARP inhibitor resistance in BRCA1/53BP1 double-deficient cells by exposing ssDNA gaps. *Mol. Cell* (2021).
24. Tzelepis, K. *et al.* A CRISPR Dropout Screen Identifies Genetic Vulnerabilities and Therapeutic Targets in Acute Myeloid Leukemia. *Cell Rep.* **17**, 1193–1205 (2016).
25. King, M. P. & Attardi, G. Human cells lacking mtDNA: Repopulation with exogenous mitochondria by complementation. *Science (80-.)*. **246**, 500–503 (1989).
26. Juhász, S. *et al.* The chromatin remodeler ALC1 underlies resistance to PARP inhibitor treatment. *Sci. Adv.* **6**, 8626–8644 (2020).
27. Blessing, C. *et al.* The Oncogenic Helicase ALC1 Regulates PARP Inhibitor Potency by Trapping PARP2 at DNA Breaks. *Mol. Cell* **80**, 862–875.e6 (2020).
28. Verma, P. *et al.* ALC1 links chromatin accessibility to PARP inhibitor response in homologous recombination-deficient cells. *Nat. Cell Biol.* **23**, 160–171 (2021).
29. Hewitt, G. *et al.* Defective ALC1 nucleosome remodeling confers PARPi sensitization and synthetic lethality with HRD. *Mol. Cell* **81**, 767–783.e11 (2021).
30. Guo, K. *et al.* Ablation of Ggnbp2 impairs meiotic DNA double-strand break repair during spermatogenesis in

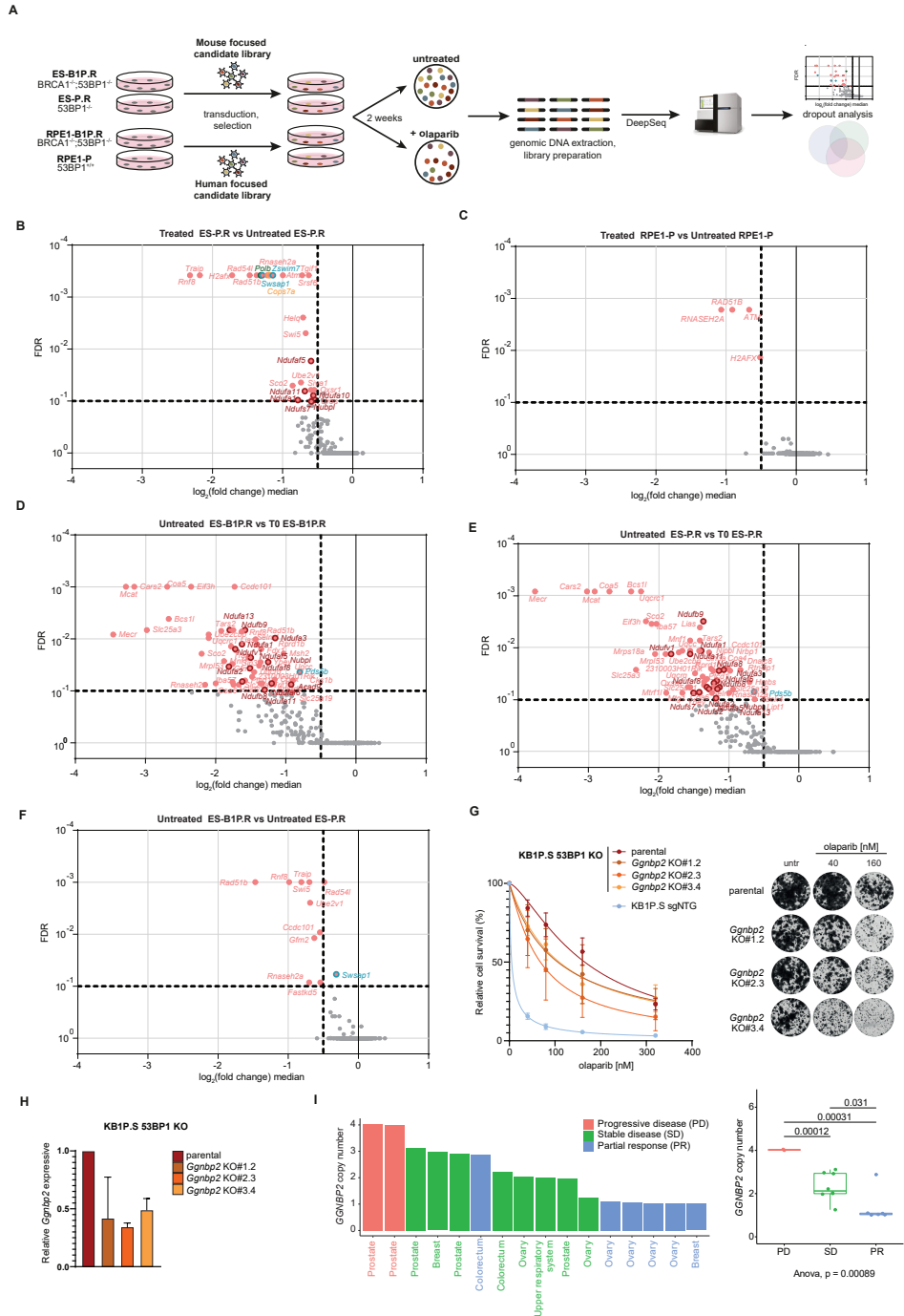
- mice. *J. Cell. Mol. Med.* **22**, 4863–4874 (2018).
31. Chen, A. *et al.* GGNBP2 is necessary for testis morphology and sperm development. *Sci. Reports* 2017 71 **7**, 1–8 (2017).
 32. Priestley, P. *et al.* Pan-cancer whole-genome analyses of metastatic solid tumours. *Nature* **575**, 210–216 (2019).
 33. Brinkman, E. K., Chen, T., Amendola, M. & van Steensel, B. Easy quantitative assessment of genome editing by sequence trace decomposition. *Nucleic Acids Res.* **42**, e168–e168 (2014).
 34. Birsoy, K. *et al.* An Essential Role of the Mitochondrial Electron Transport Chain in Cell Proliferation Is to Enable Aspartate Synthesis. *Cell* **162**, 540–551 (2015).
 35. Gui, D. Y. *et al.* Environment Dictates Dependence on Mitochondrial Complex I for NAD⁺ and Aspartate Production and Determines Cancer Cell Sensitivity to Metformin. *Cell Metab.* **24**, 716–727 (2016).
 36. Sullivan, L. B. *et al.* Supporting Aspartate Biosynthesis Is an Essential Function of Respiration in Proliferating Cells Article Supporting Aspartate Biosynthesis Is an Essential Function of Respiration in Proliferating Cells. *Cell* **162**, 552–563 (2015).
 37. Evers, B. *et al.* Selective Inhibition of BRCA2-Deficient Mammary Tumor Cell Growth by AZD2281 and Cisplatin. *Clin. Cancer Res.* **14**, 3916–3925 (2008).
 38. Abreu, C. M. *et al.* Shu complex SWS1-SWSAP1 promotes early steps in mouse meiotic recombination. *Nat. Commun.* **9**, 1–13 (2018).
 39. Liu, T., Wan, L., Wu, Y., Chen, J. & Huang, J. hSWS1•SWSAP1 is an evolutionarily conserved complex required for efficient homologous recombination repair. *J. Biol. Chem.* **286**, 41758–41766 (2011).
 40. Martino, J. *et al.* The human Shu complex functions with PDS5B and SPIDR to promote homologous recombination. *Nucleic Acids Res.* **47**, 10151 (2019).
 41. Prakash, R. *et al.* Distinct pathways of homologous recombination controlled by the SWS1-SWSAP1-SPIDR complex. *Nat. Commun.* **12**, (2021).
 42. Barazas, M. *et al.* Radiosensitivity Is an Acquired Vulnerability of PARPi-Resistant BRCA1-Deficient Tumors. *Cancer Res.* **79**, 452–460 (2019).
 43. Rein, H. L., Bernstein, K. A. & Baldock, R. A. RAD51 paralog function in replicative DNA damage and tolerance. *Curr. Opin. Genet. Dev.* **71**, 86–91 (2021).
 44. Ray Chaudhuri, A. *et al.* Replication fork stability confers chemoresistance in BRCA-deficient cells. *Nature* **535**, 382–387 (2016).
 45. Pulver, E. M. *et al.* A BRCA1 Coiled-Coil Domain Variant Disrupting PALB2 Interaction Promotes the Development of Mammary Tumors and Confers a Targetable Defect in Homologous Recombination Repair. *Cancer Res.* **81**, 6171–6182 (2021).
 46. Gogola, E. *et al.* Selective Loss of PARG Restores PARylation and Counteracts PARP Inhibitor-Mediated Synthetic Lethality. *Cancer Cell* **33**, 1078–1093.e12 (2018).
 47. Knijnenburg, T. A. *et al.* Genomic and Molecular Landscape of DNA Damage Repair Deficiency across The Cancer Genome Atlas. *Cell Rep.* **23**, 239–254.e6 (2018).
 48. Paes Dias, M., Rottenberg, S. & Jonkers, J. Functional genetic dropout screens and in vivo validation of candidate therapeutic targets using mouse mammary tumoroids. *STAR Protoc.* **3**, 101132 (2022).
 49. Bajrami, I. *et al.* Synthetic lethality of PARP and NAMPT inhibition in triple-negative breast cancer cells. *EMBO Mol. Med.* **4**, 1087–1096 (2012).
 50. Bian, C. *et al.* NADP⁺ is an endogenous PARP inhibitor in DNA damage response and tumor suppression. *Nat. Commun.* **10**, 693 (2019).
 51. Lahiguera, Á. *et al.* Tumors defective in homologous recombination rely on oxidative metabolism: relevance to treatments with PARP inhibitors. *EMBO Mol. Med.* **12**, e11217 (2020).
 52. Prakash, R., Zhang, Y., Feng, W. & Jasin, M. Homologous recombination and human health: The roles of BRCA1, BRCA2, and associated proteins. *Cold Spring Harb. Perspect. Biol.* **7**, (2015).
 53. Couturier, A. M. *et al.* Roles for APRIN (PDS5B) in homologous recombination and in ovarian cancer prediction. *Nucleic Acids Res.* **44**, 10879–10897 (2016).
 54. Bonilla, B. *et al.* The Shu complex prevents mutagenesis and cytotoxicity of single-strand specific alkylation lesions. *Elife* **10**, (2021).
 55. Godin, S. K. *et al.* The Shu complex promotes error-free tolerance of alkylation-induced base excision repair products. *Nucleic Acids Res.* **44**, 8199–8215 (2016).
 56. Bernstein, K. A., Juanchich, A., Sunjevaric, I. & Rothstein, R. The Shu complex regulates Rad52 localization during rDNA repair. *DNA Repair (Amst)*. **12**, 786–790 (2013).
 57. Jaspers, J. E. *et al.* Loss of 53BP1 Causes PARP Inhibitor Resistance in Brca1 -Mutated Mouse Mammary Tumors. *Cancer Discov.* **3**, 68–81 (2013).
 58. Love, M. I., Huber, W. & Anders, S. Moderated estimation of fold change and dispersion for RNA-seq data with DESeq2. *Genome Biol.* **15**, 550 (2014).
 59. Li, W. *et al.* MAGeCK enables robust identification of essential genes from genome-scale CRISPR/Cas9 knockout screens. *Genome Biol.* **15**, 554 (2014).
 60. Joung, J. *et al.* Genome-scale CRISPR-Cas9 knockout and transcriptional activation screening. *Nat. Protoc.* **12**,

- 828–863 (2017).
61. Ray Chaudhuri, A. *et al.* Topoisomerase α poisoning results in PARP-mediated replication fork reversal. *Nat. Struct. Mol. Biol.* **19**, 417–423 (2012).
62. Cameron, D. L. *et al.* Gridss, purple, linx: Unscrambling the tumor genome via integrated analysis of structural variation and copy number. *bioRxiv* 781013 (2019).

SUPPLEMENTARY FILES

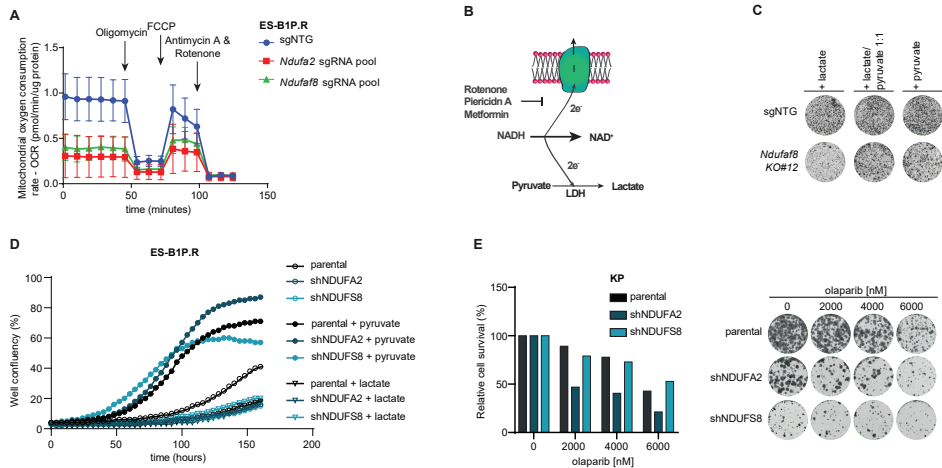


Supplementary figure 1 | STRING and KEGG pathway analysis of all genes included in the focused screen library (FDRs3). Related to figure 1. A | Genome-wide screen hit selection criteria. B-C | STRING network (<https://string-db.org/>) (B) and KEGG pathway (C) analysis of genes included in the focused library.



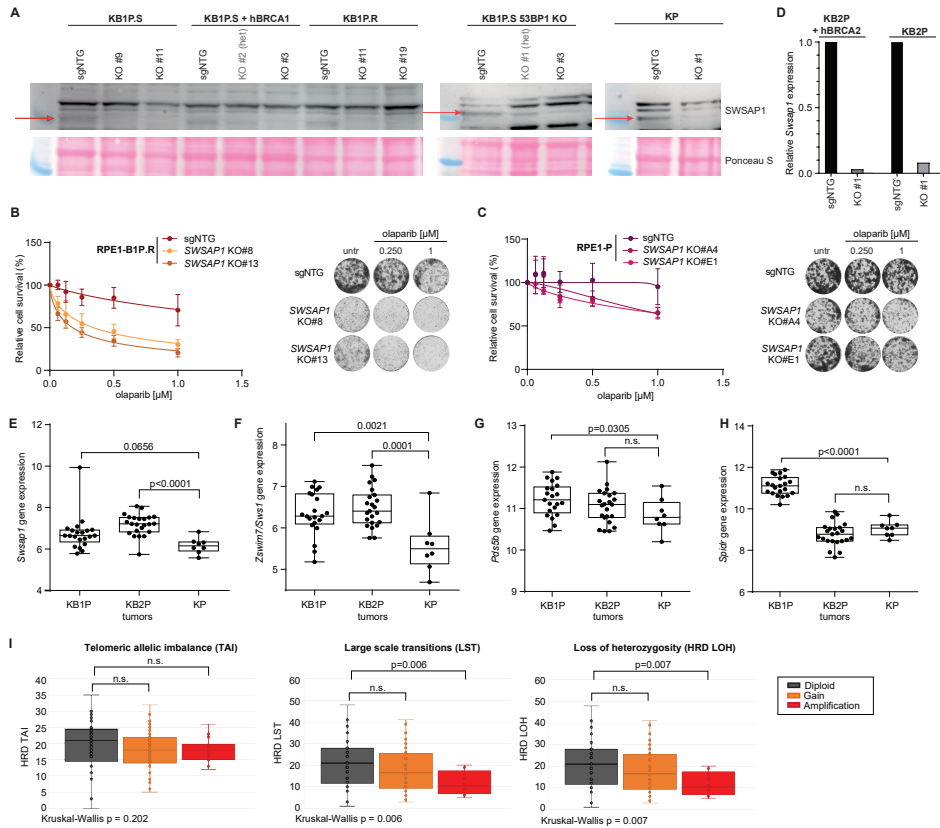
Supplementary figure 2 | Focused candidate screens identify GGNBP2 as candidate modulator of PARPi response in BRCA1/53BP1 double-deficient cells. Related to figure 1. A | Outline of focused candidate screens in ES-P.R versus ES-B1P.R cells, and in RPE1-P versus RPE1-B1P.R cells. ES-P.R and ES-B1P.R cells were treated with 25nM olaparib for two weeks or left untreated; RPE1-P and RPE1-B1P.R were treated with 100nM olaparib for two weeks or left untreated. **B |** Plot of distribution \log_2 ratio (fold change (treated versus

untreated)) median for all genes versus false discovery rate (FDR) of results from screen using focused candidate library in ES-P.R cells. **C** | Plot of distribution \log_2 ratio (fold change (treated versus untreated)) median for all genes versus FDR of results from screen using focused candidate library in RPE1-P cells. **D** | Plot of distribution \log_2 ratio (fold change (untreated versus T0)) median for all genes versus FDR of results from screen using focused candidate library in ES-B1P.R cells. **E** | Plot of distribution \log_2 ratio (fold change (untreated versus T0)) median for all genes versus FDR of results from screen using focused candidate library in ES-P.R cells. **F** | Plot of distribution \log_2 ratio (fold change (untreated ES-B1P.R versus untreated ES-P.R)) median for all genes versus false FDR of results from screen using focused candidate library in mES cells. **G** | Quantification and representative images of long-term clonogenic assays in *Trp53bp1*-deleted KB1P.S (KB1P.S-53BP1KO) cells; treated with olaparib. Cells were treated for the whole extent of the assay. **H** | Relative *Ggnbp2* expression quantified by RT-PCR. **I** | Correlation between *GGNBP2* copy number aberrations and PARPi response in patients. Y-axis indicates *GGNBP2* copy number status of metastatic solid tumors prior to PARPi (olaparib or niraparib) treatment. The description of the tumor types corresponds to the primary tumor location. First treatment response was evaluated according to RECIST (response was measured every 8 to 12 weeks) and categorized into PD, Progressive disease; SD, stable disease; or PR, partial response. PARPi was given as single agent or combination with other drugs. Data was obtained from the Hartwig Medical Foundation.



Supplementary figure 3 | Effect of pyruvate supplementation in MCI-deficient cells. Related to figure 2.

A | Mito stress test assay used to quantify mitochondrial oxygen consumption rate (OCR) with the Seahorse Bioanalyzer XFe24 in ES-B1P.R transduced with sgRNA non-targeting (sgNTG) or with sgRNA targeting the genes *Ndufa2* and *Ndufa8*. **B** | Schematic illustration of how oxygen allows cells to regenerate NAD⁺ from NADH via MCI activity and the MCI inhibitors used in this study. Exogenous pyruvate provides an alternate way to regenerate NAD⁺ through lactate dehydrogenase (LDH) activity. Adapted from Gui et al.³⁵. **C** | Representative images of ES-B1P.R cells cultured for 10 days in medium supplemented with 1mM lactate and/or 1mM pyruvate. **D** | Quantification of proliferation assays in ES-B1P.R cells. Media was supplemented with 1 mM pyruvate or 1mM lactate, as indicated. Cell confluency was measured every 4h with IncuCyte. **E** | Quantification and representative images of long-term clonogenic assays in KP cells, treated with olaparib. Cells were treated for the whole extent of the assay.




Supplementary figure 4 | BRCA1/2-deficient cells may display increased dependency on the Shu complex. Related to figure 3 and 5. A | Western blot analysis of SWSAP1 in mouse tumor cells. **B-C |** Quantification and representative images of long-term clonogenic assays in RPE1-B1P.R (E) and RPE1-P (F) cells treated with olaparib. Cells were treated for the whole extent of the assay. **D |** Relative *Swsap1* gene expression in the indicated cells quantified by RT-PCR. **E-H |** Gene expression of Shu complex factors *Swsap1* (E), *Zswim7* (F), *Pds5b* (G) and *Spidr* (H), in KB1P, KB2P and KP naïve tumors, measured by RNA-seq. Statistical analysis was carried out using unpaired t test. **I |** Association between SWSAP1 amplification and HRD sub scores: telomeric allelic imbalance (TAI), large-scale transition (LST), and loss-of-heterozygosity (HRD LOH).

Supplementary Table 1 | Log₂ fold change (treated versus untreated) of each sgRNA scoring as hit. Related to figure 1.

log₂(fold change)

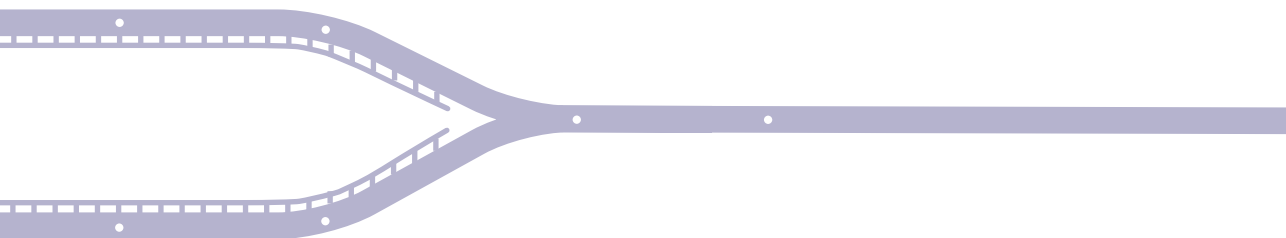
0 2 4 6



	treated vs T0	untreated vs T0	treated vs untreated
<i>Ndufa8-4</i>	-4.23	1.08	-5.31
<i>Ndufa8-1</i>	-4.24	0.64	-4.88
<i>Ndufa8-3</i>	-3.02	0.75	-3.77
<i>Ndufa2-5</i>	-3.26	0.67	-3.94
<i>Ndufa2-1</i>	-3.33	0.28	-3.61
<i>Ndufa2-4</i>	-3.32	-0.11	-3.21
<i>Ndufb8-1</i>	-3.9	0.67	-4.57
<i>Ndufb8-5</i>	-3.58	0.51	-4.09
<i>Ndufb8-2</i>	-3.26	0.77	-4.03
<i>Ndufb8-3</i>	-3.32	0.48	-3.81
<i>Ndufs8-2</i>	-3.18	0.99	-4.18
<i>Ndufs8-1</i>	-3	0.54	-3.54
<i>Ndufa1-3</i>	-3.69	0.28	-3.97
<i>Ndufa1-1</i>	-3.66	0.26	-3.92
<i>Ndufs7-5</i>	-4.34	0.81	-5.15
<i>Ndufs7-2</i>	-4.57	0.53	-5.1
<i>Ndufs7-3</i>	-4.27	0.55	-4.81
<i>Ndufs7-4</i>	-3.04	0.57	-3.61
<i>Ndufs1-1</i>	-4.27	0.38	-4.65
<i>Ndufs1-2</i>	-4.08	0.08	-4.16
<i>Ndufs1-4</i>	-3.07	0.8	-3.87
<i>Ndufb4-1</i>	-3.47	0.84	-4.31
<i>Ndufb4-3</i>	-3.02	0.86	-3.88
<i>Ndufb4-2</i>	-3.43	-0.1	-3.34
<i>Ndufa3-3</i>	-3.32	0.6	-3.92
<i>Ndufa3-5</i>	-3.04	0.57	-3.61
<i>Zswim7-5</i>	-7.59	-0.82	-6.77
<i>Zswim7-4</i>	-6.49	-1.02	-5.47
<i>Zswim7-2</i>	-5.72	-1.34	-4.38
<i>Zswim7-1</i>	-4.94	-0.77	-4.17
<i>Polb-2</i>	-7.22	0.26	-7.49
<i>Polb-5</i>	-3.86	0.16	-4.02
<i>Swsap1-5</i>	-5.36	-0.56	-4.8
<i>Swsap1-4</i>	-5.71	-1.34	-4.37
<i>Swsap1-2</i>	-4.44	-0.57	-3.88
<i>Ndufb7-3</i>	-4.06	0.44	-4.49
<i>Ndufb7-5</i>	-3.51	0.66	-4.18
<i>Nubpl-2</i>	-3.42	1.01	-4.43
<i>Nubpl-4</i>	-3.32	0.85	-4.17
<i>Ndufb10-2</i>	-4.16	0.27	-4.43
<i>Ndufb10-1</i>	-3.14	0.65	-3.79
<i>Cops7a-2</i>	-6.5	-1.19	-5.31
<i>Cops7a-4</i>	-5.03	-0.5	-4.54
<i>Ndufaf5-3</i>	-4.05	0.46	-4.51
<i>Ndufaf5-5</i>	-3.08	0.53	-3.6
<i>Ndufaf5-1</i>	-3	0.42	-3.42

Supplementary Table 2 | genes included in focused candidate library (FDR≤0.3). Related to figure 1.

Gene	FDR	Gene	FDR	Gene	FDR	Gene	FDR	Gene	FDR	Gene	FDR	Gene	FDR
Ndufa8	0.000075	Ndufa2	0.000075	Cox6b1	0.000193	Oxsl1	0.004624	Dusp11	0.031564	Fasickd5	0.082668	Seld2	0.137277
3110001D03Rik	0.000075	Ndufa3	0.000075	Lprt1	0.000193	Poib	0.005321	Spidr	0.032875	Hoxd10	0.084774	Hs2bp	0.142774
Adck4	0.000075	Ndufa8	0.000075	Ndufa11	0.000193	Ndufa11	0.005638	Hngcs1	0.035	Rads1b	0.092029	Mnos1	0.142774
Atpsl	0.000075	Ndufa5	0.000075	Ndufa3	0.000193	2810006K23Rik	0.005768	Siva1	0.036544	Ddx17	0.09521	Wash	0.146872
Cars2	0.000075	Ndufa6	0.000075	Ndufa2	0.000193	Ptpn2	0.006616	Cand1	0.036634	Agc2	0.095427	Mps18a	0.153235
Ccdc101	0.000075	Ndufa7	0.000075	Rad54l	0.000193	4930432K21Rik	0.006703	Wtsc1	0.042011	Prr12	0.095427	Tgfr1	0.156468
Chic1	0.000075	Ndufb10	0.000075	Srsf6	0.000193	Ints12	0.006703	Rrfb	0.043183	Polidip2	0.098275	Tic7b	0.162773
Clpp	0.000075	Ndufb4	0.000075	Ndufb2	0.000254	Mtrf11	0.006703	Smarrcal	0.043183	Dnajb6	0.098768	Pds5b	0.164343
Cjpx	0.000075	Ndufb6	0.000075	Cox3	0.000306	Xrcc6bp1	0.006731	Tmem70	0.045552	Tsc22d2	0.098768	Pced1a	0.166531
Coa4	0.000075	Ndufb8	0.000075	Hmnmpr	0.000306	Fdx1	0.007017	Cenpf	0.048614	Coas5	0.10074	Pds2	0.17401
Cops7a	0.000075	Ndufb9	0.000075	Phka1a	0.000306	Mpl63	0.007468	Ankrd11	0.050026	Ndufa5	0.10074	Yap1	0.176359
Coq4	0.000075	Ndufc2	0.000075	Mnd1	0.000362	Cdk2	0.00952	Ogfd3	0.050026	Helq	0.102954	Sos2	0.17717
Coq5	0.000075	Ndufs1	0.000075	Msh2	0.000413	Ndufs5	0.009607	Iba57	0.051414	Mtg1	0.103122	Mtmt	0.183986
Coq6	0.000075	Ndufs2	0.000075	Ndufa3	0.000413	Arpp19	0.010442	Ube2f	0.052044	Ndufa2	0.103122	Sulf1c1	0.183986
Cox18	0.000075	Ndufs6	0.000075	Ndufa9	0.000524	Cks1b	0.010685	Ten1	0.053561	Khsrp	0.105775	Cnga1	0.185687
Cox41	0.000075	Ndufs7	0.000075	Uqcq	0.000633	Garn1	0.012151	Ngn	0.053789	Mtpap	0.105775	Gli1	0.185687
Cox5a	0.000075	Ndufs8	0.000075	Nubpl	0.001309	Ube2v1	0.013594	Pgfr1	0.053825	Chd1l	0.1061	Atm	0.193331
Opox	0.000075	Ndufv1	0.000075	Ndufb7	0.001406	Trifsf8	0.013725	Oxsm	0.054144	Sic25a32	0.10632	Six4	0.198085
Ddx5	0.000075	Pds1	0.000075	Coq7	0.001502	Sp2	0.013774	Sm3a	0.054144	Rprdt1b	0.106946	Lphn1	0.204311
Dhx30	0.000075	Ppox	0.000075	Coa6	0.001776	Ndufb5	0.014535	Bre	0.055255	Pcdha9	0.108403	Bos1l	0.20579
Ecsit	0.000075	Psmc3ip	0.000075	Lip2	0.001776	Bcof1	0.015362	Tralp	0.055255	4930427A07Rik	0.108441	Cttn1	0.212957
Foxed1	0.000075	Rth4ip1	0.000075	Uqcq	0.001776	Plecxl1	0.016489	Nbp1	0.055831	Coq3	0.111489	Axnm73	0.213021
Gfm2	0.000075	Selc1	0.000075	Sp1	0.001863	Uqcrl1	0.017597	Lhx1	0.058768	Zkscan17	0.113836	Baz1b	0.216271
Gtpbp3	0.000075	Sic25a51	0.000075	Gnbp2	0.002159	Tmem126b	0.018966	Ptcd1	0.061489	Ahsa1	0.116051	Ssh1	0.221186
Higd2a	0.000075	Swi5	0.000075	Ndufa1	0.002241	Cyc1	0.020373	Prc2b	0.063156	Sic25a3	0.116906	Cik1	0.222351
Hmbs	0.000075	Swap1	0.000075	Ndufc1	0.002424	Mecr	0.025982	H2afx	0.063561	Ttk2	0.121989	1200014J11Rik	0.223381
Kmt2b	0.000075	Tmmdc1	0.000075	Ndufa4	0.002501	Igf2bp1	0.026365	Torg4	0.063561	Eme1	0.127512	Zbb44	0.228329
Lin28a	0.000075	Ttrt1	0.000075	Sic25a19	0.00298	Lias	0.026614	Ybey	0.063561	Tmtt1	0.128445	Scnm1	0.231779
Mcat	0.000075	Uros	0.000075	Gtpbp8	0.003317	Cox6a1	0.029226	Zfp933	0.064825	Lym2	0.12864	2310003H01R-ik	0.24042
Mn1	0.000075	Usp22	0.000075	Uqcrl1	0.003317	Uba6	0.029226	Hmnpab	0.065609	C1qbp	0.130621	Scaf11	0.244823
Mrrf	0.000075	Zswim7	0.000075	Hat1	0.003382	Topors	0.029233	Mif3	0.071912	Znrf3	0.131092	Mterf3	0.245491
Mto1	0.000075	Coq2	0.000148	Cabin1	0.003446	Ube2cbp	0.029233	Tars2	0.075322	Ahdct1	0.132021	Rnaaseh2a	0.245956
Ndufa1	0.000075	Abhd11	0.000193	Ndufb3	0.003605	Pph1	0.030313	Nsun4	0.078753	Dnajc6	0.132021	Sub1	0.245956
Ndufa10	0.000075	Acard9	0.000193	Ndufs4	0.003913	Morc2a	0.030807	Tnrc6c	0.078753	Dscr3	0.133142	Gsch1	0.249209
Ndufa13	0.000075	Bola3	0.000193	Prc2a	0.003913	Rfox13	0.030941	Scd2	0.079802	Pmk1	0.137129	Zmym4	0.249768



Chapter 6

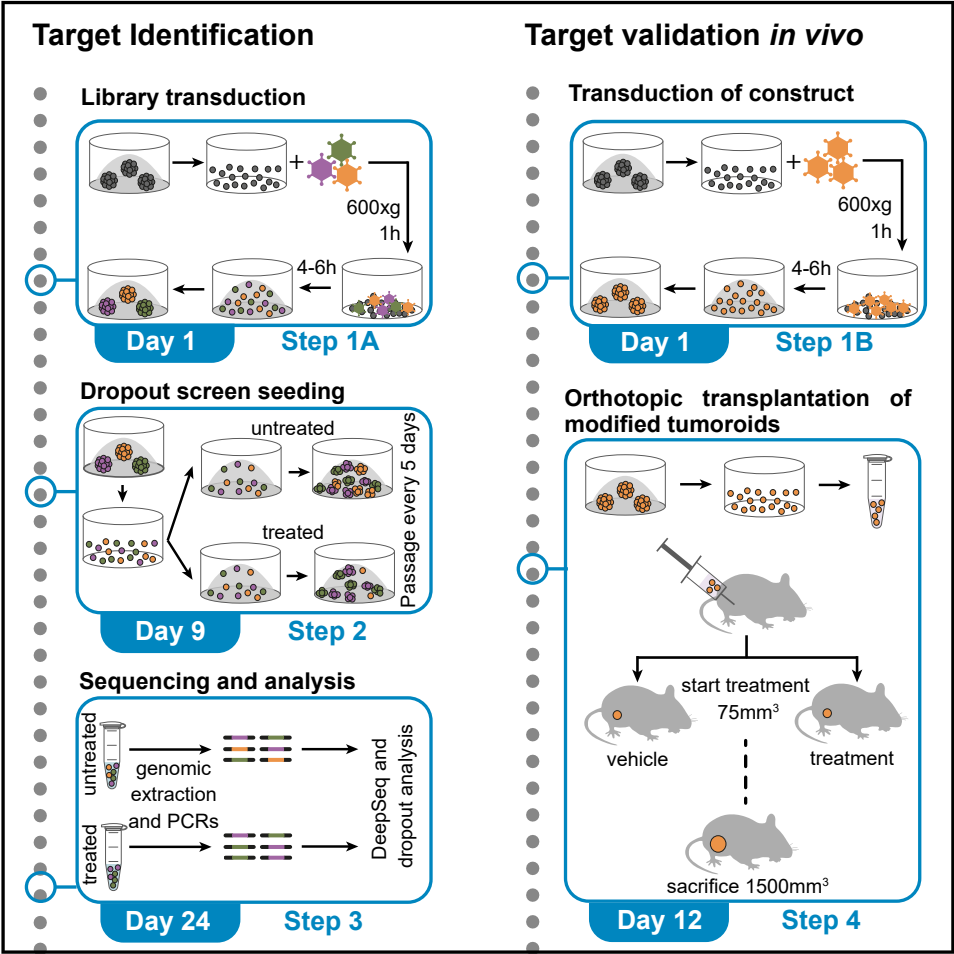
Functional genetic dropout screens and *in vivo* validation of candidate therapeutic targets using mouse mammary tumoroids

Mariana Paes Dias, Sven Rottenberg, Jos Jonkers
STAR Protocols, 2022; 3(1):101132

ABSTRACT

We have previously developed 3D tumoroids derived from genetically engineered mouse models (GEMMs) of BRCA1/2-deficient breast cancer. Here, we describe how to genetically modify tumoroids, use them for functional genetic dropout screens, and carry out orthotopic transplantation of modified tumoroids. The purpose of this protocol is to screen for therapeutic targets and allow rapid and straightforward *in vivo* validation of the candidate targets.

Grapical abstract



BEFORE YOU BEGIN

Poly(ADP-ribose) polymerase (PARP) inhibitors (PARPi) are a promising new therapeutic approach for the treatment of cancers with homologous recombination deficiency such as BRCA1/2-mutated cancers. Despite the success of this approach, drug resistance remains a clinical hurdle¹.

Tumoroids can be easily genetically modified and, compared to 2D, screens in 3D tumoroids have the advantage of using cells that retain crucial features of the original tumor (e.g., morphology, drug response, 3D structure) and that require a small culturing surface area (1 million tumoroid cells can fit in a few wells while 1 million 2D cells require one or more 15 cm dishes). The protocol below describes the specific steps to carry out functional genetic dropout screens using PARPi-resistant mouse mammary tumoroids to identify new therapeutic targets to improve response to PARPi and revert resistance, as in Paes Dias et al., (2021)². Additionally, this protocol describes how tumoroids can be used to validate the identified candidate targets *in vivo*.

The steps below focus on the use of tumoroids to study PARPi response, however a similar protocol can be used to identify drug targets to sensitize to other therapeutic interventions. While this protocol assumes the use of previously established tumoroid lines^{3,4}, one could also derive new tumoroid lines with different characteristics (e.g., GEMMs with different genotype or treated with other inhibitors) as previously described in Duarte et al., (2018)³.

Virus preparation and concentration

Timing: 4 days

1. Culture HEK293FT cells in IMDM media supplemented with 10% FBS and 50 units/mL penicillin/streptomycin.
2. Produce lentiviral stocks, pseudotyped with the VSV-G envelope, by transient transfection of HEK293FT cells as described before⁵.
 - a. Seed 7–8 million cells in one 15 cm dish.
 - b. The next day (approx. 24 h), transfect cells with the library/construct of interest.
 - c. The following day, refresh medium (16 mL).
 - d. Collect viral supernatant 48 h post transient transfection using a 0.22 µm filter and syringe to avoid collection of cells into the supernatant.
3. Concentrate viral supernatant using ultracentrifugation.
 - a. Upon collection of viral supernatants, ultracentrifuge for 2 h at $70,000 \times g$ at 7°C in ultracentrifuge specific tubes.
 - b. Remove supernatant by inverting the tube once and let it dry while inverted on a tissue for 2 min. The viral pellet will stay attached to the tube.

- c. Resuspend the viral pellet corresponding to one 15 cm plate in 200 μ L PBS.

Note: Per construct, we suggest collecting supernatant from two 15 cm dishes. For sgRNA/shRNA libraries, the number of plates may increase according to the size of the screen (complexity/coverage).

Optional: Instead of ultracentrifugation, one can use commercial protein concentration filter tubes (e.g., MilliporeSigma UFC905024).

4. Calculate lentiviral titer. This can be done by using a qPCR lentivirus titration kit for small sample volumes, such as the kit from Applied Biological Materials <https://www.abmgood.com/qpcr-lentivirus-titration-titer-kit.html>. Ideal virus titer should vary from 0.2×10^9 to 1×10^9 units/mL.

Optional: Lentiviral titer can also be calculated by limiting dilution and colony counting.

Culture and passage of tumoroid lines

Timing: 1 h

5. Spin down tumoroids at $300 \times g$ for 5 min at 4°C. If tumoroids have been dissociated and are single cells (please see *dissociation of tumoroids into single cells*), centrifugation should be done at 1,000 g .

Critical: Tumoroids tend to stick to plastic surfaces. Always coat tubes and pipettes with media before use by inverting the tube or pipetting medium up and down. Coating can also be done with bovine serum albumin (BSA).

6. Resuspend pellet in Cultrex Reduced Growth Factor Basement Membrane Extract (BME) Type 2 mixed 1:1 with cold mouse mammary gland tumoroid complete medium (ADDF6+) and seed in 40 μ L droplets per well, on 24-well suspension plates. **Troubleshooting 1.** For regular culture, we usually seed three to six droplets/wells for each line.

Critical: It is very important to maintain BME at 4°C as it solidifies when at temperatures superior to 8°C. If this happens, freezing BME at -20°C followed by thawing at 4°C is required to revert to liquid form.

7. Incubate 24-well plate at 37°C for 30 min and add 0.5 mL warm ADDF6+ medium per well. ADDF6+ medium must be pre-warmed at 37°C. Cold medium disrupts BME droplets.

8. Culture tumoroids under standard conditions (37°C, 5% CO₂).
9. Passage tumoroids twice per week, at dilutions between 1:3 to 1:6.
 - a. Carefully aspirate warm media from each well without disrupting the BME droplet.
 - b. Place 2 mL cold ADFF3+ medium in 15 mL tube (on ice), take 1 mL using a P1,000 pipette and collect BME droplet(s) containing tumoroids.
 - c. Resuspend tumoroids in the 2 mL.
 - d. Spin down at 300 × *g* for 5 min at 4°C.

Critical: Use of cold media to collect tumoroids is critical for BME to be dissolved.

Note: Tumoroids do not grow well if seeded too sparsely. It is preferable to seed organoids confluent when in doubt. In case they are too big, dissociate tumoroids to enable better growth (**Fig. 1A–1D**). Depending on the tumoroid line, this may be required every 3–6 weeks.

Dissociation of tumoroids into single cells

Timing: 20–40 min

10. Collect tumoroids in one tube as described in step 9 and centrifuge at 300 × *g* for 5 min at 4°C.
11. Aspirate supernatant and resuspend pellet in TrypLE Express Enzyme. 1 mL of TrypLE can be used to dissociate tumoroids from 12 droplets. For bigger tumoroids, higher volume and/or longer incubation might be required (we do not advise longer than 30 min).
 - a. Resuspend tumoroid pellet in TrypLE.
 - b. Incubate at 37°C for 10 min. Resuspend pellet every 5 min using a P1000 pipette. A glass slide can be used to observe tumoroid disruption into single cells by microscope. **Troubleshooting 2.**

Critical: Keep tube vertical and do not invert during incubation with TrypLE to avoid tumoroids sticking to the tube wall.

- c. Add 1 volume of ADFF3+ to neutralize TrypLE.
- d. Seed cells as described in steps 5 to 8. Dissociation of tumoroids into single cells will be used in *transduction and selection of mouse mammary tumoroids* (step 1), *seeding of tumoroids for functional genetic dropout screen* (steps 9, 12 and 13), and *In vivo validation of target* (step 18).

RESOURCES TABLE

REAGENT or RESOURCE	SOURCE	IDENTIFIER
Chemicals, peptides, and recombinant proteins		
IMDM	Gibco	Cat#21980-032
Advanced DMEM/F12	Gibco	Cat#12634-010
B-27 Supplement (50X)	Gibco	Cat#17504-044
HEPES Buffer Solution (1M)	Gibco	Cat#15630-056
N-acetylcysteine	Sigma-Aldrich	Cat#A9165
GlutaMAX (100X)	Gibco	Cat#35050-061
EGF Mouse Protein, Native	ThermoFisher Scientific	Cat#53003-018
Penicillin-Streptomycin (5,000 U/mL)	Gibco	Cat#15070-063
TrypLE™ Express Enzyme (1X)	Gibco	Cat#12605010
Cultrex Reduced Growth Factor Basement Membrane Extract Type 2 (BME)	Trevigen	Cat#3533-001-02
Polybrene	Sigma-Aldrich	Cat#28728-55-4
Olaparib (AZD2281), PARP inhibitor	Syncom, Groningen, the Netherlands	CAS: 763113-22-0
Critical commercial assays		
qPCR Lentivirus Titer Kit	Applied Biological Materials	Cat#LV900
Gentra Puregene Cell Kit	Qiagen	Cat#158745
Phusion™ High-Fidelity DNA Polymerase (2 U/μL)	ThermoFisher Scientific	Cat#F-530L
MiniElute PCR Purification Kit	Qiagen	Cat#28004
DNA 7500 Kit	Agilent	Cat#5067-1506
Experimental models: Cell lines		
HEK293FT	ATCC	RRID:CVCL_6911
ORG-KB1P4N.1 (PARPi-naïve)	(Duarte et al., 2018)	N/A
ORG-KB1P4R.1 (PARPi-resistant)	(Duarte et al., 2018)	N/A
ORG-KB1PM7N.1 (PARPi-naïve)	(Duarte et al., 2018)	N/A
ORG-KB1PM7R.1(PARPi-resistant)	(Duarte et al., 2018)	N/A
ORG-KB2P17N.1 (PARPi-naïve)	(Duarte et al., 2018)	N/A
ORG-KB2P17R.1 (PARPi-resistant)	(Duarte et al., 2018)	N/A
ORG-KP.5	(Duarte et al., 2018)	N/A
ORG-KPM.1	(Duarte et al., 2018)	N/A
ORG-WB1P	(Annunziato et al., 2019)	N/A
ORG-WB1P.Myc	(Annunziato et al., 2019)	N/A
Experimental models: Organisms/strains		
Mouse: FVB/NRj, 6 weeks, female	Janvier Labs	N/A
Mouse: (FVB/N X 129/Ola)F1, 6 weeks, female	N/A	N/A
Mouse: NMRI nude (or other immunocompromised strain) , 6 weeks, female	Janvier Labs	N/A
Oligonucleotides		
PCR1 Fwd-5'ACACTCTTTCCCTACACGACGCTCTTCCGATCTNNN NNNGGCTTTATATCTTGTGGAAGGACG3'		
NNNNNN represents a sequence of six-nucleotide barcodes (e.g. CGTGAT, ACATCG, GCCTAA, TGGTCA, CACTGT, ATTGGC, GATCTG, TCAAGT, CTGATC, AAGCTA, GTAGCC, TACAAG, etc)	N/A	N/A

REAGENT or RESOURCE	SOURCE	IDENTIFIER
PCR 1 Rev (pLKO.1 backbone library)- 5'GTGACTGGAGTTCAGAC-GTGTGCTCTTCCGATCTGTGGATGAATACTGCCATTTGTCTC3'	N/A	N/A
PCR 1 Rev (plentiGuide backbone library)-5'GTGACTG-GAGTTCAGACGTGTGCTCTTCCGATCTTCTACTATTCTTTCCCT-GCACTGT3'	N/A	N/A
PCR 1 Rev (plentiCRISPRv2 backbone library)-5'GTGACTGGAGTTCAGACGTGTGCTCTTCCGATCTACTGACGGGCACCGGAGCCAATTCC3'	N/A	N/A
PCR2 Fwd-5'AATGATACGGCGACCAACCGAGATCTACACTCTTTCCCTACACGACGCTCTTCCGATCT3'	N/A	N/A
PCR2 Rev-5'CAAGCAGAAGACGGCATACGAGATNNNNNNGTGACTGGAGTTCAGACGTGTGCTCTTCCGATCT3'	N/A	N/A
NNNNNN represents a sequence of six-nucleotide barcodes (e.g. CGTGAT, ACATCG, GCCTAA, TGGTCA, CACTGT, ATTGGC, GATCTG, TCAAGT, CTGATC, AAGCTA, GTAGCC, TACAAG, etc)	N/A	N/A
Software and algorithms		
MAGeCK	(Li et al., 2014)	N/A
Other		
24-well suspension plates	Greiner CELLSTAR	662102

MATERIALS AND EQUIPMENT

ADDF3+

Reagent	Final concentration	Amount
Advanced DMEM/F12 (1X)	1X	485 mL
Penicillin-streptomycin (5,000 U/mL)	50 units/mL	5 mL
HEPES (1M)	10 µM	5 mL
GlutaMAX (100X)	1X	5 mL
Total	n/a	500 mL

Store at 4°C for a maximum of 6 months

ADDF6+ (tumoroid complete medium)

Reagent	Final concentration	Amount
ADDF3+ (1X)	1X	490 mL
N-acetylcysteine (500 mM)	125 µM	125 µL
B-27 Supplement (50X)	1X	10 mL
EGF (100 µg/mL)	250 ng/mL	250 µL
Total	n/a	500 mL

Store at 4°C for a maximum of 6 months

Alternatives: For culturing tumoroids, other basement membrane matrixes can be used such as Matrigel. For genomic extraction of screening samples, other methods or kits can

be used such as QIAmp DNA Mini Kit (Qiagen). For measuring molarity after PCR2, an alternative is the Qubit dsDNA HS Assay Kit (Thermo Fisher Scientific).

STEP-BY-STEP METHOD DETAILS

Transduction and selection of mouse mammary tumoroids

Timing: 4 days

In this step viral transduction of tumoroids is carried out by spinoculation as previously described⁶. The same step should be followed for the screen library transduction (graphical abstract step 1A, required for carrying out functional genetic dropout screens and target identification) as well as for transduction of single constructs (graphical abstract step 1B, required for single gene modification and target validation *in vivo*).

1. Dissociate tumoroids into single cells as described in preparation steps 10 and 11 and count.

Note: We advise to transduce between 0.25 million to 1 million cells per well. We advise using a multiplicity of transduction (MOI) of 0.3–1 for library transduction (A) and a MOI of 50–100 for single constructs (B). **Troubleshooting 3.** For screens, the number of cells to be transduced should be at least three times the coverage to compensate for possible cell death with antibiotic selection. Example of library transduction: for one screen using a library with a complexity of 2,000 sgRNA/shRNAs and carried out with a coverage of 1,000 \times , 6 million cells should be transduced per replicate.

2. Pellet the required number of cells by centrifuging at 1,000 $\times g$ for 5 min, discard supernatant and resuspend in virus suspension (concentrated virus in PBS plus ADDF6+ medium, supplemented with 8 $\mu\text{g/mL}$ polybrene). The total volume of virus suspension should be between 250 and 1000 μL ; the volume of concentrated virus should not be more than the volume of ADDF6+ medium.

Critical: Spinoculation is carried out in 24-well suspension plates.

3. Transfer cell suspensions to the 24-well suspension plate and centrifuge at 600 $\times g$ for 60 min at 25°C.
4. After centrifugation, single cells should be at the bottom of the well. Incubate the plate at 37°C for 4–6 h.
5. Resuspend single cells in the supernatant and transfer cell suspensions into tubes. Centrifuge at 1,000 $\times g$ for 5 min.
6. Discard the supernatant, resuspend pellet in BME-ADDF6+ mix and seed as described in preparation steps 6 to 8 (**Fig, 1B**). Single cells transduced in one well can be seeded in one to three wells.
7. 24 h post transduction, add selection reagent (e.g., puromycin). Expand tumoroids

without dissociation for the following step. For *in vivo* target validation (graphical abstract step 1B), target modification must be confirmed prior to experiment (e.g., western blot, PCR and/or sanger sequencing)

Note: After transduction, dissociation of tumoroids using TrypLE should be avoided for the following few days (approx. 5 days) as tumoroids do not respond well to additional stress post transduction.

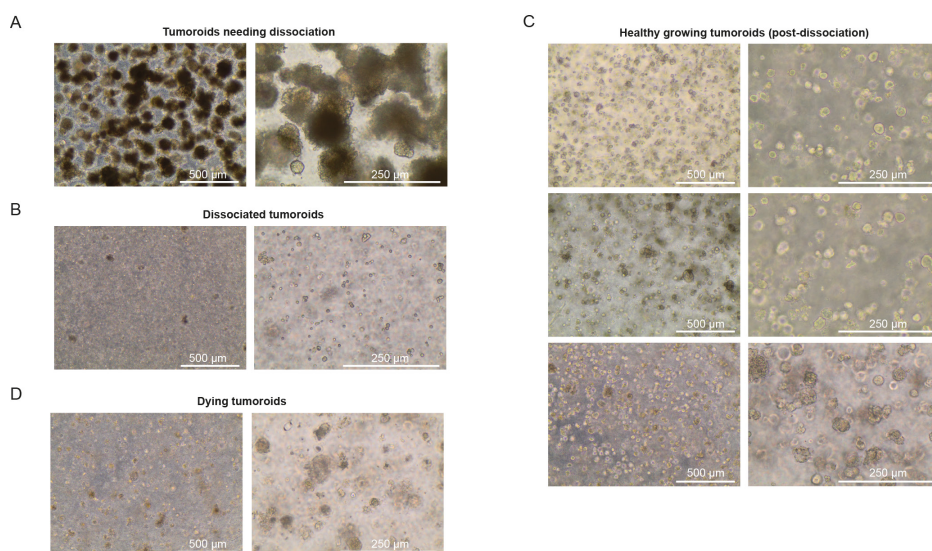


Figure 1 | Tumoroid cultures. **A** | Large tumoroids in need of dissociation in order to maintain proliferation. Medium color changes to yellow very fast (1–2 days), tumoroids form large dense aggregates that appear opaque. **B** | Tumoroids immediately after dissociation. **C** | Healthy growing tumoroids post-dissociation. After 3–5 days, the medium starts to change to yellow, tumoroids look visibly transparent and form smooth spheres. **D** | Dying tumoroids. Medium stays pink, cells are sparse, and do not form tumoroids. Images taken with 40× magnification, scale bar: 500 µm; images taken with 100× magnification, scale bar: 250 µm.

Seeding of tumoroids for functional genetic dropout screen

Timing: 15–21 days

This step follows screen library transduction as defined in *transduction and selection of mouse mammary tumoroids* (graphical abstract step 1A) and describes how to seed tumoroids for a functional genetic dropout screen and how to keep them in culture throughout the assay. Screens using tumoroids should be carried out for 2–3 weeks, depending on the cycling time of the tumoroid line and drug used (for screens in the absence of drug treatment to study direct lethality, 2 weeks should suffice; in the presence of olaparib, three weeks is advised). For functional genetic dropout screens using drug treatment as negative selection, we suggest a coverage of 500× to 1,000× due to increased variability across replicates.

Here, we use the PARPi olaparib as treatment. Olaparib concentration should be titrated in order to find a drug concentration where resistant cells remain alive (IC_{50} – IC_{100}) while responsive cells do not survive (IC_0 – IC_{20}). Competition assays where both resistant and responsive lines are cultured together under drug selection conditions can help identify optimal drug concentration in a screen setting. The effect of frequent dissociation on tumoroid proliferation and drug sensitivity should be accounted for.

8. After transduction of tumoroids with the screen library, make sure there are enough cells for the different conditions and replicates. Expansion of tumoroids for 1 to 3 passages is usually required.

Note: Example of number of cells required before seeding the screen: for one screen using a library with a complexity of 2,000 sgRNA/shRNAs, carried out with a coverage of 1,000x and with two different treatment conditions (untreated and treated), one should make sure to have at least 6 million cells per replicate (2 million for untreated condition, 2 million for treated condition and 2 million for Day 0 control (T0)).

9. Dissociate tumoroids into single cells as described in preparation steps 10 and 11 and count cells.
10. Collect cells equivalent to coverage for a Day 0 control (T0) and freeze pellet.
11. Seed tumoroids for screen.
 - a. Pellet cells by spinning down at $1,000 \times g$ for 5 min.
 - b. Seed and culture tumoroids as described in preparation steps 6 to 8. The same number of single cells should be present in each 40 μ L BME-ADDF6+ droplets. Untreated and olaparib treated tumoroids should be seeded at equal densities.
 - c. Add olaparib to the medium on the same day of seeding.

Optional: Olaparib treatment can start at later time points if required (e.g., to look for effects in formed tumoroids, treatment combinations), however this can increase the drug concentration required to sensitize tumoroids.

12. Every 5 days, dissociate tumoroids into single cells and re-seed as in step 11. Olaparib treatment should be maintained across the entirety of the screen.
13. At the end of the screen, collect all tumoroids, dissociate into single cells, count (maintain screen coverage) and pellet. Take along T0 pellets collected in step 10 and proceed to genomic extraction (step 25). Optionally, screen pellets can also be frozen before proceeding to step 14.

Critical: Dissociation of tumoroids before genomic extraction (as well as for RNA and protein extraction) is critical for optimal lysis.

Note: The number of cells per matrix droplet depends on the tumoroid line. The number of cells seeded should allow tumoroids to grow for 5 days without getting overconfluent. We suggest between 50,000 and 200,000 cells per well. Example of seeding conditions: for one screen using a library with a complexity of 2,000 sgRNA/shRNAs and carried out with a coverage of 1,000×, 2 million cells should be seeded per replicate per condition (50,000 cells/well results into forty wells and corresponds to two 24-well plates), 2 million cells should be collected at T0 and 2 million cells should be collected at the end of the screen per replicate per condition.

Sequencing and analysis of screen

Timing: 3–4 weeks

In this step, genomic DNA extraction, library preparation (two-step PCR⁷ and sequencing, and screen analysis are outlined.

14. Proceed to genomic extraction of all samples, including the T0 controls, using the Gentra Puregene Cell Kit according to the manufacturer's protocol: <https://www.qiagen.com/us/products/discovery-and-translational-research/dna-rna-purification/dna-purification/genomic-dna/gentra-puregene-kits/>. The protocol is optimized for genomic extraction of 1–2 million or 10–20 million cells. Depending on the size of the screen, different approaches may be followed.

Critical: Resuspend/vortex cell pellet in the leftover medium supernatant before proceeding to cell lysis. If cell clumps are present after adding cell lysis solution (occurs when pellet was not well resuspended prior to addition of cell lysis buffer), samples can be incubated for 6–16 h at 37°C. Pre-cooling of precipitation buffer to 4°C can improve precipitation. Incubation at 65°C with hydration solution is critical when pellets are very big.

15. After genomic extraction, prepare the library for next generation sequencing (NGS). The steps below were designed for NGS using the Illumina HiSeq 2500. Primers that amplify the sgRNA/shRNA target region with Illumina adaptor sequences for NGS are listed in the *resources table*.

Note: Other NGS machines can be used, however the library preparation protocol may differ.

- a. PCR1 reaction mix should be prepared as described in the Phusion™ High-Fidelity DNA Polymerase (2 U/μL) manufacturer's protocol <https://www.thermofisher.com/order/catalog/product/F530L#/F530L>, and the table below. Different barcodes can be used for PCR1 forward primers in order to label different samples. The PCR1 reverse primer sequence varies depending on the library backbone. The amount of PCR1 reactions should be according to the coverage of the screen and assumes that 1 million cells is equivalent to 6 μg of genomic DNA.

Note: Example of the amount of PCR1 reactions required to maintain a coverage of 1,000× in a screen using a library with a complexity of 2,000 sg/shRNAs: DNA corresponding to 2 million cells should be used for PCR1 reaction (2 million cells correspond to 12 µg of genomic DNA; for PCR1 one reaction should contain 1 µg of DNA template which results in 12 reactions per sample).

PCR1/2 mix for 1 reaction (according to manufacturer's protocol)	
Reagent	Amount
DNA template	1 µg (PCR1) – 2,5 µL (PCR2)
Phusion polymerase 2 units/µL	0.5 µL
dNTPs (10 mM)	1 µL
GC buffer (5X)	10 µL
PCR1 or PCR2 forward primer (Fwd) (100 µM)	0.25 µL
PCR1 or PCR2 reverse primer (Rev) (100 µM)	0.25 µL
DMSO	1.5 µL
ddH ₂ O	X
Total	50 µL

PCR 1/2 cycling conditions			
Steps	Temperature	Time	Cycles
Initial Denaturation	98 °C	30 sec	1
Denaturation	98 °C	10 sec	16 cycles
Annealing	60 °C	20 sec	
Extension	72 °C	1 min	
Final extension	72 °C	5 min	1
Hold	4 °C	forever	

- b. After PCR1 is complete, pool all the products from one barcode. Check PCR1 product by running 10 µL on agarose gel. A smeared band should appear around the expected PCR product size (approx. 300 bp).
- c. Prepare PCR2 reaction as described in step a. Add 2.5 µL of the pooled PCR1 per PCR2 reaction. Carry out 1 to 2 reactions of PCR2 per barcode. Different barcodes can also be used in PCR2 reverse primer to increase complexity of labeled samples.

Note: Barcodes represent a sequence of six-nucleotide barcodes (e.g. CGTGAT, ACATCG, etc). PCR1 barcode is read as the forward read while PCR2 barcode reads as the illumina indexing read.

- d. Pool PCR2 products of one barcode. Check 10 µL of PCR2 by agarose gel electrophoresis. A clear band should appear at the expected PCR

- product size (approx. 300 bp).
- e. Purify PCR2 products using MiniElute PCR Cleanup according to the manufacturer's protocol <https://www.qiagen.com/us/products/discovery-and-translational-research/dna-rna-purification/dna-purification/dna-clean-up/minelute-pcr-purification-kit/>, with one exception - do not add pH indicator to buffer PB, it may affect sequencing. Purify products with the same barcodes separately and elute each in 10 μ L molecular grade nuclease-free water.
 - f. Pool all samples before deep sequencing at the equivalent molarity. Molarity can be checked using the Agilent DNA 7500 Kit in Bioanalyzer 2100. This procedure allows to measure molarity corresponding to PCR products of the right size.
16. Deep sequence with Illumina HiSeq 2500.
 17. Analyze screen using MAGeCK⁸.
 - a. For hit selection one should filter using the following thresholds:
 - i. False discovery rate ($\text{FDR} \leq 0.1$; $\text{FDR} \leq 0.25$).
 - ii. Aggregated fold change ($\text{median/mean log2Fc} \leq -1$).

***In vivo* validation of target**

Timing: 3 months

This step follows target modification as defined in *transduction and selection of mouse mammary tumoroids* (graphical abstract step 1B) and describes preparation of tumoroid samples for orthotopic transplantation and *in vivo* treatment. Note, all animal experiments need to be performed in accordance with a protocol approved by the Institutional Animal Care and Use Committee.

18. After target modification and validation, dissociate tumoroids into single cells as described in preparation steps 10 and 11 and count the cells. **Troubleshooting 4.**
19. Pellet the required cell number by centrifuging at $1,000 \times g$ for 5 min, discard supernatant and resuspend in 1:1 BME/ADDF6+ (40–50 μ L per mammary gland/sample). Per gland, the number of tumoroid cells can vary between 20,000 and 500,000 depending on the tumoroid line (e.g., for tumor latencies of 2–3 weeks: ORG-KB1P4N.1, 40,000 cells; ORG-KB1P4R.1, 10,000 cells; ORG-KPM1, 500,000 cells).
20. Proceed to orthotopic transplantations (**Fig. 2**).
 - a. Make a small incision (approx. 0.5 cm) just below the nipple using iris scissors.
 - b. Inject cells into the mammary gland fat pad. Avoid the lymph node while injecting.
 - c. Suture the skin, place the mouse back in its cage, and monitor recovery until it is completely awake.

Optional: Different protocols for intramammary injections can be followed. With our protocol, we use isoflurane (3% (start) → 2%) as anesthesia and rimadyl (0.26 mL in 200 mL of drinking water) for analgesia.

Critical: Tumoroid lines derived from KB1P(M) and KP(M) mice can be transplanted into isogenic FVB mice, while tumoroids derived from KB2P mice should be transplanted into (FVB/N X 129/Ola)F1 mice³. All tumoroids lines can be transplanted into immunodeficient mice. Transplantation of tumoroids modified with Cas9 should be carried out in immunodeficient or Cas9-tolerant mice to avoid immunogenic rejection of the graft.

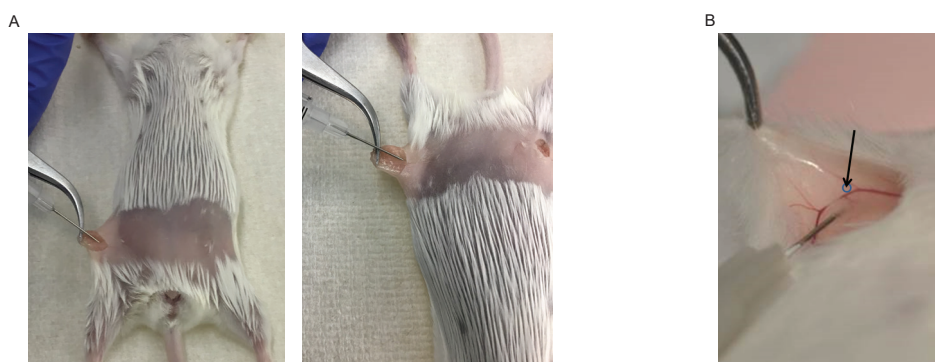


Figure 2 | Orthotopic transplantation of tumoroids. A | Injection of tumoroid suspension into the mouse mammary fat pad. **B |** Mouse mammary fat pad. Arrow indicates the site of the lymph node to avoid.

21. Initiate treatment upon tumor outgrowth (75 mm³). **Troubleshooting 5.**

- a. Mammary tumor size can be determined by caliper measurements, and tumor volume can be calculated by the following formula: $0.5 \times \text{length} \times \text{width}^2$.
- b. Vehicle (20% (2-Hydroxypropyl)- β -cyclodextrin) and olaparib (100 mg/kg) treatment is carried out for 28 consecutive days. This is done via intraperitoneal injection (5 mg/mL stock solution → 20 μ L/g injected; max. 1 mL/mouse).
 - i. Pre-heat the treatment substances to body temperature before injecting.
 - ii. Inject gradually on the left side of the median, towards the groin area and between the fourth and third nipple.
 - iii. Insert the needle maximally 0.5 cm, with a 45° angle and the bevel of the needle facing up.
 - iv. Remove the needle gradually and put the mouse back in the cage.

Note: The site of injection can be alternated to avoid irritation from consecutive injections in the same site. Macroscopically, we do not observe irritation or swelling, although microscopic examination occasionally reveals skin irritation.

Note: While a cycle of 28 days is standard for olaparib treatment, 56 days can also be used in order to observe a better window between the different lines. For hypersensitization experiments (increase response in already responsive lines/combination experiments), 50 mg/kg olaparib may be ideal².

22. Sacrifice animals with CO₂ when the tumor volume reaches 1500 mm³.

Optional: Sterile collection and cryopreservation of multiple tumor pieces can be carried out for future engrafting experiments. Fresh tumor samples can be preserved by snap-freezing them in tubes on dry ice (possibly mixed with methanol) for DNA, RNA or protein extraction, by freezing them in OCT for the generation of cryosections, or by fixing them for 24 h in 4% formaldehyde solution in PBS (wt/vol) for the generation of formalin-fixed paraffin-embedded biobanking and (immuno-)histochemical stainings.

EXPECTED OUTCOMES

This protocol details the steps for carrying out functional genetic dropout screens using mouse mammary tumoroids. While this protocol can be applied to other research aims, we focused on the use of PARPi-resistant tumoroids for the identification of genes whose loss reverts resistance to PARPi, as in Paes Dias et al. (2021)².

During the routine culture of tumoroids, the size of each tumoroid within the same well tends to be uniform. However, throughout the screen, the size of tumoroids within the same well will differ more than the parental lines, as different tumoroids will express different sgRNA/shRNAs targeting different genes (**Fig. 3A**). This is similar to the size variation that is also seen in 2D culture screens. Additionally, at the end of the screen, it is expected that drug-treated tumoroids will look less confluent and display increased cell death compared to untreated controls (**Fig. 3A**).

There are multiple ways to present screen analysis data. Dispersion of sgRNA/shRNAs as plotted in **Fig. 3B** helps to determine how each sgRNA/shRNA scores. sgRNA/shRNAs plotted on the left extreme of the plot might be underrepresented (too few counts), whereas sgRNA/shRNAs on the bottom region of the cloud represent putative hits that are depleted in the treated versus untreated condition. Thus, candidate targets should ideally have corresponding sgRNA/shRNAs that fall within the bottom right area of the scatter plot (**Fig. 3B**). If only a small portion of sgRNA/shRNAs are observed in the bottom right of the cloud, this indicates that few or no dependencies are present or that the screen set up was not optimal. At the gene level, one can plot all genes based on their p value as in **Fig. 3C**. While this is helpful to rank all genes and evaluate significance, this plot does not depict the

strength of the depletion, which is better plotted in **Fig. 3D**.

Following target identification, we describe the steps for using tumoroids for the validation of candidates *in vivo*. Olaparib-treated mice bearing ORG-KB1P4N.1 tumors should respond to treatment, with a survival of 40–60 days. In contrast, olaparib-treated mice bearing ORG-KB1P4R.1 tumors do not respond to therapy and have a similar survival as vehicle-treated mice. Olaparib-treated mice bearing ORG-KB1P4R.1 with target modification are expected to show similar survival curves as mice bearing ORG-KB1P4N.1 tumors. If mice bearing target-modified ORG-KB1P4R.1 tumors already display increased survival in vehicle-treated conditions, this can indicate that target modification affects tumor progression independently of drug treatment.

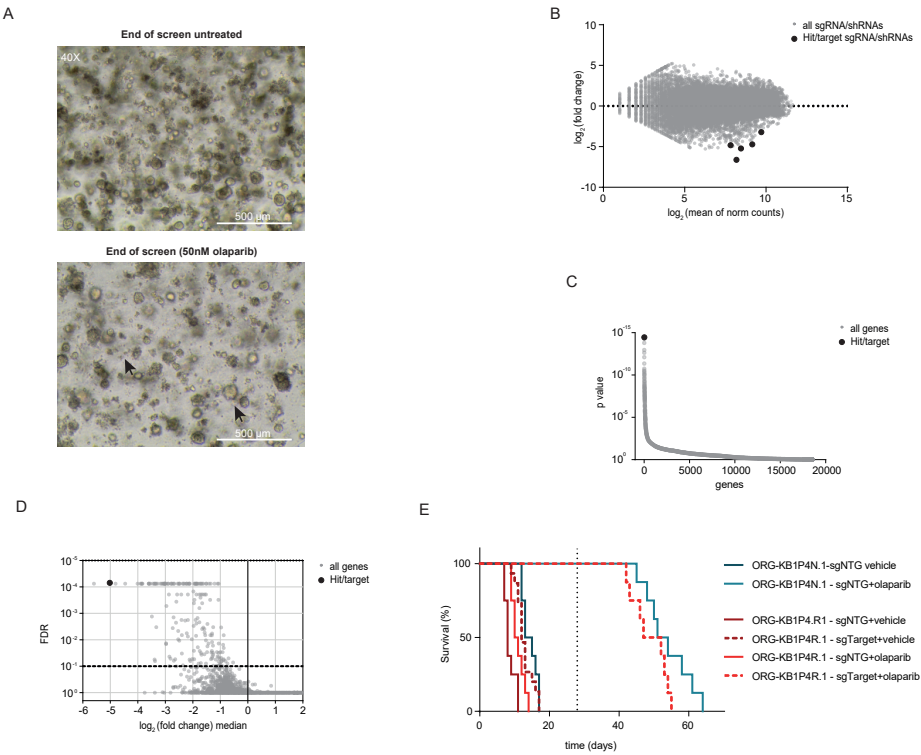


Figure 3 | Expected outcome of tumoroid-based dropout screen and in vivo validation. A | Example of ORG-KB1P4R.1 tumoroids at the end of the dropout screen. Left arrow points at dead cells, right arrow points at large tumoroid. Images taken with 40 \times magnification, scale bar: 500 μ m. **B |** Example of plot of \log_2 ratio (fold change (treated versus untreated)) versus abundance (mean of normalized (norm) counts) of sgRNA/shRNAs. **C |** Example of plot of distribution of the one-sided p value (gene dropout) for all genes targeted by the shRNA/sgRNA library. **D |** Example of plot of distribution \log_2 ratio (fold change (treated versus untreated)) median for all genes versus false discovery rate (FDR). **E |** Example of expected Kaplan–Meier survival curves of mice transplanted with ORG-KB1P4N.1 and ORG-KB1P4R.1 tumoroids lines, and treated with 100 mg/kg olaparib. End of treatment (28 days) is indicated by a dotted line.

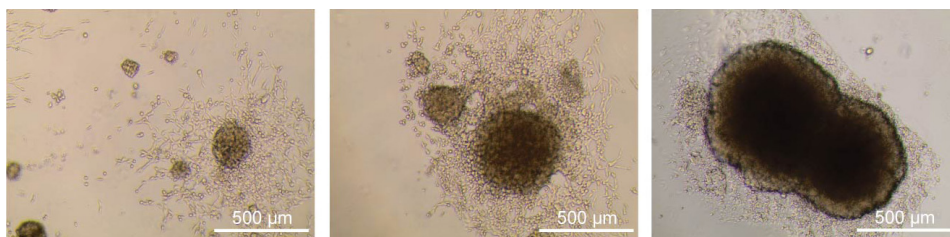


Figure 4 | Problem 1 – Tumoroids spreading as 2D cells in the bottom of the plate. Images taken with 40x magnification, scale bar: 500 µm.

LIMITATIONS

Retaining crucial features of the original tumor, displaying small size combined with 3D growth, and easy genetic modification make GEMM-derived mammary tumoroids especially suitable for genetic (and pharmacologic) screens. High complexity screens can require high numbers of tumoroids in order to keep the ideal screen coverage. However, after multiple passages, proliferation of tumoroids can plateau and original tumor characteristics can be lost. Hence, the library size might be limited by how many tumoroids need to be propagated. Although less straightforward, one could overcome this problem via orthotopic transplantations of the original tumor pieces back in mice and subsequently derive 3D cultures from these tumors right before library transduction. This results in higher amounts of cells without extensive passaging of tumoroid lines.

Another potential disadvantage are the elevated costs of the components required to culture tumoroids (e.g., BME, B27). Additionally, we observed that the variability between BME batches can affect experimental outcomes. We recommend testing BME between new batches by measuring proliferation/survival of the same chosen lines cultured with old vs. new batches.

Screens in 3D tumoroids have the advantage of using cells that closely resemble *in vivo* characteristics. A drawback of all *in vitro* culture systems, including 3D tumoroid lines, is the lack of stroma. This prevents screening for factors involved in tumor microenvironment interactions, which has been found to influence treatment response in breast cancer (reviewed in⁹). One could overcome this by using co-culture systems with stromal elements such as fibroblasts and/or immune cells.

Finally, in this protocol we describe the use of mouse tumoroid lines that resemble triple-negative breast cancer. However, we have not been able to successfully establish long-term mouse tumoroids from GEMMs of invasive lobular carcinoma^{10,11}. Hence, the approach described in this protocol might not be feasible for every breast cancer subtype.

TROUBLESHOOTING

Problem 1

Some tumoroid lines tend to sink to the bottom of the matrix droplet/well and start adhering to the plate as 2D lines (**Fig. 4**). We have observed this mainly in tumoroid lines derived

from epithelial-to-mesenchymal transition (EMT)-like tumors (also known as claudin-low), such as ORG-KB2P, ORG-KP(M) and ORG-WB1P-Myc lines. This may also happen when tumoroids are very big.

Potential solution

Keeping organoids at an ideal size is important to keep the 3D culture going. Flipping the plate upside down during the 30 min incubation at 37°C while BME solidifies helps tumoroids to stay at the top of the matrix droplet and avoids 2D expansion. 2D cells can also be a result of residual stromal cells. This can happen in freshly-derived tumoroids. In this case we advise a short treatment with 5 μ M Nutlin-3a (5–7 days). Nutlin-3a kills P53-proficient cells and, as the lines we describe in this paper are P53-deficient, treatment with Nutlin-3a will make sure to eliminate non-tumor cells.

Problem 2

When tumoroids are larger, it can be difficult to dissociate them into single cells.

Potential solution

To help dissociate bigger tumoroids, one can use a fire-polished glass pipette during incubation with TrypLE. By pipetting up and down with the glass pipette, tumoroids are subjected to mechanical dissociation. The use of a fire-polished glass pipette can also be helpful in case a tumoroid line does not respond well to the frequent use of TrypLE. We have not observed increased cell death as a result of this procedure. Note that it is important to coat the glass pipette with medium or BSA as described in preparation step 5. Coating of the glass pipette is important as tumoroids tend to stick to the pipette surface.

Problem 3

Difficult transduction of tumoroids can happen. Bigger constructs tend to be more difficult to transduce, especially in tumoroids. This can be observed when no or few cells survive antibiotic selection. To confirm the problem is not low viral titer, transduction of the same virus should be tested in 2D cells.

Potential solution

For difficult constructs, we found the use of a high virus titer to be crucial. For this, good viral production efficacy as well as viral concentration are important.

Problem 4

Engrafting of some tumoroid lines can be less efficient. This can result in a longer time before tumor outgrowth and/or in reduced penetrance.

Potential solution

In this protocol we describe the dissociation of tumoroids before transplantation. Transplantation of tumoroids that are not single cells but comprising 150–200 cells each, as previously reported in Duarte et al., (2018)³, can improve the engrafting of tumoroids. In this case, cell counting is carried out by dissociating and counting a representative well and by extrapolating cell number in the identical non-dissociated wells. This method could result in less consistent cell counting and consequently in slightly higher variability in tumor growth speed between different animals.

Problem 5

For some tumoroid lines tumor outgrowth is highly accelerated and can rapidly achieve the humane endpoint tumor size (1500 mm³) before the treatment has an effect.

Potential solution

For these lines (e.g., ORG-KB1P4R.1) we suggest starting treatment at a smaller tumor size (e.g., 40–50 mm³). The amount of tumoroid cells transplanted can also be adjusted to optimize the growth curve.

ACKNOWLEDGMENTS

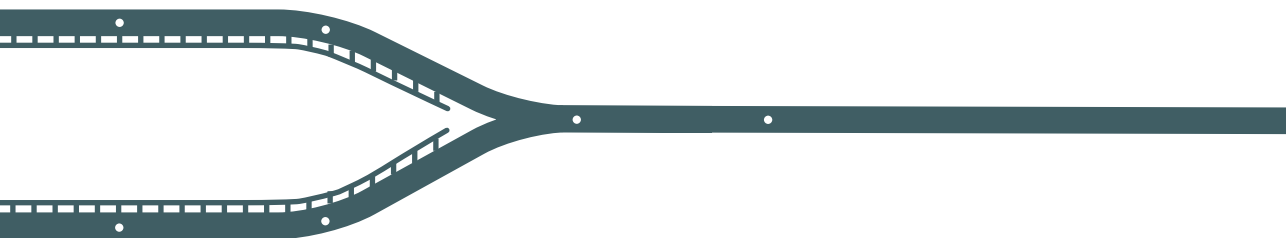
We are grateful to Dario Zimmerli (The Netherlands Cancer Institute), Paola Francica (University of Bern), and Emilia Pulver (The Netherlands Cancer Institute) for critical reading of the protocol. We thank Anne Paulien Drenth (The Netherlands Cancer Institute), Eline van der Burg (The Netherlands Cancer Institute), and the NKI Animal laboratory facility for providing the images of orthotopic transplantation of tumoroids. Our work is supported by grants from the European Union Horizon 2020 research and innovation program (agreement 722729), the European Research Council (ERC-2019-AdG-883877), Oncode Institute, the Swiss National Science Foundation (310030_179360), and the Swiss Cancer League (KLS-4282-08-2017). We would like to thank the NKI Genomics Core facility, NKI Robotics, and Screening Center, NKI Preclinical Intervention Unit and Animal laboratory facility for technical assistance.

AUTHOR CONTRIBUTIONS

M.P.D. wrote the manuscript and prepared figures. S.R. and J.J. supervised the project and reviewed/edited the manuscript.

REFERENCES

1. Paes Dias, M., Moser, S. C., Ganesan, S. & Jonkers, J. Understanding and overcoming resistance to PARP inhibitors in cancer therapy. *Nature Reviews Clinical Oncology* 1–19 (2021).
2. Paes Dias, M. *et al.* Loss of nuclear DNA ligase III reverts PARP inhibitor resistance in BRCA1/53BP1 double-deficient cells by exposing ssDNA gaps. *Mol. Cell* (2021).
3. Duarte, A. A. *et al.* BRCA-deficient mouse mammary tumor organoids to study cancer-drug resistance. *Nat. Methods* **15**, 134–140 (2018).
4. Annunziato, S. *et al.* Comparative oncogenomics identifies combinations of driver genes and drug targets in BRCA1-mutated breast cancer. *Nat. Commun.* 2019 101 **10**, 1–12 (2019).
5. Follenzi, A., Ailles, L. E., Bakovic, S., Geuna, M. & Naldini, L. Gene transfer by lentiviral vectors is limited by nuclear translocation and rescued by HIV-1 pol sequences. *Nat. Genet.* **25**, 217–222 (2000).
6. Koo, B.-K. *et al.* Controlled gene expression in primary Lgr5 organoid cultures. *Nat. Methods* **9**, (2012).
7. Xu, G. *et al.* REV7 counteracts DNA double-strand break resection and affects PARP inhibition. *Nature* **521**, 541–544 (2015).
8. Li, W. *et al.* MAGeCK enables robust identification of essential genes from genome-scale CRISPR/Cas9 knockout screens. *Genome Biol.* **15**, 554 (2014).
9. Mcmillin, D. W., Negri, J. M. & Mitsiades, C. S. The role of tumour-stromal interactions in modifying drug response: Challenges and opportunities. *Nature Reviews Drug Discovery* **12**, (2013).
10. Boelens, M. C. *et al.* PTEN Loss in E-Cadherin-Deficient Mouse Mammary Epithelial Cells Rescues Apoptosis and Results in Development of Classical Invasive Lobular Carcinoma. *Cell Rep.* **16**, 2087–2101 (2016).
11. Derksen, P. W. B. *et al.* Somatic inactivation of E-cadherin and p53 in mice leads to metastatic lobular mammary carcinoma through induction of anoikis resistance and angiogenesis. *Cancer Cell* **10**, 437–449 (2006).



Chapter 7

General discussion and conclusions

The successful development of PARP inhibitors (PARPi) to target *BRCA1/2*-mutant cancers provides breakthrough evidence that exploiting synthetic lethal interactions is a promising therapeutic strategy that could be applicable to several cancers. Nonetheless, as with all targeted therapies that have entered the clinic, PARPi resistance is common and develops through multiple mechanisms. The major focus of this thesis is to understand the molecular mechanisms behind PARPi resistance and to find potential therapeutic targets that could be exploited to design combination treatment regimens that inhibit or delay resistance.

PARPi AS SINGLE-AGENT THERAPY – IS IT ENOUGH?

Over the past 14 years, multiple mechanisms of PARPi resistance have been identified and characterized. Even though the clinical relevance is yet to be confirmed for most mechanisms, they suggest that tumor cells can find several ways to escape PARPi therapy. As discussed in **Chapter 2**, most clinical trials testing PARPi have been initiated within the past few years and thus progression-free survival (PFS) is currently the most widely used primary outcome in these studies whereas overall survival (OS) data remain limited. One of the few pieces of evidence that PARPi can improve OS comes from a preplanned OS analysis on the phase III SOLO2 trial, which demonstrated that maintenance treatment with olaparib extends the median OS of patients with relapsed platinum-sensitive advanced-stage *BRCA1/2*-mutant ovarian cancer by 12.9 months in comparison to placebo¹. Nevertheless, the OS benefit remains to be determined for other PARPi and for other indications. Although emerging data show that PARPi delay disease recurrence and prolong OS in certain settings, the lack of prolonged responses in patients receiving PARPi points towards acquired mechanisms of resistance to single-agent therapy, highlighting the need for rational combination treatments. The use of combination therapies aimed at further amplifying the antitumor efficacy of PARPi, such as indirect inhibition of homologous recombination (HR), abrogation of cell-cycle checkpoint signaling or immunotherapy, targeting acquired vulnerabilities of resistant cells (e.g., the increased sensitivity of 53BP1- and PARG-deficient cells to ionizing radiation), and suppressing the mutator phenotype of *BRCA1/2*-mutated tumors with inhibitors of POLQ are promising approaches to tackle PARPi resistance (**Chapter 2**). Overall, PARPi as single-agents may not lead to prolonged responses and complete tumor eradication, but there are several approaches that can be explored to improve this promising targeted therapy in order to reduce the mortality rate in patients with *BRCA1/2*-mutated tumors.

PREDICTION OF PARPi RESPONSE AND DETECTING RESISTANCE

Currently, four different PARPi have been approved for the treatment of ovarian, breast,

prostate and pancreatic cancer. In these settings, biomarkers such as sensitivity to platinum-based chemotherapy, *BRCA1/2* mutations and HR deficiency (HRD) tests enable patient selection for PARPi therapy. Nevertheless, these biomarkers may fail to provide an accurate functional status of HR or predict the benefit from PARPi therapy. Recent studies have explored the clinical utility of RAD51 nuclear foci as a surrogate marker of HR activity and predictor of PARPi response, and found that RAD51 foci detection in tumor cells derived from established patient-derived xenograft models from breast, ovarian and pancreatic cancers recapitulated patient HRD status and treatment response²⁻⁵. Moreover, The RAD51 test showed higher accuracy than HR gene mutations and genomic HRD analysis for predicting PARPi response.

Close monitoring of treatment response and early detection of PARPi-resistant subclones are crucial to the success of a treatment regimen. Studies testing the clinical utility of RAD51 nuclear foci also found that this method captured dynamic changes in HR status upon acquisition of PARPi resistance². However, RAD51 nuclear foci as tool for detecting acquired resistance also has potential limitations as pointed out by our work, where we show that PARPi resistance can be triggered independently of HR, in both *BRCA1*- and *BRCA2*-mutated tumors (**Chapter 3, Fig1**). Moreover, standard tumor biopsy sampling, required for RAD51 nuclear foci detection, is typically invasive and thus often cannot be conducted on a regular basis. Therefore, non-invasive methods of assessing tumor genomics using blood or plasma samples, such analysis of circulating tumor DNA (ctDNA) in liquid biopsies, are being investigated, as these can be performed serially and might provide a better indication of tumor heterogeneity and emergence of therapy-resistant subclones (**Chapter 2, Box 3**). Although further research is required, liquid biopsies and ctDNA based assays could provide a fast and cost-effective method for early detection of known alterations associated with PARPi resistance, eventually indicating the need for further treatment. Finally, monitoring of PARPi treatment response in patients will also generate molecular data that may be used to assess the clinical relevance of the various PARPi resistance mechanisms identified in preclinical studies.

HR-RESTORATION VIA LOSS OF 53BP1 EMERGES AS A CRUCIAL RESISTANCE MECHANISM IN *BRCA1*-DEFICIENT TUMORS

To date, the best clinically documented mechanism of resistance is (epi)genetic reactivation of *BRCA1/2* function. This is most likely because most clinical data are from trials testing PARPi as second-line therapy following first-line treatment with platinum-based chemotherapies. Since *BRCA1/2* reactivation has been shown to be the dominant mechanism of platinum resistance in *BRCA1/2*-mutated tumors, patients who received first-line platinum therapy may have already developed *BRCA1/2*-proficient tumor subclones, which are cross-resistant to PARPi. It is thus conceivable that the landscape of PARPi resistance mechanisms will be

different in patients who receive PARPi as first-line therapy. Evaluation of the relevance of previously reported BRCA1/2-independent PARPi resistance mechanisms in a realistic and experimentally tractable preclinical *in vivo* setting is therefore warranted. In **Chapter 3**, we used a collection of matched PARPi-naïve and PARPi-resistant mammary tumors derived from genetically engineered mouse models (GEMMs) of *BRCA1/2*-associated breast cancer. These panels of tumors were generated by treating tumor-bearing mice with PARPi until they spontaneously developed resistance. Analysis of these tumors showed that PARPi resistance via restoration of HR occurred in the majority of BRCA1-deficient tumors but in none of the BRCA2-deficient tumors (**Chapter 3, Fig. 1**). Moreover, we found that nearly half of the HR-restored tumors could be explained by downregulation or loss-of-function mutations in 53BP1 whereas loss of other DNA double-strand break (DSB) end-protection factors was only sporadically observed (**Chapter 3, Fig. 2**). In line with this, PARPi resistance induced by 53BP1 loss is much stronger than resistance induced by depletion of *Shld1/2* or *Ctcf1* in BRCA1-deficient mouse mammary tumors^{6,7}. Loss of 53BP1 has also been observed in patient-derived tumor xenografts with acquired resistance to PARPi, and mutations in *TP53BP1* have been reported in tumor biopsies from patients with metastatic BRCA1-associated breast cancer receiving PARPi, providing additional evidence that loss of 53BP1 may play an important role in driving resistance in the clinic^{3,8,9}. Altogether, these data suggest BRCA1-deficient tumors treated with PARPi are under high selective pressure to restore HR and if they cannot reactivate BRCA1, HR restoration via 53BP1 loss will most likely be the prevalent mechanism of PARPi resistance, stressing the need to design treatment strategies to combat 53BP1 loss-mediated resistance. In this thesis, we discuss potential strategies to overcome 53BP1 loss-mediated resistance in **Chapter 2**, and used functional genetic screens to identify vulnerabilities of BRCA1/53BP1 double-deficient cells in **Chapters 4 and 5**.

FUNCTIONAL GENETIC SCREENS AS TOOLS TO UNDERSTAND PARPi RESPONSE AND IDENTIFY CANDIDATE DRUG TARGETS

In this thesis, we performed several functional genetic screens with the purpose of finding novel PARPi resistance mechanisms and candidate therapeutic targets to improve PARPi response. In **Chapters 3, 4 and 5**, we carried out enrichment as well as dropout screens, using focused and genome-wide shRNA and CRISPR knockout (CRISPRko) libraries, in different mouse and human cell line models. Together, our work shows that functional genetic screens provide a powerful unbiased discovery tool for identifying genes that modulate PARPi response. Importantly, several considerations should be made regarding the choice of perturbations and the model systems, in order to improve chances of validation and the translational value of the identified factors.

Screens using CRISPRko libraries have been shown to outperform those using shRNA libraries, mostly due to their reduced off-target effects¹⁰. Moreover, screens using shRNA technology might miss potential hits that would be detected with CRISPRko technology, since gene downregulation may result in no or a weaker phenotype compared to gene deletion. Another advantage of CRISPR/Cas9 technology is the fast and cost-effective development of customized CRISPRko libraries for secondary validation screens, which can be very powerful to further prioritize hits from the initial screen (**Chapter 5**). Nevertheless, our work shows that shRNA library screens may also have some advantages because they can probe both non-essential and essential genes, allowing identification of essential genes that modulate PARPi response upon shRNA-mediated downregulation. For example, since complete loss of mitochondrial LIG3 activity is lethal, we wouldn't have identified LIG3 as a modulator of PARPi response if the screens were carried out using a CRISPRko library. This is not only the case for LIG3, but for several DNA damage response (DDR)-associated genes. Additionally, gene downregulation allows residual protein expression which more closely resembles the effect of a chemical inhibitor, and is therefore more suitable to look for therapeutic targets. The recent development of CRISPR interference (CRISPRi), which allows for sequence-specific repression of gene expression, combines the advantages of CRISPR technology with the benefits of gene downregulation. Lastly, gain-of-function screens, such as CRISPR activation (CRISPRa) screens, are still largely unexplored. CRISPRa screens have the potential to find gain-of-function factors driving PARPi resistance, which could potentially be therapeutically targeted to combat or prevent resistance.

In addition to the screening library, the results yielded by the screen will also depend on the model system in which the screen is performed. For example, in the screens carried out in **Chapter 4**, LIG3 was the only overlapping hit in embryonic stem cells and mammary tumoroids, even though both models were deficient for BRCA1, p53 and 53BP1. Similarly, the hits from the focused screens in **Chapters 3** and **5** showed limited overlap between the cell lines used. Thus, it is important to consider carrying out the same screen in several relevant model systems in order to identify common hits and avoid pursuing candidates that are model/cell line-specific.

Besides screening in multiple models, choosing *in vitro* models that better represent how cells grow *in vivo* also increases the chances of making clinically relevant discoveries. In **Chapter 6**, we described a detailed protocol for screening in three-dimensional (3D) mouse mammary tumor-derived organoids (tumoroids). Compared to 2D cell line models, 3D tumoroids retain crucial *in vivo* features, such as morphology and 3D structure, and are able to recapitulate drug response of the original tumor from which they were derived¹¹. Nevertheless, screens in tumoroids still don't capture all the biological processes present in tumors in patients. For example, a drawback of screens in 3D tumoroid lines (and other *in vitro* culture systems) is the lack of stromal cells including immune cells. This prevents screening for factors involved in tumor-microenvironment interactions, which have been found to influence PARPi response^{12–14}. Indeed, in **Chapter 3** we found increased immune

infiltration in PARPi-resistant BRCA1-deficient tumors that did not restore HR (**Chapter 3, Fig. 3**). Moreover, tumoroids derived from one of our PARPi-resistant BRCA1-deficient tumors did not recapitulate PARPi resistance *in vitro* but upheld PARPi resistance *in vivo*, suggesting PARPi resistance in this tumor may be driven via cell-extrinsic mechanisms¹¹. Together, these results underscore the importance of screening in model systems that adequately recapitulate the complexities of the tumor microenvironment, such as co-culture systems with stromal elements (e.g., fibroblasts, immune cells^{14–18}). Another disadvantage of *in vitro* models, including 3D tumoroids, is the non-physiological medium composition, which make it difficult to screen for metabolic pathways, such as oxidative phosphorylation and fatty acid metabolism, found to be upregulated in PARPi-resistant BRCA2-deficient tumors (**Chapter 3, Fig. 4**). In line with this, the genome-wide screen carried out in **Chapter 5** identified several subunits from mitochondrial Complex I as modulators of PARPi response, but these results could not be reproduced in the secondary screens with focused libraries, nor in individual validation experiments, most likely due to variations in cell density and medium conditions across experiments. Hence, while 3D model systems better mimic *in vivo* conditions and offer certain advantages for functional genetic screens, current technologies still fail to fully recapitulate the *in vivo* physiological environment.

The need to perform functional genetic screens in cancer models that more accurately recapitulate human disease, including the tumor microenvironment and the interactions between different cell types, makes *in vivo* screens particularly attractive. To date, the majority of *in vivo* CRISPR screens have aimed to investigate cancer phenotypes (e.g., tumor initiation, metastasis) and the use of *in vivo* screens to study modulators of therapy response remains largely unexplored. *In vivo* screens can be performed by directly delivering the CRISPR library to the animal or by transplanting cancer cell lines or organoids that were modified with the CRISPR library *in vitro*. Direct *in vivo* gene editing in somatic cells enables screens in tumor cells that originated *de novo* from endogenous cells. For example, *in vivo* CRISPR knockout screens have been performed in genetically engineered mouse models (GEMMs) of *Brat*^{*Δ600E*}- or *Kras*^{*G12D*}-driven lung cancer to identify modulators of response to immunotherapy and carboplatin^{19,20}. These studies used pooled libraries in which the constructs harbor a sgRNA for CRISPR-mediated gene editing as well as cre-recombinase for tumor initiation. A similar approach could involve intraductal injection of a lentiviral sgRNA-Cre library in GEMMs of BRCA1/2-deficient breast cancer to study PARPi response *in vivo*^{21–24}.

A limitation of direct *in vivo* approaches is the difficulty in predicting the number of tumor-initiating cells that are being targeted, which makes it challenging to calculate the multiplicity of infection (MOI) required to maintain adequate representation of the library *in vivo*. Such technical parameters are more easily achievable in transplant-based screens using tumor-derived cell lines or organoids. Another advantage of *in vivo* CRISPR screens using transplantable models is that it allows screening in diverse genetic contexts without the need of a pre-existing GEMM. There are a few studies that used *in vivo* CRISPR screens

to study drug response by transplanting mouse cancer cell lines into immunocompetent animals. For example, one study carried out an *in vivo* CRISPRko screen by transplanting the murine B16 melanoma cell line into syngeneic immunocompetent mice to identify genes that modulate response to immunotherapy²⁵. Another report used CRISPRa *in vivo* screens to study resistance to temozolomide by transplanting a murine acute B-cell lymphoblastic leukemia cell line into syngeneic immunocompetent animals²⁶. GEMM-derived mammary tumoroids retain key characteristics of the original tumor (e.g., morphology, treatment response) and can be easily manipulated *in vitro* and subsequently orthotopically engrafted with high efficiency¹¹. They are therefore promising tools to perform *in vivo* CRISPR screens to identify modulators of PARPi response (**Chapter 6**). Importantly, library size remains a limiting factor in both direct and transplant-based *in vivo* CRISPR screening approaches, as high-complexity screens can require large numbers of recipient mice in order to maintain the desired library coverage (which is usually higher in dropout screens than in enrichment screens).

Altogether, *in vivo* CRISPR screens are a powerful tool that enables the identification of factors modulating therapy response in physiological conditions. Developing and optimizing technologies for *in vivo* screens in immunocompetent animals is therefore important to further unravel the biological processes underlying PARPi response and to enhance the translational relevance of our findings.

POTENTIAL USE OF LIG3 INHIBITORS TO IMPROVE PARPi RESPONSE

In **chapter 4**, functional genetic screens performed in cells and tumoroids identified depletion of LIG3 as an enhancer of PARPi toxicity in BRCA1-deficient cells. The improved response to PARPi mediated by LIG3 depletion was dependent on BRCA1 deficiency but independent of the loss of 53BP1-RIF1-shieldin pathway. In line with these observations, LIG3 depletion enhanced the efficacy of PARPi against BRCA1-deficient and BRCA1/53BP1 double-deficient mammary tumors in mice. Together, these results highlight LIG3 as a potential therapeutic target to improve response to PARPi and possibly inhibit or delay emergence of resistance. Our work also showed that LIG3 loss promotes formation of MRE11-mediated post-replicative single-stranded DNA (ssDNA) gaps in PARPi-exposed BRCA1-deficient and BRCA1/53BP1 double-deficient cells, ultimately leading to an accumulation of chromosomal abnormalities. These observations, together with work from Cong and colleagues, reveal ssDNA gap exposure as a vulnerability in BRCA1/2-deficient cells and as a predictor of PARPi sensitivity, and propose targeting LIG3 (and ssDNA gap suppression) as a novel approach to improve response to PARPi²⁷. In support of the latter, we found LIG3 to be overexpressed in a portion of triple-negative breast cancers and in serous ovarian cancers, suggesting that LIG3 could possibly be targeted in these cancer types, which are often HR-

deficient and therefore treated with PARPi in the clinic.

The *LIG3* gene encodes both mitochondrial and nuclear protein isoforms²⁸. Mitochondrial LIG3 is essential for cellular viability as it ensures mtDNA integrity, and consequently, complete loss of *Lig3* results in cell death and early embryonic lethality in mice²⁹. In contrast, nuclear LIG3 has been shown to be dispensable for cell viability³⁰. Targeting both nuclear and mitochondrial isoforms of LIG3 with small-molecule inhibitors might therefore result in undesirable toxicity. Importantly, our work shows that loss of the nuclear LIG3 isoform is sufficient to improve response of BRCA1/53BP1 double-deficient cells to PARPi, indicating that PARPi-resistance in these cells is mediated by nuclear LIG3. Moreover, shRNA-mediated depletion of LIG3 (which targets both mitochondrial and nuclear LIG3) had no or minor effects on cell growth and did not affect tumor growth in mice (**Chapter 4, Fig. 2, 6 and supplementary Fig. 4**), indicating that low levels of mitochondrial LIG3 are sufficient for cell survival. Hence, while complete loss of LIG3 is detrimental for normal cells, it is conceivable that reducing LIG3 activity with selective inhibitors might result in a clinically useful therapeutic window. Indeed, several inhibitors for other DDR targets that are essential for normal cell viability, such as ATR and WEE1 inhibitors, have been developed as anti-cancer drugs and are currently evaluated in clinical trials³¹. Lastly, toxicity derived from loss of mitochondrial LIG3 can be mitigated by targeting the BRCT domain, which is crucial for nuclear LIG3-mediated DNA repair and required for LIG3-mediated PARPi resistance in BRCA1/53BP1 double-deficient cells (**Chapter 4, Fig. 2**), but dispensable for mitochondrial DNA repair. Further experiments are ongoing to assess the effect of mutations in the catalytic and BRCT domain of *LIG3* in the response to PARP inhibition, *in vitro* and *in vivo*. Altogether, our work shows that pharmacological inhibition of LIG3 activity, or other strategies that increase exposure to ssDNA gaps, may constitute a novel approach to counteract PARPi resistance and thereby improve progression-free survival of patients.

ssDNA GAPS AS KEY DETERMINANTS OF PARPI RESPONSE

Until recently, the synthetic lethality observed between PARPi and *BRCA1/2* mutations has been attributed to two key functions of BRCA1 and BRCA2 during DNA replication: (i) their requirement for error-free repair of DSBs via HR and (ii) their role in the protection of stalled replication forks from degradation by nucleases³². By showing that depletion of LIG3 resensitizes HR-proficient BRCA1/53BP1 double-deficient cells to PARPi by exposing ssDNA gaps behind replication forks, our work (**Chapter 4 and Chapter 4 addendum**) and that of others revealed a third role of BRCA1 (and BRCA2) in post-replicative ssDNA gap suppression²⁷. Importantly, the induction of PARPi-mediated ssDNA gap exposure in LIG3-depleted BRCA1/53BP1 double-deficient cells was not a result of decreased HR, indicating that HRD does not fully explain PARPi response. Moreover, depletion of BRIP1,

which phenocopies loss of BRCA1 in regards to its HR and fork protection (FP) functions, does not result in exposure to PARPi-induced ssDNA gaps, which goes in line with the (unexpected) lack of response of BRIP1-deficient cells to PARPi²⁷. Further evidence that PARPi sensitivity cannot be explained by HRD and loss of FP alone arises from observations in Fanconi anemia (FA) patient fibroblasts that carry a dominant RAD51 mutant allele, RAD51-T131P, which was reported to destabilize RAD51 nucleofilaments, leading to unscheduled nucleolytic processing of replicating DNA^{33–35}. Unexpectedly, RAD51-T131P cells are HR proficient but sensitive to PARPi, suggesting that the FP defect underlies the sensitivity^{27,33}. However, restoration of fork protection by depletion of RADX did not render cells resistant to PARPi^{27,36,37}. Instead, PARPi-exposed RAD51-T131P cells displayed increased ssDNA gap exposure which was not reduced upon depletion of RADX, hinting that PARPi-sensitivity of these cells was due to their inability to suppress PARPi-induced ssDNA gaps²⁷. Altogether, these data indicate that PARPi-mediated ssDNA gap exposure can explain PARPi response in models in which HR and FP cannot.

It remains unclear, however, if PARPi toxicity stems only from DNA replication-associated ssDNA gaps and if HR and FP can be uncoupled from PARPi response. To understand if ssDNA gaps are better predictors of PARPi response than HR or FP, one should measure PARPi-mediated ssDNA gap formation in all available HR-deficient models of PARPi resistance, as well as in BRCA1/2- and/or HR-proficient PARPi-sensitive cells (e.g., cells deficient for PBRM1, ARID1A or PTEN, which have been reported to be sensitive to PARPi)^{32,38–40}. Finally, while the ssDNA gap model remains to be validated in the clinic, one could test the potential clinical relevance of using ssDNA gaps as PARPi response predictors by analyzing PARPi-mediated ssDNA exposure in tumoroids derived from matched PARPi-naïve and PARPi-resistant PDX tumors or the mouse mammary tumors described in **Chapter 3**. If loss of ssDNA gap suppression stands as an ideal PARPi response biomarker, it could improve patient stratification and broaden the range of cancers eligible for PARPi therapy.

CONCLUSIONS

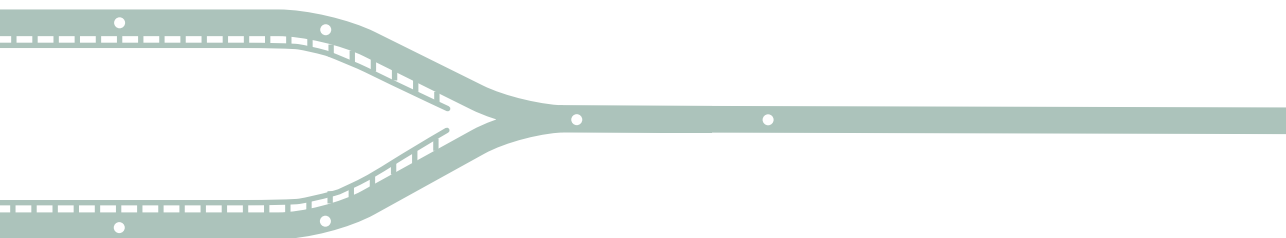
Understanding the biology of PARPi response and resistance in HR-deficient cancers will enable the development of rational treatment strategies to prevent and/or delay the onset of resistance and will ultimately lead to improved outcomes for patients. This thesis contributed to these efforts by providing an unbiased and effective assessment of the contribution of previously reported BRCA1/2-independent resistance mechanisms in an experimentally tractable preclinical *in vivo* setting; and by identifying several candidate genes and pathways that could potentially be exploited in the clinic to improve PARPi response, such as inhibition of LIG3 and ssDNA gap suppression. Moreover, we show that functional genetic screens are key to advance our knowledge on PARPi response and resistance, and that, in order to improve translational value of the results from these screens, it is important to perform

screens in multiple models and to invest in the optimization of *in vivo* screens. Finally, emerging data show that PARPi delay disease recurrence and can prolong OS in certain settings; however, most patients receiving PARPi will ultimately develop progressive disease. It will therefore be important to determine which mechanisms drive PARPi resistance in patients, and whether improvements in PFS and OS can be achieved by giving PARPi earlier in the course of treatment.

REFERENCES

1. Poveda, A. *et al.* Olaparib tablets as maintenance therapy in patients with platinum-sensitive relapsed ovarian cancer and a BRCA1/2 mutation (SOLO2/ENGOT-Ov21): a final analysis of a double-blind, randomised, placebo-controlled, phase 3 trial. *Lancet Oncol.* **2045**, 1–12 (2021).
2. Pellegrino, B. *et al.* Preclinical In Vivo Validation of the RAD51 Test for Identification of Homologous Recombination-Deficient Tumors and Patient Stratification. *Cancer Res.* **82**, 1646–1657 (2022).
3. Cruz, C. *et al.* RAD51 foci as a functional biomarker of homologous recombination repair and PARP inhibitor resistance in germline BRCA-mutated breast cancer. *Ann. Oncol.* **29**, 1203–1210 (2018).
4. Castroviejo-Bermejo, M. *et al.* A RAD51 assay feasible in routine tumor samples calls PARP inhibitor response beyond BRCA mutation. *EMBO Mol. Med.* **10**, e9172 (2018).
5. Llop-Guevara, A. *et al.* Identification of homologous recombination deficiency (HRD) by RAD51 in a tumor molecular profiling program for precision medicine.
6. Noordermeer, S. M. *et al.* The shieldin complex mediates 53BP1-dependent DNA repair. *Nature* **560**, 117–121 (2018).
7. Barazas, M. *et al.* The CST Complex Mediates End Protection at Double-Strand Breaks and Promotes PARP Inhibitor Sensitivity in BRCA1-Deficient Cells. *Cell Rep.* **23**, 2107–2118 (2018).
8. Dev, H. *et al.* Shieldin complex promotes DNA end-joining and counters homologous recombination in BRCA1-null cells. *Nat. Cell Biol.* **20**, 954–965 (2018).
9. Waks, A. G. *et al.* Reversion and non-reversion mechanisms of resistance to PARP inhibitor or platinum chemotherapy in BRCA1/2-mutant metastatic breast cancer. *Ann. Oncol.* **31**, 590–598 (2020).
10. Evers, B. *et al.* CRISPR knockout screening outperforms shRNA and CRISPRi in identifying essential genes. (2016).
11. Duarte, A. A. *et al.* BRCA-deficient mouse mammary tumor organoids to study cancer-drug resistance. *Nat. Methods* **15**, 134–140 (2018).
12. Pantelidou, C. *et al.* PARP Inhibitor Efficacy Depends on CD8 + T-cell Recruitment via Intratumoral STING Pathway Activation in BRCA-Deficient Models of Triple-Negative Breast Cancer. *Cancer Discov.* **9**, 722–737 (2019).
13. Pellegrino, B. *et al.* PARP inhibition increases immune infiltration in homologous recombination repair (HRR)-deficient tumors. *Ann. Oncol.* **30**, v760 (2019).
14. Mehibel, M. *et al.* Modulating the tumor microenvironment to enhance efficacy of PARP inhibitors. *J. Clin. Oncol.* **37**, e14715–e14715 (2019).
15. Dijkstra, K. K. *et al.* Generation of Tumor-Reactive T Cells by Co-culture of Peripheral Blood Lymphocytes and Tumor Organoids. *Cell* **174**, 1586–1598.e12 (2018).
16. Cattaneo, C. M. *et al.* Tumor organoid–T-cell coculture systems. *Nat. Protoc.* **2019 151** **15**, 15–39 (2019).
17. Liu, J. *et al.* Cancer-Associated Fibroblasts Provide a Stromal Niche for Liver Cancer Organoids That Confers Trophic Effects and Therapy Resistance. *CMGH* **11**, 407–431 (2021).
18. Joung, J. *et al.* CRISPR activation screen identifies BCL-2 proteins and B3GNT2 as drivers of cancer resistance to T cell-mediated cytotoxicity. *Nat. Commun.* **13**, (2022).
19. Li, C. *et al.* Quantitative in vivo analyses reveal a complex pharmacogenomic landscape in lung adenocarcinoma. *Cancer Res.* **81**, 4570–4580 (2021).
20. Dervovic, D. *et al.* In vivo CRISPR screens reveal Serpinb9 and Adam2 as regulators of immune therapy response in lung cancer. *bioRxiv* 2022.03.13.484176 (2022).
21. Liu, X. *et al.* Somatic loss of BRCA1 and p53 in mice induces mammary tumors with features of human BRCA1-mutated basal-like breast cancer. *Proc. Natl. Acad. Sci.* **104**, 12111–12116 (2007).
22. Jonkers, J. *et al.* Synergistic tumor suppressor activity of BRCA2 and p53 in a conditional mouse model for breast cancer. *Nat. Genet.* **29**, 418–425 (2001).
23. Annunziato, S. *et al.* Comparative oncogenomics identifies combinations of driver genes and drug targets in BRCA1-mutated breast cancer. *Nat. Commun.* **2019 101** **10**, 1–12 (2019).
24. Annunziato, S. *et al.* Modeling invasive lobular breast carcinoma by CRISPR/Cas9-mediated somatic genome editing of the mammary gland. *Genes Dev.* **30**, 1470–1480 (2016).
25. Manguso, R. T. *et al.* In vivo CRISPR screening identifies Ptpn2 as a cancer immunotherapy target. *Nature* **547**, 413–418 (2017).
26. Brauna, C. J. *et al.* Versatile in vivo regulation of tumor phenotypes by dCas9-mediated transcriptional perturbation. *Proc. Natl. Acad. Sci. U. S. A.* **113**, E3892–E3900 (2016).
27. Cong, K. *et al.* Replication gaps are a key determinant of PARP inhibitor synthetic lethality with BRCA deficiency. *Mol. Cell* (2021).
28. Lakshminpathy, U. & Campbell, C. The human DNA ligase III gene encodes nuclear and mitochondrial proteins. *Mol. Cell. Biol.* **19**, 3869–76 (1999).
29. Puebla-Osorio, N., Lacey, D. B., Alt, F. W. & Zhu, C. Early Embryonic Lethality Due to Targeted Inactivation of

- DNA Ligase III. *Mol. Cell. Biol.* **26**, 3935–3941 (2006).
30. Simsek, D. *et al.* Crucial role for DNA ligase III in mitochondria but not in Xrcc1-dependent repair. *Nature* **471**, 245–8 (2011).
 31. Pilié, P. G., Tang, C., Mills, G. B. & Yap, T. A. State-of-the-art strategies for targeting the DNA damage response in cancer. *Nature Reviews Clinical Oncology* **16**, 81–104 (2019).
 32. Paes Dias, M., Moser, S. C., Ganesan, S. & Jonkers, J. Understanding and overcoming resistance to PARP inhibitors in cancer therapy. *Nature Reviews Clinical Oncology* 1–19 (2021).
 33. Wang, A. T. *et al.* A Dominant Mutation in Human RAD51 Reveals Its Function in DNA Interstrand Crosslink Repair Independent of Homologous Recombination. *Mol. Cell* **59**, 478–490 (2015).
 34. Zadorozhny, K. *et al.* Fanconi-Anemia-Associated Mutations Destabilize RAD51 Filaments and Impair Replication Fork Protection. *Cell Rep.* **21**, 333–340 (2017).
 35. Mijic, S. *et al.* Replication fork reversal triggers fork degradation in BRCA2-defective cells. *Nat. Commun.* **8**, 859 (2017).
 36. Bhat, K. P. *et al.* RADX Modulates RAD51 Activity to Control Replication Fork Protection. *Cell Rep.* **24**, 538–545 (2018).
 37. Dugrawala, H. *et al.* RADX Promotes Genome Stability and Modulates Chemosensitivity by Regulating RAD51 at Replication Forks. *Mol. Cell* **67**, 374–386.e5 (2017).
 38. Chabanon, R. M. *et al.* PBRM1 Deficiency Confers Synthetic Lethality to DNA Repair Inhibitors in Cancer. *Cancer Res.* **81**, 2888–2902 (2021).
 39. Shen, J. *et al.* ARID1A Deficiency Impairs the DNA Damage Checkpoint and Sensitizes Cells to PARP Inhibitors. *Cancer Discov.* **5**, 752–767 (2015).
 40. Mendes-Pereira, A. M. *et al.* Synthetic lethal targeting of PTEN mutant cells with PARP inhibitors.



Appendices

English summary
Nederlandse samenvatting
Curriculum Vitae
List of publications

ENGLISH SUMMARY

Heterozygous germ-line mutations in *BRCA1* and *BRCA2* predispose to several types of cancer in which the remaining wild-type allele is lost. Owing to their roles in the error-free repair of DNA double-strand breaks (DSBs) via homologous recombination (HR), lack of *BRCA1/2* in these tumors results in DNA damage defects that can be specifically targeted by the inhibition of Poly-(ADP-ribose) polymerase 1 (PARP1). PARP1 is a key sensor of DNA damage and its inhibition has been shown to be synthetically lethal with deficiencies in HR, resulting in the selective killing of *BRCA1/2*-deficient tumor cells, while sparing *BRCA1/2*-proficient non-tumor cells. The success of this approach has resulted in the approval of four PARP1 inhibitors (PARPi) for the treatment of ovarian, breast, prostate and pancreatic cancers. However, drug resistance poses a major obstacle as, despite initial responses, patients receiving PARPi often develop resistance to the treatment. Understanding the molecular mechanisms behind PARPi resistance is therefore crucial to identify key determinants of PARPi response and to find combination treatment strategies to overcome resistance to PARPi by preventing, delaying or targeting resistant clones.

In this thesis, we expanded our insights into the molecular mechanisms underlying PARPi resistance by carrying out molecular profiling of mouse mammary tumors that have developed PARPi resistance *in vivo* and by conducting functional genetic screens in PARPi-resistance cell lines. **Chapter 2** provides a general introduction summarizing our current knowledge of the mechanisms behind PARPi response and resistance as well as potential strategies that might overcome PARPi resistance. In **Chapter 3**, we show that, while the restoration of HR is a frequent PARPi resistance mechanism in *BRCA1*-deficient tumors, HR cannot be reactivated in the absence of *BRCA2*. Moreover, our data suggest that 53BP1 loss is the prevalent resistance mechanism in HR-restored *BRCA1*-deficient tumors, whereas resistance in *BRCA2*-deficient tumors is mainly induced by PARG loss. In **Chapter 4** and **5**, we use functional genetic dropout screens to identify vulnerabilities of PARPi-resistant *BRCA1/53BP1* double-deficient cells that could potentially be exploited therapeutically to overcome resistance. In **Chapter 4**, we identified DNA ligase III (LIG3) as a critical mediator of PARPi resistance in *BRCA1/53BP1* double-deficient cells. We show that loss of LIG3 enhances PARPi-mediated toxicity in *BRCA1/53BP1* double-deficient cells as well as in *BRCA1*-deficient cells, rendering LIG3 a potential therapeutic target. Moreover, we show that loss of LIG3 exposes cells to MRE11-mediated post-replicative single-stranded DNA (ssDNA) gaps upon treatment with PARPi, and suggest that ssDNA gaps are a novel determinant of PARPi response. In **Chapter 5**, we generated a comprehensive list of potential therapeutic targets, including several subunits from the mitochondrial complex I (MCI) as well as multiple genes associated with DNA damage response pathways, such as *SWSAP1*. While individual validation of the MCI subunits proved technically difficult and requires further validation, we show that loss of *SWSAP1* enhances toxicity of PARPi, *in vitro* and *in vivo*. Finally, in **Chapter 6** we describe a detailed protocol for the use three-dimensional mouse tumoroids (tumor-

derived organoids) to carry out functional genetic dropout screens for the identification of new therapeutic targets and for the rapid and straightforward *in vivo* validation of these candidates.

In summary, the work described in this thesis extends our knowledge of the mechanisms behind PARPi response and resistance, and identifies potential therapeutic candidates to improve response to PARPi. In **Chapter 7**, we discuss the results of our research in the context of the current literature while highlighting some of the remaining questions.

NEDERLANDSE SAMENVATTING

Dragers van heterozygote kiembaanmutaties in *BRCA1* en *BRCA2* zijn vatbaar voor verschillende soorten kanker, waarbij het resterende wildtype allel verloren gaat. Vanwege hun rol bij het foutloos repareren van dubbelstrengs DNA-breuken via homologe recombinatie (HR), resulteert het verlies van *BRCA1/2* in deze tumoren defecten in DNA-schadeherstel die leiden tot hypergevoeligheid voor remming van poly-(ADP-ribose) polymerase 1 (PARP1). PARP1 is een belangrijke sensor van DNA-schade en de remming ervan resulteert in het selectief doden van *BRCA1/2*-deficiënte tumorcellen, terwijl de (*BRCA1/2*-proficiënte) lichaamscellen van de patiënt worden gespaard. Het succes van deze aanpak heeft geresulteerd in de goedkeuring van vier PARP-remmers (PARPi) voor de behandeling van eierstok-, borst-, prostaat- en alvleesklierkanker. Geneesmiddelresistentie vormt echter een groot obstakel, aangezien patiënten die PARPi krijgen, na een initiële respons vaak resistentie tegen de behandeling ontwikkelen. Het is daarom belangrijk om de oorzaken van de resistentie tegen PARPi te identificeren teneinde combinaties van behandelingsstrategieën te vinden om de ontwikkeling van PARPi-resistentie te voorkomen of te vertragen, of om tumoren te behandelen nadat PARPi-resistentie is opgetreden.

In dit proefschrift hebben we nieuwe inzichten in PARPi-resistentie verkregen door moleculaire profilering uit te voeren op borsttumoren bij muizen die PARPi-resistentie hebben ontwikkeld en door functionele genetische screens uit te voeren in PARPi-resistente cellijnen.

Hoofdstuk 2 biedt een algemeen overzicht van onze huidige kennis omtrent de mechanismen achter PARPi-respons en -resistentie, evenals mogelijke strategieën om PARPi-resistentie te kunnen overwinnen. In **Hoofdstuk 3** beschrijven we de PARPi-resistentiemechanismen die optreden in *BRCA1/2*-deficiënte borsttumoren die geen resistentie kunnen verwerven via reactivatie van *BRCA1/2*. We laten zien dat, hoewel het herstel van HR een frequent PARPi-resistentiemechanisme is in *BRCA1*-deficiënte tumoren, HR niet kan worden gereactiveerd in *BRCA2*-deficiënte tumoren. Bovendien suggereren onze resultaten dat 53BP1-verlies het meest voorkomende PARPi-resistentiemechanisme is in *BRCA1*-deficiënte tumoren, terwijl resistentie in *BRCA2*-deficiënte tumoren voornamelijk wordt veroorzaakt door PARG-verlies. In **Hoofdstuk 4** en **5** gebruiken we functionele genetische screens om kwetsbaarheden van PARPi-resistente *BRCA1/53BP1* dubbel-deficiënte cellen te identificeren, die mogelijk kunnen worden gebruikt om resistentie te overwinnen. In **Hoofdstuk 4** identificeren we DNA-ligase III (LIG3) als een cruciale mediator van PARPi-resistentie in *BRCA1/53BP1* dubbel-deficiënte cellen. We laten zien dat LIG3 een potentieel therapeutisch doelwit is omdat verlies van LIG3 de PARPi toxiciteit in *BRCA1*-deficiënte en *BRCA1/53BP1*-dubbel-deficiënte tumorcellen verhoogt. Bovendien laten we zien dat verlies van LIG3, cellen blootstelt aan MRE11-gemedieerde post-replicatieve gaten van enkelstrengs DNA (ssDNA) na behandeling met PARPi, en suggereren dat gaten van ssDNA een nieuwe determinant zijn van de PARPi-respons. In **Hoofdstuk 5** presenteren we een uitgebreide lijst van potentiële therapeutische 'targets', waaronder verschillende subeenheden van het mitochondriale complex I (MCI)

en genen die geassocieerd zijn met DNA-schade herstel routes, zoals *SWSAP1*. Hoewel individuele validatie van de MCI-subeenheden technisch moeilijk bleek en verdere validatie vereist, laten we zien dat verlies van *SWSAP1* de toxiciteit van PARPi verhoogt. Ten slotte beschrijven we in **Hoofdstuk 6** een gedetailleerd protocol voor het gebruik van driedimensionale muistumoroïden (van tumoren afgeleide organoïden) om functionele genetische screens uit te voeren voor de identificatie van kandidaat-targets voor nieuwe therapieën en voor snelle *in vivo* validatie van deze kandidaten.

Het in dit proefschrift beschreven werk draagt bij aan onze kennis omtrent de mechanismen achter PARPi respons en resistentie, en identificeert potentiële therapeutische kandidaten om de gevoeligheid voor PARPi te verbeteren. In **Hoofdstuk 7** bespreken we de resultaten van ons onderzoek in de context van de huidige literatuur, en belichten daarnaast enkele van de resterende vragen.

CURRICULUM VITAE

Mariana Paes Lobo Lopes Dias was born on August 29th, 1994 in Faro, Portugal. She graduated high school in 2012 to start her bachelor's degree in Cell and Molecular Biology at the NOVA University (Lisbon, Portugal). During her bachelor's, she performed internships at the Molecular Genetics Unit of the National Health Institute Doutor Ricardo (Lisbon, Portugal), learning about different molecular techniques used in molecular diagnosis of various genetic hereditary diseases; and at the lab of Prof. José António Belo at the Chronic Diseases Research Center (CEDOC) (Lisbon, Portugal), where she had her first experience in a research lab. After obtaining her degree in 2015, Mariana enrolled into the Molecular Medicine and Oncology master's degree programme of the University of Porto (Porto, Portugal). During the first year of her master's, she joined the lab of Prof. José Carlos Machado at the Instituto de Investigação e Inovação em Saúde (i3S) (Porto, Portugal) where she participated in a project aimed at studying the influence of somatic mutations on immune surveillance in colorectal cancer. She was then awarded an Erasmus+ fellowship which allowed her to join the lab of Dr. Jacqueline Jacobs at the Netherlands Cancer Institute (NKI) (Amsterdam, the Netherlands) to develop her master's degree dissertation project on the role of BRCA1-A and BRCA1-B complexes in DNA repair pathway choice, replication stress and PARPi response. She successfully defended her dissertation and graduated from her master's degree in 2017. During her last internship, Mariana became very interested in the study of DNA repair pathways and in the biological mechanisms behind the anti-cancer activity of PARPi. That is why in 2017 she started her PhD at the lab of Prof. Jos Jonkers at the Netherlands Cancer Institute (NKI) (Amsterdam, the Netherlands) where she could follow her interest in the study of PARPi response by conducting several functional genetic screens to identify mechanisms of PARPi resistance and to find potential therapeutic targets that could be exploited to improve response to PARPi treatment. The results of her work are presented in this thesis.

LIST OF PUBLICATIONS AND PREPRINTS

Multi-omics analysis reveals distinct non-reversion mechanisms of PARPi resistance in BRCA1- versus BRCA2-deficient mammary tumors

Jinhyuk Bhin*, [Mariana Paes Dias](#)*, Ewa Gogola*, Frank Rolfs, Sander R. Piersma, Roebi de Bruijn, Julian R. de Ruiter, Bram van den Broek, Alexandra A. Duarte, Wendy Sol, Ingrid van der Heijden, Lara Bakker, Taina S. Kaiponen, Cor Liefink, Ben Morris, Roderick L. Beijersbergen, Marieke van de Ven, Connie R. Jimenez, Lodewyk F. A. Wessels, Sven Rottenberg and Jos Jonkers

BioRxiv, 2022; 2022.09.07.506927, doi:10.1101/2022.09.07.506927.

Functional genetic dropout screens and *in vivo* validation of candidate therapeutic targets using mouse mammary tumoroids

[Mariana Paes Dias](#), Sven Rottenberg, Jos Jonkers

STAR Protoc., 2022; 3(1):101132, doi:10.1016/j.xpro.2022.101132.

Filling in the gaps in PARP inhibitor-induced synthetic lethality

[Mariana Paes Dias](#) and Jos Jonkers

Mol. Cell Oncol., 2021; 8(6): 2010512, doi:10.1080/23723556.2021.2010512.

Loss of nuclear DNA ligase III reverts PARP inhibitor resistance in BRCA1/53BP1 double-deficient cells by exposing ssDNA gaps

[Mariana Paes Dias](#)*, Vivek Tripathi*, Ingrid van der Heijden, Ke Cong, Eleni-Maria Manolika, Jinhyuk Bhin, Ewa Gogola, Panagiotis Galanos, Stefano Annunziato, Cor Liefink, Miguel Andujar-Sanchez, Sanjiban Chakrabarty, Graeme C.M. Smith, Marieke van de Ven, Roderick L. Beijersbergen, Jirina Bartkova, Sven Rottenberg, Sharon Cantor, Jiri Bartek, Arnab Ray Chaudhuri, and Jos Jonkers

Mol. Cell, 2021; 81, 4692-4708.e9, doi:10.1016/J.MOLCEL.2021.09.005.

Understanding and overcoming resistance to PARP inhibitors in cancer therapy

[Mariana Paes Dias](#)*, Sarah C. Moser*, Shridar Ganesan and Jos Jonkers

Nat. Rev. Clin. Oncol., 2021; 18,773–791, doi:10.1038/s41571-021-00532-x.

Feasibility of phosphoproteomics on leftover samples after RNA extraction with guanidinium thiocyanate

Frank Rolfs, Sander R. Piersma, [Mariana Paes Dias](#), Jos Jonkers, Connie R. Jimenez

Mol. Cell Proteomics, 2021; 20:100078, doi:10.1016/j.mcpro.2021.100078.

SMARCAD1-mediated active replication fork stability maintains genome integrity

Calvin Shun Yu Lo, Marvin van Toorn, Vincent Gaggioli, [Mariana Paes Dias](#), Yifan Zhu, Eleni

Maria Manolika, Wei Zhao, Marit van der Does, Chirantani Mukherjee, João G S C Souto Gonçalves, Martin E van Royen, Pim J French, Jeroen Demmers, Ihor Smal, Hannes Lans, David Wheeler, Jos Jonkers, Arnab Ray Chaudhuri , Jurgén A Martéijn, Nitika Taneja
Sci. Adv., 2021; 7(19):eabe7804, doi:10.1126/sciadv.abe7804.

